HYDRAULIC ANALYSIS OF UNSTEADY NON-UNIFORM OPEN CHANNEL FLOWS IN VIEW OF SIMPLIFIED MODELING

MANOJKUMAR NAMDEO LANGHI

2013

HYDRAULIC ANALYSIS OF UNSTEADY NON-UNIFORM OPEN CHANNEL FLOWS IN VIEW OF SIMPLIFIED MODELING

MANOJKUMAR NAMDEO LANGHI

Department of Urban Management
Kyoto University

Submitted in partial fulfillment of the requirements
for the degree of
Doctor of Philosophy

March 2013

ABSTRACT

Flows in the rivers and open channels are often unsteady non-uniform flows. Due to nature of the unsteady varied flows, the hydrodynamic properties of the flows changes in different stages of the flows. Therefore, to investigate the characteristics of such unsteady varied flows; simple, accurate and efficient numerical and analytical models are developed in this research.

A one-dimensional depth-averaged model is a convenient tool to resolve the actual problems in rivers due to its small computational loads. Concerning this view, a simple one-dimensional depth-averaged velocity deformation model is developed. The fundamental form of the streamwise velocity in a power series of depth is assumed initially, and the coefficients of the velocity are evaluated using the unsteady equation of motion. A concise form of the friction velocity for unsteady non-uniform flow is then proposed by utilizing the coefficients of the power series. The applicability of the model is validated with experimental data over smooth and rough beds. The comparisons produced reasonably good agreement between the model results and the observed data. Finally, the deformation of velocity at the surface is assured by comparing velocity distribution of numerical model with the computational results from the Engelund model.

The limitations of one-dimensional modeling in evaluation of turbulence characteristics are overcome by three-dimensional unsteady Reynolds Averaged Navier Stokes (RANS) model. The hydrodynamic properties of unsteady varied flows are examined in view of free surface effects by using the standard and non-linear k-ε model. The flow properties obtained from 3D modeling followed the same trend in smooth bed case. Although some deviations encountered in fewer properties of the flows in high unsteady case, the distributions of flow properties for small unsteady case are in good agreement with the steady state condition. In rough bed case, the comparisons between the numerical results and the experimental data produced much better agreement. The significance of non-linear k-ε model

is more pronounced for rough bed case, indicating turbulence characteristics of non-linear k-ε model are well compared to the empirical condition than the standard k-ε model.

To improve the velocity distributions in depth-averaged modeling, further analysis is performed theoretically by using the standard k-ε model. Additionally, to check the effect of the damping function in correlation with the wake law; analysis is conducted in uniform flow by including and excluding the damping function. The validity of the model is tested using numerical results of the finite difference scheme. However, very negligible effects of the damping function on velocity distribution are observed. Except on the turbulent kinetic energy, the effect of damping function on energy dissipation rate and eddy viscosity is observed through the modelled results. Nevertheless, the overall tendencies of the distributions are maintained well by the analytical results.

With the success of theoretical solution in uniform flow, non-uniform flow analysis is conducted by using the standard k-ε model. In this case, the validity of the theoretical model is verified in comparisons with the experimental data. Although some deviations observed in fewer cases, the distributions of the flow properties are acquired well by the analytical solutions. Similar to the uniform flow analysis, in this case also the distribution of kinetic energy failed to reproduce the damping effect near the free surface zone. However, the nature of the distributions of turbulent kinetic energy, energy dissipation rate and eddy viscosity satisfied the conditions of the non-uniform flows.

Following the deformation principle from first objective, an analytical solution in rapidly varied unsteady flow is performed. Initially the fundamental form of the streamwise velocity in a power series of depth is used and the dependency of the coefficients on a spatial coordinate are considered. The relations between the coefficients are later derived by using 2D continuity and momentum equations. These relations are successively utilized into the depth-averaged continuity and momentum equations to obtain the set of equations for water surface profile analysis. A simple depth-averaged flow model derived based on the deformation principle is discussed in comparison with the previous experimental data. Although further improvement is necessary, the proposed model reproduced the comparisons with the experimental data effectively.

In addition to the depth-averaged modeling, the numerical simulation of 3D unsteady RANS model by using the standard and non-linear k-ε model is conducted. The comparisons

between the numerical and the experimental data showed that the water surface profile obtained for non-linear k-ε model is exhibited more local energy dissipations. The pronounced effect of non-linearity is observed in streamwise turbulence intensity distributions. The vertical distribution of streamwise turbulence intensity for non-linear k-ε model reproduced the reasonable agreement with the theoretical data as compared to the standard k-ε model.

Finally, concerning the relationship between the Froude number and the turbulent diffusivity coefficient in a hydraulic jump case, an empirical formula is proposed. From the numerical simulation of Boussinesq equation, the applicability of the empirical relationship between the Froude number and the proportionality factor is verified. Different types of jumps are analyzed to ascertain the water surface profile evaluation. Through these assurances, the breaking processes of undular jump and transition from weak jump to strong hydraulic jump is confirmed.

ACKNOWLEDGEMENTS

I would like to express my heartfelt gratitude to my supervisor Prof. Takashi Hosoda, for his invaluable guidance, constant encouragement, talented and versed advice and helpful suggestions throughout the period of doctoral course. His kind cooperation not only in academic activities but also in extra-curricular life during my stay in Japan is beyond any repayment.

I express my sincere thanks to Assoc. Prof. Kiyoshi Kishida and Asst. Prof. Schinichiro Onda for their cooperation during the research work, the latter, especially for ensuring the availability of all software and hardware and other stationary necessary for research. I am also thankful to my lecturer-cum-colleague Dr. Puay How Tion for his assistance and fruitful discussions over many issues.

I am indebted to the examiners of my thesis, Prof. Hitoshi Gotoh and Prof. Keiichi Toda for their comments and suggestions to improve my thesis. I am grateful to Assoc. Prof. Ichiro Kimura for allowing me to use his three-dimensional code for my research work. I am also thankful to Assoc. Prof. Eiji Harada for his advice and suggestions.

I wish to convey my thanks to my tutor-cum-colleague Mr. Hidekazu Shirai for his constant help and support in all aspect. Special thanks to my senior research colleagues Mr. Fredrick Paul and Mr. Saif Al Hinai for all their assistance, during the course of my research. I would also like to thanks my Indian friends, specially Shivaji sir, Victor, Shraddha, Mahesh as well as foreign friends Mishra, Songkeart, Tian for their wonderful company in my everyday life.

I would like to take this opportunity to acknowledge my previous supervisor Prof. Subhasish Dey for his ample guidance and suggestions for pursuing some technical issues.

Special thanks also goes to my lab mates, Mr. Hamid Bashiri, Mr. Tsuyoshi Araki and all other Japanese students for their support and friendship.

Finally, I owe a great deal of love, to my parents, my sister, brothers, sister in law and brother in law, for their blessing and consistent moral support during my research.

TABLE OF CONTENTS

TABLE OF CONTENTS

LIST OF FIGURES

LIST OF TABLES

Chapter 1
INTRODUCTION

1.1 Preliminaries

Flows in the rivers and open channels are often unsteady non-uniform flows. Common examples of unsteady varied flows includes flood flows in rivers and tidal flows in estuaries, flows in irrigation channels, headrace and tailrace channel of hydropower plants, navigation canals, stormwater systems and spillway operation. Due to nature of the flows the flow processes, distributions of suspended load and bed load movements in unsteady varied flows are different from the one in steady flows (Song and Graf 1996). The behaviour of the flow also changes with the unsteadiness indicating various sediment transport properties to be different in the different stages of the flows; that is as rising and falling stages of flood flows. Investigations of hydrodynamic properties of the unsteady varied flows are therefore necessary to predict the different aspects of the flows. For instance, the distribution of velocity and Reynolds stress quantify the suspended load of sediments. On the other hand, the bed shear stress is pertinent to determine the sediment threshold and bed load of sediment (Dey and Lambert 2005). The examination of these properties is therefore important for estimation of sediment transport rate and for designing a stable channel section.

Many researchers have conducted turbulence measurements in unsteady open channel flows despite the measuring difficulties in near free surface flow zone. The varieties of techniques and instruments have been developed so far to measure the turbulence in the unsteady varied flows. These instruments are classified into different types according to their measurements principles. The descriptions of those instruments and the chronicles of turbulence in open channel flows until 1984 are reported in Nezu and Nakagawa (1993). From mid 80's onwards contributions from few researchers in turbulence measurements in

unsteady varied flows is presented herein. Hayashi et al. (1988) seems to be the first to perform experiments by using hot-film anemometer and concluded that the degree of turbulence is stronger in the rising stage than in the falling stage. Tu and Graf (1992) also measured and analyzed the unsteady flow over rough bed by using micro-propeller to verify the applicability of logarithmic and Coles' wake laws. They evaluated the friction velocity using Saint Venant equation and suggested that according to the unsteadiness, a slight modification should be taken into consideration while using logarithmic and Coles' wake laws. Song and Graf (1994), on the other hand, used acoustic Doppler velocity profiler (ADVP) to study the turbulence characteristics in steady varied flows. Not only in steady varied flows but also in unsteady flows over rough bed, Song and Graf (1996) used ADVP to obtain the instantaneous velocity profiles. Their experiments investigated thirty-three different hydrographs to characterize the flow by unsteadiness parameter and longitudinal pressure gradient parameter. Owing to the complications of turbulence measurements in unsteady open channel flows, Nezu et al. (1997) conducted the flow measurements over a smooth bed simultaneously by using two-component laser Doppler anemometry (LDA) and water-wave gauge. Their conclusions were similar to that of Hayashi et al. (1988) except very close to the free surface zone. Recently, Bagherimiyab et al. (2010) investigated the hydrodynamic aspects of unsteady (accelerating and decelerating) flows over gravel bed using acoustic Doppler and imaging methods.

Based on the understandings of the basics of the flows theoretical studies have been conducted to evaluate some of the characteristics of the unsteady varied flows. For example, Song and Graf (1994) proposed theoretical expression for friction velocity, vertical velocity and Reynolds stress distribution in non-uniform open channel flows. In addition, Song and Graf (1996) developed theoretical expression for vertical velocity and Reynolds stress distribution in unsteady flows over rough beds. On the other hand, Dey and Lambert (2005), proposed expression for Reynolds stress and bed shear stress on sloping beds in unsteady varied flows.

These chronologies (though reported only recent studies) indicated that, firstly conceptual models were designed based on the experimental investigations and mathematical models started playing role in order to distinguish the different features of the flows. In 19th century, Barre de Saint Venant and Valentin Joseph Boussinesq formulated the basic

equations in the form of partial differential equations to represent the hydraulic principles. Analytical solutions of these basic equations are nearly impossible due to their non-linearity (Chanson 2004). Instead, with the advent of computer technology, numerical techniques are used to approximate the solution of these equations.

Numerical simulation of unsteady flows in open channel flow is an important, interesting and difficult subject in hydraulic engineering. Several researchers contributed their efforts to characterize the unsteady flows numerically. For instance, Iwasa et al. (1976) conducted the numerical simulation of floods in rivers by means of method of characteristics, Lax-Wendroff scheme. Onda et al. (2004) developed simple one-dimensional model for non-uniform flows including the accelerating and decelerating effects. Recently, numerical simulation of flood flows is carried out by Hosoda et al (2010) to reproduce the previous flood flows for the case of lack of data at upstream and downstream boundary conditions. These all models simulated with the one-dimensional modeling. Moreover, with the advancements of numerical methods, numerical simulations in 2D unsteady flows are also performed. (Wu 2004; Ahmadi et al. 2009). The availability of supercomputers and the increasing popularity of turbulence modeling made the feasibility of computations of 3D flow field. (Kimura et al. 2003; Ge and Sotropoulos 2005).

These all studies indicated that the investigation of the unsteady varied flows is a subject of interest for many researchers.

1.2 Objective and justification of the Study

The main objective of this study is to develop simple, accurate and efficient models to predict the various characteristics of rivers or open channel flows.

According to Steffler and Jin (1993), one-dimensional flow does not exist in the nature actually, but equations remain valid provided the flow is approximately one-dimensional. Concerning this view and because of the small computational load of one-dimensional model, initial objective of the research is to develop a simple depth-averaged model for unsteady varied flows. Reviewing the work of Engelund (1974) in uniform flows and Onda et al. (2004) in steady non-uniform flows, the idea of development of simple depth-averaged model including the velocity deformation is emerged. The inadequacy of the previous models for the evaluation of velocity distributions in unsteady varied flows is a

primary concern of this objective. In addition, determination of the general expression for friction velocity for unsteady varied flows is an adjacent topic of the study.

Although practical depth-averaged model is a powerful tool to resolve actual problems in the rivers, it has limitations to predict the 3D turbulent flow field. This lead to study the characteristics of unsteady varied flows using 3D unsteady Reynolds Averaged Navier Stokes (RANS) model. The advantage of 3D modeling over previous one-dimensional modeling is that turbulence characteristics of the unsteady flows can be studied well by this modeling. Therefore, in order to check the flow field in consideration with the free surface effects of unsteady non-uniform flows, numerical simulation of 3D unsteady RANS model will be performed in the next objective.

The one-dimensional depth-averaged velocity deformation model will be based on the Engelund model. The deficiency of Engelund model is that, it is not in compatible with the universal logarithmic law of velocity distributions. Thus, even though depth-averaged model includes deformation principle, it is not sure that the velocity distributions obtained will be in agreement with the logarithmic velocity distributions. To resolve this kind of problem it is necessary to modify the depth-averaged model, which further provides the assurance of reproduction of hydrodynamic properties of the flows. However, before doing so, it is essential to evaluate some properties of the flows analytically. For that purpose there will not be any other good choice than using the standard k-ε turbulence model. Therefore, for further analysis objective is define to determine the analytical solution of the standard k-ε model. Additionally, the effect of damping function on velocity distribution near free surface zone will also be analyzed to correlate it with the wake law of the velocity distribution.

After analyzing the gradually varied unsteady flows, the next objective of the research is to evaluate the rapidly varied unsteady flows. Thus, the objective is set to determine the analytical solution of the hydraulic jump. Due to nature of the flow in hydraulic jump, it is difficult to determine the water surface profile of the hydraulic jump. Only few researchers (for example Madsen et al. 1983) made an attempt to explain the characteristics of hydraulic jump analytically. However, their model is based on the turbulent closure and hence, little complicated. Rather, this study will plan to use simple depth-averaged model for evaluation of water surface profile of the jump. Moreover, based on the

deformation principle, which will be used in initial objective, the velocity distributions in hydraulic jump will be determined analytically.

Undular jump is one of the fundamental phenomenons that considered the effect of vertical acceleration term. Undular jump and strong hydraulic jump are different in the sense that the continuous water surface profile is seen for undular jump. Contrary, because of intense mixing and the roller formation the breaking of the water surface is observed for the strong hydraulic jump. Thus, concerning the evaluation of water surface profile, the Boussinesq equation will be solved numerically in order to characterize the undular jump. Finally, numerical simulation will be done to describe the phenomenon of transition of the flow from undular jump to the strong hydraulic jump.

1.3 Structure of the Dissertation

In this dissertation the characteristics of the unsteady varied open channel flows are studied numerically and analytically. The main content of the dissertation are comprised into four main chapters followed by the conclusions in the last chapter. The chronological orders of the chapters are briefly described below:

In Chapter 2, development of one-dimensional depth-averaged velocity deformation model is discussed. Initially, the vertical distribution of the streamwise velocity is expressed in a power series of depth and the coefficients of the velocity are evaluated using the unsteady equation of motion. A concise form of the friction velocity for unsteady non-uniform flow is then proposed utilizing the coefficients of the power series. The applicability of the model is validated with the experimental data over smooth and rough beds. Finally, the deformation of velocity at the surface is assured by comparing the velocity distribution of numerical model with the computational results of the Engelund model.

After analyzing one of the main feature of the hydraulics in previous chapter, all other characteristics of the unsteady varied flows are explained using 3D unsteady RANS model in Chapter 3. Similar to one-dimensional modeling, two experimental cases; smooth and rough beds are used for the comparisons. Beginning with the descriptions of RANS modeling, numerical results obtained by using the standard and non-linear k-ε model are compared with each other and with the experimental data as well.

Chapter 4 described an analytical solution of the standard k-ε model. It is well known that, the damping effect of the turbulence near the free surface affects the eddy viscosity distribution indicating parabolic shape. Therefore, to examine the effect of such damping function also on the velocity distribution, analysis is conducted in uniform flow by including and excluding the damping function. The validity of the model is tested using numerical results of the finite difference scheme. The investigations of turbulence characteristics of the uniform open channel flow is not enough, because the flow encountered in the river/open channel is often non-uniform flow. Thus, to characterize the non-uniform flow, an analytical solution of the standard k-ε model for non-uniform flow is also developed in a successive step. Similar to the uniform flow case, the effect of damping function is also considered in the analysis. The validity of the theoretical model is then checked in comparisons with the experimental data.

In Chapter 5, the derivation of a simple depth-averaged flow model considering the deformation principle of velocity is explained. Similar to the one-dimensional model in Chapter 2, in this case also, the fundamental form of the streamwise velocity in a power series of depth is used. However, in this chapter additional dependency of the coefficients on a spatial coordinate is considered. The relations between the coefficients are later derived by using the two-dimensional continuity and momentum equations. These relations are then successively utilized into the depth-averaged continuity and momentum equations in order to obtain the water surface profile and velocity distribution of the hydraulic jump. The obtained model results are then discussed in comparisons with the previous experimental results. Additionally, the numerical simulation of hydraulic jump using 3D unsteady RANS model are also discussed. Likewise in Chapter 3, both the standard and non-linear k-ε model are used for the simulation. The computed results of the 3D model are verified in comparisons with the previous experimental data.

Following the continuous profile of the strong hydraulic jump, in Chapter 6, the numerical simulations for different types of jumps are performed. The strong hydraulic jump can be evaluated numerically without considering the vertical acceleration term in Boussinesq equation. However, in order to achieve the water surface profile of the undular jump, vertical acceleration term needs to take into consideration in Boussinesq equation. The numerical simulations are performed by including the proposed relationship of the Froude

number and the proportionality factor of turbulent diffusivity coefficient. Finally, by reviewing the previous studies, the transition of the flow from undular jump to the strong hydraulic jump is explained through the numerical analysis.

1.4 References

Ahmadi, M., Ayyoubzadeh, S., Namin, M., and Samani, J. (2009). "A 2D numerical depth-averaged model for unsteady flow in open channel bends. " *J. Agr. Sci. Tech*.,11, 457-468.

Bagherimiyab, F., and Lemmin, U. (2010). "Aspects of turbulence and fine sediment resuspension in accelerating and decelerating open channel flow." River Flow 2010-Dittrich, Koll, Aberle and Geisenhainer (eds), 121-127.

Chanson, H. (2004). "Environmental hydraulics of open channel flows." Elsevier Butterworth Heinemann publications, Great Britain.

Dey, S., and Lambert, F. (2005). "Reynolds stress and bed shear in non-uniform unsteady open channel flow." *J. Hydraul. Eng*., 131(7), 610-614.

Ge, L., and Sotiropoulos, F. (2005). "3D unsteady RANS modeling of complex hydraulic engineering flows. I:Numerical methods." *J. Hydraul. Eng*., 131(9), 800-808.

Hayashi, T., Ohashi, M., and Oshima, M. (1988). "Unsteadiness and turbulence structure of a flood wave." *Proc. 20th Symposium on Turbulence,* Tokyo, Japan, 154-159 (in Japanese).

Hosoda, T., Onda, S., Murakami, T., Iwata, M., Shibayama, Y., and Puay, H. T. (2010). "Flood flow simulation in the case of lack of both upstream and downstream boundary conditions." *Prof. 17th IAHR-APD Congress and 7th IUWM Conference*, Auckland, New Zealand.

Iwasa, Y., and Inoue, K. (1976). "Numerical simulation of floods by means of various methods. " *Proc. Int. Sympo. Unsteady flow in open channels*, University of Newcastle-upon-Tyne, England, K2-17-K2-25.

Kimura, I., and Hosoda, T. (2003). "A non-linear *k*-ε model with realizability for prediction of flows around bluff bodies." *Int. J. Numer. Meth. Fluids*, 42, 813-837.

Madsen, P. A., and Svendsen, I. A. (1983). "Turbulent bores and hydraulic jumps." *J. Fluid Mech*., 129, 1-25.

Nezu, I., and Nakagawa, H. (1993). Turbulence in open-channel flows. IAHR Monograph, A.A. Balkema Publishers, Rotterdam, Netherlands.

Nezu, I., Kadota, A., and Nakagawa, H. (1997). "Turbulent structure in unsteady depth varying open-channel flows." *J. Hydraul. Eng*., 123(9), 752-763.

Onda, S., Hosoda, T., and Kimura, I. (2004). "A simple model of a velocity distribution in accelerating/decelerating flows and its application to depth averaged flow model." *Shallow Flows, Proc. International Symposium on Shallow Flows*, Delft, The Netherlands, 637-644.

Song, T., and Graf, W. H. (1994). "Non-uniform open-channel flow over a rough bed." *J. Hydrosci. Hydraul. Eng*., 12(1). 1-25.

Song, T., and Graf, W. H. (1996). "Velocity and turbulence distribution in unsteady open channel flows." *J. Hydraul. Eng*., 122(3), 141-154.

Steffler, P. M., and Jin, Y. C. (1993). "Depth-averaged and moment equations for moderately shallow free surface flows. " *J. Hydraul. Resear*., 31(1), 5-18.

Tu, H., and Graf, W. H. (1992). "Velocity distribution in unsteady open channel flow over gravel beds." *J. Hydrosci. Hydraul. Eng*., 10(1), 11-25.

Wu, W. (2004). "Depth-averaged two-dimensional numerical modeling of unsteady flow and non-uniform sediment transport in open channels." *J. Hydraul. Eng*., 130(10), 1013-1024.

Chapter 2
ONE-DIMENSIONAL VELOCITY DEFORMATION MODEL FOR UNSTEADY FLOWS

2.1 Preliminaries

In natural rivers, the effect of unsteadiness plays an important role during the flood events. Various characteristics of the flow changes with the flood flow during its rising and falling stages. Therefore, an investigation of velocity distribution is essential to understand the hydrodynamic characteristics of unsteady flows in rivers. A one-dimensional depth-averaged model is a convenient way to resolve the actual problems in rivers due to its small computational load. The basic idea behind it is to assume the velocity distribution over the entire depth and to determine the bed shear stress by using the momentum equation.

Engelund (1974) proposed a theory to describe the bed topography and main features of hydraulics in meander bends with movable beds. Based on the study of Engelund (1974), Onda et al. (2004) developed simple one-dimensional model for steady non-uniform flows including the accelerating and decelerating effects. Their model and also the Engelund (1974) model did not account for the unsteadiness. Numerical simulation of flood flows was also carried out by Hosoda et al (2010). They used one-dimensional depth-averaged model to reproduce the previous flood flows for the case of lack of data at upstream and downstream boundary conditions. However, their model is tested to only the idealized flood flow.

Thus, to understand the characteristics of such unsteady flows, the aim of this chapter is to develop a simple depth-averaged velocity deformation model and to propose a concise

form of friction velocity formula. The applicability of the model is validated by using the experimental data over smooth and rough beds. The results obtained from the proposed model are also compared with the computational results of the Engelund model (EM).

2.2 Model Formulation

2.2.1 Velocity distribution

Engelund (1974) assumed that the velocity distribution along a depth follows the defect law that describe one of the main feature of the hydraulics. The model is derived on the basis of the Boussinesq approximation of the constant eddy viscosity ε in the equation of motion. Thus,

$$\frac{\tau}{\rho} = \varepsilon \frac{du}{dy}; \qquad \varepsilon = \beta u_* h, \qquad \text{and } \beta = 0.077 \tag{2.1}$$

where τ = Reynolds or turbulent shear stress; ρ = mass density of fluid; u = time-averaged streamwise velocity; y = vertical distance; β = coefficient (= 0.077); and h = flow depth. Engelund model is valid only for a steady uniform flow in a wide channel. Thus, to simulate an unsteady flow, the effect of unsteadiness of the flow in the model is incorporated.

Initially, for one-dimensional flow, the fundamental form of the distribution of streamwise velocity along vertical is expressed as a power series of dimensionless depth as

$$\frac{u}{U} = u_0 + u_1\eta + u_2\eta^2 + u_3\eta^3 + u_4\eta^4 \tag{2.2}$$

where U = depth-averaged velocity; u_0, u_1, u_2, u_3, u_4 = coefficients**;** and η = y/h. The graphical representation of unsteady flow is shown in Fig. 1.

The continuity equation is

$$\frac{\partial u}{\partial x} + \frac{\partial v}{\partial y} = 0 \tag{2.3}$$

where v = time-averaged vertical velocity; and x = streamwise distance. Integrating Eq. (2.3) from bottom to the free surface, the vertical velocity obtained as the form of a power series of streamwise velocity. That is

$$v = \int \frac{\partial v}{\partial \eta}\, d\eta = -h \int \frac{\partial u}{\partial x}\, d\eta \tag{2.4a}$$

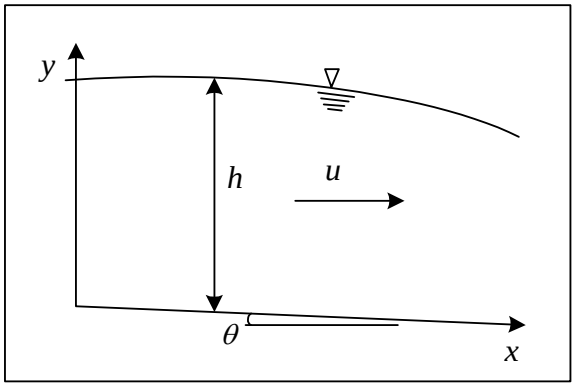

Figure 2.1. Sketch of unsteady flow

$$v = -h\int\left[\frac{\partial U}{\partial x}\left(u_0 + u_1\eta + u_2\eta^2 + u_3\eta^3 + u_4\eta^4\right)\right]d\eta + \int\left[U\frac{\partial h}{\partial x}\left(u_1\eta + 2u_2\eta^2 + 3u_3\eta^3 + 4u_4\eta^4\right)\right]d\eta \tag{2.4b}$$

Thus the vertical velocity is

$$v = -h\frac{\partial U}{\partial x}\left(u_0\eta + \frac{1}{2}u_1\eta^2 + \frac{1}{3}u_2\eta^3 + \frac{1}{4}u_3\eta^4 + \frac{1}{5}u_4\eta^5\right) + U\frac{\partial h}{\partial x}\left(\frac{1}{2}u_1\eta^2 + \frac{2}{3}u_2\eta^3 + \frac{3}{4}u_3\eta^4 + \frac{4}{5}u_4\eta^5\right) \tag{2.4c}$$

The hydrostatic pressure p and its streamwise gradient are expressed as

$$p = \rho g(h - y)\cos\theta \tag{2.5a}$$

$$\frac{1}{\rho}\frac{\partial p}{\partial x} = g\cos\theta\frac{\partial h}{\partial x} \tag{2.5b}$$

where g = gravitational acceleration; and θ = angle made by the streamwise slope with the horizontal.

To include the effect of unsteadiness in the model and to determine the coefficients of power series, the expressions in Eqs. (2.1), (2.2), (2.4c) and (2.5b) are substituted into the equation of motion in x-direction.

$$\frac{\partial u}{\partial t} + u\frac{\partial u}{\partial x} + v\frac{\partial u}{\partial y} = g\sin\theta - \frac{1}{\rho}\frac{\partial p}{\partial x} + \frac{\partial}{\partial y}\left(\frac{\tau_{xy}}{\rho}\right) \tag{2.6}$$

Rearranging the terms to the different power of η, the following equation is obtained:

$$\begin{aligned}
&\frac{\partial U}{\partial t}u_0 + U\frac{\partial U}{\partial x}u_0^2 + \left[\left(\frac{\partial U}{\partial t}u_1 - \frac{U}{h}\frac{\partial h}{\partial t}u_1\right) + U\frac{\partial U}{\partial x}u_0u_1 - \frac{U^2}{h}\frac{\partial h}{\partial x}(u_0u_1)\right]\eta \\
&\quad + \left[\left(\frac{\partial U}{\partial t}u_2 - 2\frac{U}{h}\frac{\partial h}{\partial t}u_2\right) + U\frac{\partial U}{\partial x}\left(\frac{1}{2}u_1^2\right) - \frac{U^2}{h}\frac{\partial h}{\partial x}\left(\frac{1}{2}u_1^2 + 2u_0u_2\right)\right]\eta^2 \\
&+ \left[\left(\frac{\partial U}{\partial t}u_3 - 3\frac{U}{h}\frac{\partial h}{\partial t}u_3\right) - U\frac{\partial U}{\partial x}\left(u_0u_3 + \frac{2}{3}u_1u_2\right) - \frac{U^2}{h}\frac{\partial h}{\partial x}\left(3u_0u_3 + \frac{4}{3}u_1u_2\right)\right]\eta^3 \\
&+ \left[\left(\frac{\partial U}{\partial t}u_4 - 4\frac{U}{h}\frac{\partial h}{\partial t}u_4\right) - U\frac{\partial U}{\partial x} + \left(-\frac{1}{3}u_2^2 + 2u_0u_4 - \frac{1}{4}u_1u_3\right)\right. \\
&\qquad \left. - \frac{U^2}{h}\frac{\partial h}{\partial x}\left(\frac{2}{3}u_2^2 + 4u_0u_4 + \frac{7}{4}u_1u_3\right)\right]\eta^4 \\
&\quad = g\sin\theta - g\cos\theta\frac{\partial h}{\partial x} + \beta h u_* \frac{U}{h^2}\left(2u_2 + 6u_3\eta + 12u_4\eta^2\right) \qquad (2.7)
\end{aligned}$$

The expression for the coefficients of power series are evaluated by sorting out the terms with similar power of η. This procedure is used to determine the coefficients u_2 and u_3 as

$$u_2 = \frac{h}{2\beta u_* U}\left(u_0\frac{\partial U}{\partial t} + u_0^2 U\frac{\partial U}{\partial x} - g\sin\theta + g\cos\theta\frac{\partial h}{\partial x}\right) \qquad (2.8)$$

$$u_3 = \frac{h}{6\beta u_* U}\left(u_1\frac{\partial U}{\partial t} - u_1\frac{U}{h}\frac{\partial h}{\partial t} + u_0u_1U\frac{\partial U}{\partial x} - u_0u_1\frac{U^2}{h}\frac{\partial h}{\partial x}\right) \qquad (2.9)$$

However, u_0 is defined by the expression of the bottom velocity and u_1 is described by using the definition of the bottom shear stress. So,

$$u_0 = r_*\frac{u_*}{U}; \qquad u_1 = \frac{u_*}{\beta U} \qquad (2.10)$$

The coefficient u_4 is determined by assuming the zero shear stress at the free surface. Thus,

$$\left.\frac{\partial u}{\partial y}\right|_{at\ y=h} = 0; \qquad u_4 = -\frac{1}{4}(u_1 + 2u_2 + 3u_3) \qquad (2.11)$$

By using this zero gradient condition at the free surface and from the expression of the coefficients, the vertical distribution of streamwise velocity can be determined once the friction velocity is known.

2.2.2 Friction velocity

The friction velocity estimation is essential in turbulence research because its value represents the velocity scale of mean velocity and turbulence (Nezu et al. 1997). There are a few methods to determine the friction velocity. The well-known methods are estimation of friction velocity from fitting a logarithmic law or Clauser method, momentum equation, and the measured Reynolds shear stress profiles. Nezu et al. (1997) proposed a new approach for determination of friction velocity by using measured velocities in the viscous sublayer. However, in the present model, the objective is set to develop the concise form of friction velocity, including the effect of non-uniformity and unsteadiness in the flows. To do so, initially by the definition of depth-averaged velocity, that is

$Uh = \int_0^h u dy$, the power series of streamwise velocity in Eq. (2.2) is integrated into the form

$$u_0 + \frac{1}{2}u_1 + \frac{1}{3}u_2 + \frac{1}{4}u_3 + \frac{1}{5}u_4 = 1 \tag{2.12}$$

Substituting the expression of the coefficients into the above equation and then simplifying, a quadratic equation of u_*/U is obtained as

$$\left.\left(r_* + \frac{1}{2\beta}\right)\left(\frac{u_*}{U}\right)^2 - \left(\frac{u_*}{U}\right) - \frac{1}{6\beta}\frac{gh\sin\theta}{U^2}\right\} \leftarrow \text{Principle term}$$

$$+\left[\frac{r_*}{60\beta}\frac{h}{U}\left(7\,r_* + \frac{1}{\beta}\right)\frac{\partial U}{\partial x} - \frac{r_*}{60\beta^2}\frac{\partial h}{\partial x} - \frac{1}{20\beta}\right]\left(\frac{u_*}{U}\right)^2 + \left[\frac{1}{60\beta}\frac{h}{U^2}\left(7\,r_* + \frac{1}{\beta}\right)\frac{\partial U}{\partial t}\right.$$

$$\left. - \frac{1}{60\beta^2}\frac{1}{U}\frac{\partial h}{\partial t}\right]\left(\frac{u_*}{U}\right) + \frac{1}{20\beta}\frac{h}{U^2}\left(g\sin\theta + \frac{7}{3}g\cos\theta\frac{\partial h}{\partial x}\right) = 0 \tag{2.13}$$

where u_* = friction velocity; and r_* = coefficient of bottom and friction velocity.

The principal terms, as indicated in Eq. (2.13), play a main role in the steady-uniform flows. On the other hand, other terms play a role during the unsteady non-uniform flows. Thus, the friction velocity for steady-uniform flows is determined by solving the principal terms. Contrarily, to predict the friction velocity for the unsteady flows, it is necessary to consider the non-uniformity and unsteadiness of the flows. Keeping that in view, the relationship for the friction velocity determined for the steady uniform flows from the

principal terms is included in the other terms. The whole equation is then rearranged and simplified to obtain the concise expression for the friction velocity u_* as

$$u_*^2 = C_f U^2 \left(1 + A_1 \frac{\partial U}{\partial t} + A_2 \frac{\partial h}{\partial t} + B_1 \frac{\partial U}{\partial x} + B_2 \frac{\partial h}{\partial x} + C\right) \tag{2.14}$$

where

$$C_f = \frac{1}{2\left(r_* + \frac{1}{2\beta}\right)^2}$$

$$A = 1 + \left[1 + \frac{2}{3\beta}\left(r_* + \frac{1}{2\beta}\right)\frac{gh\sin\theta}{U^2}\right]^{0.5}; \qquad B = A + \frac{1}{3\beta}\left(r_* + \frac{1}{2\beta}\right)\frac{gh\sin\theta}{U^2}$$

$$A_1 = -\frac{1}{60\beta}\frac{h}{U^2}\left(7\, r_* + \frac{1}{\beta}\right)A; \qquad A_2 = \frac{1}{60\beta^2}\frac{h}{U}A; \qquad B_1 = -\frac{r_*}{60\beta}\frac{h}{U}\frac{(7r_* + 1/\beta)}{(r_* + 1/2\beta)}B$$

$$B_2 = \frac{r_*}{60\beta^2}\frac{B}{(r_* + 1/2\beta)} - \frac{7}{30\beta}\left(r_* + \frac{1}{2\beta}\right)\frac{gh\cos\theta}{U^2}$$

$$C' = \frac{1}{20\beta}\frac{B}{(r_* + 1/2\beta)} + \frac{7}{30\beta}\left(r_* + \frac{1}{2\beta}\right)\frac{gh\sin\theta}{U^2}$$

$$C = C' + \left[1 + 2\left(A_1 \frac{\partial U}{\partial t} + A_2 \frac{\partial h}{\partial t} + B_1 \frac{\partial U}{\partial x} + B_2 \frac{\partial h}{\partial x} + C'\right)\right]^{0.5}$$

The friction velocity represented in the formulation is valid for the steady-uniform flows and the unsteady non-uniform flows as well.

2.2.3 Computational Condition

During the simulation of unsteady flows, sine hydrograph for the discharge is given at the upstream end, and depth is fixed at the downstream end as a boundary condition. The value of the coefficient r_* is adjusted until the base flow discharge is obtained as an initial condition. The depth-averaged equation is later solved by including the effect of vertical distribution of streamwise velocity in the momentum equation. Thus,

$$\frac{\partial Uh}{\partial t}+\left[u_0^2+u_0u_1+\frac{1}{3}\left(u_1^2+2u_0u_2\right)+\frac{1}{4}\left(2u_0u_3+2u_1u_2\right)+\frac{1}{5}\left(u_2^2+2u_0u_4+2u_1u_3\right)\right.$$
$$\left.+\frac{1}{6}\left(2u_1u_4+2u_2u_3\right)\right]\frac{\partial}{\partial x}\left(U^2h\right)+\frac{\partial}{\partial x}\left(g\frac{h^2}{2}\right)=gh\sin\theta-u_*^2 \qquad (2.15)$$

Four experimental cases, two for smooth bed with large and small unsteadiness parameters, as defined by Nezu et al. (1997) and another two for rough bed (Song and Graf 1996; Tu and Graf 1992) are simulated. The hydraulic conditions along with r_* value for four experimental cases are tabulated in Table 2.1. For all simulations, Δx and Δt are set to be 0.05 and 0.01, respectively.

Table 2.1. Hydraulic parameters considered during the simulation

Case	**Slope**	T_d **(Sec)**	Q_b **(m^3/s)**	Q_p **(m^3/s)**	h_b **(m)**	r_*
NZ1	0.00167	60	0.005	0.0154	0.0405	7.67
NZ2	0.00167	120	0.005	0.0158	0.041	7.451
SG	0.003	52	0.0585	0.0891	0.11	9.152
TG	0.002	55	0.022	0.0121	0.09	5.385

Note - T_d is duration from base flow discharge to peak flow discharge; Q_b is base flow discharge; Q_p is the peak flow discharge and h_b is the base flow depth.

2.3 Results

2.3.1 Smooth Bed Case

2.3.1.1 Bed shear stress

The friction velocity represented by Eq. (2.14) is used to determined the bed shear stress, $\tau_w=\rho u_*^2$. However, for the experimental cases, the friction velocity is estimated by using the logarithmic law. The bed shear stress is then normalized by the mean bed shear stress, and plotted against normalized time for two cases, NZ1 (large unsteadiness parameter) and NZ2 (small unsteadiness parameter) as illustrated in Fig. 2.2. Depth hydrograph $\left(\Delta h=h-h_b\right)$ (depth versus time) for these cases are also depicted in Fig. 2.2. Similar to the experimental results, the normalized bed shear stress increases with an increase in time in the

rising stage attaining a peak value before the peak depth occurs and decreasing monotonously in the falling stage. It leads to the various sediment transport properties to be higher in rising stage than falling stage. This difference of the bed shear stress between the rising and the falling branches, as reported by Nezu et al. (1993), is responsible for the loop characteristics against the depth. The maximum value of normalized bed shear stress decreases with a decrease in the unsteadiness parameter. The unsteadiness parameters resulted from numerical (Num) simulation along with the experimental unsteadiness parameters are tabulated in Table 2.2.

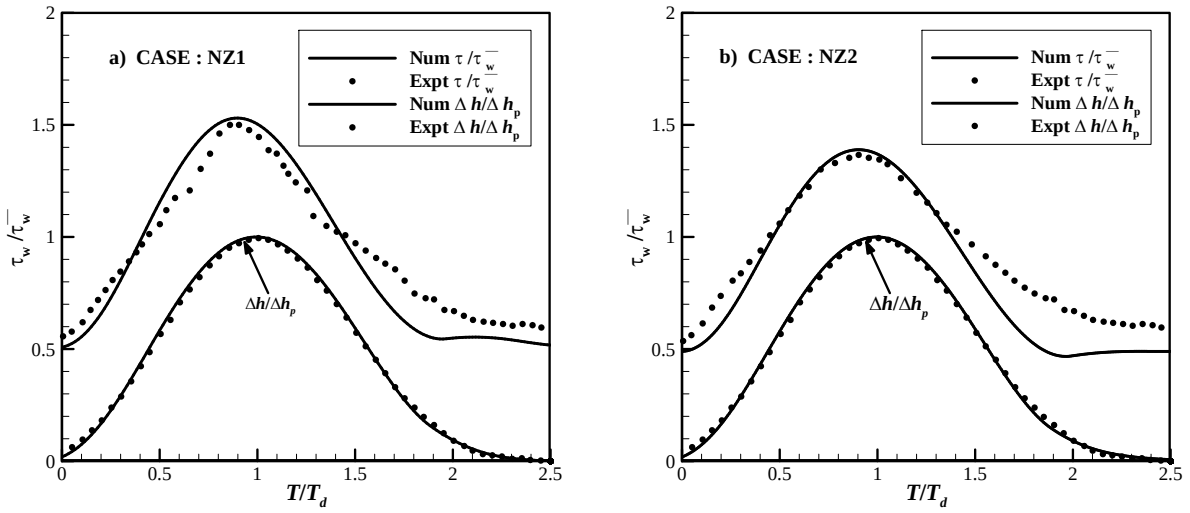

Figure 2.2. Normalized bed shear stress $\overline{\tau_w}$ against time $t\ (=T/T_d)$. a) Case NZ1; b) Case NZ2 (measuring point at x =7 m in 10 m long flume)

Table 2.2. Unsteadiness parameter (X 10^{-3})

Case	Num Model	Experiment
NZ1	1.066	0.95
NZ2	0.708	0.52

2.3.1.2 Loop Characteristics

The distribution of streamwise velocity for three representative regions of flows, wall, intermediate and free surface regions, are compared with the experimental data. The streamwise velocity, u, normalized by the maximum mean velocity, $u_{\max}$, is plotted against normalized depth for the above mentioned regions (Fig. 2.3). The variation of the normalized streamwise velocity with normalized depth for wall and intermediate regions exhibits the loop characteristics, as is observed in the experiments. Although the variation in the intermediate region shows small departure, the loop characteristics in the wall region is in good agreement with the experimental data. The resulting velocity of the Num model in the rising stage is higher than that in the falling stage. Like experiments, the Num model shows the thickness of the loop increases with an increase in the unsteadiness parameter.

The loop characteristics in the free surface region observed in experiments showed an *8-shaped* loop caused by a probable effect of the surface wave fluctuations, but the Num model could not produce an *8-shaped* loop at the free surface region. This could be resulted from the lack of the generation of fluctuations because of incorporation of additional stresses. These additional stresses are provided from the fluid flow but not from the turbulence of the flow.

2.3.1.3 Velocity deformation

The main aim of the present study is to verify the velocity deformation in the vicinity of the free surface caused due to unsteadiness and non-uniformity of the flow. For that reason, the vertical distribution of streamwise velocity obtained from the Num model is compared with the uniform flow velocity distribution of Engelund model (EM), U_{EM}, as depicted in Fig. 2.4. Both the distributions are well comparable in the lower region; however, in the outer region, the distribution of velocity obtained from the Num model departs from that obtained from the Engelund model. This deformation occurs as a result of the unsteadiness and non-uniformity of the flow in the Num model.

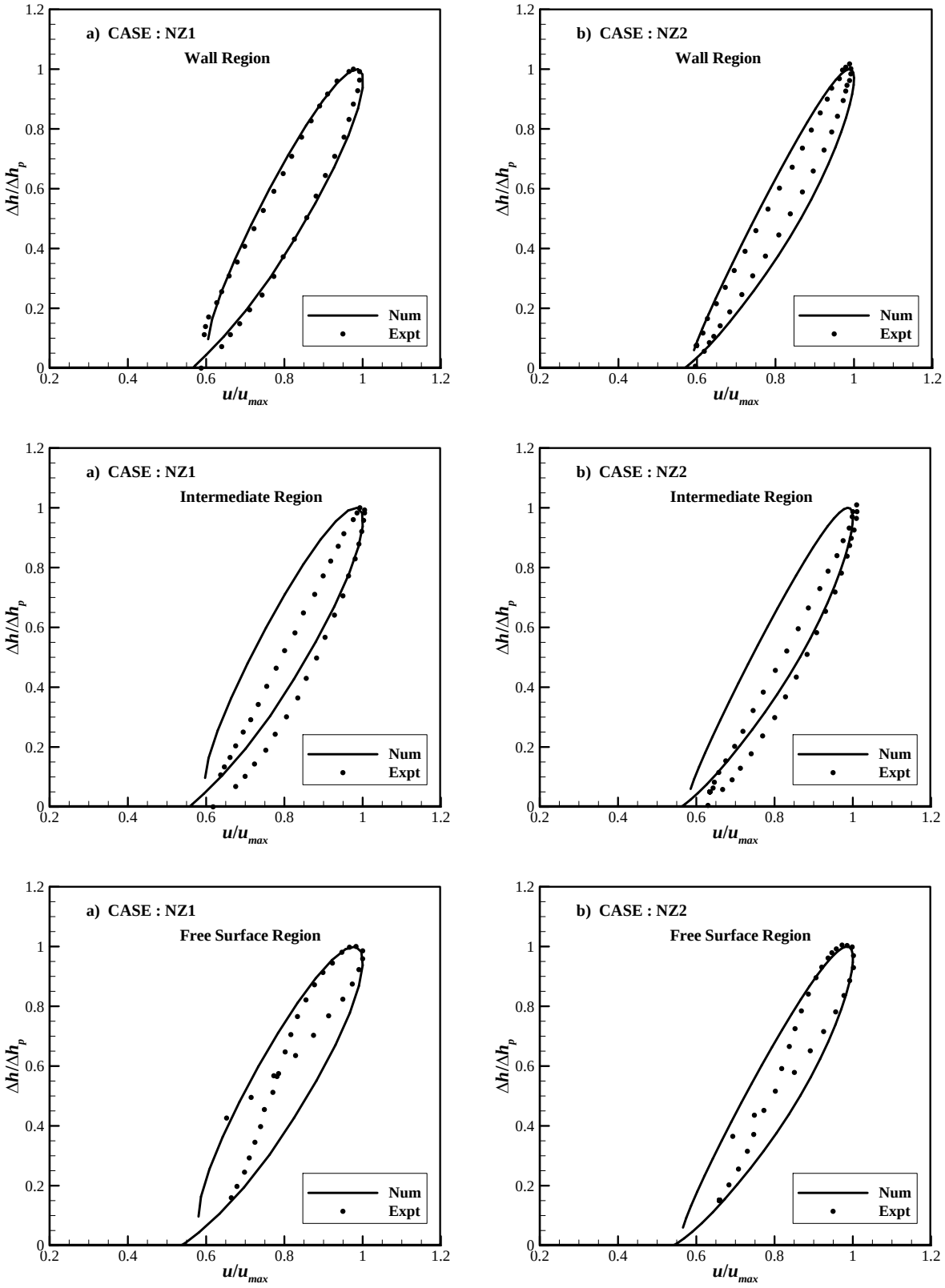

Figure 2.3. Loop characteristics of streamwise velocity for three representative sections. a) Case NZ1; b) Case NZ2

The temporal change of difference of velocity between Num and EM model at the surface is normalized by the friction velocity and compared with the experimental data for both the cases, as shown in Fig. 2.5. For the experimental case, the distribution is calculated using the logarithmic law with wake parameter Π considered as 0.1 for steady flow (Steffler et al. 1985; Kirkgoz 1989). The distribution does not agree well with the experimental data because the velocity distribution of the Num model is not compatible with the logarithmic law. The model is derived from the Engelund model that, itself, is not compatible with the logarithmic law. Therefore, only the pattern of the distribution is similar to the experimental data with the peak values of the normalized velocity that attains before the full depth reaches and the maximum value at the peak decreases with a decrease in the unsteadiness parameter.

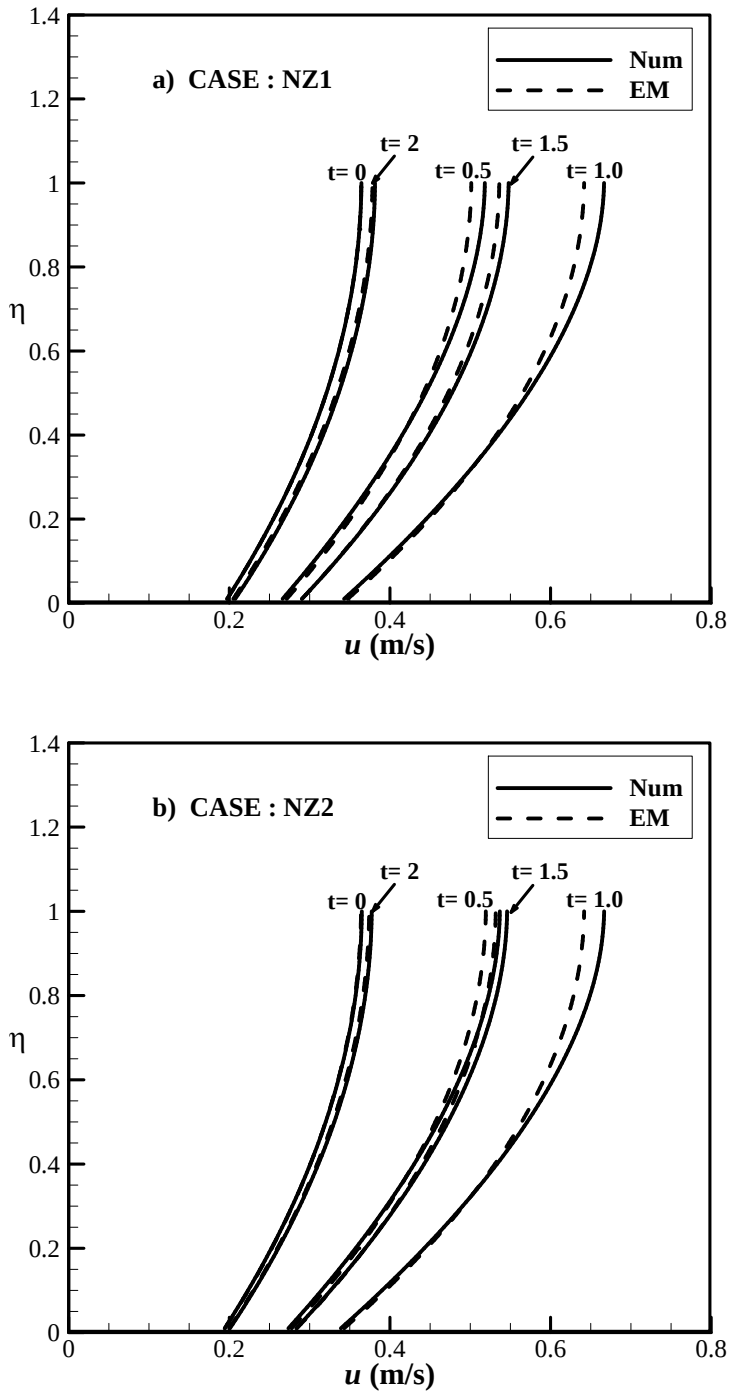

Figure 2.4. Comparison of vertical distribution of streamwise velocity with Engelund Model. a) Case NZ1; b) Case NZ2

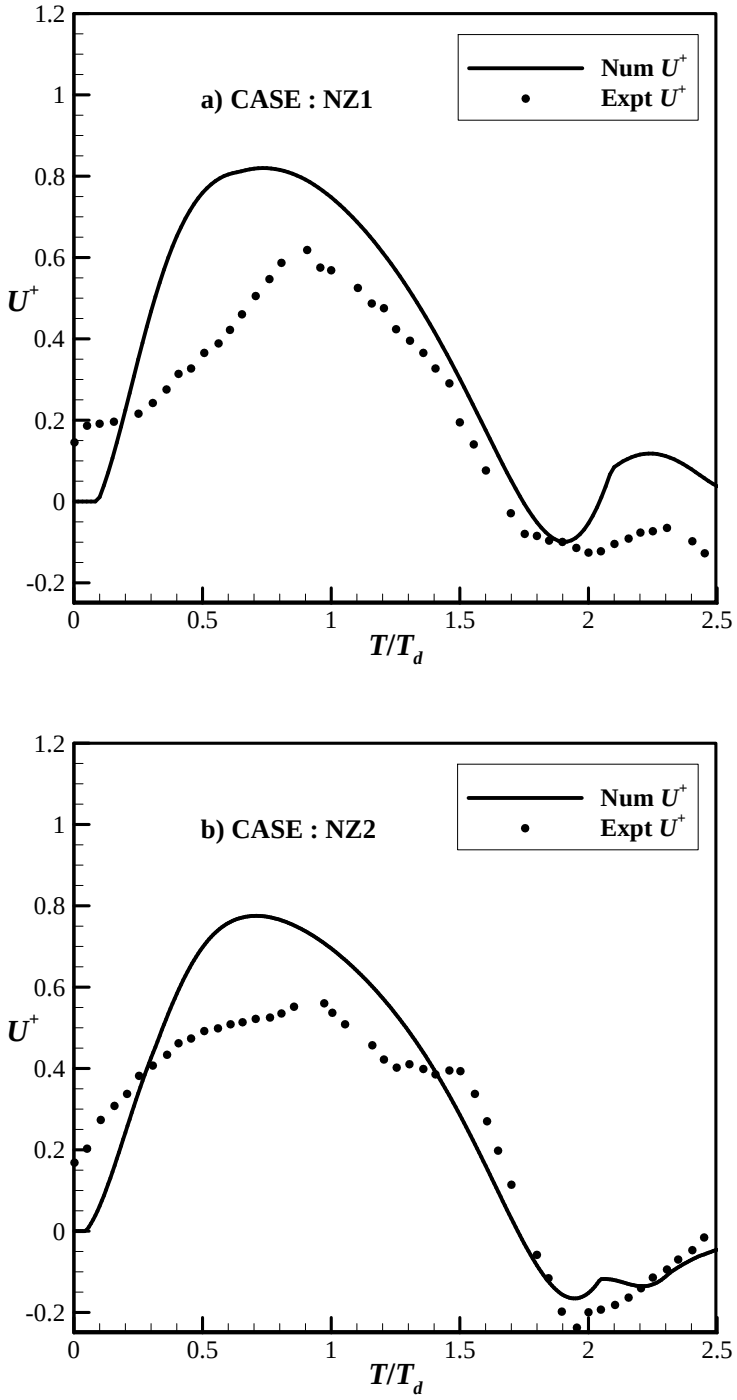

Figure 2.5. Normalized Velocity $U^+ = (U - U_{EM})/u_*$ against time t in the surface region.

a) Case NZ1; b) Case NZ2

2.3.2 Rough Bed Case

To check the compatibility of the model for the flows over a rough bed, two experimental conditions, as mentioned previously, are used. The details of the distribution with the cases of the large and the small unsteadiness parameters are explained in the succeeding subsections.

2.3.2.1 Distribution of Hydraulic Variables

Temporal distribution of the hydraulic variables with experimental data for the less unsteadiness case is presented in Fig. 2.6 (Song and Graf 1996); and that for the high unsteadiness case is plotted in Fig. 2.7 (Tu and Graf 1992). All hydrographs under the case of the less unsteadiness are in good agreement with the experimental data, but under the case of the high unsteadiness, the numerical values are underestimated. This is attributed to the setting of a constant depth, as the downstream boundary condition dampens the depth causing maximum velocity at the peak discharge than on the experimental curve. However, in both the cases, the peak of friction velocity is obtained first, and then, the maximum value of average velocity and discharge appears in succession. The peak value of the depth is attained in the end indicating the loop rating curve for flood flows.

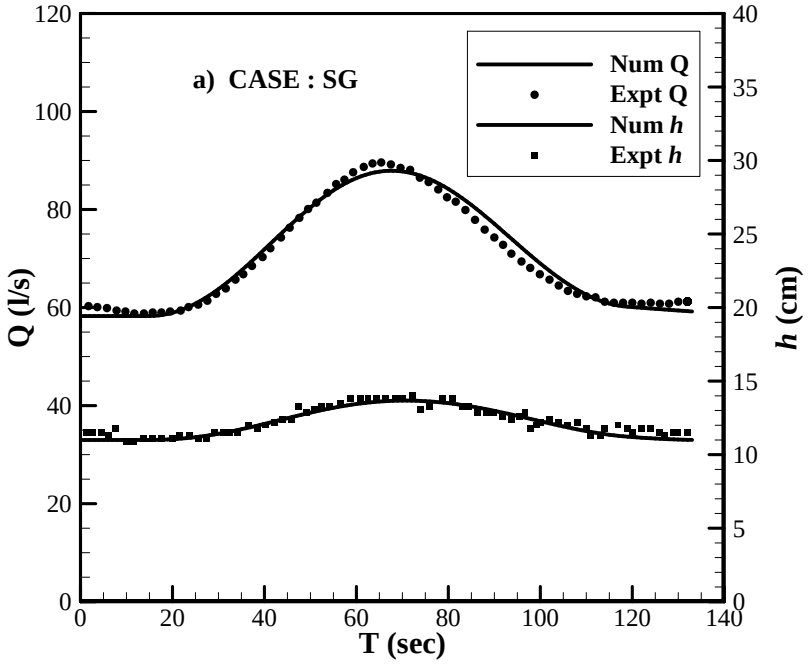

Figure 2.6a. Time variation of discharge and depth hydrographs for SG case

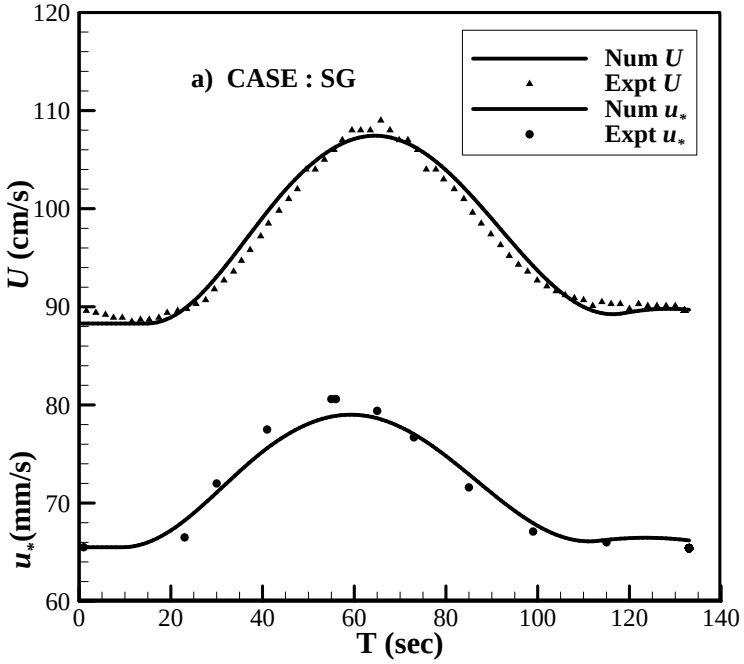

Figure 2.6b. Time variation of averaged and friction velocity hydrographs for SG case

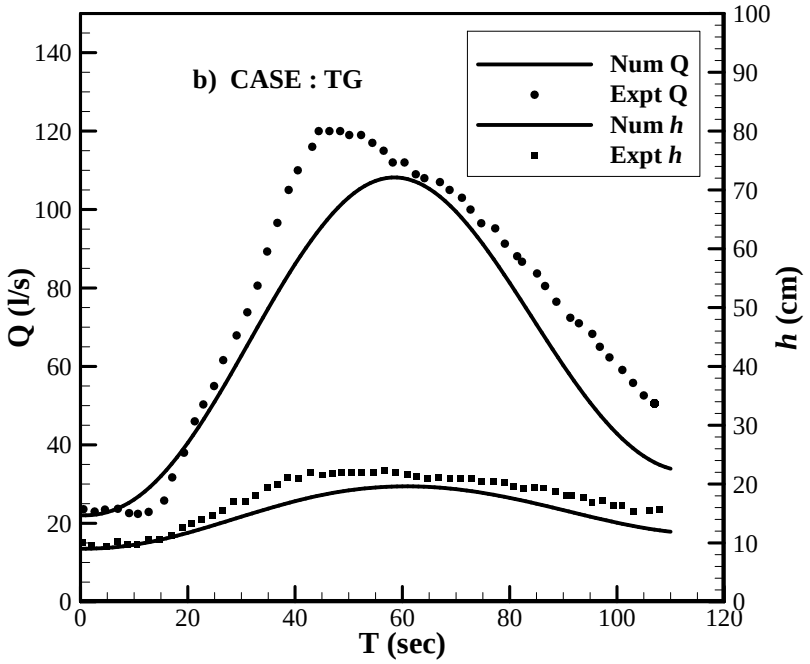

Figure 2.7a. Time variation of discharge and depth hydrographs for TG case

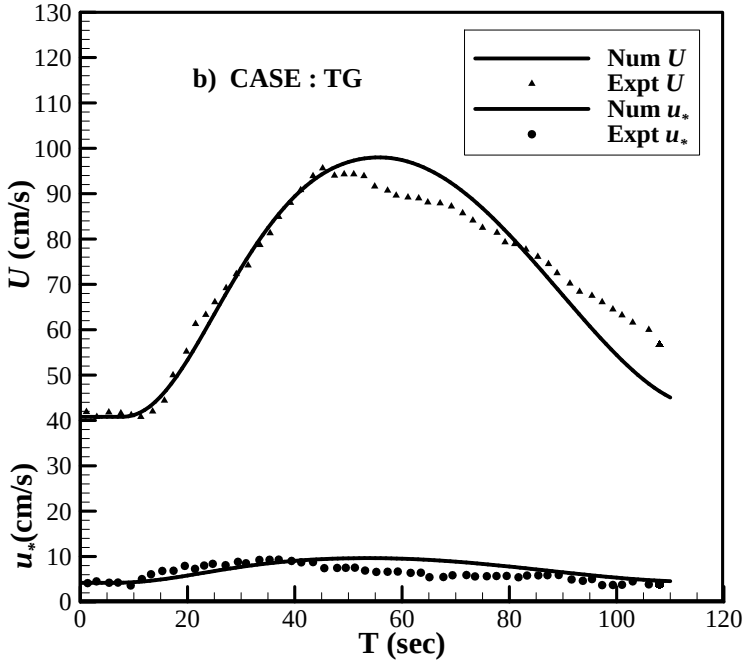

Figure 2.7b. Time variation of averaged and friction velocity hydrographs for TG case.

2.3.2.2 Time variation of streamwise velocity

Time variations of streamwise velocities over entire depth are shown in Fig. 2.8 (Song and Graf 1996) and 2.9 (Tu and Graf 1992). In Fig. 2.8, computed values show less friction due to the r_* value selected for the model. Hence, at the wall region, the horizontal velocity overestimates the experimental data, but in the intermediate region, the distribution is similar to that obtained in the experiments. Further, up in the region, the values are underestimated and at the free surface, it again matches with the experimental data indicating full development of the flow caused due to inclusion of additional stresses. (Note - for more visibility Num and Expt distribution of velocity at y = 5.77cm; y = 7.76cm and y = 9.75cm are shifted from its original position by subtracting 10, 7, and 3 units, respectively).

For the case of the large unsteadiness parameter, as shown in Fig. 2.9, the Num model shows a close agreement with the experimental data. The velocity near the bottom is well comparable with the experimental data, except at the peak, where the velocity attains slightly higher value than the experimental data. Superimposing both the figures for respective cases indicates that the velocity in the vicinity of the free surface arrives at the peak values earlier than that near the bed because of a probable effect of the friction.

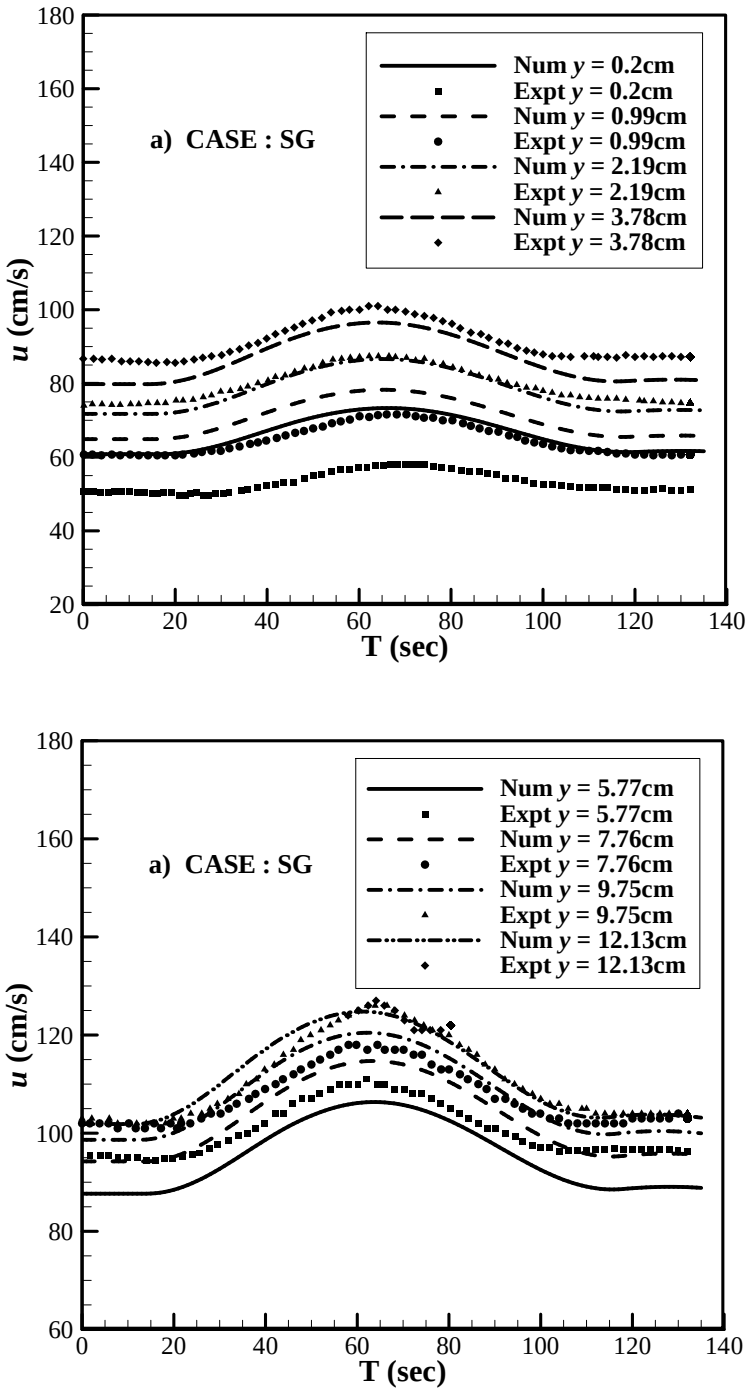

Figure 2.8. Time variation of streamwise velocity over entire flow depth for SG case

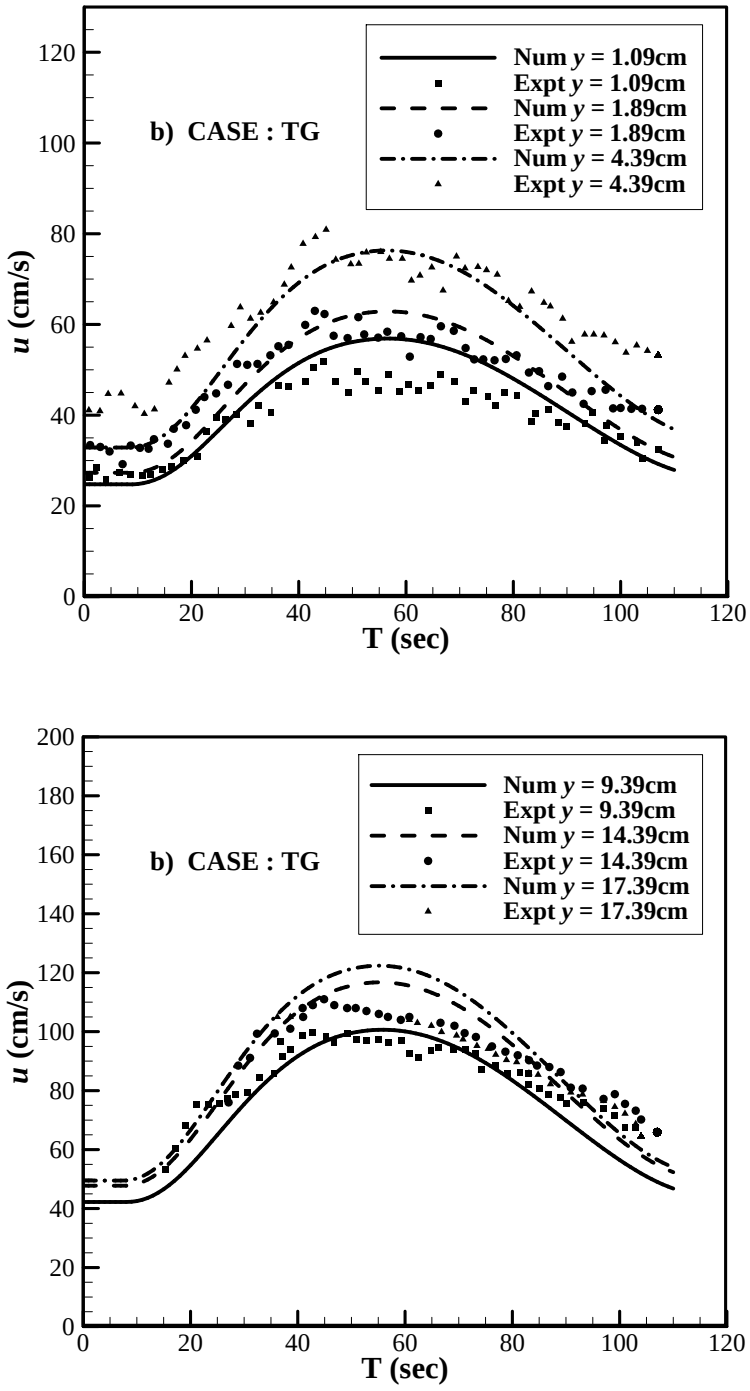

Figure 2.9. Time variation of streamwise velocity over entire flow depth for TG case

2.3.2.2 Velocity Distribution and Deformation

The velocity profiles for the equivalent depth during the rising and the falling stages for both the cases are depicted in Fig 2.10. Here, only two distributions for each case are presented. The corresponding hydraulic variables for an equivalent depth are tabulated in Tables 2.3 and 2.4. For the case of high unsteadiness, the velocity variation for equal averaged velocity, in the rising and the falling stages, with the corresponding hydraulic parameters are shown in Fig. 2.11 and tabulated in Table 2.5. As mentioned previously, for the case of the small unsteadiness parameter, the velocity distribution at the wall region is not comparable with the experimental data. During the passage of a flood flow to the peak time, the distribution of velocity obtained from the Num model comes closer to the experimental data and departs thereafter during the falling stage. However, the case of the high unsteadiness shows a reasonably good comparison with the experimental data. Similar to the experiment, the distribution of velocity during the rising stage shows a higher value than the falling stage.

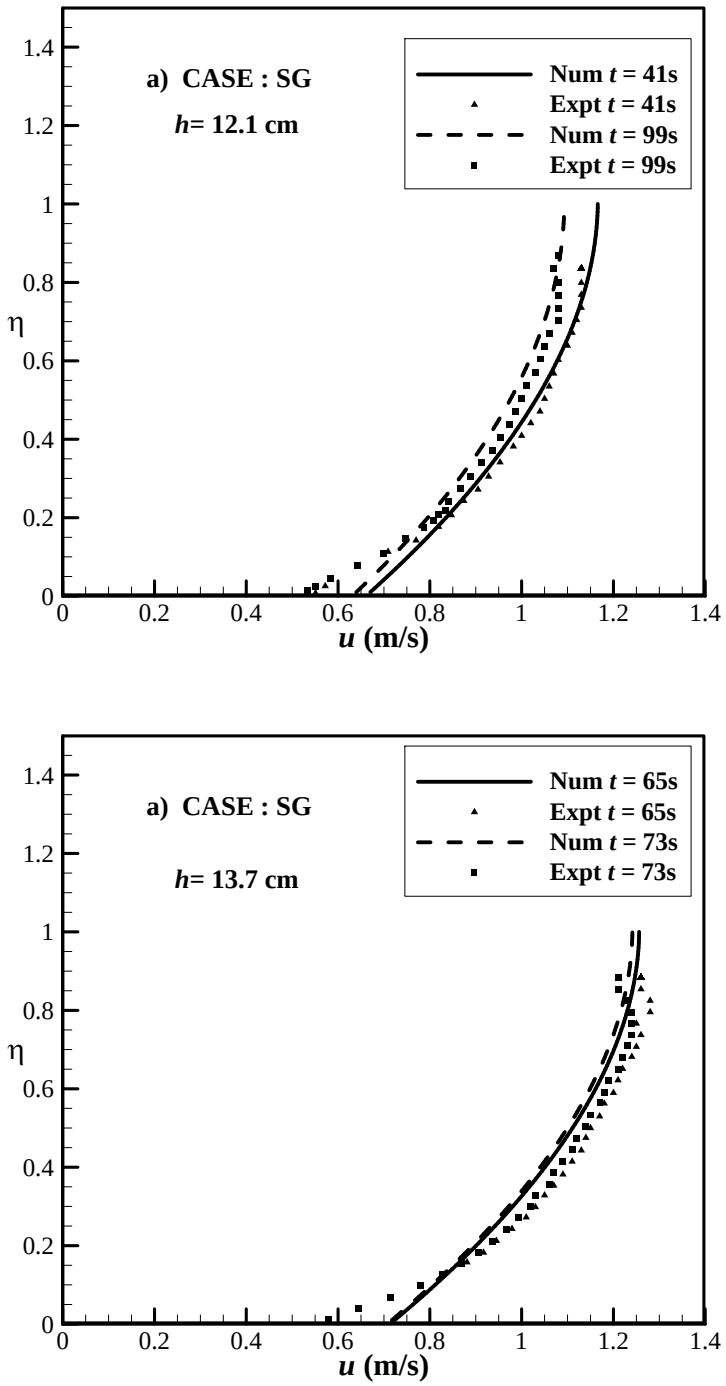

Figure 2.10a. Distribution of streamwise velocity for equivalent depth for SG case

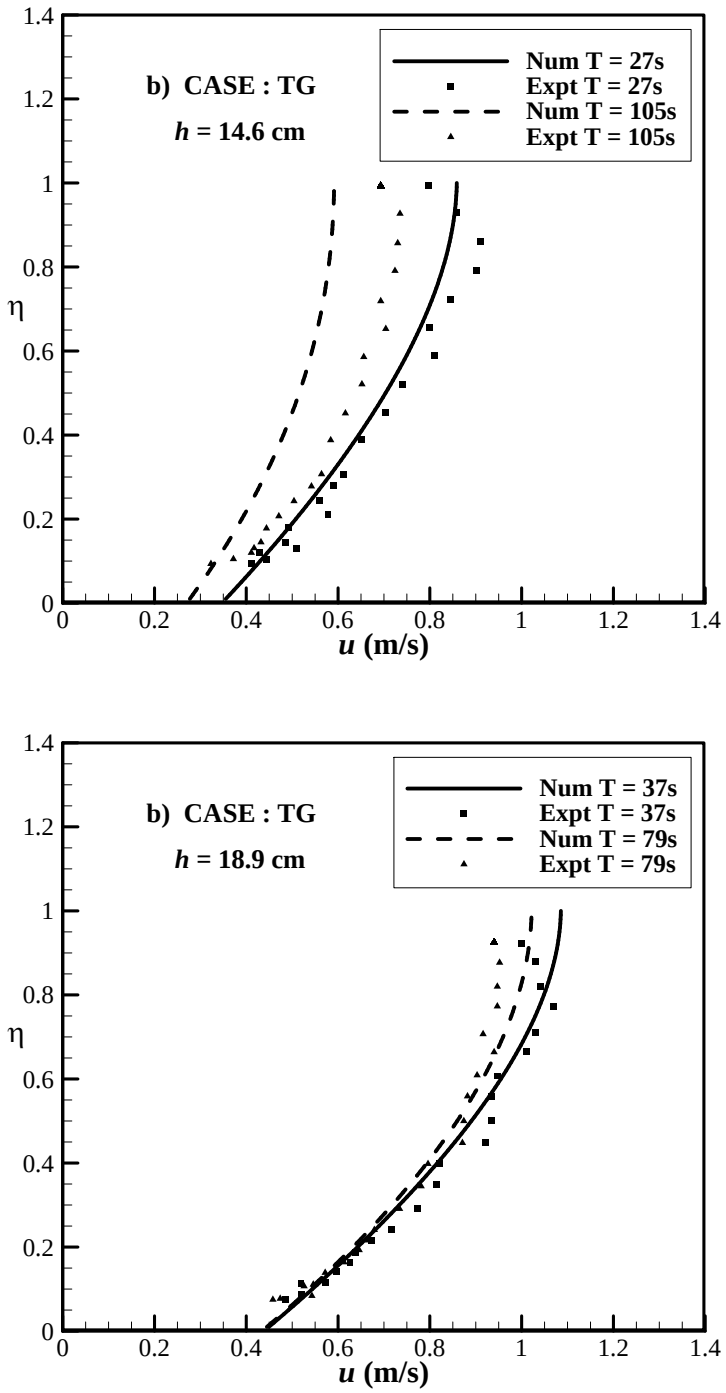

Figure 2.10b. Distribution of streamwise velocity for equivalent depth for TG case

Table 2.3. Numerical and experimental hydraulic variables for SG case

T (sec)	Expt *h* (cm)	Num *h* (cm)	Expt u_* (cm/s)	Num u_* (cm/s)
1	11.3	11	6.55	6.55
133	11.3	11	6.54	6.62
41	12.1	12.17	7.75	7.56
99	12.1	12.35	6.71	6.80
55	13.2	13.19	8.06	7.88
85	13.2	13.28	7.16	7.29
65	13.7	13.61	7.94	7.86
73	13.7	13.66	7.67	7.70

Table 2.4. Hydraulic variables for equivalent depth for TG case

T (sec)	Experiment				Numerical			
	***h*(cm/s)**	***U* (cm/s)**	***Q* (l/s)**	u_* **(cm/s)**	***h*(cm/s)**	***U* (cm/s)**	***Q* (l/s)**	u_* **(cm/s)**
27	14.6	69.1	60.7	8.0	13.6	67.6	55.6	6.6
105	14.6	59.1	52.3	3.8	12.6	49.0	37.1	5.1
31	16.3	74.4	72.9	8.3	14.7	75.5	65.2	7.4
95	16.3	67.9	67.4	4.6	14.5	60.8	50.8	6.3
37	18.9	84.3	95.9	8.4	16.4	85.5	79.4	8.3
79	18.9	79.2	90	5.8	17.8	82.2	83.4	8.3
43	20.5	93.2	114.9	7.7	17.8	92.6	92.1	9.1
59	20.5	89.2	111	6.1	19.6	97.6	108.2	9.6

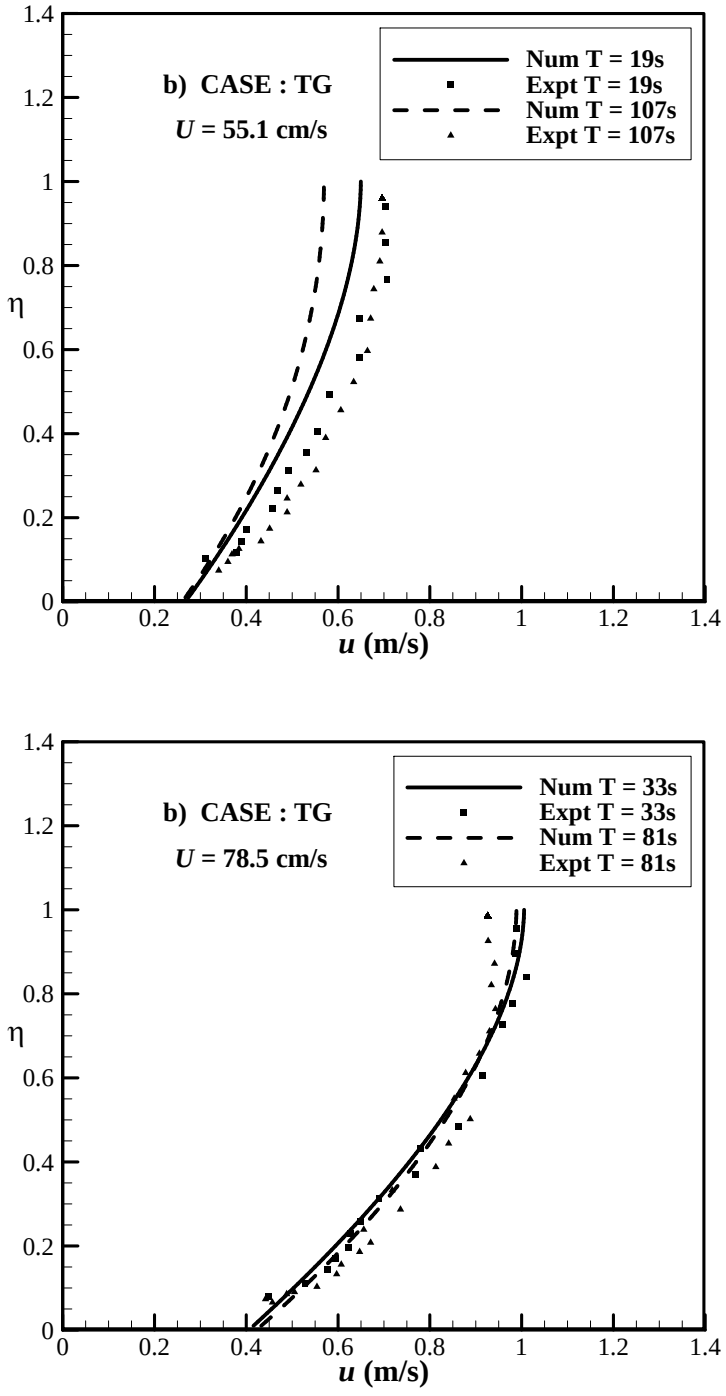

Figure 2.11. Distribution of streamwise velocity for equal averaged velocity for TG Case

Table 2.5. Hydraulic variables for equivalent velocity for TG case

T (sec)	**Experiment**				**Numerical**			
	***h*(cm/s)**	***U* (cm/s)**	***Q* (l/s)**	u_* **(cm/s)**	***h*(cm/s)**	***U* (cm/s)**	***Q* (l/s)**	u_* **(cm/s)**
19	11.2	55.1	37.2	7.0	11.5	51.5	38.6	5.1
107	14.3	55.1	49.2	3.6	12.3	47.2	35.5	5.0
25	13.7	66.0	54.4	7.8	13.0	63.4	51.0	6.2
97	16.2	66.0	64.0	4.3	14.0	58.2	47.4	6.0
33	17.1	78.5	80.7	8.4	15.3	79.1	70.0	7.7
81	18.7	78.5	87.9	5.7	17.5	79.7	79.2	8.0
39	19.7	87.8	103.9	8.3	16.8	88.2	83.9	8.6
67	20.1	87.8	106.3	5.8	19.4	94.0	103.3	9.3

Additionally, the distribution of the velocities for each 20 s apart, for the case of the high unsteadiness, is illustrated in Fig. 2.12. It shows somewhat lower velocity than that in the experiments at the beginning of flow and when returning to the base flow. On the other hand, at the peak time of flow, the distribution is in good agreement with the experimental data. The representative hydraulic parameters for such a case during the rising and the falling branches are given in Table 2.6.

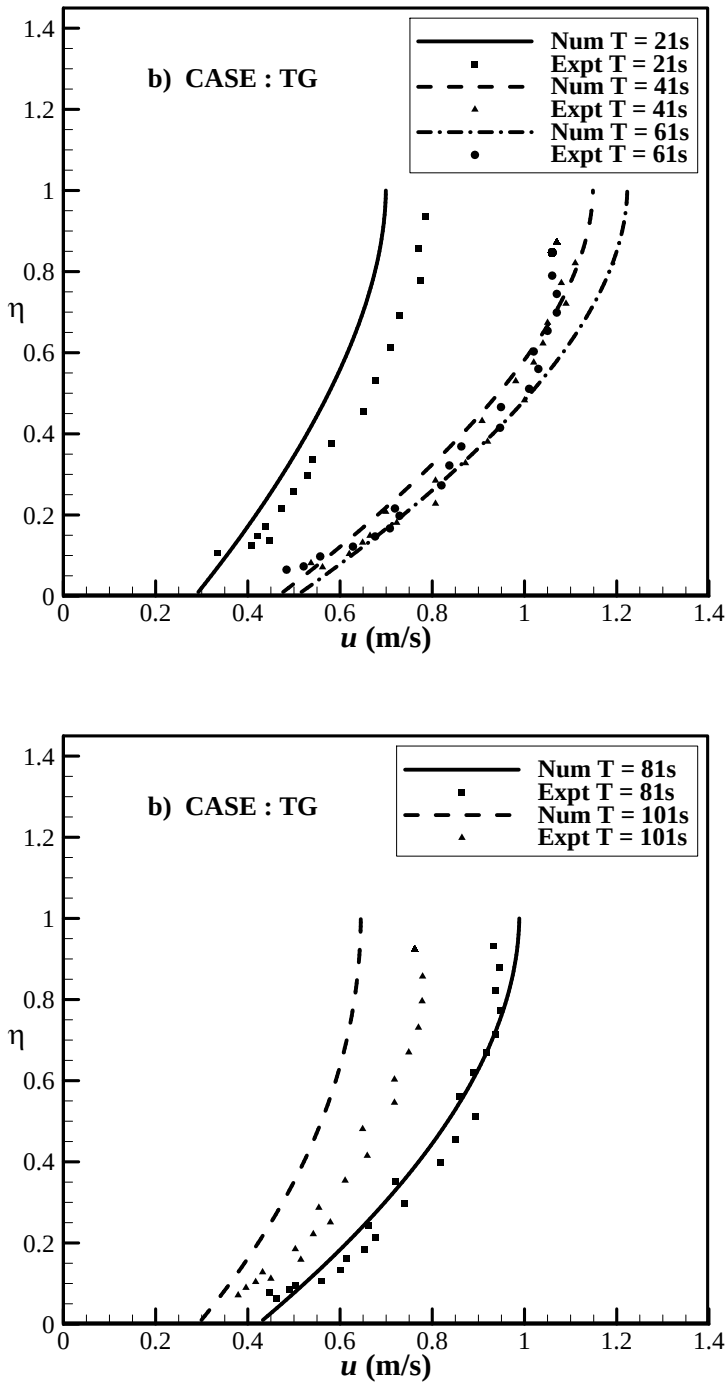

Figure 2.12. Velocity profiles each 20 seconds apart for TG Case

Table 2.6. Numerical and experimental hydraulic variables for TG case

T (sec)	**Experiment**				**Numerical**			
	***h*(cm/s)**	***U* (cm/s)**	***Q* (l/s)**	u_* **(cm/s)**	***h*(cm/s)**	***U* (cm/s)**	***Q* (l/s)**	u_* **(cm/s)**
21	12.2	60.6	44.5	7.3	12.0	55.3	42.5	5.4
41	20.1	90.5	109.3	8.0	17.3	90.5	88.1	8.8
61	20.7	88.9	110.7	6.0	19.6	97.1	107.8	9.6
81	18.7	78.2	87.9	5.7	17.5	79.7	79.2	8.0
101	15.5	62.8	58.6	4.0	13.2	53.3	41.5	5.6

The deformation of the velocity distribution in these cases is also verified by comparing the velocity distributions obtained by the Num model and with those by Engelund model, as shown in Fig. 2.13. In Fig. 2.13(a), for more visibility and to avoid the overlapping, the distributions at t = 0.5 and 1.5 are shifted little bit from their original position by adding 0.03 to former and subtracting 0.05 from the latter, respectively. As mentioned previously, instead of vertical turbulence intensity, the additional stresses, which are formed because of the correlation of the time-averaged vertical and streamwise velocities, are incorporated in the present model. These additional stresses in the Num model results in the vertical distribution of streamwise velocity to depart from the uniform flow velocity distribution obtained from the Engelund model (EM) U_{EM}. The deviation between the models in the vicinity of the free surface is apparent, indicating that the deformation increases with an increase in unsteadiness of flows. This is, in turn, related to the value r_* selected for the particular case. It means that if the r_* value increases, then the unsteadiness decreases and vice versa.

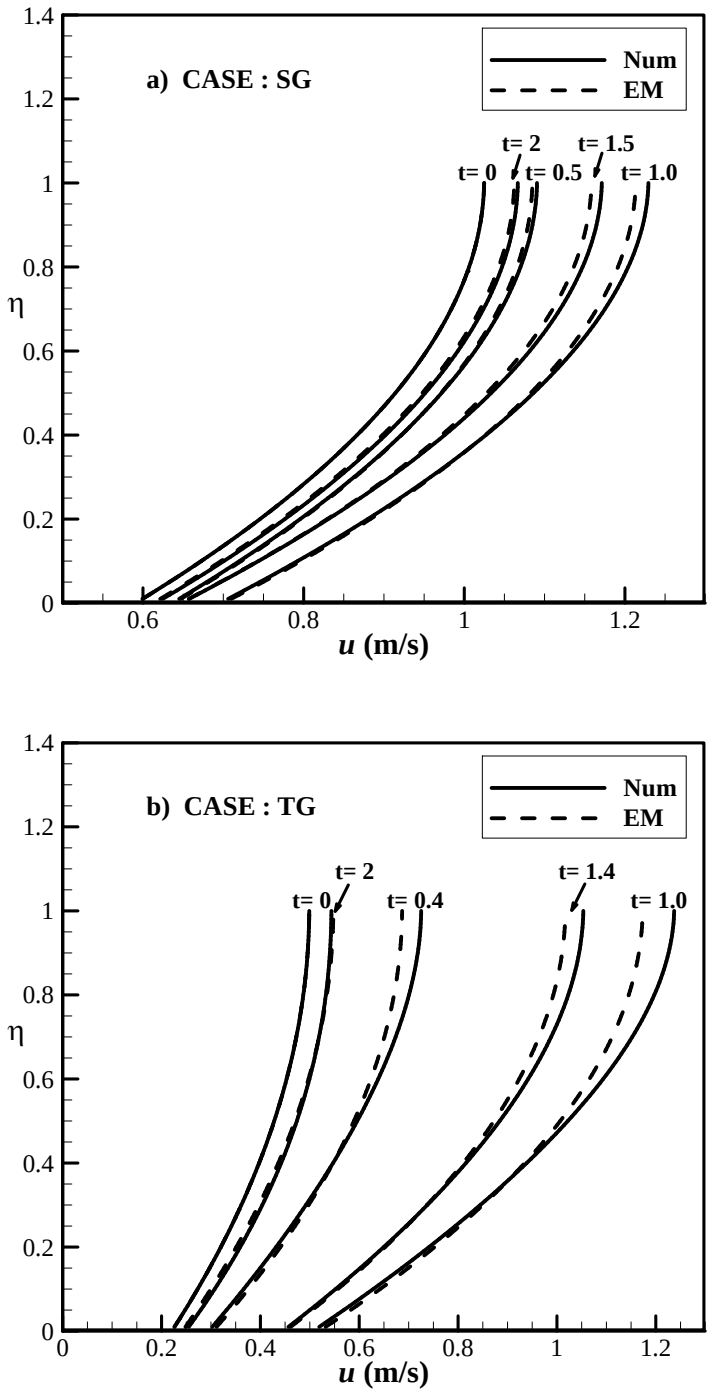

Figure 2.13. Comparisons of vertical distribution of streamwise velocity with Engelund Model. a) Case SG; b) Case TG

2.4 Summary

One-dimensional depth-averaged velocity deformation model for unsteady open channel flows has been developed. The comparison of Num model with the experimental data and the computational results of Engelund model enable the conclusions of the following aspects:

The bed shear stress evaluated by using the friction velocity formula reaches a maximum value earlier than the peak depth. The maximum value of normalized bed shear stress increases with an increase in unsteadiness of the flows.

The thickness of the loop characteristics of the streamwise velocity over smooth bed, similar to the experiments, increases with an increase in unsteadiness parameter. This is also similar for the rough bed case, indicating the distribution of streamwise velocity in the rising stage is higher than that in the falling stage for the equivalent depth.

Similar to the experiments, the velocity near the free surface zone attains a maximum value earlier than the velocity near the wall.

Additional shear stresses incorporated into the model are responsible for the deformation of velocity between the Num model and EM model. The deformation between the models increases with an increase in unsteadiness and decreases with a decrease in unsteadiness. This is, in turn, analogous to the value of the coefficient r_* selected for the model, which has major influence on the deformation. Thus, if the value of the r_* decreases, then the unsteadiness increases and vice versa.

The concise form of the friction velocity formula including the unsteadiness and non-uniformity of the flow, produces reasonable results with the experimental data. This suggests that the present model is adequate for the unsteady flows over the smooth bed and rough bed as well.

2.5 References

Engelund, F. (1974). “Flow and bed topography in channel bends.” *J. Hydraul. Div.*, 100(11), 1631-1648.

Hosoda, T., Onda, S., Murakami, T., Iwata, M., Shibayama, Y., and Puay, H. T. (2010). “Flood flow simulation in the case of lack of both upstream and downstream

boundary conditions." *Prof. 17th IAHR-APD Congress and 7th IUWM Conference*, Auckland, New Zealand.

Kirkgoz, M. S. (1989). "Turbulence velocity profiles for smooth and rough open-channel flow." *J. Hydraul. Eng.*, 115(11), 1543-1561.

Nezu, I., Kadota, A., and Nakagawa, H. (1997). "Turbulent structure in unsteady depth varying open-channel flows." *J. Hydraul. Eng.*, 123(9), 752-763.

Onda, S., Hosoda, T., and Kimura, I. (2004). "A simple model of a velocity distribution in accelerating/decelerating flows and its application to depth averaged flow model." *Shallow Flows, Proc. International Symposium on Shallow Flows*, Delft, The Netherlands, 637-644.

Steffler, P. M., Rajaratnam, N., and Peterson, A. W. (1985). "LDA measurements in open channel." *J. Hydraul. Eng.*, 111(1), 119-130.

Song, T., and Graf, W. H. (1996). "Velocity and turbulence distribution in unsteady open channel flows." *J. Hydraul. Eng.*, 122(3), 141-154.

Tu, H., and Graf, W. H. (1992). "Velocity distribution in unsteady open channel flow over gravel beds." *J. Hydrosci. Hydraul. Eng.*, 10(1), 11-25.

Chapter 3

THREE-DIMENSIONAL UNSTEADY RANS MODEL FOR OPEN CHANNEL FLOWS

3.1 Preliminaries

Turbulence (sometimes) designated as having complexity in time and space. This phenomenon is ubiquitous, occurs because of instabilities in a flow. From engineering point of view some quantitative properties of turbulent flow, such as the average forces on a surface and its distribution, the degree of mixing between two incoming streams of fluid; are important to examine (Ferziger and Peric 1999). Therefore, various techniques and instruments have been developed to identify the physical description of open-channel turbulence/flows experimentally. The methods of turbulence measurements are categories into point or probe measurements and flow visualization techniques. The descriptions of the techniques and chronicle of turbulence measurements in open-channel flows are provided in Chapter 1.

In Computational Fluid Dynamics (CFD), the solution of any fluid problem requires the solution of the general equations of fluid motion, the continuity and Navier Stokes equations. Because of the complexity of the turbulence measurements in the fluid flows, numerical investigation of turbulent flows is achieved by averaging out all of the unsteadiness of the turbulence. On averaging, the nonlinearity of the Navier-Stokes equations generates the additional set of terms, the Reynolds stresses, which need to model in order to close the equations. This ensemble or time averaged form of Navier Stokes equations are called as Reynolds Averaged Navier Stokes (RANS) equations. The approximation, which prescribes the Reynolds stress tensor and turbulent scalar fluxes in terms of the mean

quantities, are considered in order to derive a closed set of exact equations. These approximate representations of the Reynolds stresses in the Reynolds equations in terms of known or calculable quantities are known as turbulence modeling (Launder 1972).

The Reynolds Averaged Navier Stokes (RANS) type turbulence models are feasible for complex engineering flows, due to its less computational time in comparisons with Large Eddy Simulation (LES) and Direct Numerical Simulation (DES) modeling. Although, there is controversy on the physical meaning of RANS equations, the unsteady RANS approach has been used in computations of unsteady flows (Kimura et al. 2009). Recently, three-dimensional URANS model simulations for hydraulic engineering flows have gained the popularity. The 3D hydrodynamic model solves the unsteady RANS equations in conjunction with a suitable turbulence model (Ge and Sotropoulos 2005). For instance, Chrisohoides et al. (2003) solved the URANS model in relation with k-ω turbulence model. On the other hand, Kimura et al. (2003) used k-ε model for the predictions of flows around bluff bodies.

Even though URANS have advantage to simulate more complex flow field, such as flows with large-scale coherent structure; in present Chapter 3D URANS model is applied to simple open channel flow over smooth and rough beds. The purpose of using 3D URANS model is to check the flow field in consideration with the free surface effects of open channel flow. In previous chapter, one-dimensional depth-averaged model is developed for unsteady flows. However, it is not enough to reproduce the hydrodynamic characteristics of open channel flows. Thus, to study the hydrodynamic behavior of the unsteady flows, 3D URANS model is applied for unsteady flows over smooth and rough beds. Both the standard and no-linear k-ε models are used for this purpose. Similar to the one-dimensional model, the characteristics of 3D URANS model is checked in comparisons with the experimental data of Nezu et al. (1997) and Song and Graf (1996).

3.2 Unsteady Reynolds Averaged Navier Stokes model

The basic equations of k-ε model employed for unsteady incompressible flows are provided by following the coordinate system for three-dimensional open channel flow as depicted in Fig. 3.1.

Continuity equation -

$$\frac{\partial U_i}{\partial x_i} = 0 \tag{3.1}$$

Momentum equation -

$$\frac{\partial U_i}{\partial t} + \frac{\partial U_j U_i}{\partial x_j} = g_i - \frac{1}{\rho}\frac{\partial p}{\partial x_i} + \frac{\partial - u_i' u_j'}{\partial x_j} + \nu \frac{\partial^2 U_i}{\partial x_j^2} \tag{3.2}$$

k - equation -

$$\frac{\partial k}{\partial t} + \frac{\partial k U_j}{\partial x_j} = -u_i' u_j' \frac{\partial U_j}{\partial x_j} - \varepsilon + \frac{\partial}{\partial x_j}\left(\frac{D}{\sigma_k}\frac{\partial k}{\partial x_j}\right) \tag{3.3}$$

ε - equation -

$$\frac{\partial \varepsilon}{\partial t} + \frac{\partial \varepsilon U_j}{\partial x_j} = -C_{\varepsilon 1}\frac{\varepsilon}{k} u_i' u_j' \frac{\partial U_j}{\partial x_j} - C_{\varepsilon 2}\frac{\varepsilon^2}{k} + \frac{\partial}{\partial x_j}\left(\frac{D}{\sigma_\varepsilon}\frac{\partial \varepsilon}{\partial x_j}\right) \tag{3.4}$$

where, x_i, x_j = the spatial coordinates, U_j, u_j' = time-averaged and turbulent velocity components, respectively, p = averaged pressure, ρ = density of the fluid, k = averaged turbulent kinetic energy, ε = averaged turbulent energy dissipation rate, D = eddy viscosity coefficient, ν = kinematic viscosity and σ_k, σ_ε, $C_{\varepsilon 1}$, $C_{\varepsilon 2}$ are model constants whose standard values are $\sigma_k = 1.0$; $\sigma_\varepsilon = 1.3$; $C_{\varepsilon 1} = 1.44$; $C_{\varepsilon 2} = 1.92$.

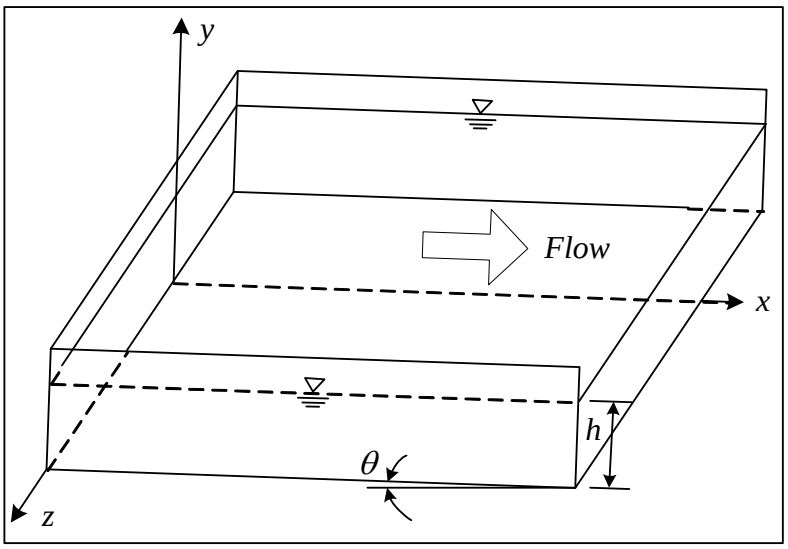

Figure 3.1. Coordinate system for 3D open channel flow

3.3 Turbulence Model

It is already mentioned in the section 3.1 that, to close the RANS equations Reynolds stresses must correlate with the mean velocity components. This closure problem is the most essential but difficult in the turbulent research. Thus, it leads to the study of turbulence closure model in CFD. In *k-ε* turbulence closure the Reynolds stress tensors, evaluated by the constitutive equations are derived from Boussinesq eddy viscosity concept. Based on the linearity of the model, the model can apply to the flows which does/ or does not take into account the anisotropy of the Reynolds stresses.

3.3.1 Standard *k-ε* model

In the standard *k-ε* turbulence model, the anisotropy of the Reynolds stresses does not take into account. Thus, the linear constitutive equation for the Reynolds stress tensor is

$$-u_i'u_j' = D\,S_{ij} - \frac{2}{3}k\delta_{ij} \tag{3.5}$$

$$S_{ij} = \frac{\partial U_i}{\partial x_j} + \frac{\partial U_j}{\partial x_i}; \qquad D = c_\mu \frac{k^2}{\varepsilon} \tag{3.6}$$

where, c_μ is the coefficient of eddy viscosity ($c_\mu = 0.09$).

3.3.2 Non-linear *k-ε* model

The shortcoming of the standard *k-ε* turbulence model for the flows, which induced secondary currents, is overcome by introducing the non-linear term in the constitutive equation.

$$-u_i'u_j' = D\,S_{ij} - \frac{2}{3}k\delta_{ij} - \frac{k}{\varepsilon}D\sum_{\beta=1}^{3}C_\beta\left(S_{\beta ij} - \frac{1}{3}S_{\beta\alpha\alpha}\delta_{ij}\right) \tag{3.7}$$

$$S_{1ij} = \frac{\partial U_i}{\partial x_\gamma}\frac{\partial U_j}{\partial x_\gamma}; \qquad S_{2ij} = \frac{1}{2}\left(\frac{\partial U_\gamma}{\partial x_i}\frac{\partial U_j}{\partial x_\gamma} + \frac{\partial U_\gamma}{\partial x_j}\frac{\partial U_i}{\partial x_\gamma}\right); \qquad S_{3ij} = \frac{\partial U_\gamma}{\partial x_i}\frac{\partial U_\gamma}{\partial x_j} \tag{3.8}$$

The last terms in the constitutive equation are equivalent to the following formula with strain and rotation tensors proposed by Pope (1976) and Gatski and Speziale (1993).

$$\alpha_1\left(S_{il}\Omega_{lj} + \Omega_{li}S_{jl}\right) + \alpha_2\left(S_{il}S_{lj} - \frac{1}{3}S_{km}S_{mk}\delta_{ij}\right) + \alpha_3\left(\Omega_{il}\Omega_{lj} - \frac{1}{3}\Omega_{km}\Omega_{mk}\delta_{ij}\right) \tag{3.9}$$

where strain and rotation parameters are defined as,

$$S = \frac{k}{\varepsilon}\sqrt{\frac{1}{2}\left(\frac{\partial U_i}{\partial x_j}+\frac{\partial U_j}{\partial x_i}\right)^2}\ ; \qquad \Omega = \frac{k}{\varepsilon}\sqrt{\frac{1}{2}\left(\frac{\partial U_i}{\partial x_j}-\frac{\partial U_j}{\partial x_i}\right)^2} \tag{3.10}$$

For the coefficients of non-linear quadratic term, $C_\beta\left(=C_1, C_2, C_3\right)$ Kimura and Hosoda (2003) used following constant values for the incompressible flow around bluff bodies.

$$C_1 = 0.4; \qquad C_2 = 0; \qquad C_3 = -0.13 \tag{3.11}$$

3.4 Free surface calculation

In open channel, presence of free surface influences the turbulence of the flow. Therefore, the calculation of free surface in the turbulence research is foremost important thing. There are several methods available to track the free surface in turbulent flow region, such as Marker and Cell (MAC), Volume of fluid method (VOF), Cubic Interpolation method (CIP). However, in the present study the Density Function method (DFM) is used to evaluate the free surface.

3.4.1 Density function method

In order to identify the free surface between liquid-gas interfaces, following density function is introduced.

$$\frac{\partial F}{\partial t}+\frac{\partial FU_i}{\partial x_i}=0 \tag{3.12}$$

By definition, F should be unity at any point occupied by fluid and zero elsewhere. Because air and water phases are modeled as a single fluid with varying properties (i.e. density, viscosity etc.) dynamic conditions in terms of stresses at the interface between the air and water are not necessary. Rather the dynamic conditions satisfy automatically. The relations between the fluid properties and density function are given as

$$\rho = F\rho_{Liquid}+\left(1-F\right)\rho_{Gas} \tag{3.13}$$

$$\mu = F\mu_{Liquid}+\left(1-F\right)\mu_{Gas} \tag{3.14}$$

The density function is solved in conjunction with the pressure field using SOLA algorithm. This does not cause sharp interface between the air and water, instead the value of *F* changes continuously between the value for air and water at the free surface.

3.5 Discretization of the basic equations

The basic equations are discretized using finite volume method on a staggered grid with the MAC method. The arrangement of hydraulic variables on a full-staggered grid is shown in Fig. 3.2. In the momentum equation, first order upwind scheme is applied to the convection terms and central differencing is used for the diffusion terms. However, for *k*-ε equations hybrid central upwind scheme is utilized. The equations are discretized in fully explicit form. To suppress the time level indexing on pressure and to solve the equations implicitly at each time step SOLA algorithm is used to calculate the pressure field. Finally, the second order Adams Bashforth scheme is used for time integration of each equation.

3.6 Computational condition

Two different experimental cases, smooth bed and rough bed case are analyzed using both linear and non-linear turbulence model. For both the cases sine hydrograph for the discharge is given as an inlet condition, this in turn provided the velocity as an initial condition at the upstream end and depth is held constant at the downstream end as a boundary condition. The numerical grids considered for smooth bed case are $\Delta x = 0.05$; $\Delta y = 0.016$ and $\Delta z = 0.002025$. On the other hand, for rough bed case these are set as $\Delta x = 0.05$; $\Delta y = 0.06$ and $\Delta z = 0.0054$. For both the simulations, Δt is set to be 0.001. The details of the hydraulic parameters are already presented into Table 2.1 of Chapter 2.

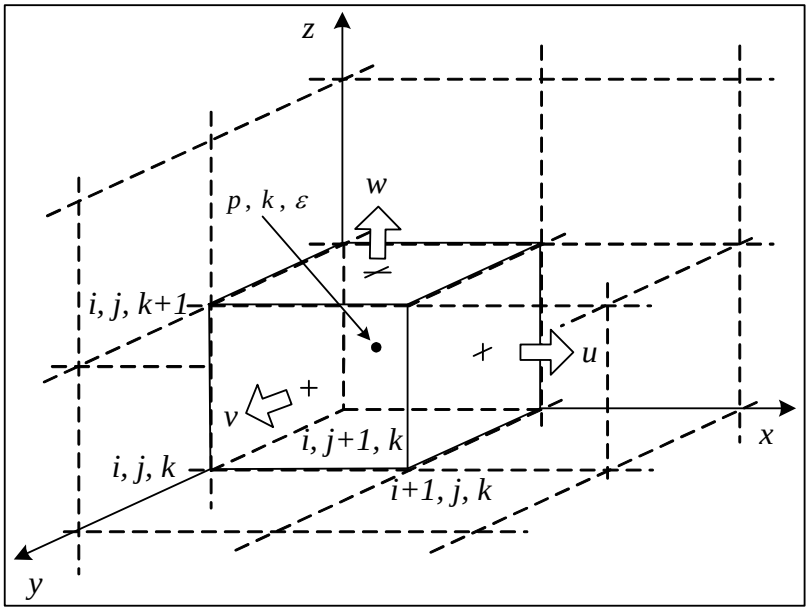

Figure 3.2. Arrangement of hydraulic variables on full staggered grid

3.7 Results and Discussions

3.7.1 Smooth Bed Case

3.7.1.1 Bed shear stress

The temporal variation of normalized bed shear stress and depth hydrograph is plotted along with the experimental data, as shown in Fig. 3.3. The distributions obtained by using the standard *k-ε* model and non-linear *k-ε* model are plotted for two smooth bed cases (NZ1 and NZ2). Here, for both the simulations, the friction velocity is evaluated by Manning's formula. This is further used to determine the bed shear stress. The Num results from both the models are in good agreement with the experimental data. In comparisons with the one-dimensional model (as described in Chapter 2), the distribution is in good agreement with the experimental data. The deviation of the Num results, as observed in previous case/model is much reduced in the present case, especially for case NZ2. The overall distribution of the bed shear stress shows a similar tendency of attainment of peak value before the peak depth occurs. The comparisons of case NZ1 and NZ2 indicates that, maximum value of the bed shear stress is decreases with a decrease in unsteadiness parameter.

3.7.1.2 Loop characteristics

The distribution of mean velocity, the longitudinal and vertical component of turbulence intensity and turbulence shear stresses are plotted for two cases (NZ1 and NZ2) by using the standard and non-linear k-ε model. As depicted in Figs. 3.4(a)-3.5(c), three representative sections of the flow depth; wall region (y/h_b = 0.05), intermediate region (y/h_b = 0.59) and free surface region (y/h_b = 1.13) are considered for the comparisons. Near wall region, both the models illustrated deviation for turbulence component from that of the experimental data. This is possibly due to the wall function values employed during the simulations. On the other hand, in the intermediate region the distributions are in good agreement with the experimental data. The numerical results of two models is distinguished from the turbulence intensity comparisons in the intermediate region, indicating that, non-linear k-ε model is in good agreement with the experimental data as compared to the standard k-ε model.

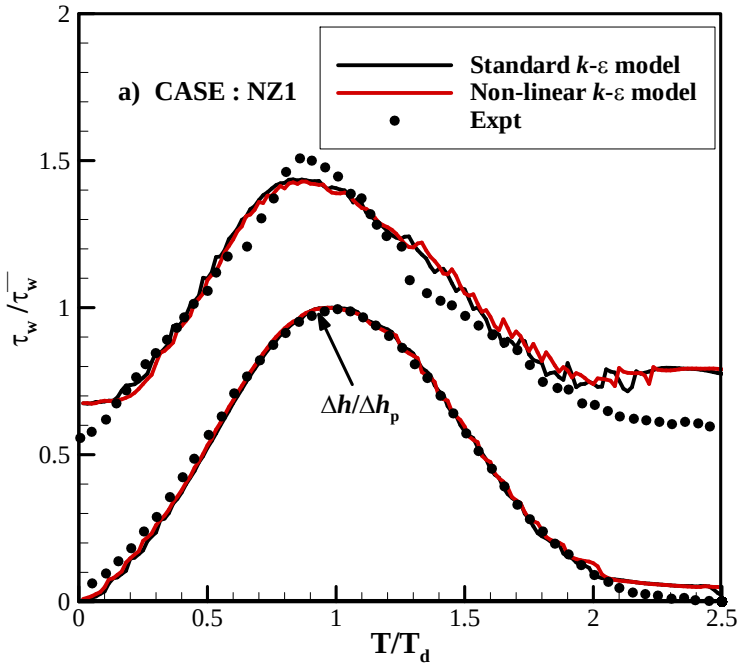

Figure 3.3a. Temporal distribution of bed shear stress for smooth bed: Case NZ1

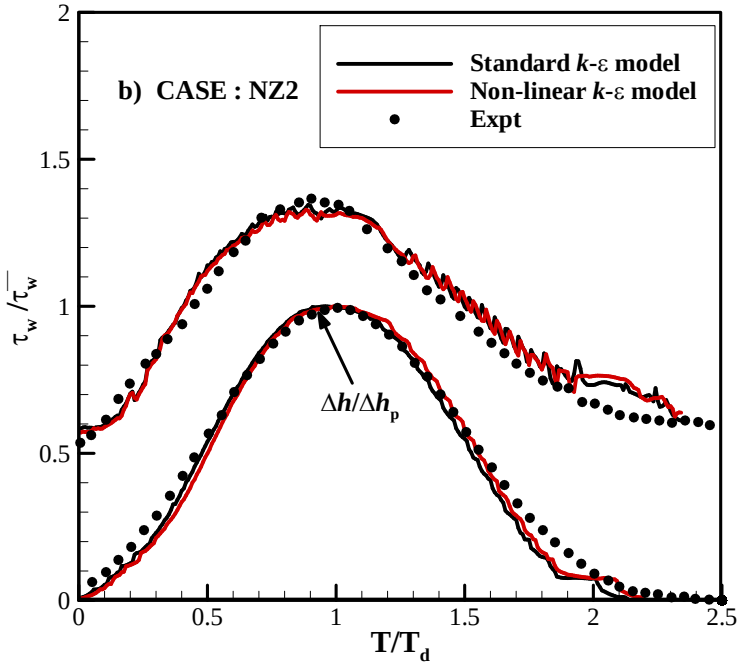

Figure 3.3b. Temporal distribution of bed shear stress for smooth bed: Case NZ2

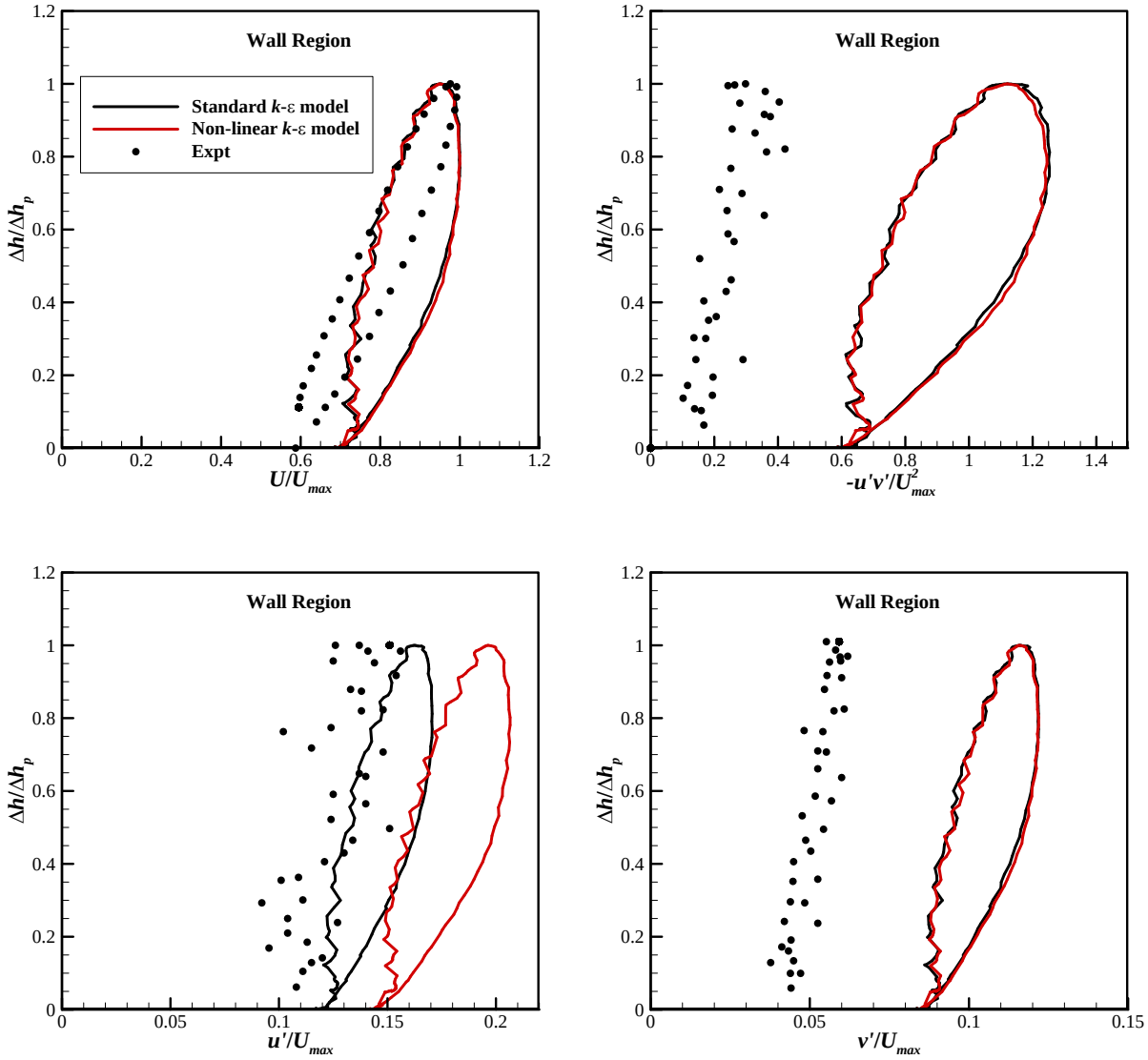

Figure 3.4a. Loop characteristics of averaged velocity U; turbulence intensities u', v' and Reynolds stress $-u'v'$ near wall region: Case NZ1

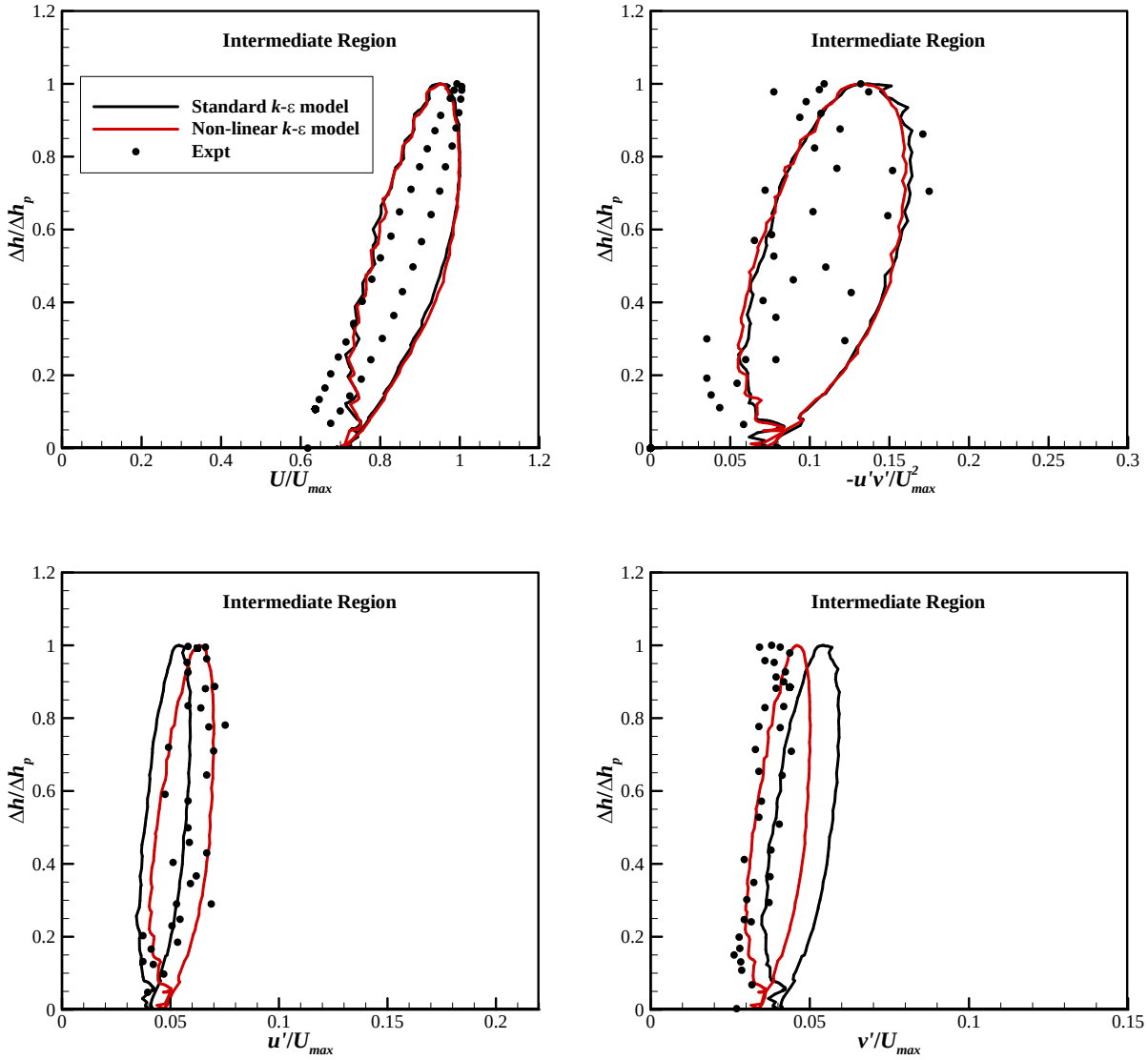

Figure 3.4b. Loop characteristics of averaged velocity U; turbulence intensities u', v' and Reynolds stress $-u'v'$ in intermediate region: Case NZ1

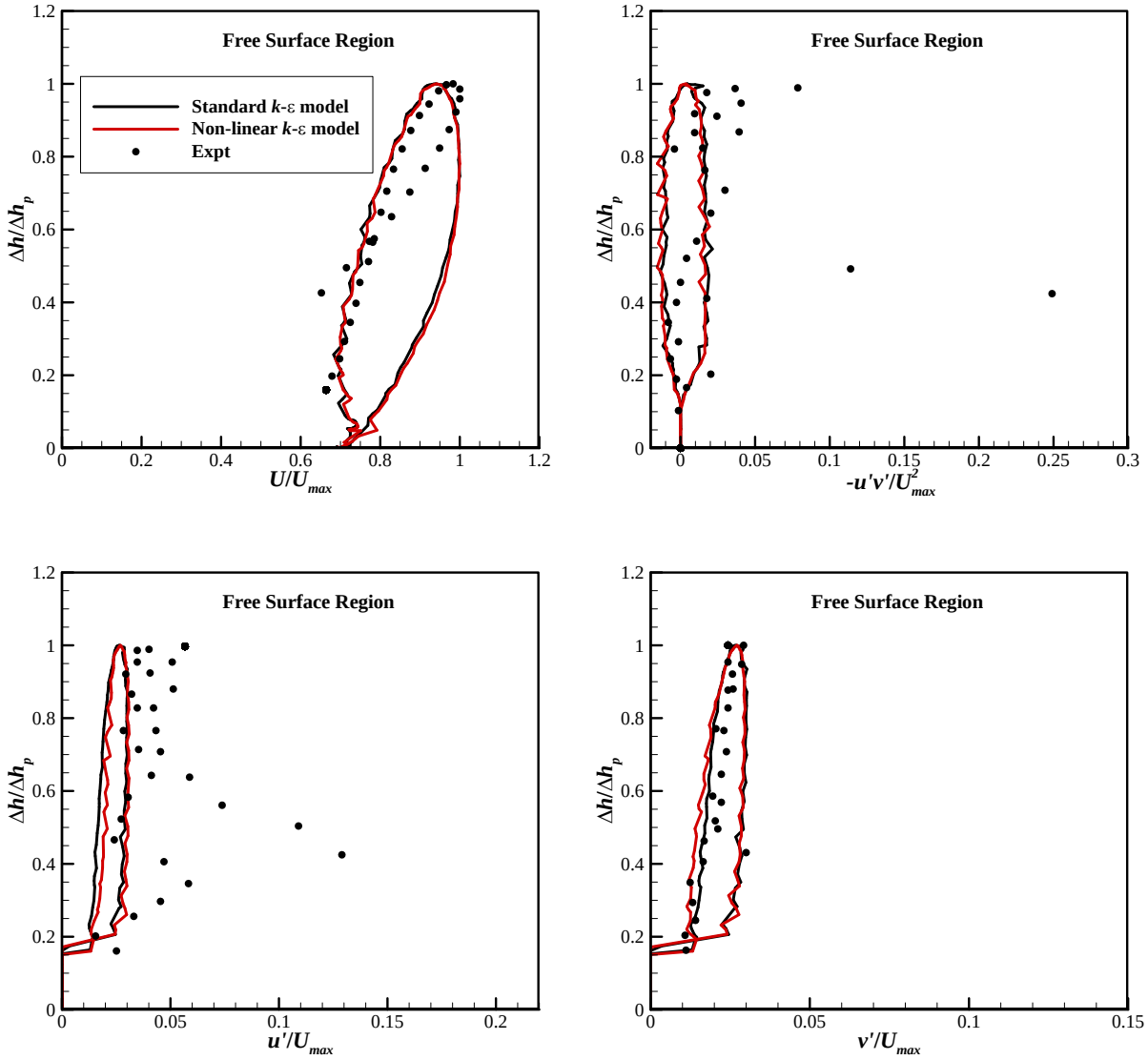

Figure 3.4c. Loop characteristics of averaged velocity U; turbulence intensities u', v' and Reynolds stress $-u'v'$ near free surface region: Case NZ1

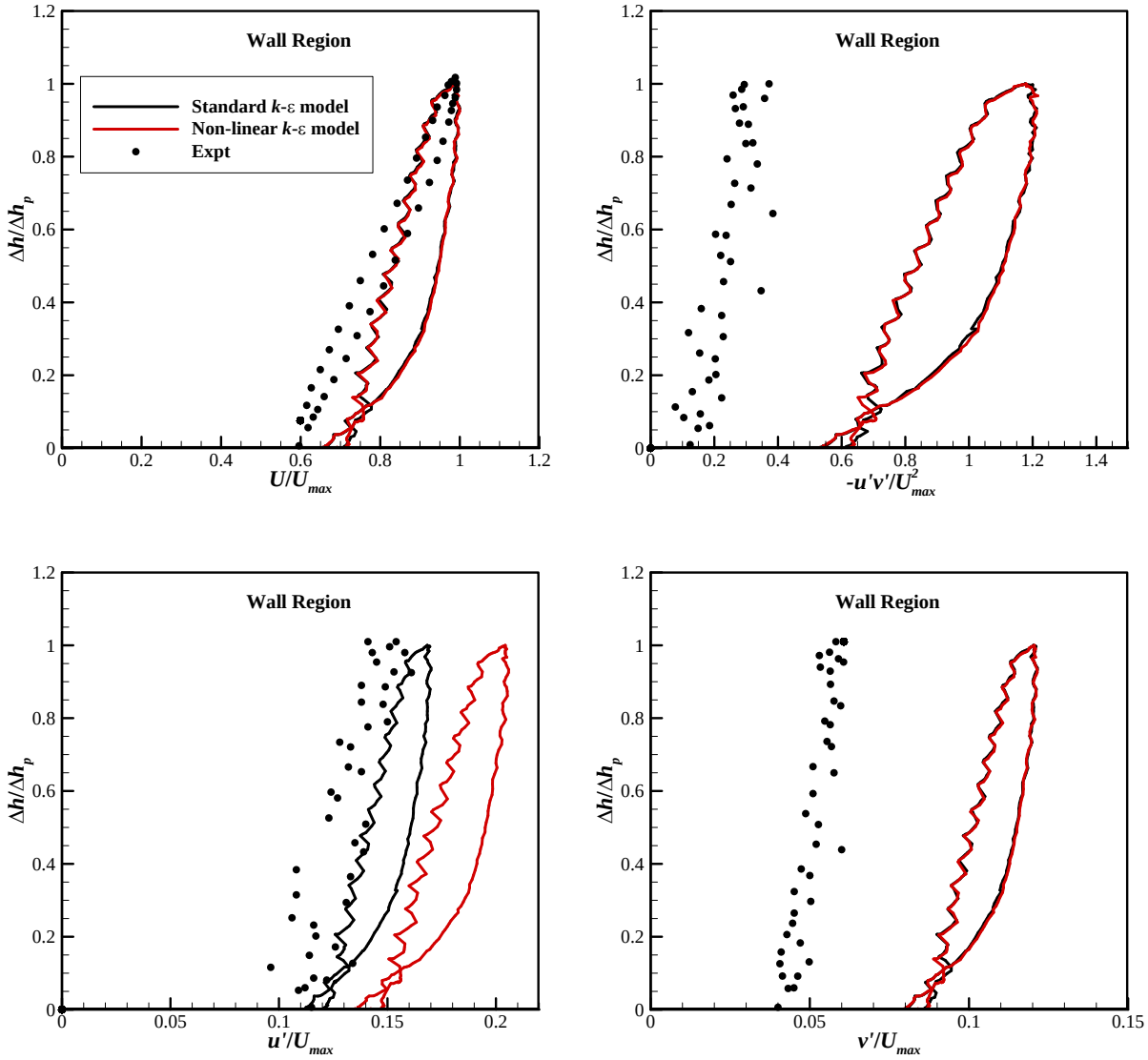

Figure 3.5a. Loop characteristics of averaged velocity U; turbulence intensities u', v' and Reynolds stress $-u'v'$ near wall region: Case NZ2

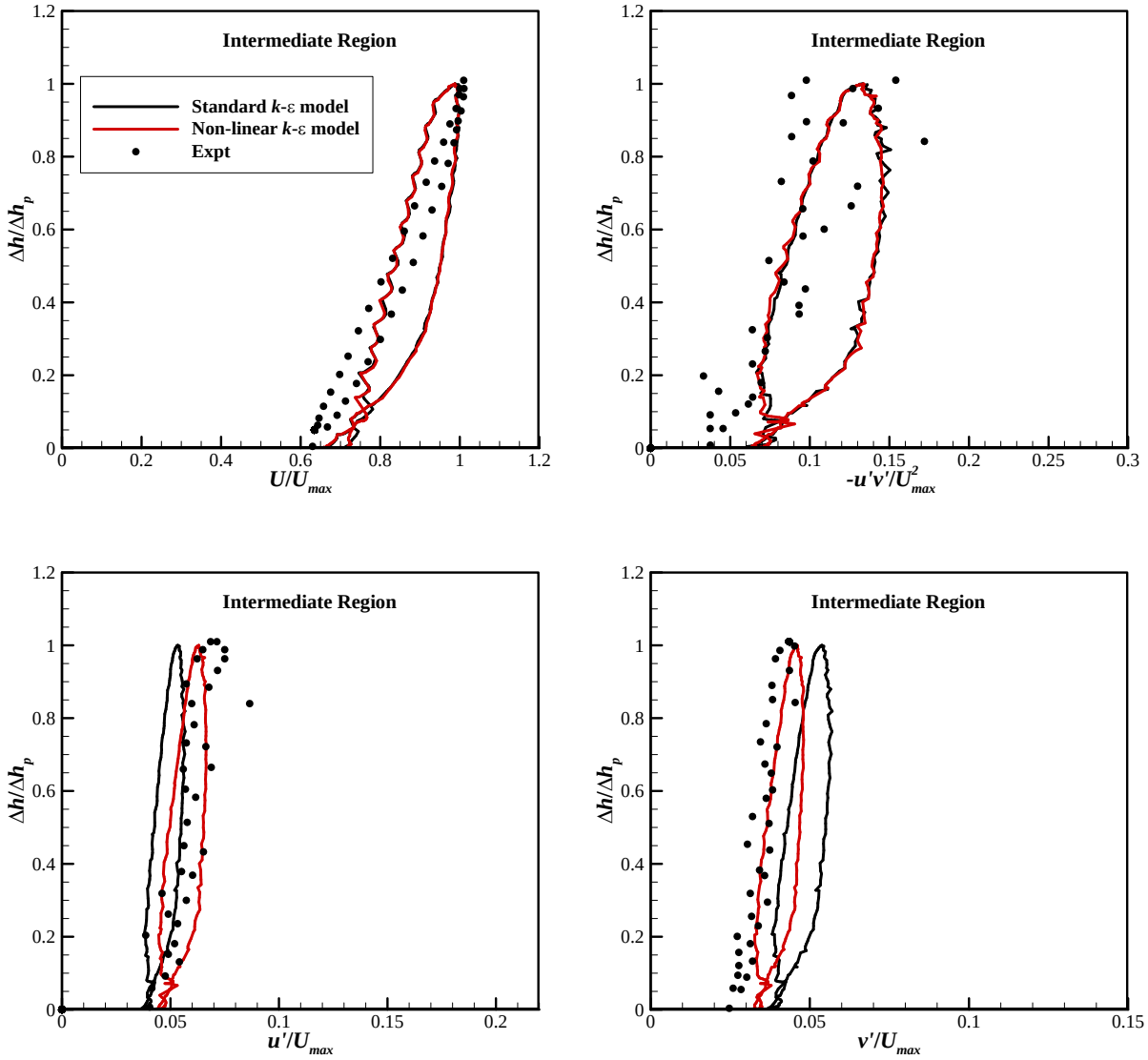

Figure 3.5b. Loop characteristics of averaged velocity U; turbulence intensities u', v' and Reynolds stress $-u'v'$ in intermediate region: Case NZ2

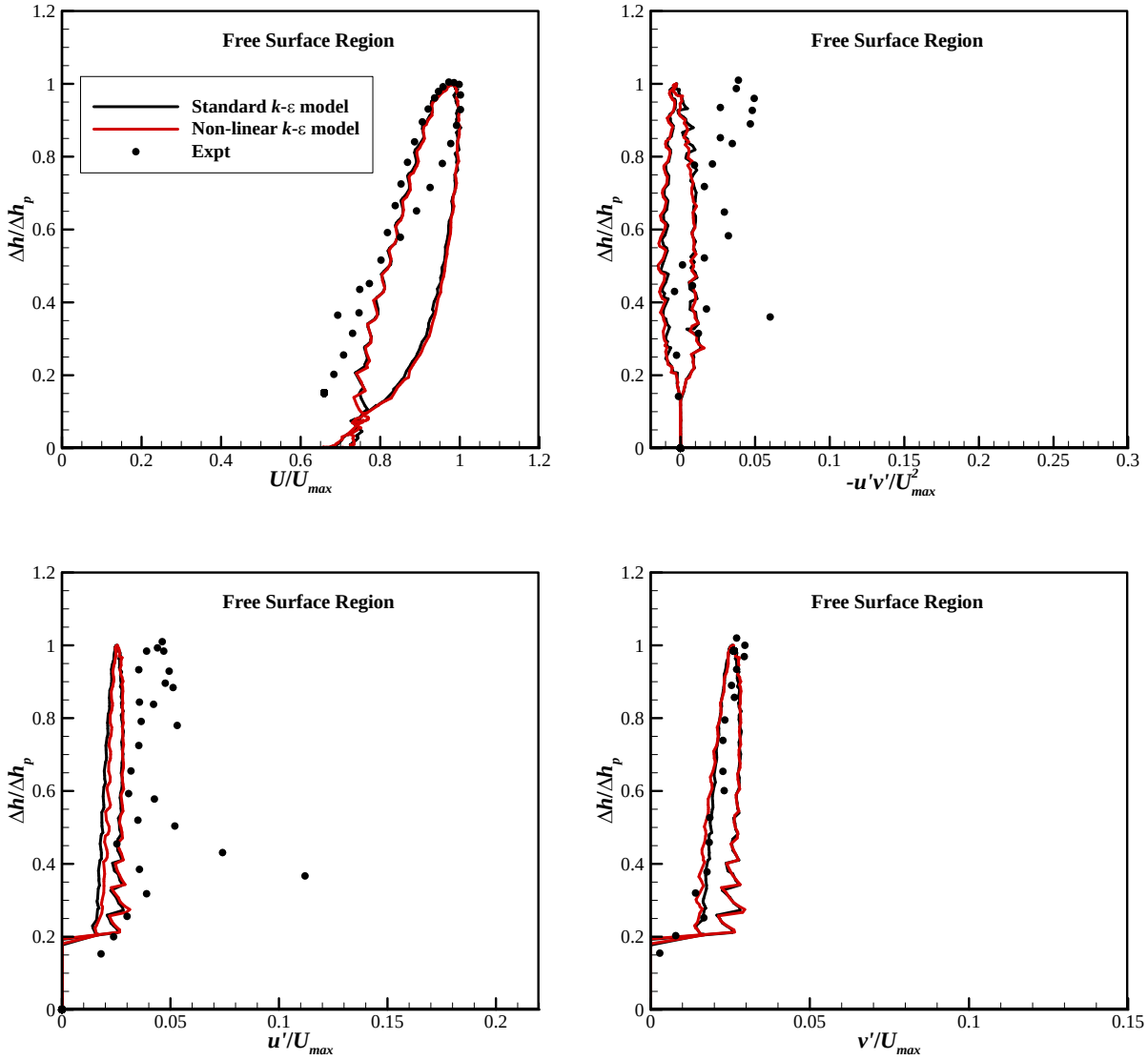

Figure 3.5c. Loop characteristics of averaged velocity *U*; turbulence intensities *u'*, *v'* and Reynolds stress *-u'v'* near free surface region: Case NZ2

Though free surface calculations performed precisely using damping function method, in this case also not even a single model could reproduced an *8-shaped* loop at the free surface. It is difficult to predict the reason of lack of generation of such distribution, because there is no concrete reason of production of *8-shaped* loop described into the experiments.

The characteristic of velocity and turbulence distributions indicates loop property against depth variation, which implies, the turbulence is larger in the rising stage than the falling stage for the same flow depth. The comparisons of two cases also showed that the thickness of the loops of mean velocity and turbulence are decreases with the decrease in unsteadiness parameter.

3.7.1.3 Turbulence intensity

The non-dimensional form of horizontal turbulent intensity along a depth for different duration is plotted in rising and falling stage, as illustrated in Fig. 3.6 (Case NZ1). Along with the standard and non-linear k-ε models, the empirical curve (blue line) for steady flow is also shown in the Fig. 3.6. Similarly, vertical turbulence intensities for both the models are shown in Fig. 3.7(a) for rising stage and in Fig. 3.7(b) for falling stage. Near wall region, turbulence intensities deviated from both the experimental and empirical curve, however near the free surface region, they are in close agreement with the empirical curve. Similar to the experiments, the tendency of being isotropic at the vicinity of the surface is observed, when two components of turbulence intensities are compared with each other.

The non-dimensional forms of the turbulence intensities for NZ2 case are depicted in Figs. 3.8 and 3.9. The distribution of horizontal turbulence intensity for high unsteady flow (Case NZ1) shows higher values as compared to the steady uniform flow. Contrary, for less unsteady flow (Case NZ2), the distributions shows lower values as compared to the steady uniform flow.

Nezu et al., (1994) and Song and Graf (1996) reported that the distributions of turbulence intensities in unsteady flows are nearly equivalent to the one in steady uniform flow. This kind of tendency is observed clearly for vertical turbulence intensity in case NZ2. In this case, the non-linear k-ε model produced good agreement with the empirical curve in comparison to the standard k-ε model.

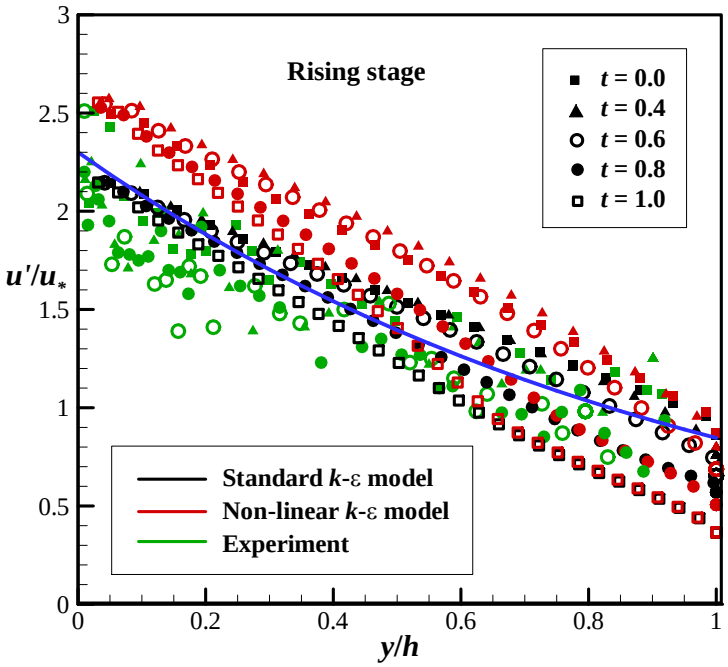

Figure 3.6a. Vertical distribution of horizontal component of turbulence intensity in rising stage: Case NZ1.

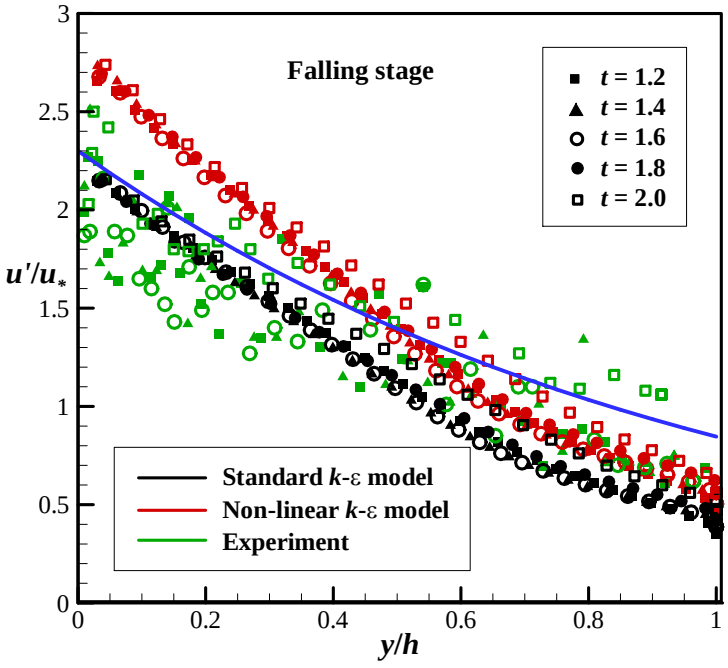

Figure 3.6b. Vertical distribution of horizontal component of turbulence intensity in falling stage: Case NZ1.

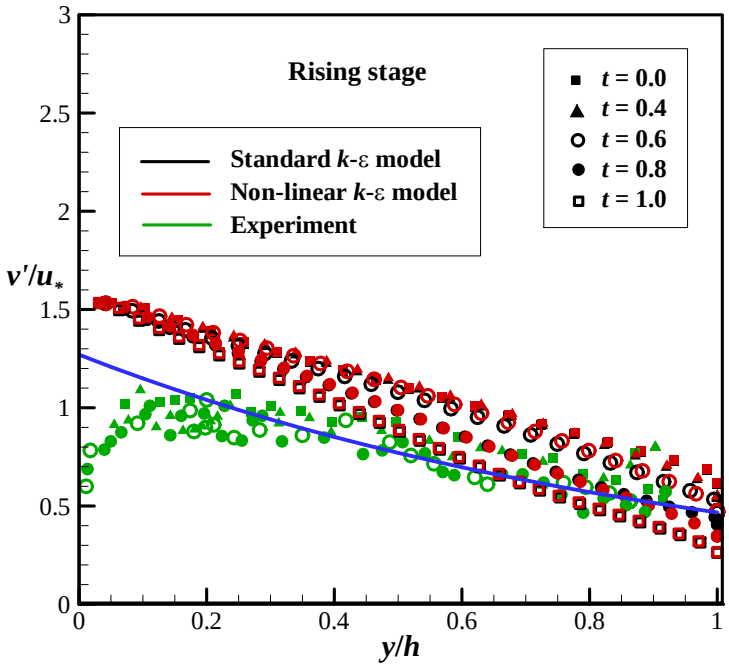

Figure 3.7a. Vertical distribution of vertical component of turbulence intensity in rising stage: Case NZ1.

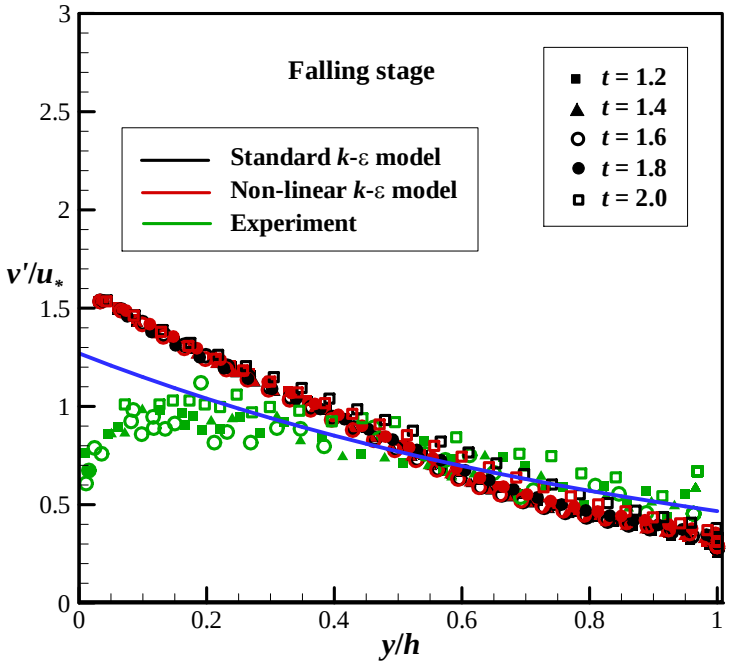

Figure 3.7b. Vertical distribution of vertical component of turbulence intensity in falling stage: Case NZ1.

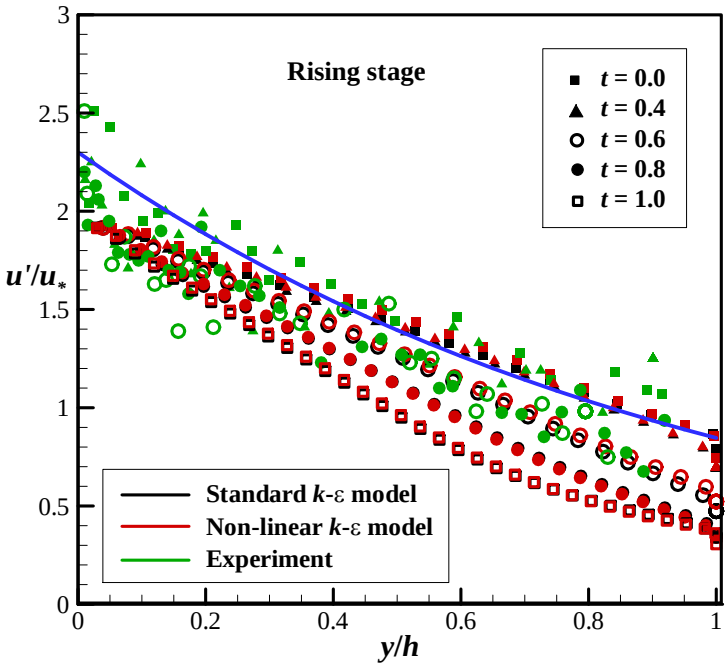

Figure 3.8a. Vertical distribution of horizontal component of turbulence intensity in rising stage: Case NZ2.

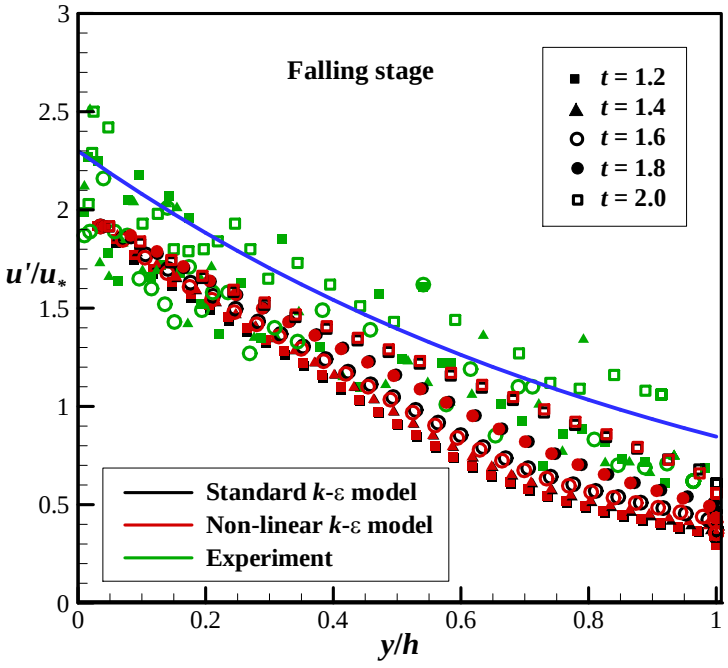

Figure 3.8b. Vertical distribution of horizontal component of turbulence intensity in falling stage: Case NZ2.

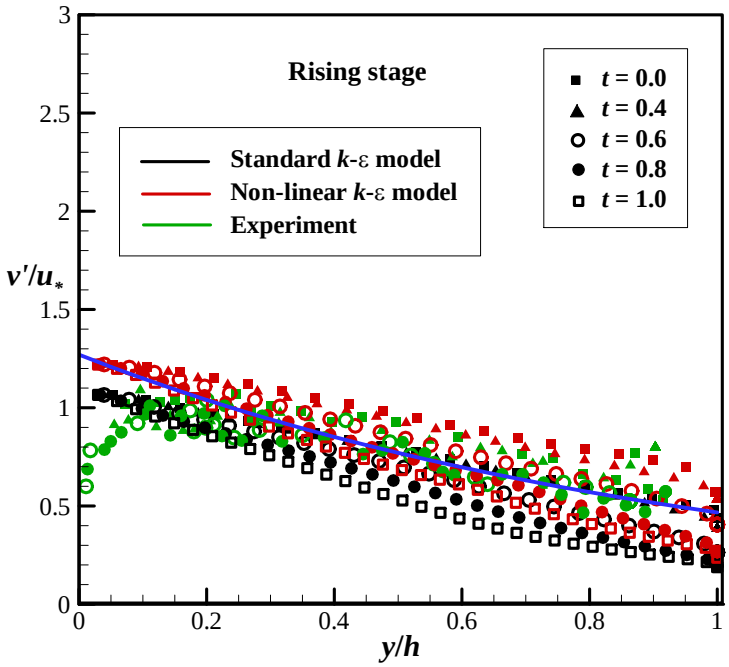

Figure 3.9a. Vertical distribution of vertical component of turbulence intensity in rising stage: Case NZ2.

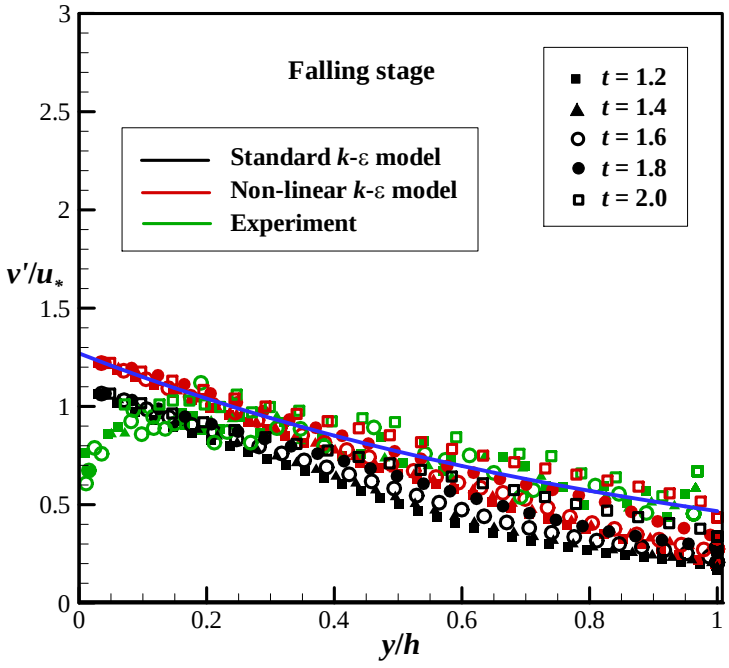

Figure 3.9b. Vertical distribution of vertical component of turbulence intensity in falling stage: Case NZ2.

3.7.1.4 Reynolds shear stress

The distributions of Reynolds shear stress normalized by local friction velocity are exhibited in Fig. 3.10 for Case NZ1 and in Fig. 3.11 for Case NZ2. As mentioned before, due to wall function values, much deviation is observed near the boundary for case NZ1 in both rising and falling stage. On the other hand, the distributions of Reynolds shear stress for case NZ2 are in good agreement with the empirical curve. This imply the findings of Nezu et al. (1997) that, irrespective of the time phase of unsteady flow the Reynolds stresses are in good agreement with the linear curve. It is also seen from both the cases that, in depth varying zone the Reynolds stresses are matching well with the empirical curve. This in turn validate the fact proposed by Nezu et al.(1997) that, the Reynolds stresses normalized by their respective local friction velocity are not affected significantly by the unsteadiness of the flow.

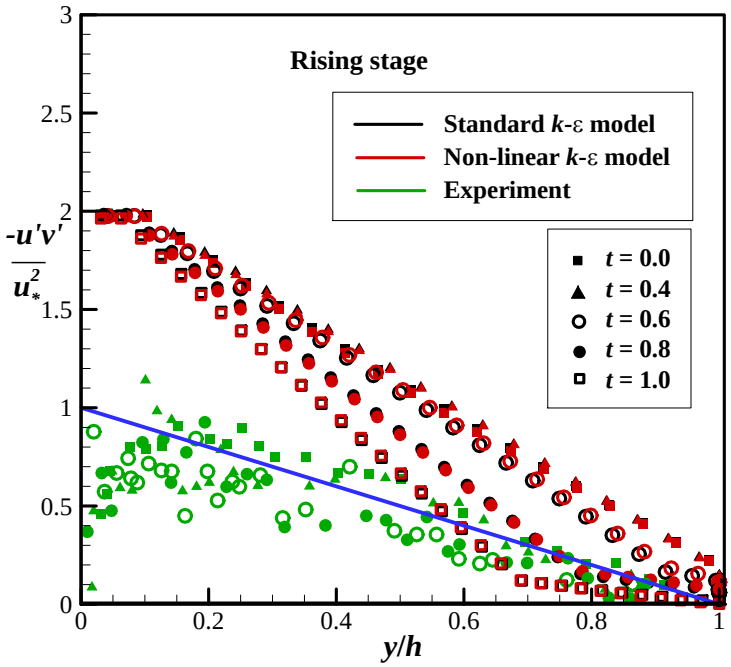

Figure 3.10a. Vertical distribution of dimensionless Reynolds shear stress in rising stage: Case NZ1.

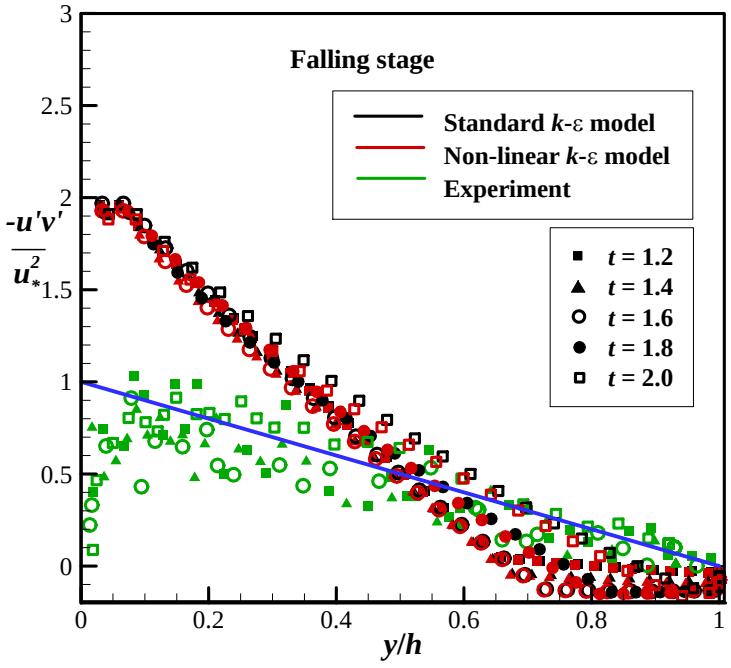

Figure 3.10b. Vertical distribution of dimensionless Reynolds shear stress in falling stage: Case NZ1.

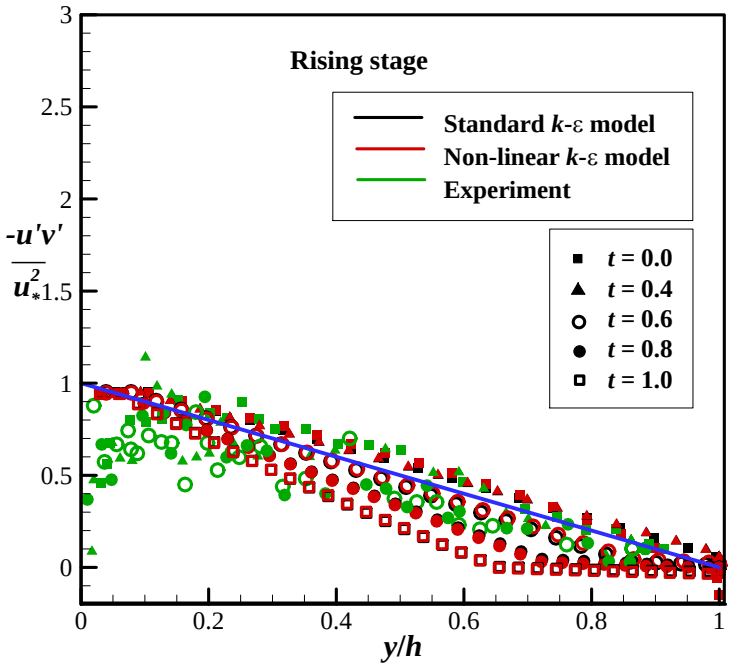

Figure 3.11a. Vertical distribution of dimensionless Reynolds shear stress in rising stage: Case NZ2.

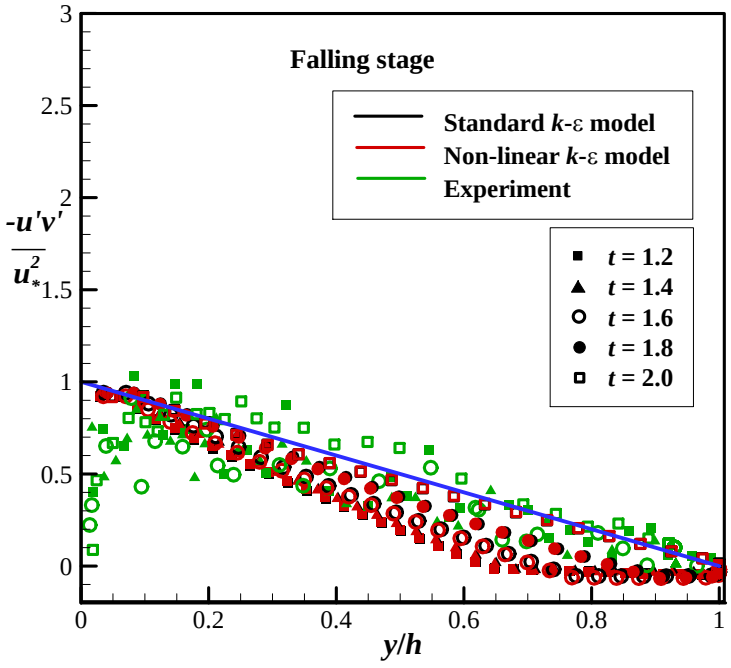

Figure 3.11b. Vertical distribution of dimensionless Reynolds shear stress in falling stage: Case NZ2.

3.7.2 Rough Bed Case

3.7.2.1 Hydrographs

During the passage of flood flow, time variations of hydraulic parameters are plotted for the standard and non-linear *k*-*ε* models. The comparison of depth and discharge hydrographs (Fig. 3.12) shows overestimation of the values in comparisons with the experimental data. Though the distribution of friction velocity underestimated the values, (see Fig. 3.13) the temporal distribution of velocity is in good agreement with the experimental data. Compared to the standard *k*-*ε* model, the non-linear model exhibited the tendency similar to the experimental case, where peak of friction velocity is obtained first and the peak of averaged velocity and discharged obtained in succession. The peak of depth hydrograph attained at the end, indicating the loop rating curves for flood flows.

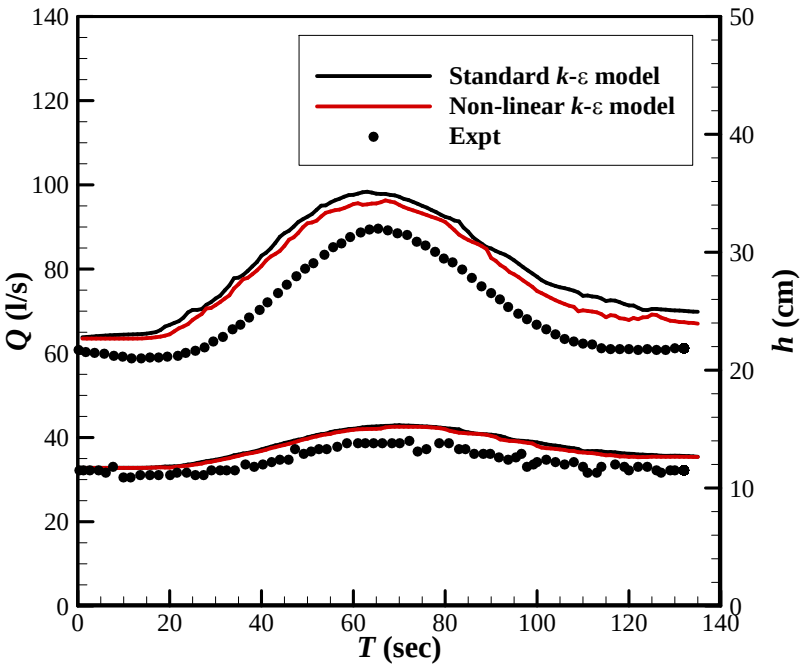

Figure 3.12. Temporal variation of discharge and depth hydrographs

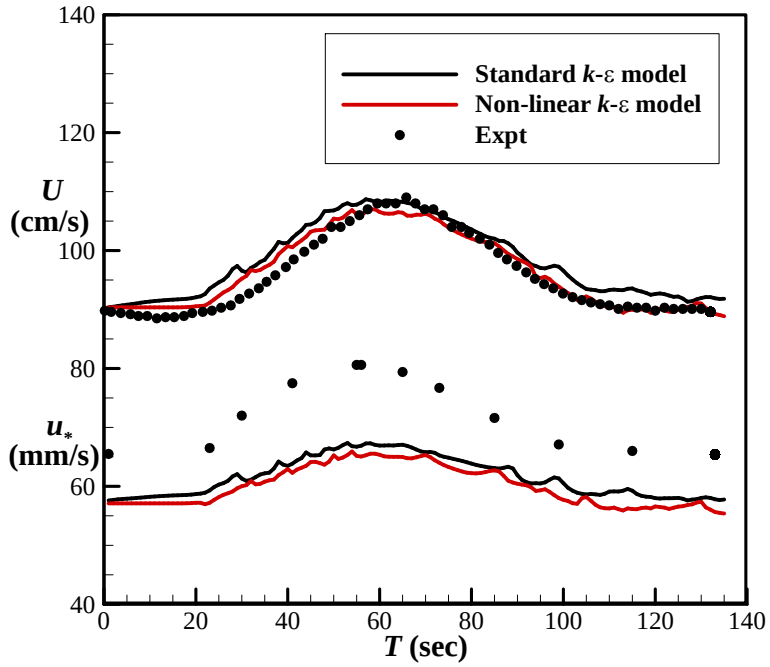

Figure 3.13. Temporal variation of averaged velocity and friction velocity hydrographs

3.7.2.2 Time variation of streamwise velocity

The temporal distributions of point velocity along different depths are plotted in Fig. 3.14. The respective depth of the flow is also included into the figures. Here, to avoid overlapping and for more visibility for distinction between numerical and the experimental results, the distributions of velocity at y = 5.77cm, y = 7.76 cm and y = 9.75cm are shifted from their original position by subtracting 35, 25 and 10 units, respectively. Fig. 3.14 shows that, near wall region and at the free surface, the numerical distributions are little lower than the experimental curves. On the other hand, the distributions of point velocities are in good agreement in the inner region of the flow. It is evident from the figure that, likewise the experiments, the peak value of the velocities near the bed attained later than the peak value of the velocity near the free surface.

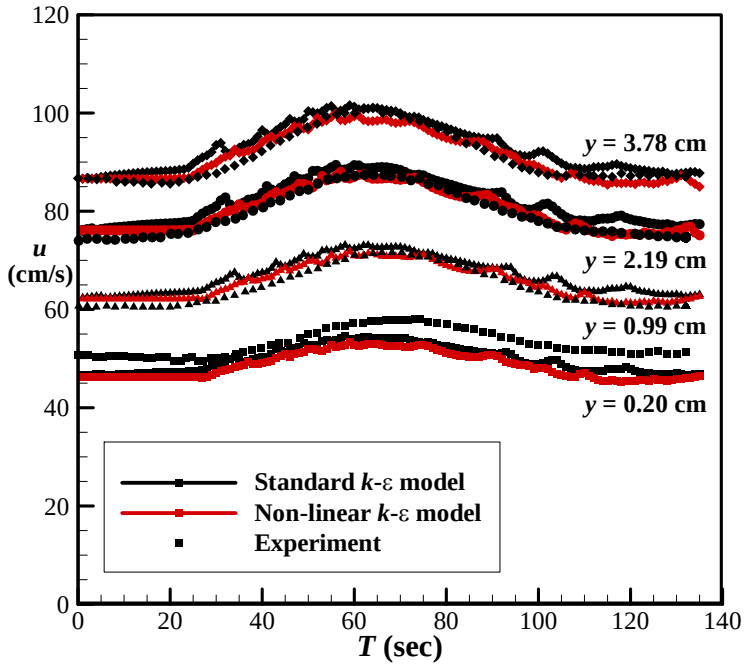

Figure 3.14a. Time variation of point velocity along the depth (in inner region)

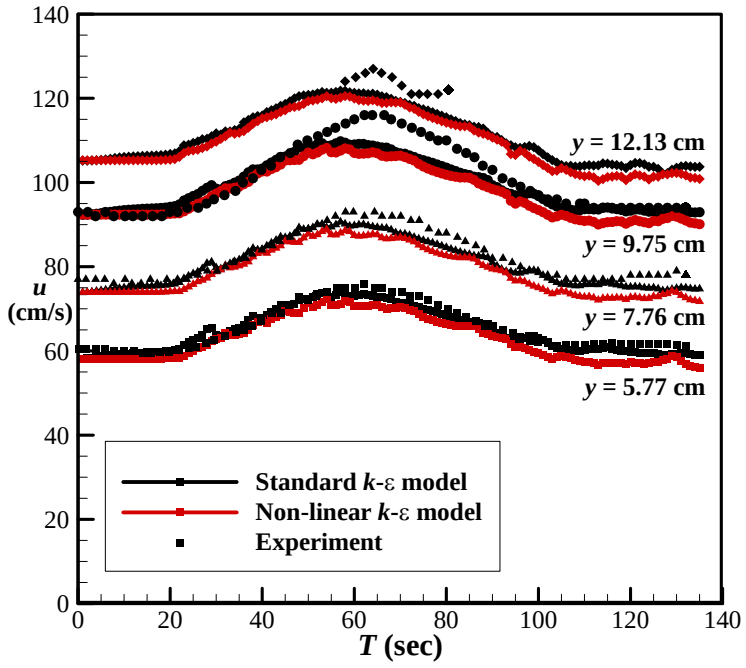

Figure 3.14b. Time variation of point velocity along the depth (in outer region)

3.7.2.3 Vertical distribution of streamwise and vertical velocity

The vertical distributions of streamwise velocity for equivalent depths during rising and falling branch are depicted in Figs. 3.15a-3.15d. The notation in the figures, NL1 stands for the standard and NL2 represents non-linear k-ε model. It is seen from the depth hydrograph that, during the passage of flood flows the peak value of depth is little higher than the experimental curves. Because of that the velocity profile for both the models indicated higher peak compared to the experiments. The overall comparisons of the velocity distributions are in good agreement with the experimental data. These distributions also implied that, the velocity in the rising stage is larger than the corresponding velocity in the falling stage.

Contrary to the streamwise velocity distribution, the distribution of vertical velocity is little deviated from the experimental data for certain depths. (see Figs. 3.16a-3.16d). Especially for non-linear k-ε model, the distribution near the peak discharge and when reaching to the base flow discharge, the vertical velocity is not able to reproduce reasonable comparison. During the intermediate stage, however, the comparisons with the experimental data are reasonably good. The distributions of vertical velocity for the standard k-ε model are in good agreement with the experimental data.

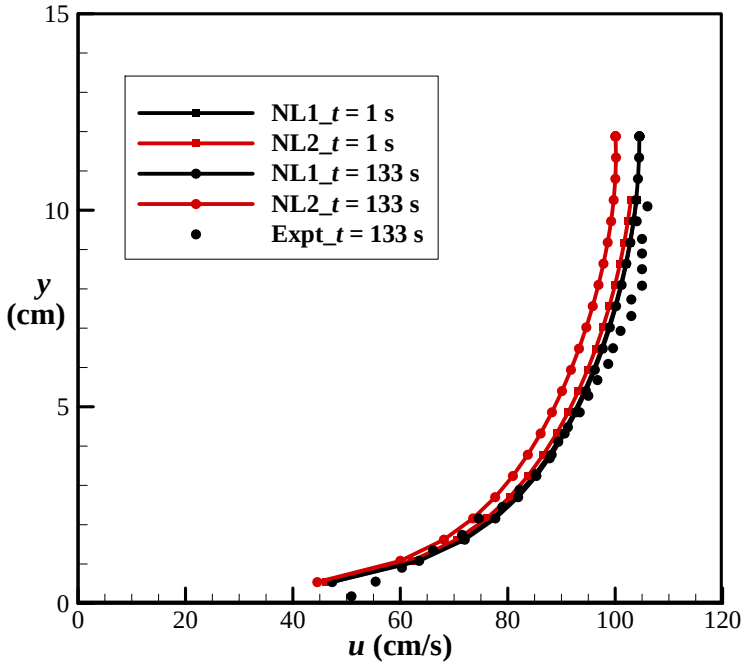

Figure 3.15a. Vertical distribution of streamwise velocity for an equivalent depth (11.3 cm)

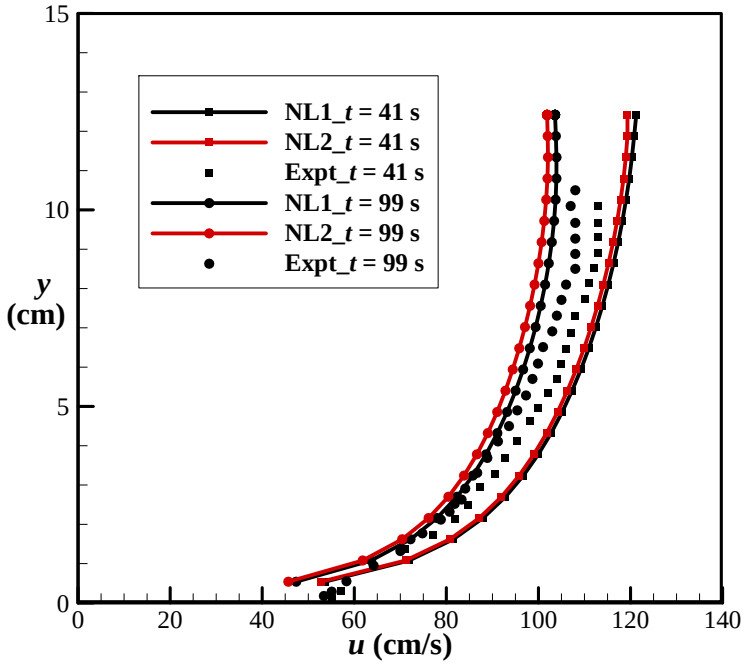

Figure 3.15b. Vertical distribution of streamwise velocity for an equivalent depth (11.9 cm)

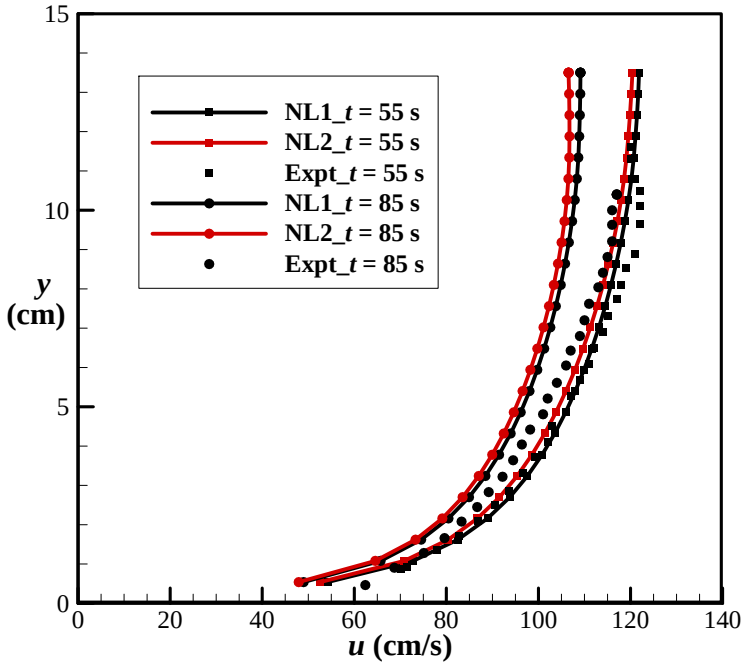

Figure 3.15c. Vertical distribution of streamwise velocity for an equivalent depth (13.5 cm)

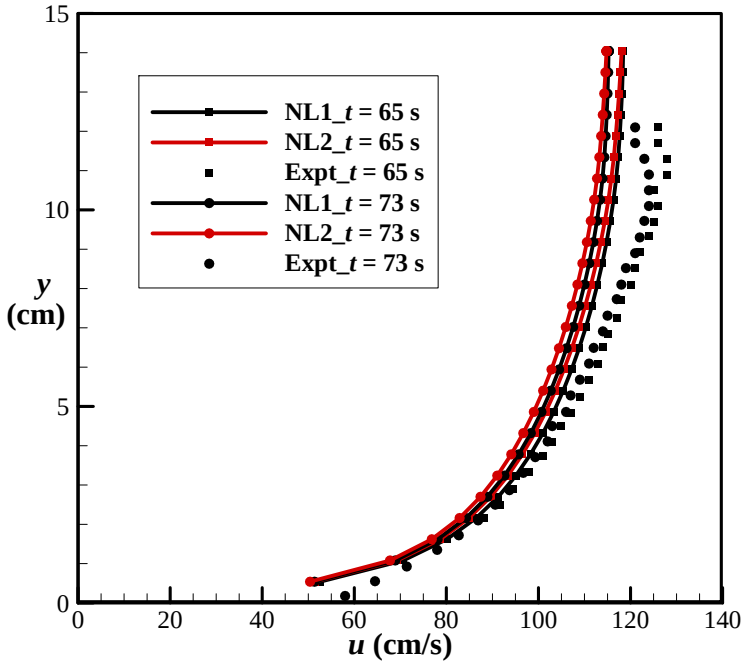

Figure 3.15d. Vertical distribution of streamwise velocity for an equivalent depth (14.0 cm)

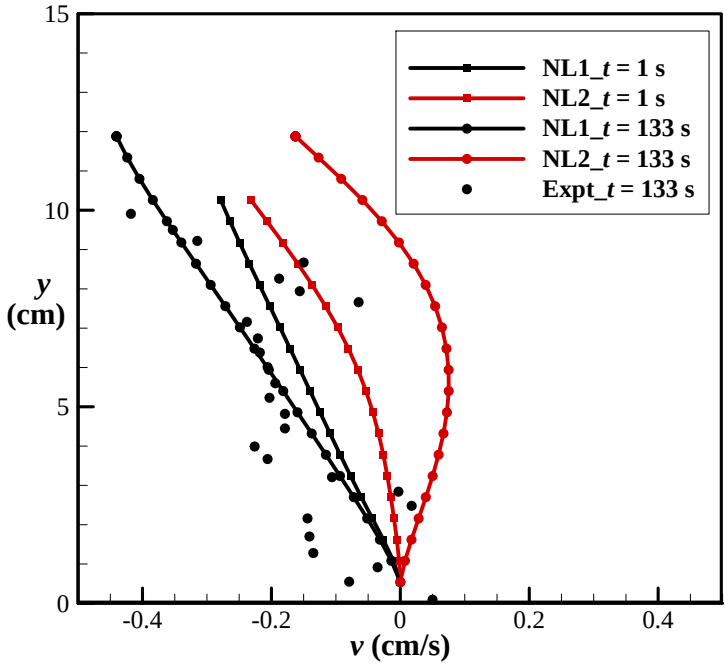

Figure 3.16a. Distribution of vertical velocity for an equivalent depth (11.3 cm)

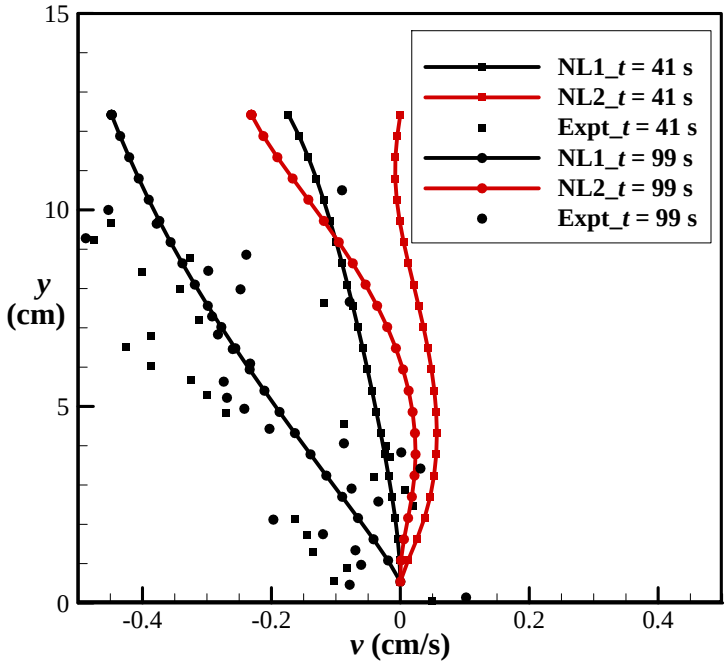

Figure 3.16b. Distribution of vertical velocity for an equivalent depth (11.9 cm)

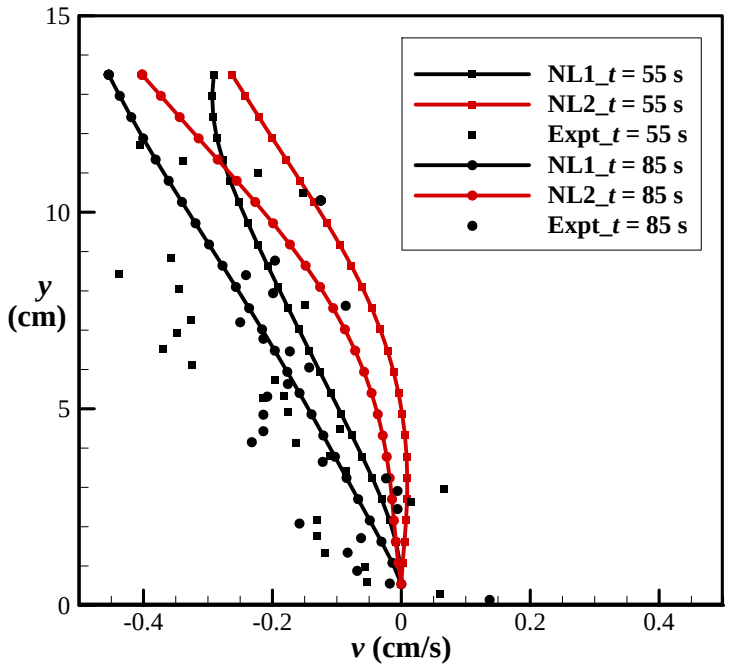

Figure 3.16c. Distribution of vertical velocity for an equivalent depth (13.5 cm)

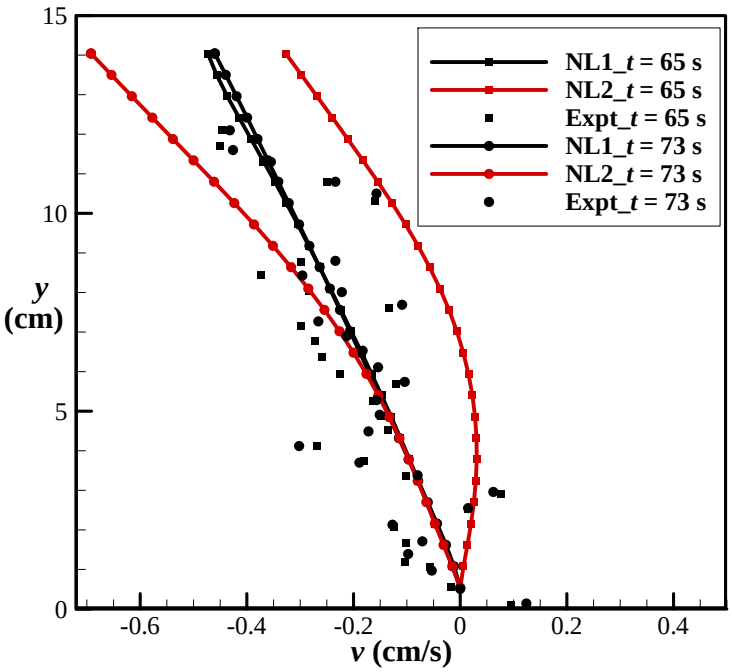

Figure 3.16d. Distribution of vertical velocity for an equivalent depth (14.0 cm)

3.7.2.4 Turbulence intensity

Similar to the smooth bed case the vertical distributions of turbulence intensities are plotted for rough bed case to check the turbulence characteristics over rough bed. As exhibited in Figs. 3.17 and 3.18, the horizontal and vertical components of turbulence intensities are normalized by local friction velocity and plotted against the flow depth. All figures are depicting the distributions of turbulence intensities for an equivalent depth extracted from the rising and falling stages of the flow. For the sake of comparison, the vertical distributions of turbulence intensities for uniform flow over rough bed are also depicted in the same figures. It is already mentioned in the smooth bed case that, the distributions of turbulence intensities in unsteady flows are similar to the one in uniform flow. This kind of behavior is more pronounced in this case as compared to the smooth bed case. Though little deviation encounters during some phases of the horizontal turbulence intensities, the distributions of vertical turbulence intensities are in consistent with the steady uniform flows. Nevertheless, the tendency of being isotropic at the free surface in depth varying zone is seen by superimposing the distributions of two components of turbulence intensities. In this case, also, besides the standard k-ε model, the non-linear k-ε model produced close agreement with the steady uniform flow curves.

3.7.2.5 Reynolds shear stress

Reynolds stresses are non-dimensionalised by respective local friction velocity and plotted against the normalized depth, as shown in Figs. 3.19. These distributions are also exhibits the Reynolds stress profile for an equal water depth that corresponds to the rising and falling branch of the unsteady flow. Comparatively, the Reynolds stress distribution in rough bed case is in close agreement with the empirical curve of uniform flow. For an equal water depth, the behavior of the distributions of Reynolds stress shows larger values in rising stage than the falling stage. Nevertheless, the overall distributions of normalized Reynolds stresses are almost similar to that of uniform flow curve. This again confirms the findings of Nezu et al. (1997). In this case also, the clear comparisons of numerical results with the linear curve in depth varying zone indicated the insignificance of unsteady flow on the normalized Reynolds stresses.

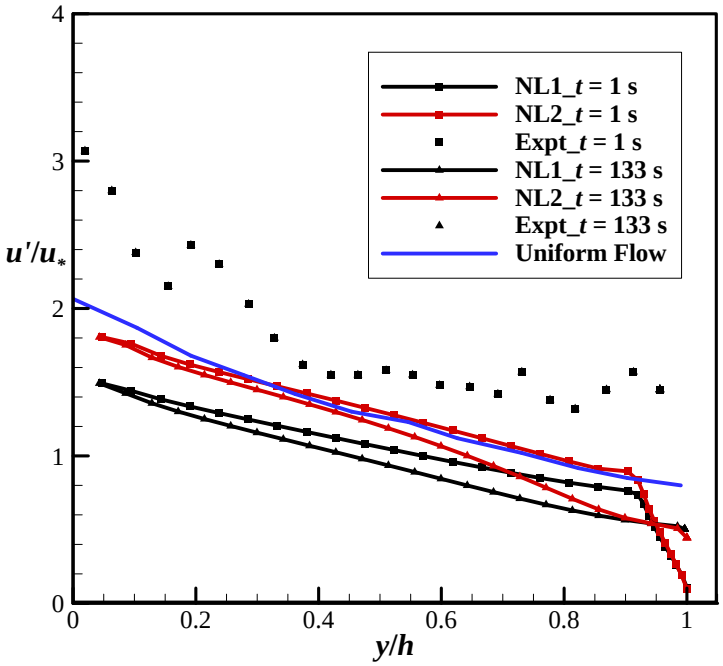

Figure 3.17a. Vertical distribution of horizontal turbulence intensity for an equivalent depth

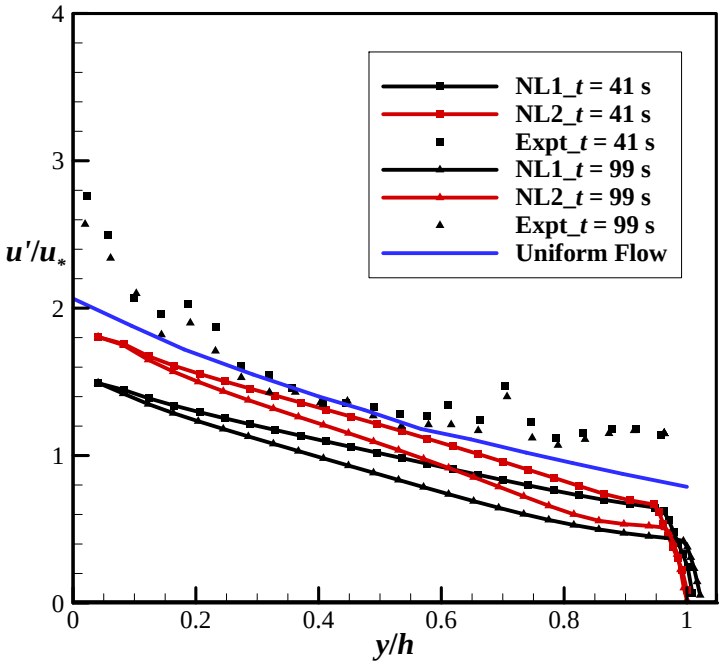

Figure 3.17b. Vertical distribution of horizontal turbulence intensity for an equivalent depth

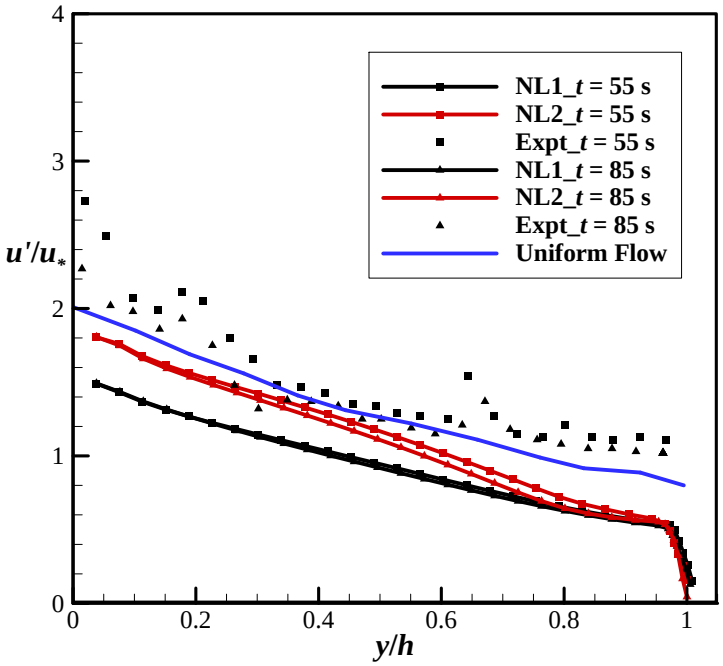

Figure 3.17c. Vertical distribution of horizontal turbulence intensity for an equivalent depth

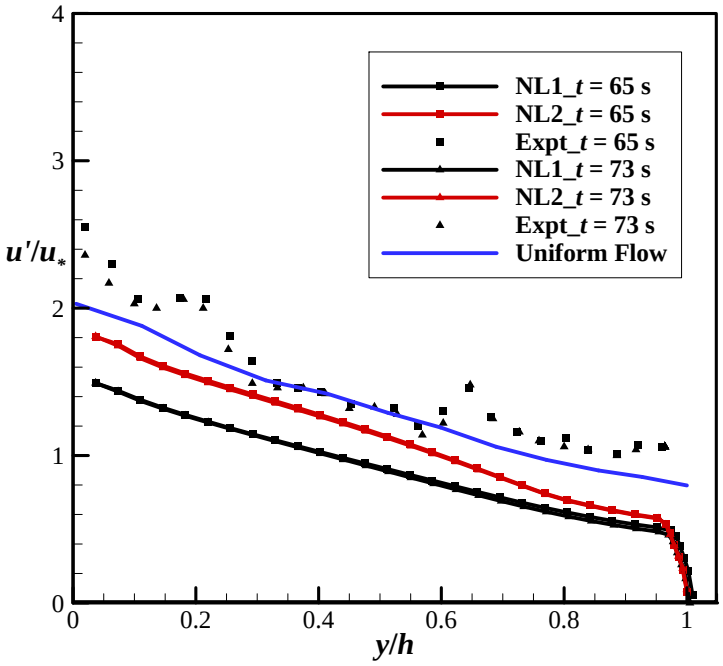

Figure 3.17d. Vertical distribution of horizontal turbulence intensity for an equivalent depth

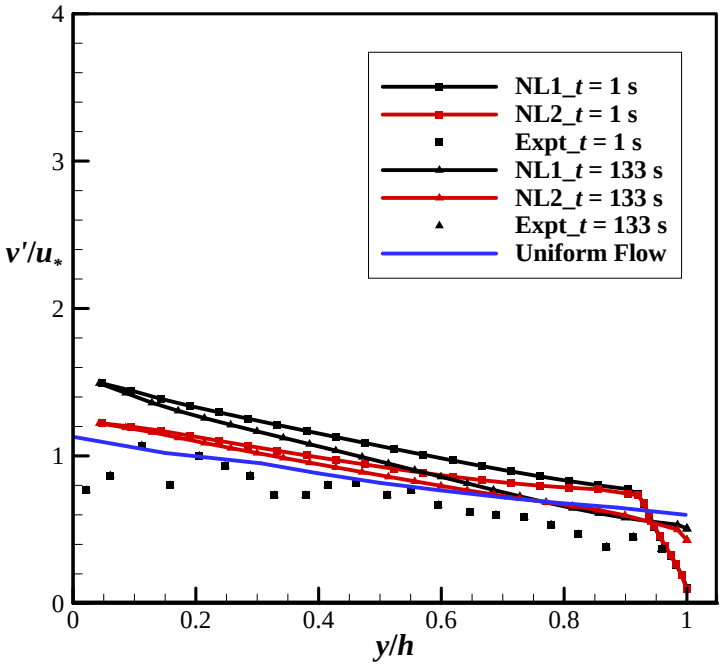

Figure 3.18a. Distribution of vertical turbulence intensity for an equivalent depth

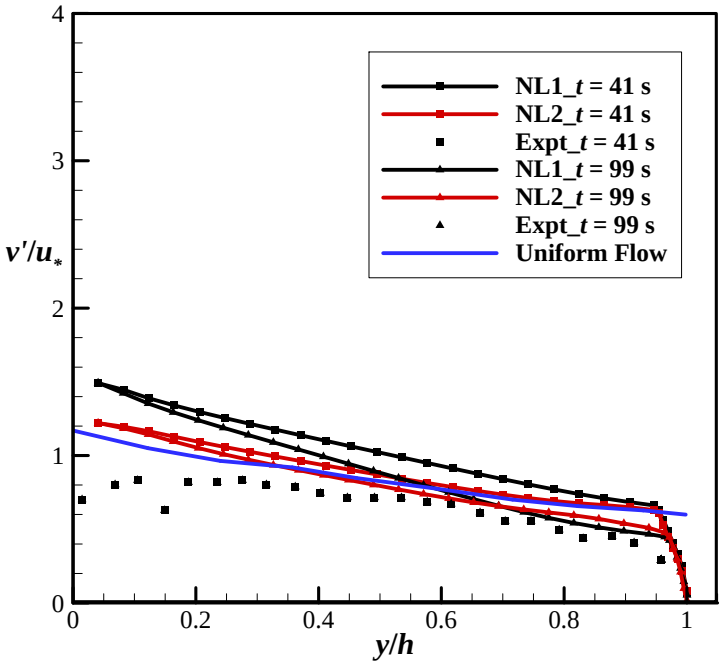

Figure 3.18b. Distribution of vertical turbulence intensity for an equivalent depth

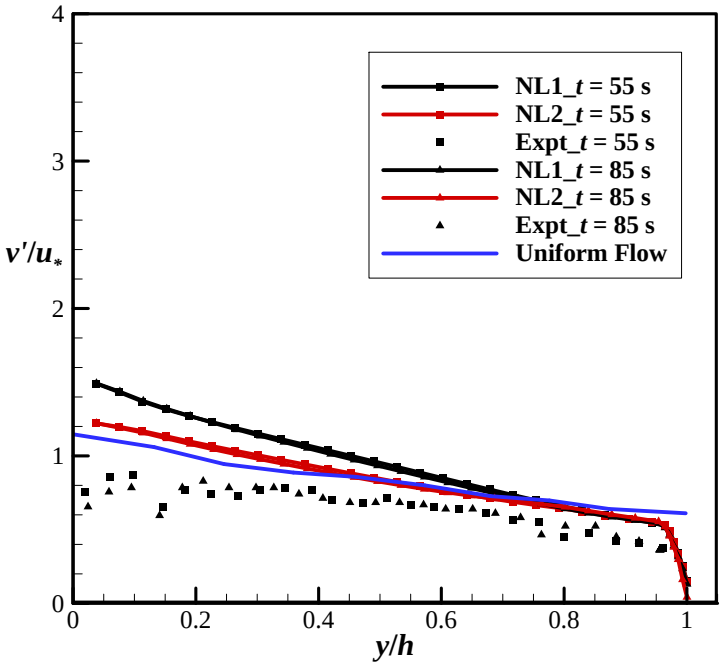

Figure 3.18c. Distribution of vertical turbulence intensity for an equivalent depth

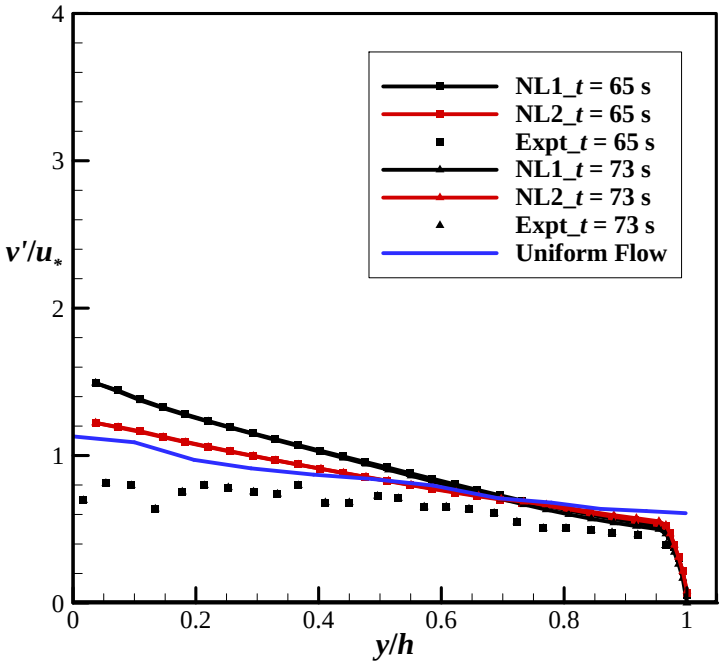

Figure 3.18d. Distribution of vertical turbulence intensity for an equivalent depth

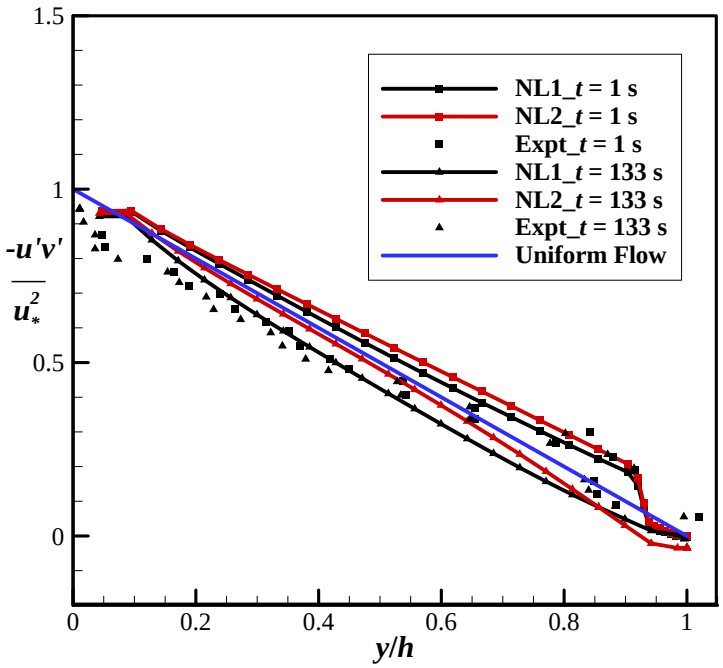

Figure 3.19a. Vertical distribution of Reynolds stress for an equivalent depth

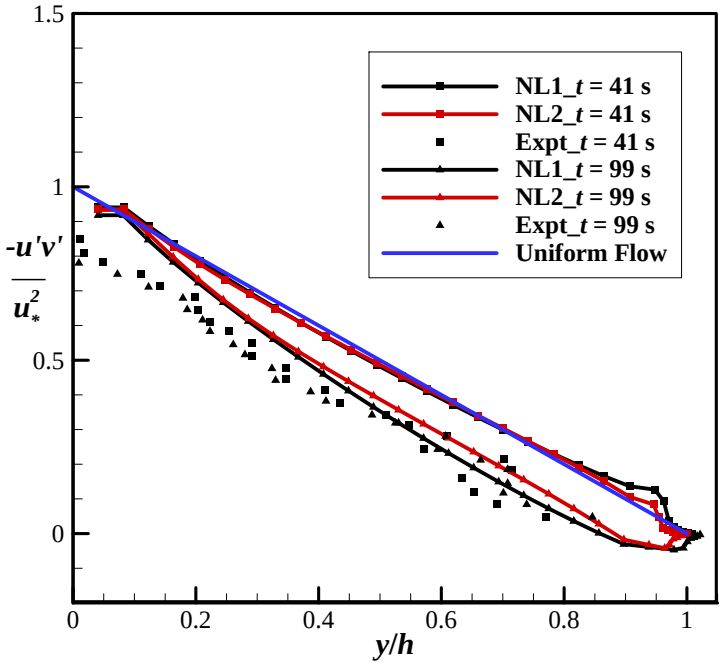

Figure 3.19b. Vertical distribution of Reynolds stress for an equivalent depth

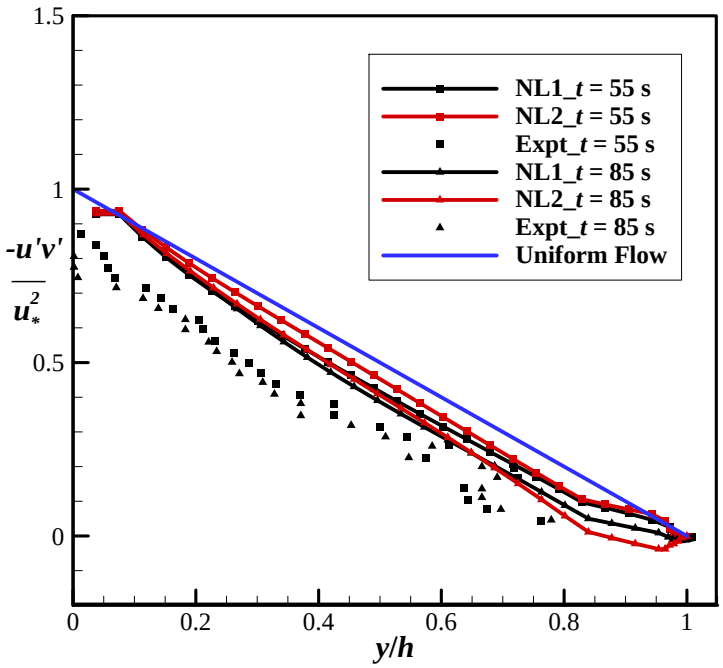

Figure 3.19c. Vertical distribution of Reynolds stress for an equivalent depth

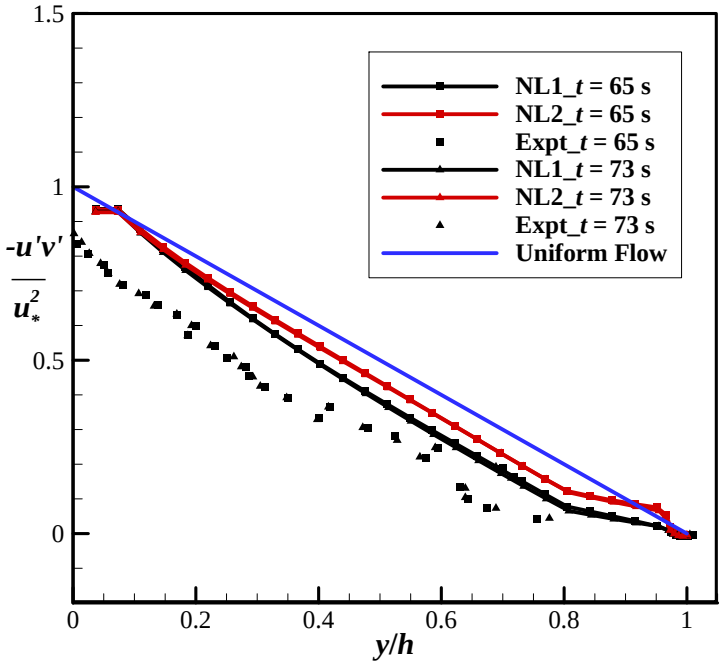

Figure 3.19d. Vertical distribution of Reynolds stress for an equivalent depth

3.8 Summary

Three-dimensional Unsteady Reynolds Averaged Navier Stokes model is used for the simulations of free surface open channel flow over smooth and rough bed. The performance of the standard and non-linear k-ε model is checked in comparison with the experimental data. The behavior of the model is discussed considering the smooth bed case in first section. The temporal distributions of the bed shear stress are employed initially to characterize the effect of unsteadiness of the flow. Following the distributions of wall shear stress, the loop property of the velocity, horizontal and vertical turbulence intensity and Reynolds stresses are compared to analyze again the effect of unsteadiness of the flow. The distributions of turbulence intensities and Reynolds stresses are then plotted for rising and falling stages to check the behavior of the distributions in comparisons with the uniform flow.

After discussing the characteristics of the hydraulic variables over smooth bed, the model is applied for rough bed case in subsequent section. Similar to the smooth bed case, the hydraulic variables for rough bed case are compared with the experimental data. Begin with the discussions of hydrographs for the hydraulic variables, the distributions of point velocities for different depths and the characteristics of distributions of streamwise and vertical velocity are explained in rising and falling stages. Finally, the characteristics of vertical distribution of normalized Reynolds stresses are discussed in rising and falling stages of the flows. Through the comparisons of numerical and experimental results, it is obvious that, the numerical results of non-linear k-ε model are in good agreement with the experiments as compared to the standard k-ε model. However, this tendency is more pronounced for rough bed case.

3.9 References

Chrisohoides, A., Sotiropoulos, F., and Sturm, T. W. (2003). “Coherent structures in flat-bed abutment flow: Computational fluid dynamics simulations and experiments.” *J. Hydraul. Eng.*, 129(3), 177-186.

Ferziger, J. H., and Peric, M. (1999). “Computational methods for fluid dynamics.” 2nd rev. ed., Springer.

Gatski, T. B., and Speziale, C. G. (1993). "On explicit algebraic stress models for complex turbulent flows." *J. Fluid Mech.*, 254, 59-78.

Ge, L., and Sotiropoulos, F. (2005). "3D unsteady RANS modeling of complex hydraulic engineering flows. I:Numerical methods." *J. Hydraul. Eng.*, 131(9), 800-808.

Kimura, I., and Hosoda, T. (2003). "A non-linear *k*-ε model with realizability for prediction of flows around bluff bodies." *Int. J. Numer. Meth. Fluids*, 42, 813-837.

Kimura, I., Wim, S. J., Hosoda, T., and. (2009). "URANS computations of shallow grid turbulence." *J. Hydraul. Eng.*, 135(2), 118-131.

Launder, B. E. (1972). "Lectures in mathematical models of turbulence." Academic Press, London, UK.

Nezu, I., Kadota, A., and Nakagawa, H. (1997). "Turbulent structure in unsteady depth varying open-channel flows." *J. Hydraul. Eng.*, 123(9), 752-763.

Nezu, I., and Nakagawa, H. (1993). "Turbulence in open-channel flows." *IAHR Monograph*.

Pope, S. B. (1975). "A more general effective viscosity hypothesis." *J. Fluid Mech.*, 72, 331-340.

Song, T., and Graf, W. H. (1996). "Velocity and turbulence distribution in unsteady open channel flows." *J. Hydraul. Eng.*, 122(3), 141-154.

Chapter 4

ANALYTICAL SOLUTION OF k - ε MODEL FOR UNIFORM AND NON-UNIFORM FLOWS

4.1 Preliminaries

It is already described in the previous chapter that, in order to derive the close sets of equations, some approximations are considered in the Reynolds equation. These approximations are then leads to the study of turbulence modeling. Turbulence modeling involves different levels of approximations, such as algebraic models, one-equation models, two-equation models and Reynolds stress models. Amongst all two-equation models have more advantage that they are independent on algebraic length scale and can be applied to more complex flow fields.

Two equation models are based on determination of two scales; time/velocity scale and length scale, which is extracted from two independent variables. Numbers of different two equation models have been proposed over the years grounded on these assumptions. (For example, *k*-ε model by Launder and Spalding 1974; *k*-ω model by Wilcox 1988; *k-t* model by Speziale et al. 1990). Amongst the most popular two-equation model is *k*-ε model. The standard *k*-ε model solves the transport equation for turbulent kinetic energy, *k*, which determines the velocity scale while an equation for the turbulence dissipation rates, ε, determines the length scale. In early 80's Rodi (1980) began to apply *k*-ε model to the hydraulic problems. Subsequently, the applicability of *k*-ε model is verified by various researchers in turbulent flows by using 2-D (Elkaim et al. 1992) and 3-D flows (Kimura and Hosoda 2003).

Not only numerical and experimental works but theoretical studies have also been performed to characterize the turbulence of the flow. Most of the approaches had been made towards the construction of the one-point turbulence model by using two-point closure theories (Yoshizawa 1994). Takemitsu (1990), on the other hand performed an analytical study of the standard *k-ε* model. The study reproduced an asymptotic solution and five model constants are determined reasonably by using the experimental data. However, the solution showed an ill-posed behavior of the standard *k-ε* model because of the presence of divergent terms in the second order solution. To avoid the mathematical ill-posed behavior of the model, he further suggested the delicate adjustments of the model constants.

To overcome this difficulty; as we have also been facing the same difficulty before we come across to Takemistu's (1990) research, an effective analytical solution for the standard *k-ε* model is proposed. The primary concern of the research is to improve the velocity distribution for depth-averaged model that failed to reproduce well by the Engelund model as described in Chapter 1. Along with the velocity distribution, to evaluate the additional flow properties analytically, the theoretical solution for uniform flow by using the standard *k-ε* model is developed.

As the damping effect of the turbulence near free surface reduces the vertical fluctuations; the distribution of eddy viscosity indicates the parabolic shape. Thus, to check the effect of such damping function also on the velocity distribution the analysis is conducted using the standard *k-ε* model by including and excluding the damping function. After successful reproduction of the distributions in uniform flow, similar analysis is performed for the non-uniform flow. The validations of the analytical results are assured by using the numerical results of finite difference scheme, experimental results of Song and Graf (1994) and the empirical results of Nezu (1977).

4.2 *k-ε* Model

The basic equations for incompressible fluid flows are:

Momentum equation -

$$\frac{\partial U_i}{\partial t} + \frac{\partial U_j U_i}{\partial x_j} = g_i - \frac{1}{\rho}\frac{\partial p}{\partial x_i} + \frac{\partial - u_i' u_j'}{\partial x_j} + \nu \frac{\partial^2 U_i}{\partial x_j^2} \tag{4.1}$$

The transport equation for turbulent kinetic energy is given as:

$$\frac{\partial k}{\partial t}+\frac{\partial kU_j}{\partial x_j}=-u_i'u_j'\frac{\partial U_j}{\partial x_j}-\varepsilon+\frac{\partial}{\partial x_j}\left(\frac{D}{\sigma_k}\frac{\partial k}{\partial x_j}\right) \tag{4.2}$$

and an equation for turbulent dissipation rate is

$$\frac{\partial \varepsilon}{\partial t}+\frac{\partial \varepsilon U_j}{\partial x_j}=-C_{\varepsilon 1}\frac{\varepsilon}{k}u_i'u_j'\frac{\partial U_j}{\partial x_j}-C_{\varepsilon 2}\frac{\varepsilon^2}{k}+\frac{\partial}{\partial x_j}\left(\frac{D}{\sigma_\varepsilon}\frac{\partial \varepsilon}{\partial x_j}\right) \tag{4.3}$$

where, x_i, x_j = the spatial coordinates, U_j, u_j' = time-averaged and turbulent velocity components, respectively, p = averaged pressure, ρ = density of the fluid, k = averaged turbulent kinetic energy, ε = averaged turbulent energy dissipation rate, D = eddy viscosity coefficient, ν = kinematic viscosity and σ_k, σ_ε, $C_{\varepsilon 1}$, $C_{\varepsilon 2}$ are model constants whose standard values are $\sigma_k=1.0$; $\sigma_\varepsilon=1.3$; $C_{\varepsilon 1}=1.44$; $C_{\varepsilon 2}=1.92$.

By using the Boussinesq approximation, eddy viscosity is defined as a proportionality factor between the Reynolds stresses and the mean strain rate. On dimensional reasoning it is estimated by employing the turbulent or mean scales.

$$-u'v'=D\frac{\partial U}{\partial y}=u_*^2(1-\eta);\qquad u_*=\sqrt{gh\sin\theta};\qquad D=c_\mu k^2/\varepsilon \tag{4.4}$$

where, U = time-averaged streamwise velocity, u_* = friction velocity; θ = angle made by the streamwise slope with the horizontal and c_μ = constant whose value is equal to 0.09.

4.3 Uniform flow

4.3.1 Analytical solution by excluding the damping function

For steady uniform flow (as depicted in Fig. 4.1), the equation of turbulent kinetic energy k and turbulent energy dissipation rate ε takes the form,

***k*-equation -**

$$D\left(\frac{\partial U}{\partial y}\right)^2-\varepsilon+\frac{\partial}{\partial y}\left(\frac{D}{\sigma_k}\frac{\partial k}{\partial y}\right)=0 \tag{4.5}$$

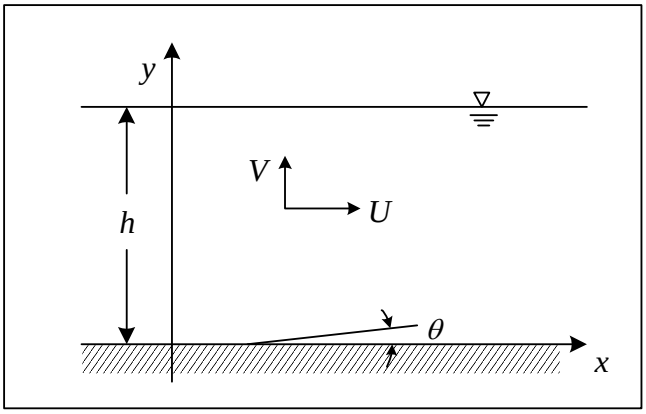

Figure 4.1. Schematic illustration of uniform flow

***ε* -equation -**

$$C_{\varepsilon 1}\frac{\varepsilon}{k}D\left(\frac{\partial U}{\partial y}\right)^2 - C_{\varepsilon 2}\frac{\varepsilon^2}{k} + \frac{\partial}{\partial y}\left(\frac{D}{\sigma_\varepsilon}\frac{\partial \varepsilon}{\partial y}\right) = 0 \qquad (4.6)$$

To derive an analytical solution for steady uniform flow, the equations for turbulent kinetic energy and dissipation rate are non-dimensionalise by the following variables.

$$\eta = y/h; \qquad k = k'k_\delta; \qquad \varepsilon = \varepsilon'\varepsilon_\delta; \qquad U = U'U_\delta$$

where, dash indicate the non-dimensional value and δ at the base indicate the value at the wall function; y is the vertical coordinate and h is the flow depth.

Assuming the local equilibrium between generation and dissipation at first grid point the wall function values are evaluated as

$$k_\delta = u_*^2/\sqrt{c_\mu}; \qquad \varepsilon_\delta = u_*^3/\kappa\delta; \qquad \text{and} \qquad U_\delta = u_*\left[\ln\left(u_*\delta/\nu\right)/\kappa + 5.3\right]$$

The non-dimensional form of Eqs. (4.4), (4.5) and (4.6), are obtained after simplification. These are

Reynolds equation -

$$\varepsilon'\left(1-\eta\right) = c_\mu\frac{k_\delta^2}{\varepsilon_\delta}\frac{U_\delta}{u_*^2 h}k'^2\left(\frac{\partial U'}{\partial \eta}\right) \qquad (4.7)$$

***k*-equation -**

$$\varepsilon' k'^2\frac{d^2k'}{d\eta^2} + 2\varepsilon' k'\left(\frac{dk'}{d\eta}\right)^2 - k'^2\left(\frac{dk'}{d\eta}\frac{d\varepsilon'}{d\eta}\right) - \frac{\varepsilon_\delta^2 h^2}{c_\mu k_\delta^3}\sigma_k\varepsilon'^3 + \sigma_k\frac{U_\delta^2}{k_\delta}\varepsilon' k'^2\left(\frac{dU'}{d\eta}\right)^2 = 0 \qquad (4.8)$$

ε -equation -

$$\varepsilon' k'^3 \frac{d^2\varepsilon'}{d\eta^2} + 2\varepsilon' k'^2 \left(\frac{dk'}{d\eta}\frac{d\varepsilon'}{d\eta}\right) - k'^3 \left(\frac{d\varepsilon'}{d\eta}\right)^2 - C_{\varepsilon 2}\sigma_\varepsilon \frac{\varepsilon_\delta^2 h^2}{c_\mu k_\delta^3}\varepsilon'^4 + C_{\varepsilon 1}\sigma_\varepsilon \frac{U_\delta^2}{k_\delta} k'^2 \varepsilon'^2 \left(\frac{dU'}{d\eta}\right)^2 = 0 \tag{4.9}$$

4.3.2 Functional form

To begin with the functional form of k, ε and U, initially, a well known form of the power series of η is considered for all three variables. The coefficients of all the series are then evaluated by solving the Eqs. (4.7), (4.8) and (4.9). But due to the interdependency of the coefficients on each other, the solution of the equations was diverted from its distribution. This led to consider the different trials, such as assume some coefficients are to be zero. Different combination of the assumption did not solve the problem of divergence. Rigorous trial for the solution of the equations did not yield the satisfactory results, thus the functional form for the variable is reconstructed. The new functional form of the turbulent energy dissipation rate was based on the empirical relationship of Nezu and Nakagawa (1993). This new functional form of ε guaranteed the distribution of ε. This time the functional form of k kept same, on the other hand, to satisfy the Reynolds equation (Eq. 4.4), the logarithmic law is incorporated into the power series of U. This idea bound the two distributions (ε and U), that after solution provided the satisfactory profiles for k and ε only. The distribution of velocity did not produce the reasonable comparison with the logarithmic velocity distribution. This was also pointed out by Takemitsu (1990). So, just as to get the acceptable distribution of the velocity, the wall functions values are changed from their original value. It is because Nezu and Nakagawa (1987) already reported that, the distribution of the standard k-ε model deviates from the semi-theoretical curve proposed by Nezu (1977), especially near the wall. This assumption improved the distributions of k, ε and U. However, the distributions obtained were not compatible with the proposed semi-theoretical curves. In addition, the distribution of eddy viscosity showed the parabolic shape; validating the functional form of ε and logarithmic distribution of velocity. But this conflict with the theme built already on inconsideration of damping function in the model. That means, even if the damping function is not included into the model, nature of the functional form (considered) still produce the parabolic shape of eddy viscosity distribution. The distribution supposed to show the

exponential type of curve (here exponential type of curve means only the nature of the curve is exponential, but in actual, it is not the exponential curve), indicating constant eddy viscosity at the water surface after exclusion of the damping function. If expected profile for eddy viscosity is sought for, again due to interdependency of the coefficients, small change in eddy viscosity profile distort the velocity distribution. Therefore, to overcome this difficulty, adjustment in the model constants, especially for the values of $C_{\varepsilon 1}$, $C_{\varepsilon 2}$ and κ (kappa) are performed. Surprisingly through this delicate adjustment reasonable results could obtained. But because we do not want to violate the initial objective of the research, as to find the effect of damping function on velocity distribution without changing the model constant, this idea also dropped. Keeping that in view, some more trials were performed by changing the functional forms of the variables. After prolonged failure, the best functional form, which is satisfying the equations, is chosen as follows.

$$U' = a_0 + a_1(1-\eta) + a_2(1-\eta)^2 + a_3(1-\eta)^3 + a_4(1-\eta)^4 + a_5(1-\eta)^5 + \cdots\cdots \tag{4.10}$$

$$k' = b_0 + b_1(1-\eta) + b_2(1-\eta)^2 + b_3(1-\eta)^3 + b_4(1-\eta)^4 + b_5(1-\eta)^5 + \cdots\cdots \tag{4.11}$$

$$\varepsilon' = c_0 + c_1(1-\eta) + c_2(1-\eta)^2 + c_3(1-\eta)^3 + c_4(1-\eta)^4 + c_5(1-\eta)^5 + \cdots\cdots \tag{4.12}$$

Substituting these functional forms into Eqs. (4.7)-(4.9), three sets of equations are obtained. These equations are then transformed into the linear equations by extracting out the different orders of η' (=1- η). Rearranging the linear equations, the values for the coefficients of power series are then obtained as:

0^{th} order:

$$a_1 = 0; \qquad b_1 = 0; \qquad c_1 = 0;$$

1^{st} order:

$$a_2 = -c_0 / 2Ab_0^2; \text{ where, } A = c_\mu \frac{k_\delta^2}{\varepsilon_\delta} \frac{U_\delta}{u_*^2 h} \tag{4.13}$$

$$b_2 = \frac{\varepsilon_\delta^2 h^2}{c_\mu k_\delta^3} \sigma_k \frac{c_0^2}{2b_0^2}; \qquad c_2 = \frac{\varepsilon_\delta^2 h^2}{c_\mu k_\delta^3} C_{\varepsilon 2} \sigma_\varepsilon \frac{c_0^3}{2b_0^3}; \tag{4.14}$$

2^{nd} order:

$$a_3 = 0; \qquad b_3 = 0; \qquad c_3 = 0;$$

3rd order:

$$a_4 = \left(-c_2 / A - 4a_2 b_0 b_2\right) / 4b_0^2 \tag{4.15}$$

$$b_4 = \frac{1}{3}\frac{b_2^2}{\sigma_k}\left(-3\frac{\sigma_k}{b_0} + 2\frac{C_{\varepsilon 2}\sigma_\varepsilon}{b_0} - \frac{k_\delta u_*^4}{\varepsilon_\delta^2 h^2}\frac{1}{c_0^2}\right) \tag{4.16}$$

$$c_4 = \frac{1}{6}C_{\varepsilon 2}\sigma_\varepsilon \frac{b_2^2}{\sigma_k^2}\left(-7\frac{c_0}{b_0^2}\sigma_k + 5\frac{c_0}{b_0^2}C_{\varepsilon 2}\sigma_\varepsilon - 2\frac{C_{\varepsilon 1}}{C_{\varepsilon 2}}\frac{k_\delta u_*^4}{\varepsilon_\delta^2 h^2}\frac{1}{c_0 b_0}\right) \tag{4.17}$$

4th order:

$$a_5 = 0; \qquad b_5 = 0; \qquad c_5 = 0;$$

5th order:

$$a_6 = \left(-c_4 / A - 8a_4 b_0 b_2 - 4a_2 b_0 b_4 - 2a_2 b_2^2\right) / 6b_0^2 \tag{4.18}$$

$$b_6 = \frac{1}{30c_0 b_0^2}\left\{-60c_0 b_0 b_2 b_4 - 10c_0 b_2^3 - 4b_0 b_2^2 c_2 - 6b_0^2 b_2 c_4 - 4b_0^2 b_4 c_2 + \sigma_k \frac{\varepsilon_\delta^2 h^2}{c_\mu k_\delta^3}\right.$$
$$\left.\left(3c_0^2 c_4 + 3c_0 c_2^2\right) + \sigma_k \frac{U_\delta^2}{k_\delta}\left[\frac{2c_0^2}{Ab_0^2}\left(\frac{c_2}{A} - \frac{2c_0 b_2}{Ab_0}\right) - \left(2c_0 b_0 b_2 + c_2 b_0^2\right)\frac{c_0^2}{A^2 b_0^4}\right]\right\} \tag{4.19}$$

$$c_6 = \frac{1}{30c_0 b_0^3}\left\{-22c_0 b_0^2 b_4 c_2 - 22c_0 b_0 b_2^2 c_2 - 2b_0^2 b_2 c_2^2 + 2b_0^3 c_2 c_4 - 52c_0 b_0^2 b_2 c_4 + C_{\varepsilon 2}\sigma_\varepsilon \frac{\varepsilon_\delta^2 h^2}{c_\mu k_\delta^3}\right.$$
$$\left.\left(4c_0^3 c_4 + 6c_0^2 c_2^2\right) - C_{\varepsilon 1}\sigma_\varepsilon \frac{U_\delta^2}{k_\delta}\left[\frac{2c_0^3}{Ab_0^2}\left(\frac{c_2}{A} - \frac{2c_0 b_2}{Ab_0}\right) - \left(2c_0^2 b_0 b_2 + 2c_0 b_0^2 c_2\right)\frac{c_0^2}{A^2 b_0^4}\right]\right\} \tag{4.20}$$

The values of all the coefficients can be evaluated once a_0, b_0 and c_0 values are known. Thus, to determine all these initial values, it is necessary to assume at least two values and third value can be calculated. Therefore, a_0 and c_0 values are assumed first and all the coefficients are expressed again in terms of a_0, b_0 and c_0. Using the boundary condition at the wall, the functional form of k becomes

$$1 = b_0 + b_1\left(1-\eta_\delta\right) + b_2\left(1-\eta_\delta\right)^2 + b_3\left(1-\eta_\delta\right)^3 + b_4\left(1-\eta_\delta\right)^4 + b_5\left(1-\eta_\delta\right)^5 + \cdots\cdots \tag{4.21}$$

Substituting all new expressions of coefficients into Eq.(4.21) and by using Newton Raphson method b_0 value is evaluated. All other coefficients are then determined using these values of a_0, b_0 and c_0. Here, only functional form of k fulfils the boundary condition but

the functional forms of ε and U are not satisfying at the boundary. Therefore, to meet these requirements at the wall and to get the required averaged velocity, additional higher order coefficients for ε and U are determined by using the boundary conditions at the wall. They are

$$a_8 = \left\{1-\left[a_0 + a_2(1-\eta_\delta)^2 + a_4(1-\eta_\delta)^4 + a_6(1-\eta_\delta)^6\right]\right\}/(1-\eta_\delta)^8 \quad (4.22)$$

$$c_8 = \left\{1-\left[c_0 + c_2(1-\eta_\delta)^2 + c_4(1-\eta_\delta)^4 + c_6(1-\eta_\delta)^6\right]\right\}/(1-\eta_\delta)^8 \quad (4.23)$$

This procedure does not violate the formulation because all initial values (a_0, b_0 and c_0) are sensitive to each other. Therefore, best selection of two values produce the required averaged velocity and satisfy all the functional forms at the boundary. By using all the known values of the coefficients of power series, the distributions of the turbulent kinetic energy, turbulent energy dissipation rate, velocity distribution and eddy viscosity can successfully be reproduced for the uniform flow in absence of the damping function.

4.3.3 Analytical solution by including the damping function

It is already reported that the damping effect of turbulence near the free surface reduce the vertical fluctuations and length scale causing the parabolic shape of eddy viscosity (Jobson and Sayre 1970; Nakagawa et al. 1979). Therefore, to model these effects, the damping function is introduced into the standard *k*-*ε* model. The damping function given by Hosoda (1990) is:

$$f_s(y) = \left\{1-\exp\left[-B\frac{h\varepsilon_s}{k_s^{1.5}}(1-\eta)\right]\right\}; \quad \text{Consider, } B' = B\frac{h\varepsilon_s}{k_s^{1.5}} \quad (4.24)$$

where, ε_s and k_s indicate the values at the free surface and constant B is equal to 10.

To incorporate this function into the analysis it is expressed in Taylor's expansion as

$$f_s(y) = B'(1-\eta) - \frac{1}{2}B'^2(1-\eta)^2 + \frac{1}{6}B'^3(1-\eta)^3 - \frac{1}{24}B'^4(1-\eta)^4 + \frac{1}{120}B'^5(1-\eta)^5 \quad (4.25)$$

where, B' is determined from the boundary condition at the wall. That is

$$1 - B'(1-\eta_\delta) + \frac{1}{2}B'^2(1-\eta_\delta)^2 - \frac{1}{6}B'^3(1-\eta_\delta)^3 + \frac{1}{24}B'^4(1-\eta_\delta)^4 - \frac{1}{120}B'^5(1-\eta_\delta)^5 = 0 \quad (4.26)$$

Inclusion of damping function into eddy viscosity definition, it is represented as

$$D = f_s(y)\, c_\mu k'^2 / \varepsilon' \tag{4.27}$$

Substituting this form of eddy viscosity into Eqs. (4.4)-(4.6) and after simplifications, new form of theses equations are obtained as:

Reynolds equation -

$$\varepsilon'(1-\eta) = f_s(y)\, c_\mu \frac{k_\delta^2}{\varepsilon_\delta}\frac{U_\delta}{u_*^2 h} k'^2 \left(\frac{\partial U'}{\partial \eta}\right) \tag{4.28}$$

***k*-equation -**

$$f_s(y)\,\varepsilon' k'^2 \frac{d^2 k'}{d\eta^2} + 2 f_s(y)\,\varepsilon' k' \left(\frac{dk'}{d\eta}\right)^2 - f_s(y)\, k'^2 \left(\frac{dk'}{d\eta}\frac{d\varepsilon'}{d\eta}\right) + f_s'(y)\,\varepsilon' k'^2 \left(\frac{dk'}{d\eta}\right) - \frac{\varepsilon_\delta^2 h^2}{c_\mu k_\delta^3}\sigma_k \varepsilon'^3$$
$$+ f_s(y)\,\sigma_k \frac{U_\delta^2}{k_\delta}\varepsilon' k'^2 \left(\frac{dU'}{d\eta}\right)^2 = 0 \tag{4.29}$$

ε -equation -

$$f_s(y)\,\varepsilon' k'^3 \frac{d^2 \varepsilon'}{d\eta^2} + 2 f_s(y)\,\varepsilon' k'^2 \left(\frac{dk'}{d\eta}\frac{d\varepsilon'}{d\eta}\right) - f_s(y)\, k'^3 \left(\frac{d\varepsilon'}{d\eta}\right)^2 + f_s'(y)\,\varepsilon' k'^3 \left(\frac{d\varepsilon'}{d\eta}\right)$$
$$- C_{\varepsilon 2}\sigma_\varepsilon \frac{\varepsilon_\delta^2 h^2}{c_\mu k_\delta^3}\varepsilon'^4 + f_s(y)\, C_{\varepsilon 1}\sigma_\varepsilon \frac{U_\delta^2}{k_\delta} k'^2 \varepsilon'^2 \left(\frac{dU'}{d\eta}\right)^2 = 0 \tag{4.30}$$

Some of the different terms of k, ε and Reynolds equations are expanded in the following manner

$$k'^2 = b_0^2 + 2b_0 b_1\,\eta' + \left(2b_0 b_2 + b_1^2\right)\eta'^2 + \left(2b_0 b_3 + 2b_1 b_2\right)\eta'^3 + \left(2b_0 b_4 + 2b_1 b_3 + b_2^2\right)\eta'^4 + \cdots \tag{4.31}$$

$$k'^3 = b_0^3 + 3b_0^2 b_1\,\eta' + \left(3b_0^2 b_2 + 3b_0 b_1^2\right)\eta'^2 + \left(3b_0^2 b_3 + 6b_0 b_1 b_2 + b_1^3\right)\eta'^3$$
$$+ \left(3b_0^2 b_4 + 6b_0 b_1 b_3 + 3b_0 b_2^2 + 3b_1^2 b_2\right)\eta'^4 + \cdots\cdots \tag{4.32}$$

$$\varepsilon'^2 = c_0^2 + 2c_0 c_1\,\eta' + \left(2c_0 c_2 + c_1^2\right)\eta'^2 + \left(2c_0 c_3 + 2c_1 c_2\right)\eta'^3 + \left(2c_0 c_4 + 2c_1 c_3 + c_2^2\right)\eta'^4 + \cdots \tag{4.33}$$

$$\varepsilon'^3 = c_0^3 + 3c_0^2 c_1\,\eta' + \left(3c_0^2 c_2 + 3c_0 c_1^2\right)\eta'^2 + \left(3c_0^2 c_3 + 6c_0 c_1 c_2 + c_1^3\right)\eta'^3$$
$$+ \left(3c_0^2 c_4 + 6c_0 c_1 c_3 + 3c_0 c_2^2 + 3c_1^2 c_2\right)\eta'^4 + \cdots\cdots \tag{4.34}$$

$$\left(\frac{dU'}{d\eta}\right)^2 = a_1^2 + 4a_1 a_2\,\eta' + \left(6a_1 a_3 + 4a_2^2\right)\eta'^2 + \left(8a_1 a_4 + 12a_2 a_3\right)\eta'^3 + \cdots\cdots \tag{4.35}$$

$$\left(\frac{dk'}{d\eta}\right)^2 = b_1^2 + 4b_1 b_2\,\eta' + \left(6b_1 b_3 + 4b_2^2\right)\eta'^2 + \left(8b_1 b_4 + 12b_2 b_3\right)\eta'^3 + \cdots\cdots \tag{4.36}$$

$$\left(\frac{d\varepsilon'}{d\eta}\right)^2 = c_1^2 + 4c_1c_2\,\eta' + \left(6c_1c_3 + 4c_2^2\right)\eta'^2 + \left(8c_1c_4 + 12c_2c_3\right)\eta'^3 + \cdots\cdots \tag{4.37}$$

$$\left(\frac{dk'}{d\eta}\frac{d\varepsilon'}{d\eta}\right) = b_1c_1 + \left(2b_1c_2 + 2b_2c_1\right)\eta' + \left(3b_1c_3 + 4b_2c_2 + 3b_3c_1\right)\eta'^2 + \left(4b_1c_4 + 6b_2c_3 + 6b_3c_2 + 4b_4c_1\right)\eta'^3 + \cdots\cdots \tag{4.38}$$

$$\varepsilon'k' = c_0b_0 + \left(b_0c_1 + b_1c_0\right)\eta' + \left(b_0c_2 + b_1c_1 + b_2c_0\right)\eta'^2 + \left(b_0c_3 + b_1c_2 + b_2c_1 + b_3c_0\right)\eta'^3 + \cdots\cdots \tag{4.39}$$

$$\varepsilon'k'^2 = c_0b_0^2 + \left(2b_0b_1c_0 + c_1b_0^2\right)\eta' + \left[c_0\left(2b_0b_2 + b_1^2\right) + 2b_0b_1c_1 + c_2b_0^2\right]\eta'^2 + \left[c_0\left(2b_0b_3 + 2b_1b_2\right) + c_1\left(2b_0b_2 + b_1^2\right) + 2b_0b_1c_2 + c_3b_0^2\right]\eta'^3 + \cdots\cdots \tag{4.40}$$

$$\varepsilon'k'^3 = c_0b_0^3 + \left(3b_0^2b_1c_0 + c_1b_0^3\right)\eta' + \left[c_0\left(3b_0^2b_2 + 3b_0b_1^2\right) + 3b_0^2b_1c_1 + c_2b_0^3\right]\eta'^2 + \left[c_0\left(3b_0^2b_3 + 6b_0b_1b_2 + b_1^3\right) + c_1\left(3b_0^2b_2 + 3b_0b_1^2\right) + 3b_0^2b_1c_2 + c_3b_0^3\right]\eta'^3 + \cdots\cdots \tag{4.41}$$

$$k'^2\varepsilon'^2 = b_0^2c_0^2 + \left(2b_0b_1c_0^2 + 2c_0c_1b_0^2\right)\eta' + \left[c_0^2\left(2b_0b_2 + b_1^2\right) + 4c_0b_0b_1c_1 + b_0^2\left(2c_0c_2 + c_1^2\right)\right]\eta'^2 + \left[c_0^2\left(2b_0b_3 + 2b_1b_2\right) + 2c_0c_1\left(2b_0b_2 + b_1^2\right) + 2b_0b_1\left(2c_0c_2 + c_1^2\right) + b_0^2\left(2c_0c_3 + 2c_1c_2\right)\right]\eta'^3 + \cdots\cdots \tag{4.42}$$

All these expressions are necessary to express the terms into simpler and in consolidated form. For example, 1st term on the right hand side of Eq. (4.31) can be expressed as k_0^2 (0th order term of k^2), 2nd term as k_1^2 (1st order term of k^2), 3rd term as k_2^2 (2nd order term of k^2) and so on. This means, hereafter suffix for k, ε, U and suffix for derivative of k, ε, U with respect to η indicates the terms related to particular order of η'.

Following the aforementioned procedure, the coefficients of the power series are evaluated as:

0th order:

$$a_1 = \frac{-c_0}{2AB'b_0^2}; \qquad b_1 = \frac{\varepsilon_\delta^2h^2}{c_\mu k_\delta^3}\frac{\sigma_k}{B'}\frac{c_0^2}{b_0^2}; \qquad c_1 = \frac{\varepsilon_\delta^2h^2}{c_\mu k_\delta^3}\frac{C_{\varepsilon 2}\sigma_\varepsilon}{B'}\frac{c_0^3}{b_0^3}; \tag{4.43}$$

1st order:

$$a_2 = \frac{1}{2b_0^2}\left[\frac{-c_1}{AB'} + \frac{1}{2}B'a_1b_0^2 - 2a_1b_0b_1\right] \tag{4.44}$$

$$b_2 = \frac{1}{4B'c_0b_0^2}\left[-4B'c_0b_0b_1^2 + B'^2c_0b_0^2b_1 + 3\sigma_k\frac{\varepsilon_\delta^2h^2}{c_\mu k_\delta^3}c_0^2c_1 - \sigma_k\frac{U_\delta^2}{k_\delta}B'c_0b_0^2a_1^2\right] \tag{4.45}$$

$$c_2 = \frac{1}{4B'c_0b_0^3}\left[-5B'c_0b_0^2b_1c_1 + B'^2c_0b_0^3c_1 + 4C_{\varepsilon 2}\sigma_\varepsilon\frac{\varepsilon_\delta^2h^2}{c_\mu k_\delta^3}c_0^3c_1 - C_{\varepsilon 1}\sigma_\varepsilon\frac{U_\delta^2}{k_\delta}B'c_0^2b_0^2a_1^2\right] \tag{4.46}$$

2nd order:

$$a_3 = \frac{1}{3k_0^2}\left[\frac{-c_2}{AB'} - \frac{1}{6}B'^2a_1k_0^2 + \frac{1}{2}B'\left(2a_2k_0^2 + a_1k_1^2\right) - \left(2a_2k_1^2 + a_1k_2^2\right)\right] \tag{4.47}$$

$$\begin{aligned} b_3 = \frac{1}{9B'(\varepsilon k^2)_0}\Bigg\{ & -4B'b_2(\varepsilon k^2)_1 - 2b_2f_{s2}(\varepsilon k^2)_0 - 2\left[f_{s1}\left((\varepsilon k)_0\left(\frac{dk}{d\eta}\right)_1^2 + (\varepsilon k)_1\left(\frac{dk}{d\eta}\right)_0^2\right)\right. \\ & \left. + f_{s2}(\varepsilon k)_0\left(\frac{dk}{d\eta}\right)_0^2\right] + \left[f_{s1}\left(k_0^2\left(\frac{dk}{d\eta}\frac{d\varepsilon}{d\eta}\right)_1 + k_1^2\left(\frac{dk}{d\eta}\frac{d\varepsilon}{d\eta}\right)_0\right) + f_{s2}k_0^2\left(\frac{dk}{d\eta}\frac{d\varepsilon}{d\eta}\right)_0\right] \\ & - B'b_1(\varepsilon k^2)_2 + B'^2\left[b_1(\varepsilon k^2)_1 + 2b_2(\varepsilon k^2)_0\right] - \frac{B'^3}{2}b_1(\varepsilon k^2)_0 + 3\sigma_k\frac{\varepsilon_\delta^2h^2}{c_\mu k_\delta^3}\left(c_0^2c_2 + c_0c_1^2\right) \\ & \left. - \sigma_k\frac{U_\delta^2}{k_\delta}\left[f_{s1}\left((\varepsilon k^2)_0\left(\frac{dU}{d\eta}\right)_1^2 + (\varepsilon k^2)_1\left(\frac{dU}{d\eta}\right)_0^2\right) + f_{s2}(\varepsilon k^2)_0\left(\frac{dU}{d\eta}\right)_0^2\right]\right\} \end{aligned} \tag{4.48}$$

$$\begin{aligned} c_3 = \frac{1}{9B'(\varepsilon k^3)_0}\Bigg\{ & -4B'c_2(\varepsilon k^3)_1 - 2c_2f_{s2}(\varepsilon k^3)_0 - 2\left[f_{s1}\left((\varepsilon k^2)_0\left(\frac{dk}{d\eta}\frac{d\varepsilon}{d\eta}\right)_1 + (\varepsilon k^2)_1\left(\frac{dk}{d\eta}\frac{d\varepsilon}{d\eta}\right)_0\right)\right. \\ & \left. + f_{s2}(\varepsilon k^2)_0\left(\frac{dk}{d\eta}\frac{d\varepsilon}{d\eta}\right)_0\right] + \left[f_{s1}\left(k_0^3\left(\frac{d\varepsilon}{d\eta}\right)_1^2 + k_1^3\left(\frac{d\varepsilon}{d\eta}\right)_0^2\right) + f_{s2}k_0^3\left(\frac{d\varepsilon}{d\eta}\right)_0^2\right] \\ & - B'c_1(\varepsilon k^3)_2 + B'^2\left[c_1(\varepsilon k^3)_1 + 2c_2(\varepsilon k^3)_0\right] - \frac{B'^3}{2}c_1(\varepsilon k^3)_0 + \frac{\varepsilon_\delta^2h^2}{c_\mu k_\delta^3}C_{\varepsilon 2}\sigma_\varepsilon\left(4c_0^3c_2 + 6c_0^2c_1^2\right) \\ & \left. - C_{\varepsilon 1}\sigma_\varepsilon\frac{U_\delta^2}{k_\delta}\left[f_{s1}\left((k^2\varepsilon^2)_0\left(\frac{dU}{d\eta}\right)_1^2 + (k^2\varepsilon^2)_1\left(\frac{dU}{d\eta}\right)_0^2\right) + f_{s2}(k^2\varepsilon^2)_0\left(\frac{dU}{d\eta}\right)_0^2\right]\right\} \end{aligned} \tag{4.49}$$

3rd order:

$$\begin{aligned} a_4 = \frac{1}{4k_0^2}\Bigg[& \frac{-c_3}{AB'} + \frac{1}{24}B'^3a_1k_0^2 - \frac{1}{6}B'^2\left(2a_2k_0^2 + a_1k_1^2\right) + \frac{1}{2}B'\left(3a_3k_0^2 + 2a_2k_1^2 + a_1k_2^2\right) \\ & - \left(3a_3k_1^2 + 2a_2k_2^2 + a_1k_3^2\right)\Bigg] \end{aligned} \tag{4.50}$$

$$b_4 = \frac{1}{16B'(\varepsilon k^2)_0}\Big\{-4B'b_2(\varepsilon k^2)_2 - 9B'b_3(\varepsilon k^2)_1 - f_{s2}\left[2b_2(\varepsilon k^2)_1 + 6b_3(\varepsilon k^2)_0\right] - 2b_2 f_{s3}(\varepsilon k^2)_0$$
$$-2\Bigg[f_{s1}\left((\varepsilon k)_0\left(\frac{dk}{d\eta}\right)_2^2 + (\varepsilon k)_1\left(\frac{dk}{d\eta}\right)_1^2 + (\varepsilon k)_2\left(\frac{dk}{d\eta}\right)_0^2\right) + f_{s2}\left((\varepsilon k)_0\left(\frac{dk}{d\eta}\right)_1^2 + (\varepsilon k)_1\left(\frac{dk}{d\eta}\right)_0^2\right)$$
$$+ f_{s3}(\varepsilon k)_0\left(\frac{dk}{d\eta}\right)_0^2\Bigg] + \Bigg[f_{s1}\left(k_0^2\left(\frac{dk}{d\eta}\frac{d\varepsilon}{d\eta}\right)_2 + k_1^2\left(\frac{dk}{d\eta}\frac{d\varepsilon}{d\eta}\right)_1 + k_2^2\left(\frac{dk}{d\eta}\frac{d\varepsilon}{d\eta}\right)_0\right)$$
$$+ f_{s1}\left(k_0^2\left(\frac{dk}{d\eta}\frac{d\varepsilon}{d\eta}\right)_1 + k_1^2\left(\frac{dk}{d\eta}\frac{d\varepsilon}{d\eta}\right)_0\right) + f_{s2}k_0^2\left(\frac{dk}{d\eta}\frac{d\varepsilon}{d\eta}\right)_0\Bigg] - B'b_1(\varepsilon k^2)_3$$
$$+ B'^2\left[b_1(\varepsilon k^2)_2 + 2b_2(\varepsilon k^2)_1 + 3b_3(\varepsilon k^2)_0\right] - \frac{B'^3}{2}\left[b_1(\varepsilon k^2)_1 + 2b_2(\varepsilon k^2)_0\right] + \frac{B'^4}{6}b_1(\varepsilon k^2)_0$$
$$+ \sigma_k\frac{\varepsilon_\delta^2 h^2}{c_\mu k_\delta^3}\left(3c_0^2c_3 + 6c_0c_1c_2 + c_1^3\right)$$
$$-\sigma_k\frac{U_\delta^2}{k_\delta}\Bigg[f_{s1}\left((\varepsilon k^2)_0\left(\frac{dU}{d\eta}\right)_2^2 + (\varepsilon k^2)_1\left(\frac{dU}{d\eta}\right)_1^2 + (\varepsilon k^2)_2\left(\frac{dU}{d\eta}\right)_0^2\right)$$
$$+ f_{s2}\left((\varepsilon k^2)_0\left(\frac{dU}{d\eta}\right)_1^2 + (\varepsilon k^2)_1\left(\frac{dU}{d\eta}\right)_0^2\right) + f_{s3}(\varepsilon k^2)_0\left(\frac{dU}{d\eta}\right)_0^2\Bigg]\Big\} \qquad (4.51)$$

$$c_4 = \frac{1}{16B'(\varepsilon k^3)_0}\Big\{-4B'c_2(\varepsilon k^3)_2 - 9B'c_3(\varepsilon k^3)_1 - f_{s2}\left[2c_2(\varepsilon k^3)_1 + 6c_3(\varepsilon k^3)_0\right] - 2c_2 f_{s3}(\varepsilon k^3)_0$$
$$-2\Bigg[f_{s1}\left((\varepsilon k^2)_0\left(\frac{dk}{d\eta}\frac{d\varepsilon}{d\eta}\right)_2 + (\varepsilon k^2)_1\left(\frac{dk}{d\eta}\frac{d\varepsilon}{d\eta}\right)_1 + (\varepsilon k^2)_2\left(\frac{dk}{d\eta}\frac{d\varepsilon}{d\eta}\right)_0\right)$$
$$+ f_{s2}\left((\varepsilon k^2)_0\left(\frac{dk}{d\eta}\frac{d\varepsilon}{d\eta}\right)_1 + (\varepsilon k^2)_1\left(\frac{dk}{d\eta}\frac{d\varepsilon}{d\eta}\right)_0\right) + f_{s3}(\varepsilon k)_0\left(\frac{dk}{d\eta}\frac{d\varepsilon}{d\eta}\right)_0\Bigg]$$
$$+ f_{s1}\left(k_0^3\left(\frac{d\varepsilon}{d\eta}\right)_2^2 + k_1^3\left(\frac{d\varepsilon}{d\eta}\right)_1^2 + k_2^3\left(\frac{d\varepsilon}{d\eta}\right)_0^2\right) + f_{s1}\left(k_0^3\left(\frac{d\varepsilon}{d\eta}\right)_1^2 + k_1^3\left(\frac{d\varepsilon}{d\eta}\right)_0^2\right) + f_{s3}k_0^3\left(\frac{d\varepsilon}{d\eta}\right)_0^2$$
$$- B'c_1(\varepsilon k^3)_3 + B'^2\left[c_1(\varepsilon k^3)_2 + 2c_2(\varepsilon k^3)_1 + 3c_3(\varepsilon k^3)_0\right] - \frac{B'^3}{2}\left[c_1(\varepsilon k^3)_1 + 2c_2(\varepsilon k^3)_0\right]$$
$$+ \frac{B'^4}{6}c_1(\varepsilon k^3)_0 + C_{\varepsilon 2}\sigma_\varepsilon\frac{\varepsilon_\delta^2 h^2}{c_\mu k_\delta^3}\left(4c_0^3c_3 + 12c_0^2c_1c_2 + 4c_0c_1^3\right)$$

$$-C_{\varepsilon 1}\sigma_{\varepsilon}\frac{U_{\delta}^{2}}{k_{\delta}}\Bigg[f_{s1}\Bigg((k^{2}\varepsilon^{2})_{0}\left(\frac{dU}{d\eta}\right)_{2}^{2}+(k^{2}\varepsilon^{2})_{1}\left(\frac{dU}{d\eta}\right)_{1}^{2}+(k^{2}\varepsilon^{2})_{2}\left(\frac{dU}{d\eta}\right)_{0}^{2}\Bigg)$$

$$+f_{s2}\Bigg((k^{2}\varepsilon^{2})_{0}\left(\frac{dU}{d\eta}\right)_{1}^{2}+(k^{2}\varepsilon^{2})_{1}\left(\frac{dU}{d\eta}\right)_{0}^{2}\Bigg)+f_{s3}(k^{2}\varepsilon^{2})_{0}\left(\frac{dU}{d\eta}\right)_{0}^{2}\Bigg]\Bigg\} \qquad (4.52)$$

Similarly, a_5, b_5, c_5, a_6, b_6 and c_6 can be expressed.

Assuming a_0 and c_0 values, b_0 value can be determined by using Newton-Raphson method. To satisfy the boundary condition at the wall and to obtain the required averaged velocity, higher order terms for ε and U are calculated as

$$a_7=\Big\{1-\Big[a_0+a_1(1-\eta_\delta)+a_2(1-\eta_\delta)^2+a_3(1-\eta_\delta)^3+a_4(1-\eta_\delta)^4+a_5(1-\eta_\delta)^5$$
$$+a_6(1-\eta_\delta)^6\Big]\Big\}/(1-\eta_\delta)^7 \qquad (4.53)$$

$$c_7=\Big\{1-\Big[c_0+c_1(1-\eta_\delta)+c_2(1-\eta_\delta)^2+c_3(1-\eta_\delta)^3+c_4(1-\eta_\delta)^4+c_5(1-\eta_\delta)^5$$
$$+c_6(1-\eta_\delta)^6\Big]\Big\}/(1-\eta_\delta)^7 \qquad (4.54)$$

By using all these new coefficients of power series the distributions of the turbulent kinetic energy, turbulent energy dissipation rate, velocity distribution and vertical parabolic distribution of eddy viscosity can successfully reproduce for the uniform flow.

4.4 Non-uniform flow

Investigation of turbulence characteristics of uniform open channel flow is not enough, because the flow encountered in the river/open channel is often non-uniform flow. Few attempts have been made so far to study the turbulent characteristics of the non-uniform flow. Tsujimoto et al. (1990) seems to be the first to study non-uniform flow over a short incline channel in open channel. On the other hand, Song and Graf (1994) conducted the measurements for accelerated and decelerated flows using Acoustics Doppler Velocity Profiler (ADVP). Based on the experimental investigations, they proposed the theoretical expressions for vertical velocity and Reynolds stress. Though the theoretical analysis provided the vertical velocity and Reynolds stress distribution in non-uniform flow, their formulas are pertained to St. Venant equations and Reynolds equation only. However, in the present case, the standard k-ε model is considered to study the turbulence characteristics of

non-uniform flow. The schematic of non-uniform flow is presented in Fig. 4.2 and the details of the analytical solution are presented in subsequent section. Similar to uniform flow analysis, an analytical solution is derived after excluding and including the damping function.

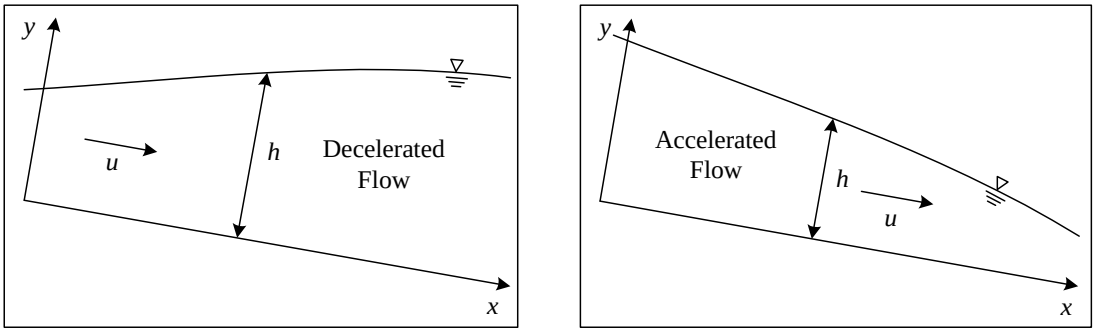

Figure 4.2. Schematic diagram of decelerated and accelerated flow

It is necessary to mention here that, the wall function values for non-uniform flow are different than those of uniform flow. Thus, the new wall function values are derived for the non-uniform flows. The derivation of new wall function values are provided below -

In turbulent sublayer, production = dissipation

Thus k - equation reduces to,

$$U\frac{\partial k}{\partial x}+V\frac{\partial k}{\partial y}=-u'v'\left(\frac{\partial U}{\partial y}\right)-\varepsilon \tag{4.55}$$

Here, $\frac{\partial k}{\partial y}=0$; $-u'v'=u_*^2$; and from log-law $\frac{\partial U}{\partial y}=\frac{u_*}{\kappa\, y}$; where κ = 0.4 (von Karman constant).

At turbulent sublayer, where $y=\delta$; above equation becomes

$$U_\delta\frac{\partial k_\delta}{\partial x}=u_*^2\,\frac{u_*}{\kappa\,\delta}-\varepsilon_\delta\,; \qquad \text{implies } \varepsilon_\delta=\frac{u_*^3}{\kappa\,\delta}-U_\delta\frac{\partial k_\delta}{\partial x} \tag{4.56}$$

From the definition of wall function in uniform flow, k_δ is expressed as $k_\delta=u_*^2/\sqrt{c_\mu}$ and friction velocity is represented as $u_*^2=c_f\bar{u}^2=c_f\ q^2/h^2$, c_f is the friction coefficient (=0.01). Substituting all these values in Eq. (4.56), it becomes

$$\varepsilon_\delta = \frac{u_*^3}{\kappa\,\delta} - \frac{U_\delta}{\sqrt{c_\mu}}\frac{\partial u_*^2}{\partial x};\ \text{and}\ \frac{\partial u_*^2}{\partial x} = -2c_f\,\frac{q^2}{h^3}\frac{dh}{dx} \tag{4.57}$$

Therefore, new ε_δ is given as,

$$\varepsilon_\delta = \frac{u_*^3}{\kappa\,\delta} + 2c_f\,\frac{U_\delta}{\sqrt{c_\mu}}\frac{q^2}{h^3}\frac{dh}{dx} \tag{4.58}$$

From Reynolds equation k_δ is expressed as

$$k_\delta = \sqrt{\frac{\varepsilon_\delta u_* \kappa\,\delta}{c_\mu}} \tag{4.58}$$

Depending on the bed (smooth or rough), the velocity at the bed is determined. In present case, rough bed is considered for the comparison. Thus, the velocity near the bed is calculated as

$$U_\delta = u_*\left[\ln\left((\delta + y_0)/K_s\right)/\kappa + Br\right] \tag{4.59}$$

where, $y_0 = 0.25K_s$, K_s is the equivalent sand roughness ($= d_{50}$) and Br is a constant of integration.

4.4.1 Analytical solution by excluding the damping function

To make the analysis for non-uniform flow simpler, some of the higher order terms of diffusion term are neglected from the equations. Therefore, the equations for steady non-uniform flow becomes

Reynolds equation -

$$U\frac{\partial U}{\partial x} + V\frac{\partial U}{\partial y} = g\sin\theta - \frac{1}{\rho}\frac{\partial p}{\partial x} + c_\mu\frac{k^2}{\varepsilon}\frac{\partial^2 U}{\partial y^2} \tag{4.60}$$

***k*- equation -**

$$U\frac{\partial k}{\partial x} + V\frac{\partial k}{\partial y} = c_\mu\frac{k^2}{\varepsilon}\left(\frac{\partial U}{\partial y}\right)^2 - \varepsilon + \frac{c_\mu}{\sigma_k}\frac{k^2}{\varepsilon}\frac{\partial^2 k}{\partial y^2} \tag{4.61}$$

***ε* -equation -**

$$U\frac{\partial \varepsilon}{\partial x} + V\frac{\partial \varepsilon}{\partial y} = c_\mu C_{\varepsilon 1} k\left(\frac{\partial U}{\partial y}\right)^2 - C_{\varepsilon 2}\frac{\varepsilon^2}{k} + \frac{c_\mu}{\sigma_\varepsilon}\frac{k^2}{\varepsilon}\frac{\partial^2 \varepsilon}{\partial y^2} \tag{4.62}$$

where, vertical velocity is determined by the continuity equation.

$$V = -h\frac{\partial}{\partial x'}\int_0^\eta U\, d\eta + U\eta\frac{\partial h}{\partial x} - \frac{\partial h}{\partial x}\int_0^\eta U\, d\eta \tag{4.63}$$

After coordinate transformation, (x, y) to (x', η), the hydrostatic pressure

$$p = \rho g(h-y)\cos\theta;\ \text{is expressed as} \qquad \frac{1}{\rho}\frac{\partial p}{\partial x} = g\cos\theta\frac{\partial h}{\partial x'} \tag{4.64}$$

and the friction velocity is calculated by

$$u_* = \left(\beta\frac{q^2}{h^2}\frac{\partial h}{\partial x} + gh\sin\theta - gh\cos\theta\frac{\partial h}{\partial x}\right)^{0.5} \tag{4.65}$$

where β is a momentum coefficient considered as equal to 1.

The purpose of neglecting the higher order terms of diffusion term in Eqs. (4.60) - (4.62) is just to make the analysis as similar as to that of the uniform flow after excluding the non-uniformity. Substituting the functional form of k, ε and U into Eqs. (4.60) - (4.62) and rearranging and simplifications, the coefficients of power series are evaluated as

0th order:

$$a_2 = \frac{h^2}{c_\mu U_\delta k_\delta^2}\frac{c_0}{2b_0^2}\varepsilon_\delta\left(U_\delta\frac{\partial U}{\partial x'}a_0 - g\sin\theta + g\cos\theta\frac{\partial h}{\partial x}\right) \tag{4.66}$$

$$b_2 = \frac{h^2}{c_\mu k_\delta^3}\frac{\sigma_k}{2b_0^2}\left(U_\delta\varepsilon_\delta\frac{\partial k}{\partial x'}a_0c_0 - \frac{c_\mu k_\delta^2 U_\delta^2}{h^2}a_1^2b_0^2 + \varepsilon_\delta^2c_0^2\right) \tag{4.67}$$

$$c_2 = \frac{h^2}{c_\mu k_\delta^3}\frac{\sigma_\varepsilon}{2b_0^3}\left(U_\delta k_\delta\frac{\partial\varepsilon}{\partial x'}a_0b_0c_0 - \frac{C_{\varepsilon1}c_\mu k_\delta^2 U_\delta^2}{h^2}a_1^2b_0^2c_0 + C_{\varepsilon2}\varepsilon_\delta^2c_0^3\right) \tag{4.68}$$

It is imply here that, a_1, b_1 and c_1 values are equal to zero.

1st order:

$$a_3 = 0; \qquad b_3 = 0; \qquad c_3 = 0;$$

2nd order:

$$a_4 = \frac{1}{12k_0^2}\left\{\frac{h^2}{c_\mu U_\delta k_\delta^2}\varepsilon_\delta\left[U_\delta\frac{\partial U}{\partial x'}(a_2c_0 + a_1c_1 + a_0c_2) - \frac{U_\delta}{h}\frac{\partial hU_\delta}{\partial x'}\left(c_0\left(\frac{a_1^2}{2} + 2a_0a_2\right) + a_0a_1c_1\right)\right.\right.$$
$$\left.\left. - c_2\left(g\sin\theta - g\cos\theta\frac{\partial h}{\partial x}\right)\right] - 2a_2k_2^2 - 6a_3k_1^2\right\} \tag{4.69}$$

$$b_4 = \frac{1}{12k_0^2}\left\{\frac{\sigma_k h^2}{c_\mu k_\delta^3}\varepsilon_\delta\left[U_\delta\frac{\partial k}{\partial x'}\left(a_2c_0+a_1c_1+a_0c_2\right)-\frac{k_\delta}{h}\frac{\partial hU_\delta}{\partial x'}\left(c_0\left(\frac{a_1b_1}{2}+2a_0b_2\right)+a_0b_1c_1\right)\right.\right.$$
$$\left.\left.-\frac{c_\mu k_\delta^2\,U_\delta^2}{\varepsilon_\delta h^2}\left(k_0^2\left(6a_1a_3+4a_2^2\right)+4a_1a_2k_1^2+a_1^2k_2^2\right)+\varepsilon_\delta\varepsilon_2^2\right]-2b_2k_2^2-6b_3k_1^2\right\} \tag{4.70}$$

$$c_4 = \frac{1}{12k_0^3}\left\{\frac{\sigma_\varepsilon h^2}{c_\mu k_\delta^2}\left[U_\delta\frac{\partial\varepsilon}{\partial x'}\left(a_2(\varepsilon k)_0+a_1(\varepsilon k)_1+a_0(\varepsilon k)_2\right)-\frac{\varepsilon_\delta}{h}\frac{\partial hU_\delta}{\partial x'}\left(a_0c_1(\varepsilon k)_1\right.\right.\right.$$
$$\left.+(\varepsilon k)_0\left(\frac{a_1c_1}{2}+2a_0c_2\right)\right)-\frac{C_{\varepsilon1}c_\mu k_\delta\,U_\delta^2}{h^2}\left((\varepsilon k^2)_0\left(6a_1a_3+4a_2^2\right)\right.$$
$$\left.\left.\left.+4a_1a_2(\varepsilon k^2)_1+a_1^2(\varepsilon k^2)_2\right)+\frac{C_{\varepsilon2}\varepsilon_\delta^2}{k_\delta}\varepsilon_2^3\right]-2c_2k_2^3-6c_3k_1^3\right\} \tag{4.71}$$

3rd order:

$$a_5 = 0\,; \qquad b_5 = 0\,; \qquad c_5 = 0\,;$$

4th order:

$$a_6 = \frac{1}{30k_0^2}\left\{\frac{h^2}{c_\mu U_\delta k_\delta^2}\varepsilon_\delta\left[U_\delta\frac{\partial U}{\partial x'}\left(a_4c_0+a_3c_1+a_2c_2+a_1c_3+a_0c_4\right)-\frac{U_\delta}{h}\frac{\partial hU_\delta}{\partial x'}\times\right.\right.$$
$$\left(c_0\left(\frac{7a_1a_3}{4}+\frac{2a_2^2}{3}+4a_0a_4\right)+c_1\left(\frac{4a_1a_2}{3}+3a_0a_3\right)+c_2\left(\frac{a_1^2}{2}+2a_0a_2\right)+a_0a_1c_3\right)$$
$$\left.\left.-c_4\left(g\sin\theta-g\cos\theta\frac{\partial h}{\partial x}\right)\right]-\left(2a_2k_4^2+6a_3k_3^2+12a_4k_2^2+20a_5k_1^2\right)\right\} \tag{4.72}$$

$$b_6 = \frac{1}{30k_0^2}\left\{\frac{\sigma_k h^2}{c_\mu k_\delta^3}\varepsilon_\delta\left[U_\delta\frac{\partial k}{\partial x'}\left(a_4c_0+a_3c_1+a_2c_2+a_1c_3+a_0c_4\right)-\frac{k_\delta}{h}\frac{\partial hU_\delta}{\partial x'}\left(a_0b_1c_3\right.\right.\right.$$
$$\left.+c_0\left(\frac{a_3b_1}{4}+\frac{2a_2b_2}{3}+\frac{3a_1b_3}{3}+4a_0b_4\right)+c_1\left(\frac{a_2b_1}{3}+\frac{2a_1b_2}{2}+3a_0b_3\right)+c_2\left(\frac{a_1b_1}{2}+2a_0b_2\right)\right)$$
$$-\frac{c_\mu k_\delta^2\,U_\delta^2}{\varepsilon_\delta h^2}\left(k_0^2\left(\frac{dU}{d\eta}\right)_4^2+k_1^2\left(\frac{dU}{d\eta}\right)_3^2+k_2^2\left(\frac{dU}{d\eta}\right)_2^2+k_3^2\left(\frac{dU}{d\eta}\right)_1^2+k_4^2\left(\frac{dU}{d\eta}\right)_0^2\right)+\varepsilon_\delta\varepsilon_4^2\Bigg]$$
$$\left.\left.-\left(2b_2k_4^2+6b_3k_3^2+12b_4k_2^2+20b_5k_1^2\right)\right\} \tag{4.73}$$

$$c_6 = \frac{1}{30k_0^3}\left\{\frac{\sigma_\varepsilon h^2}{c_\mu k_\delta^2}\left[U_\delta \frac{\partial \varepsilon}{\partial x'}\left(a_4(\varepsilon k)_0 + a_3(\varepsilon k)_1 + a_2(\varepsilon k)_2 + a_1(\varepsilon k)_3 + a_0(\varepsilon k)_4\right)\right.\right.$$

$$-\frac{\varepsilon_\delta}{h}\frac{\partial h U_\delta}{\partial x'}\left((\varepsilon k)_0\left(\frac{a_3c_1}{4}+\frac{2a_2c_2}{3}+\frac{3a_1c_3}{3}+4a_0c_4\right)+(\varepsilon k)_1\left(\frac{a_2c_1}{3}+\frac{2a_1c_2}{2}+3a_0c_3\right)\right.$$

$$\left.+(\varepsilon k)_2\left(\frac{a_1c_1}{2}+2a_0c_2\right)+(\varepsilon k)_3 a_0c_1\right)$$

$$-\frac{C_{\varepsilon 1}c_\mu k_\delta\, U_\delta^2}{h^2}\left((\varepsilon k^2)_0\left(\frac{dU}{d\eta}\right)_4^2+(\varepsilon k^2)_1\left(\frac{dU}{d\eta}\right)_3^2+(\varepsilon k^2)_2\left(\frac{dU}{d\eta}\right)_2^2+(\varepsilon k^2)_3\left(\frac{dU}{d\eta}\right)_1^2\right.$$

$$\left.\left.+(\varepsilon k^2)_4\left(\frac{dU}{d\eta}\right)_0^2\right)+\frac{C_{\varepsilon 2}\varepsilon_\delta^2}{k_\delta}\varepsilon_4^3\right]-\left(2c_2k_4^3+6c_3k_3^3+12c_4k_2^3+20c_5k_1^3\right)\Bigg\} \tag{4.74}$$

Higher order terms of ε and U are determined as

$$a_8 = \left\{1-\left[a_0+a_2(1-\eta_\delta)^2+a_4(1-\eta_\delta)^4+a_6(1-\eta_\delta)^6\right]\right\}\Big/(1-\eta_\delta)^8 \tag{4.75}$$

$$c_8 = \left\{1-\left[c_0+c_2(1-\eta_\delta)^2+c_4(1-\eta_\delta)^4+c_6(1-\eta_\delta)^6\right]\right\}\Big/(1-\eta_\delta)^8 \tag{4.76}$$

a_0, b_0 and c_0 values are evaluated by previous mentioned procedure. From the known values of the coefficients, the distributions of the velocity, turbulent kinetic energy, turbulent energy dissipation rate and eddy viscosity can be determine for non-uniform flow.

4.4.2 Analytical solution by including the damping function

Owing to the importance of the damping function in turbulence research, an analytical solution for non-uniform flow by including the damping function is proposed. The similar form of the damping function, as reported earlier (Eq.4.25) is considered. The dimensional form of the basic equations for the standard k-ε model after admitting the damping function becomes:

Reynolds equation -

$$\varepsilon^2 U\frac{\partial U}{\partial x}+\varepsilon^2 V\frac{\partial U}{\partial y}=\varepsilon^2\left(g\sin\theta-g\cos\theta\frac{\partial h}{\partial x}\right)+\frac{c_\mu}{h}f_s'(y)\,\varepsilon k^2\left(\frac{dU}{dy}\right)+c_\mu f_s(y)\,\varepsilon k^2\frac{\partial^2 U}{\partial y^2}$$

$$+2c_\mu f_s(y)\,\varepsilon k\left(\frac{dk}{dy}\frac{dU}{dy}\right)-c_\mu f_s(y)\,k^2\left(\frac{d\varepsilon}{dy}\frac{dU}{dy}\right) \tag{4.77}$$

***k*- equation -**

$$\varepsilon^2 U\frac{\partial k}{\partial x}+\varepsilon^2 V\frac{\partial k}{\partial y}=c_\mu f_s(y)\,\varepsilon k^2\left(\frac{dU}{dy}\right)^2-\varepsilon^3+\frac{c_\mu}{\sigma_k h}f_s'(y)\,\varepsilon k^2\left(\frac{dk}{dy}\right)+\frac{c_\mu}{\sigma_k}f_s(y)\,\varepsilon k^2\frac{\partial^2 k}{\partial y^2}$$
$$+2\frac{c_\mu}{\sigma_k}f_s(y)\,\varepsilon k\left(\frac{dk}{dy}\right)^2-\frac{c_\mu}{\sigma_k}f_s(y)\,k^2\left(\frac{dk}{dy}\frac{d\varepsilon}{dy}\right) \tag{4.78}$$

***ε* -equation -**

$$k\varepsilon^2 U\frac{\partial \varepsilon}{\partial x}+k\varepsilon^2 V\frac{\partial \varepsilon}{\partial y}=c_\mu C_{\varepsilon 1}f_s(y)\,k^2\varepsilon^2\left(\frac{dU}{dy}\right)^2-C_{\varepsilon 2}\varepsilon^4+\frac{c_\mu}{\sigma_\varepsilon h}f_s'(y)\,\varepsilon k^3\left(\frac{d\varepsilon}{dy}\right)$$
$$+\frac{c_\mu}{\sigma_\varepsilon}f_s(y)\,\varepsilon k^3\frac{\partial^2\varepsilon}{\partial y^2}+2\frac{c_\mu}{\sigma_\varepsilon}f_s(y)\,\varepsilon k^2\left(\frac{dk}{dy}\frac{d\varepsilon}{dy}\right)-\frac{c_\mu}{\sigma_\varepsilon}f_s(y)\,k^3\left(\frac{d\varepsilon}{dy}\right)^2 \tag{4.79}$$

Expansion of some of the terms of Eqs. (4.77)-(4.79) are given below

$$\varepsilon'^4=c_0^4+4c_0^3c_1\,\eta'+\left(4c_0^3c_2+6c_0^2c_1^2\right)\eta'^2+\left(4c_0^2c_3+12c_0^2c_1c_2+4c_0c_1^3\right)\eta'^3$$
$$+\left(4c_0^3c_4+12c_0^2c_1c_3+6c_0^2c_2^2+12c_0c_1^2c_2+c_1^4\right)\eta'^4+\cdots\cdots \tag{4.80}$$

$$k'\varepsilon'^2=b_0\varepsilon_0^2+\left(b_0\varepsilon_1^2+b_1\varepsilon_0^2\right)\eta'+\left(b_0\varepsilon_2^2+b_1\varepsilon_1^2+b_2\varepsilon_0^2\right)\eta'^2+\left(b_0\varepsilon_3^2+b_1\varepsilon_2^2+b_2\varepsilon_1^2+b_3\varepsilon_0^2\right)\eta'^3$$
$$+\left(b_0\varepsilon_4^2+b_1\varepsilon_3^2+b_2\varepsilon_2^2+b_3\varepsilon_1^2+b_4\varepsilon_0^2\right)\eta'^4+\cdots\cdots \tag{4.81}$$

$$\left(\frac{dU'}{d\eta}\frac{dk'}{d\eta}\right)=a_1b_1+\left(2a_1b_2+2a_2b_1\right)\eta'+\left(3a_1b_3+4a_2b_2+3a_3b_1\right)\eta'^2$$
$$+\left(4a_1b_4+6a_2b_3+6a_3b_2+4a_4b_1\right)\eta'^3+\cdots\cdots \tag{4.82}$$

$$\left(\frac{dU'}{d\eta}\frac{d\varepsilon'}{d\eta}\right)=a_1c_1+\left(2a_1c_2+2a_2c_1\right)\eta'+\left(3a_1c_3+4a_2c_2+3a_3c_1\right)\eta'^2$$
$$+\left(4a_1c_4+6a_2c_3+6a_3c_2+4a_4c_1\right)\eta'^3+\cdots\cdots \tag{4.83}$$

Replacing k, ε and U from Eqs. (4.77)-(4.79) to their respective functional forms and by solving the equations by aforementioned procedure, the expressions for each coefficients are obtained as follows:

0^{th} order:

$$a_1=\frac{h^2}{c_\mu U_\delta k_\delta^2}\frac{c_0}{B'b_0^2}\varepsilon_\delta\left(U_\delta\frac{\partial U}{\partial x'}a_0-g\sin\theta+g\cos\theta\frac{\partial h}{\partial x}\right) \tag{4.84}$$

$$b_1 = \frac{h^2}{c_\mu k_\delta^3}\frac{\sigma_k}{B' b_0^2}\left(U_\delta \varepsilon_\delta \frac{\partial k}{\partial x'} a_0 c_0 + \varepsilon_\delta^2 c_0^2\right) \tag{4.85}$$

$$c_1 = \frac{h^2}{c_\mu k_\delta^3}\frac{\sigma_\varepsilon}{B' b_0^3}\left(U_\delta k_\delta \frac{\partial \varepsilon}{\partial x'} a_0 b_0 c_0 + C_{\varepsilon 2}\varepsilon_\delta^2 c_0^3\right) \tag{4.86}$$

1st order:

$$a_2 = \frac{1}{4B'(\varepsilon k^2)_0}\frac{h^2}{c_\mu U_\delta k_\delta^2}\left\{\varepsilon_\delta\left[U_\delta\left(a_1\varepsilon_0^2 + a_0\varepsilon_1^2\right)\frac{\partial U}{\partial x'} - \frac{U_\delta}{h}\frac{\partial h U_\delta}{\partial x'}\varepsilon_0^2 a_0 a_1\right.\right.$$
$$\left. - \varepsilon_1^2\left(g\sin\theta - g\cos\theta\frac{\partial h}{\partial x}\right)\right] - \frac{c_\mu}{h^2}U_\delta k_\delta^2\left[-a_1\left(-B'(\varepsilon k^2)_1 + B'^2(\varepsilon k^2)_0\right)\right.$$
$$\left.\left. + 2 f_{s1}(\varepsilon k)_0\left(\frac{dU}{d\eta}\frac{dk}{d\eta}\right)_0 - f_{s1}k_0^2\left(\frac{dU}{d\eta}\frac{d\varepsilon}{d\eta}\right)_0\right]\right\} \tag{4.87}$$

$$b_2 = \frac{1}{4B'(\varepsilon k^2)_0}\frac{\sigma_k h^2}{c_\mu k_\delta^3}\left\{\varepsilon_\delta\left[U_\delta\left(a_1\varepsilon_0^2 + a_0\varepsilon_1^2\right)\frac{\partial k}{\partial x'} - \frac{k_\delta}{h}\frac{\partial h U_\delta}{\partial x'}\varepsilon_0^2 a_0 b_1 + \varepsilon_\delta\varepsilon_1^3\right]\right.$$
$$- \frac{c_\mu}{h^2}\, f_{s1}k_\delta^2 U_\delta^2(\varepsilon k^2)_0\left(\frac{\partial U}{\partial \eta}\right)_0^2$$
$$\left. - \frac{c_\mu}{\sigma_k h^2}k_\delta^3\left[-b_1\left(-B'(\varepsilon k^2)_1 + B'^2(\varepsilon k^2)_0\right) + 2 f_{s1}c_0 b_0 b_1^2 - f_{s1}k_0^2\left(\frac{dk}{d\eta}\frac{d\varepsilon}{d\eta}\right)_0\right]\right\} \tag{4.88}$$

$$c_2 = \frac{1}{4B'(\varepsilon k^3)_0}\frac{\sigma_\varepsilon h^2}{c_\mu k_\delta^3}\left\{k_\delta\left[U_\delta\left(a_1(k\varepsilon^2)_0 + a_0(k\varepsilon^2)_1\right)\frac{\partial \varepsilon}{\partial x'} - \frac{\varepsilon_\delta}{h}\frac{\partial h U_\delta}{\partial x'}(k\varepsilon^2)_0 a_0 c_1\right] + C_{\varepsilon 2}\varepsilon_\delta^2\varepsilon_1^4\right.$$
$$- \frac{C_{\varepsilon 1}c_\mu}{h^2}\, f_{s1}k_\delta^2 U_\delta^2(k^2\varepsilon^2)_0\left(\frac{\partial U}{\partial \eta}\right)_0^2 - \frac{c_\mu}{\sigma_\varepsilon h^2}k_\delta^3\left[-c_1\left(-B'(\varepsilon k^3)_1 + B'^2(\varepsilon k^3)_0\right)\right.$$
$$\left.\left. + 2 f_{s1}(\varepsilon k^2)_0\left(\frac{dk}{d\eta}\frac{d\varepsilon}{d\eta}\right)_0 - f_{s1}k_0^3\left(\frac{d\varepsilon}{d\eta}\right)_0^2\right]\right\} \tag{4.89}$$

2nd order:

$$a_3 = \frac{1}{9B'(\varepsilon k^2)_0}\frac{h^2}{c_\mu U_\delta k_\delta^2}\left\{\varepsilon_\delta\left[U_\delta\left(a_2\varepsilon_0^2 + a_1\varepsilon_1^2 + a_0\varepsilon_2^2\right)\frac{\partial U}{\partial x'} - \frac{U_\delta}{h}\frac{\partial hU_\delta}{\partial x'}\left(\varepsilon_0^2\left(\frac{a_1^2}{2} + 2a_0a_2\right)\right.\right.\right.$$

$$\left.\left.\left. + \varepsilon_1^2 a_0 a_1\right) - \varepsilon_2^2\left(g\sin\theta - g\cos\theta\frac{\partial h}{\partial x}\right)\right]\right.$$

$$-\frac{c_\mu}{h^2}U_\delta k_\delta^2\left[B'\left(a_1(\varepsilon k^2)_2 + 2a_2(\varepsilon k^2)_1\right) - B'^2\left(a_1(\varepsilon k^2)_1 + 2a_2(\varepsilon k^2)_0\right)\right.$$

$$+\frac{B'^3}{2}a_1(\varepsilon k^2)_0 + 2f_{s2}a_2(\varepsilon k^2)_0 + 2f_{s1}a_2(\varepsilon k^2)_1$$

$$+2f_{s1}\left((\varepsilon k)_0\left(\frac{dU}{d\eta}\frac{dk}{d\eta}\right)_1 + (\varepsilon k)_1\left(\frac{dU}{d\eta}\frac{dk}{d\eta}\right)_0\right) + 2f_{s2}(\varepsilon k)_0\left(\frac{dU}{d\eta}\frac{dk}{d\eta}\right)_0$$

$$\left. - f_{s1}\left(k_0^2\left(\frac{dU}{d\eta}\frac{d\varepsilon}{d\eta}\right)_1 + k_1^2\left(\frac{dU}{d\eta}\frac{d\varepsilon}{d\eta}\right)_0\right) - f_{s2}k_0^2\left(\frac{dU}{d\eta}\frac{d\varepsilon}{d\eta}\right)_0\right]\Bigg\} \tag{4.90}$$

$$b_3 = \frac{1}{9B'(\varepsilon k^2)_0}\frac{\sigma_k h^2}{c_\mu k_\delta^3}\left\{\varepsilon_\delta\left[U_\delta\left(a_2\varepsilon_0^2 + a_1\varepsilon_1^2 + a_0\varepsilon_2^2\right)\frac{\partial k}{\partial x'} - \frac{k_\delta}{h}\frac{\partial hU_\delta}{\partial x'}\left(\varepsilon_0^2\left(\frac{a_1b_1}{2} + 2a_0b_2\right)\right.\right.\right.$$

$$\left.\left.\left. + \varepsilon_1^2 a_0 b_1 + \varepsilon_\delta\varepsilon_2^3\right)\right]\right.$$

$$-\frac{c_\mu}{h^2}k_\delta^2U_\delta^2\left[f_{s1}\left((\varepsilon k^2)_0\left(\frac{\partial U}{\partial\eta}\right)_1^2 + (\varepsilon k^2)_1\left(\frac{\partial U}{\partial\eta}\right)_0^2\right) + f_{s2}(\varepsilon k^2)_0\left(\frac{\partial U}{\partial\eta}\right)_0^2\right]$$

$$-\frac{c_\mu}{\sigma_k h^2}k_\delta^3\left[B'\left(b_1(\varepsilon k^2)_2 + 2b_2(\varepsilon k^2)_1\right) - B'^2\left(b_1(\varepsilon k^2)_1 + 2b_2(\varepsilon k^2)_0\right)\right.$$

$$+\frac{B'^3}{2}b_1(\varepsilon k^2)_0 + 2f_{s2}b_2(\varepsilon k^2)_0 + 2f_{s1}b_2(\varepsilon k^2)_1$$

$$+2f_{s1}\left((\varepsilon k)_0\left(\frac{dk}{d\eta}\right)_1^2 + (\varepsilon k)_1\left(\frac{dk}{d\eta}\right)_0^2\right) + 2f_{s2}(\varepsilon k)_0\left(\frac{dk}{d\eta}\right)_0^2$$

$$\left. - f_{s1}\left(k_0^2\left(\frac{dk}{d\eta}\frac{d\varepsilon}{d\eta}\right)_1 + k_1^2\left(\frac{dk}{d\eta}\frac{d\varepsilon}{d\eta}\right)_0\right) - f_{s2}k_0^2\left(\frac{dk}{d\eta}\frac{d\varepsilon}{d\eta}\right)_0\right]\Bigg\} \tag{4.91}$$

$$c_3 = \frac{1}{9B'(\varepsilon k^3)_0}\frac{\sigma_\varepsilon h^2}{c_\mu k_\delta^3}\Bigg\{k_\delta\Bigg[U_\delta\left(a_2(k\varepsilon^2)_0 + a_1(k\varepsilon^2)_1 + a_0(k\varepsilon^2)_2\right)\frac{\partial\varepsilon}{\partial x'} - \frac{\varepsilon_\delta}{h}\frac{\partial hU_\delta}{\partial x'}\left((k\varepsilon^2)_0 a_1 c_1 + (k\varepsilon^2)_0\left(\frac{a_1c_1}{2} + 2a_0c_2\right) + C_{\varepsilon 2}\varepsilon_\delta^2\varepsilon_2^4\right]$$
$$- \frac{C_{\varepsilon 1}c_\mu}{h^2}k_\delta^2U_\delta^2\Bigg[f_{s1}\left((k^2\varepsilon^2)_0\left(\frac{\partial U}{\partial\eta}\right)_1^2 + (k^2\varepsilon^2)_1\left(\frac{\partial U}{\partial\eta}\right)_0^2\right) + f_{s2}(k^2\varepsilon^2)_0\left(\frac{\partial U}{\partial\eta}\right)_0^2\Bigg]$$
$$- \frac{c_\mu}{\sigma_\varepsilon h^2}k_\delta^3\Big[B'\left(c_1(\varepsilon k^3)_2 + 2c_2(\varepsilon k^3)_1\right) - B'^2\left(c_1(\varepsilon k^3)_1 + 2c_2(\varepsilon k^3)_0\right)$$
$$+ \frac{B'^3}{2}c_1(\varepsilon k^3)_0 + 2f_{s2}c_2(\varepsilon k^3)_0 + 2f_{s1}c_2(\varepsilon k^3)_1$$
$$+ 2f_{s1}\left((\varepsilon k^2)_0\left(\frac{dk}{d\eta}\frac{d\varepsilon}{d\eta}\right)_1 + (\varepsilon k^2)_1\left(\frac{dk}{d\eta}\frac{d\varepsilon}{d\eta}\right)_0\right) + 2f_{s2}(\varepsilon k^2)_0\left(\frac{dk}{d\eta}\frac{d\varepsilon}{d\eta}\right)_0$$
$$- f_{s1}\left(k_0^3\left(\frac{d\varepsilon}{d\eta}\right)_1^2 - k_1^3\left(\frac{d\varepsilon}{d\eta}\right)_0^2\right) - f_{s2}k_0^3\left(\frac{d\varepsilon}{d\eta}\right)_0^2\Bigg]\Bigg\} \tag{4.92}$$

Similarly, a_4, b_4, c_4, a_5, b_5, c_5, a_6, b_6 and c_6 can be evaluated.

Following the aforementioned procedure of a_0, b_0 and c_0 values determination, all other coefficients of power series can be calculated. By using the boundary condition at the wall higher order terms for ε and U are estimated as

$$a_7 = \Big\{1 - \Big[a_0 + a_1(1-\eta_\delta) + a_2(1-\eta_\delta)^2 + a_3(1-\eta_\delta)^3 + a_4(1-\eta_\delta)^4 + a_5(1-\eta_\delta)^5 + a_6(1-\eta_\delta)^6\Big]\Big\}/(1-\eta_\delta)^7 \tag{4.93}$$

$$c_7 = \Big\{1 - \Big[c_0 + c_1(1-\eta_\delta) + c_2(1-\eta_\delta)^2 + c_3(1-\eta_\delta)^3 + c_4(1-\eta_\delta)^4 + c_5(1-\eta_\delta)^5 + c_6(1-\eta_\delta)^6\Big]\Big\}/(1-\eta_\delta)^7 \tag{4.94}$$

With these new values of the coefficients, the distribution of the turbulent kinetic energy, turbulent energy dissipation rate, velocity distribution and vertical parabolic distribution of eddy viscosity can be reproduce for non-uniform flow.

4.5 Finite Difference Scheme

To validate the analytical results of the standard k-ε model, numerical results of finite difference scheme are used. For finite difference method, the unsteady uniform flow equations, that is Reynolds equation, k- and ε-equations are simulated in the vertical direction (see Fig. 4.3).

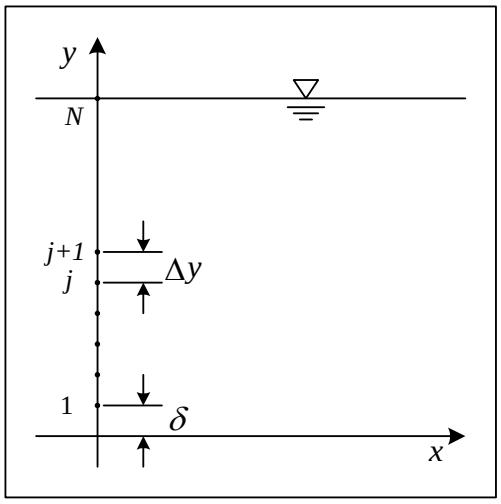

Figure 4.3. Discretization of cells for Finite difference scheme

Referring to Fig. 4.3, the discretizations of the basic equations for unsteady uniform flow by using finite difference scheme are described as:

For $j < N$

Reynolds equation -

$$\frac{U_j^{n+1}-U_j^n}{\Delta t}=g\sin\theta+\frac{1}{2}\left(D_{j+1}^n+D_j^n\right)\frac{U_{j+1}^n-U_j^n}{\Delta y^2}-\frac{1}{2}\left(D_j^n+D_{j-1}^n\right)\frac{U_j^n-U_{j-1}^n}{\Delta y^2} \tag{4.95}$$

***k*- equation -**

$$\frac{k_j^{n+1}-k_j^n}{\Delta t}=D_j^n\left(\frac{1}{2}\frac{U_{j+1}^n-U_j^n}{\Delta y}+\frac{1}{2}\frac{U_j^n-U_{j-1}^n}{\Delta y}\right)^2-\varepsilon_j^n$$

$$+\frac{1}{\sigma_k}\left[\frac{1}{2}\left(D_{j+1}^n-D_j^n\right)\frac{k_{j+1}^n-k_j^n}{\Delta y^2}-\frac{1}{2}\left(D_j^n-D_{j-1}^n\right)\frac{k_j^n-k_{j-1}^n}{\Delta y^2}\right] \tag{4.96}$$

***ε* -equation -**

$$\frac{\varepsilon_j^{n+1}-\varepsilon_j^n}{\Delta t}=C_{\varepsilon 1}\frac{\varepsilon_j^n}{k_j^n}D_j^n\left(\frac{1}{2}\frac{U_{j+1}^n-U_j^n}{\Delta y}+\frac{1}{2}\frac{U_j^n-U_{j-1}^n}{\Delta y}\right)^2-C_{\varepsilon 2}\frac{\varepsilon_j^{2n}}{k_j^n}$$
$$+\frac{1}{\sigma_\varepsilon}\left[\frac{1}{2}\left(D_{j+1}^n+D_j^n\right)\frac{\varepsilon_{j+1}^n-\varepsilon_j^n}{\Delta y^2}-\frac{1}{2}\left(D_j^n+D_{j-1}^n\right)\frac{\varepsilon_j^n-\varepsilon_{j-1}^n}{\Delta y^2}\right] \quad (4.97)$$

For $j = N$

Reynolds equation -

$$\frac{U_j^{n+1}-U_j^n}{\Delta t}=g\sin\theta+\left(D_j^n-D_{j-1}^n\right)\frac{U_j^n-U_{j-1}^n}{\Delta y^2}+\frac{1}{2}\left(D_j^n+D_{j-1}^n\right)\frac{0-U_j^n+U_{j-1}^n}{\Delta y^2} \quad (4.98)$$

***k*- equation -**

$$\frac{k_j^{n+1}-k_j^n}{\Delta t}=D_j^n\left(\frac{U_j^n-U_{j-1}^n}{\Delta y}\right)^2-\varepsilon_j^n$$
$$+\frac{1}{\sigma_k}\left[\left(D_j^n-D_{j-1}^n\right)\frac{k_j^n-k_{j-1}^n}{\Delta y^2}+\frac{1}{2}\left(D_j^n+D_{j-1}^n\right)\frac{0-k_j^n+k_{j-1}^n}{\Delta y^2}\right] \quad (4.99)$$

***ε* -equation -**

$$\frac{\varepsilon_j^{n+1}-\varepsilon_j^n}{\Delta t}=C_{\varepsilon 1}\frac{\varepsilon_j^n}{k_j^n}D_j^n\left(\frac{U_j^n-U_{j-1}^n}{\Delta y}\right)^2-C_{\varepsilon 2}\frac{\varepsilon_j^{2n}}{k_j^n}$$
$$+\frac{1}{\sigma_\varepsilon}\left[\left(D_j^n-D_{j-1}^n\right)\frac{\varepsilon_j^n-\varepsilon_{j-1}^n}{\Delta y^2}+\frac{1}{2}\left(D_j^n+D_{j-1}^n\right)\frac{0-\varepsilon_j^n+\varepsilon_{j-1}^n}{\Delta y^2}\right] \quad (4.100)$$

The calculation begins with the wall function values at the boundary as an initial condition. With these wall function values calculation proceeds in the vertical direction until the steady state is reached. After some iteration, uniform distributions of velocity, turbulent kinetic energy, turbulent energy dissipation rate and eddy viscosity are obtained. The numerical simulations are conducted for both the cases by excluding and including the damping function in the uniform flow.

For non-uniform flow, the unsteady non-uniform flow equations are solved by aforementioned procedure at a single point, considering the flow is in equilibrium. Two non-

uniform flows: accelerated and decelerated flows are simulated by including and excluding the damping function. The experimental data of Song and Graf (1994) is used for the simulation of non-uniform equilibrium flow.

4.6 Results and discussions

To ensure the applicability of the analytical study, the numerical results of the finite difference scheme, empirical results of Nezu (1977) for uniform flow and the experimental data of Song and Graf (1994) for non-uniform flow are used.

4.6.1 Uniform Flow

The theoretical distributions of dimensionless velocity by including and excluding the damping function (hereafter referred as with and without damping function case) on semi-logarithmic scale are depicted in Fig. 4.4. The logarithmic law and the results of finite difference scheme are also included in Fig. 4.4. The theoretical distribution of velocity is in close agreement with the logarithmic law and the finite difference results. The possibility of slenderness observed in without damping function case is caused due to inconsideration of odd number coefficients in the solutions. Because all values of the coefficients are sensitive to each other, small changes in the initial values of the coefficients distort any of the distribution. Keeping that in view, two optimum values (a_0 and c_0) are selected in the initial condition. Based on these two optimum values third coefficient (b_0) is determined. Thus, required averaged velocity is obtained and all the boundary conditions at the wall are satisfied.

For with damping function case analysis, the distribution is in good agreement at the free surface. However, in the inner region it shows little deviation from the logarithmic law distribution. Inclusion of higher order terms can remove this discrepancy, but it leads to the complexity in the derivation. Therefore, to avoid the complexity only up to seventh order terms are included in the derivation.

The comparisons of the velocity distributions by including and excluding the damping function shows negligible effects of damping function near the free surface zone. This implied the validity of the findings of Nezu and Nakagawa (1993).

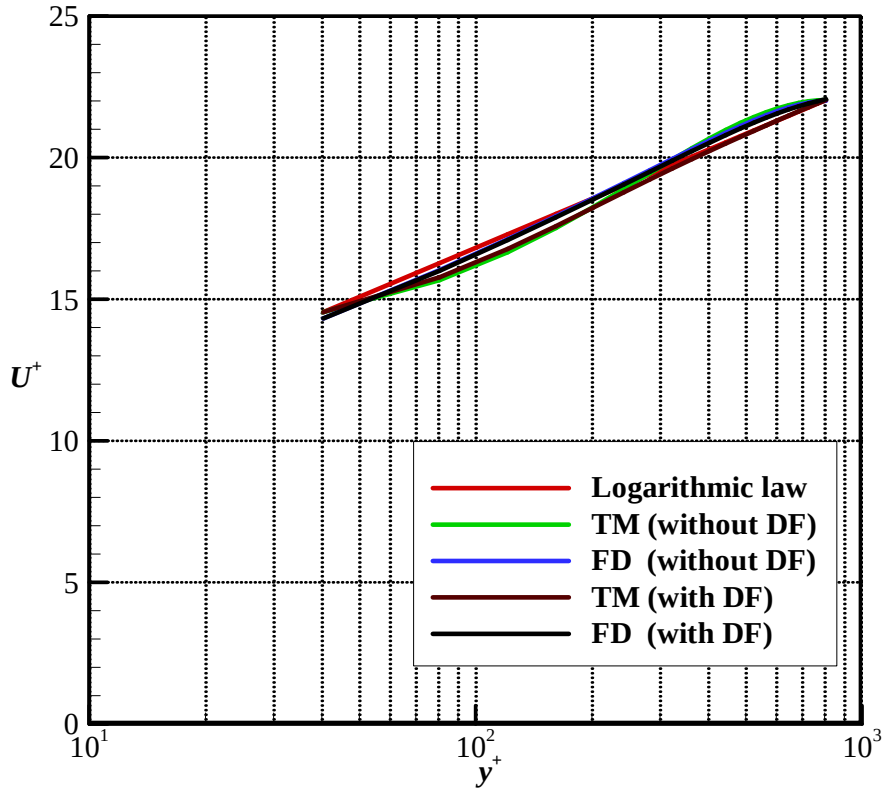

Figure 4.4. Vertical distribution of streamwise velocity (U^+ vs. $y^+ = u_* y / \nu$)

Fig. 4.5 illustrates the vertical distributions of dimensionless turbulent energy dissipation rate. Because of the wall function value, empirical curve of Nezu (1977) shows lower value at the boundary than the analytical and numerical results. Away from the wall, the distributions of numerical results of the finite difference scheme are in good agreement with the empirical curve. However, owing to the consistency with the slenderness observed in velocity distribution, the theoretical curves are diverted from both the empirical and the numerical curve. This in turn indicates bit less energy dissipation rate at some distance above the wall. Further away from the wall, distribution is similar to the numerical results. This designated the discrepancy is in consistent with that of the velocity profile. The comparisons of turbulent energy distributions for with and without damping function case exhibits negligible effect of the damping function at the free surface zone.

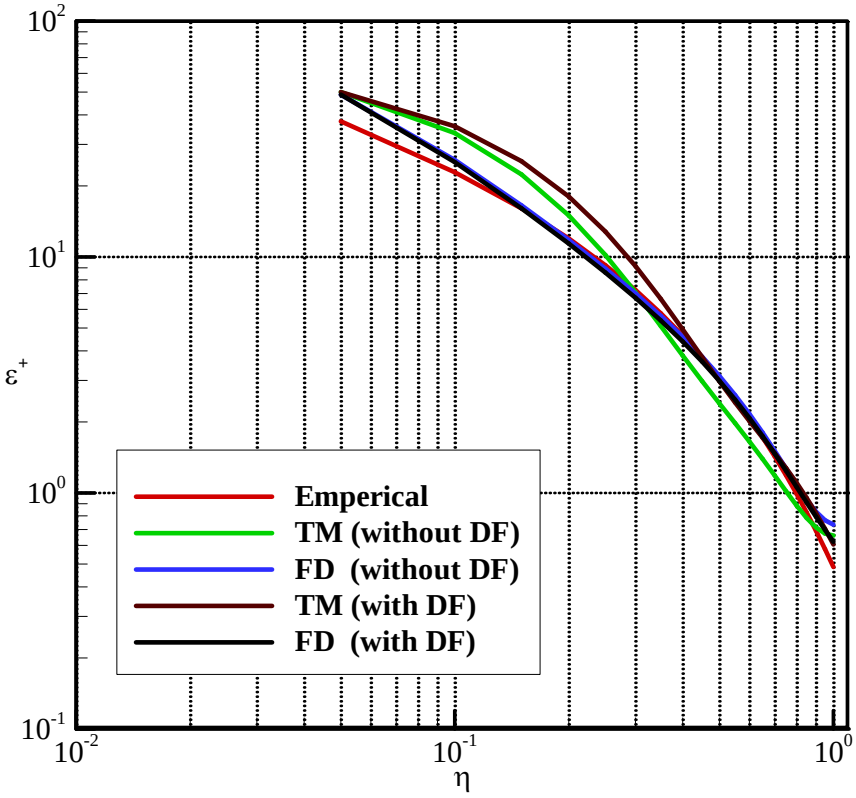

Figure 4.5. Vertical distribution of turbulent energy dissipation rate

$(\varepsilon^+ = \varepsilon\, h/u_*^3$ vs. $\eta)$

Apart from the velocity and energy dissipation rate, the theoretical distribution of the turbulent energy (without damping function case) is nearly in good agreement with the numerical result, as shown in Fig. 4.6. Again, in this case wall function value caused the empirical curve to show a higher value near the boundary. Incorporation of the damping function dampens the vertical fluctuations at the surface causing turbulent energy to be bit smaller than the case of without damping function. This can easily be seen from the comparisons of the numerical results of the finite difference scheme. On the other hand, theoretical model failed to produce the effect of such damping function on turbulent energy distribution near the free surface. This is caused due to the influence of B' value considered into the damping function. Thus, further improvement in B' calculation may reproduce the required distribution of turbulent energy in with damping function case.

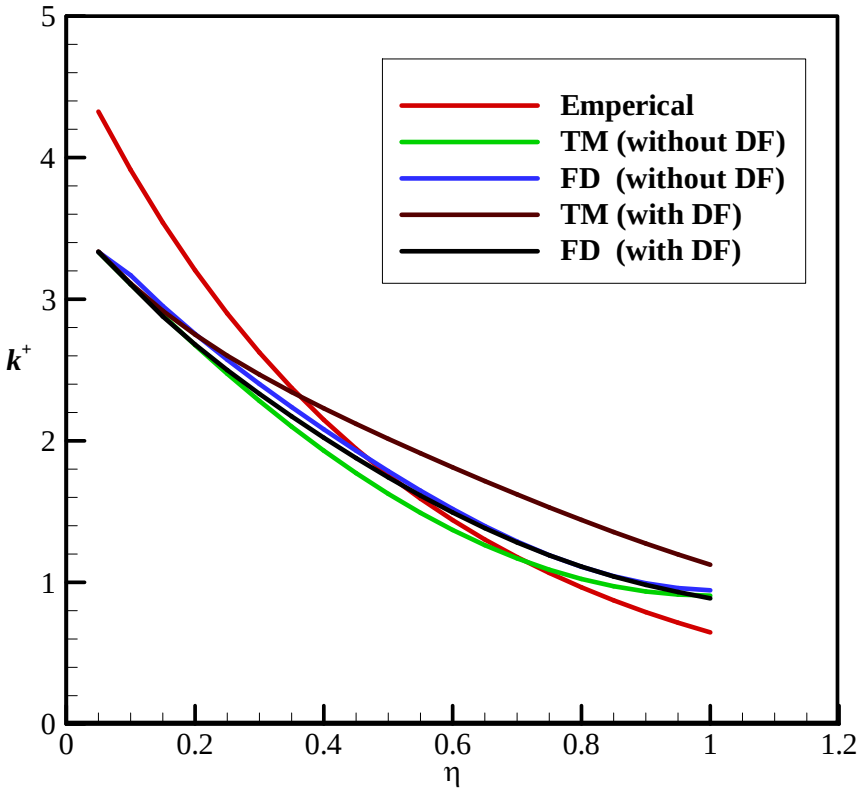

Figure 4.6. Vertical distribution of turbulent kinetic energy

($k^+ = k/u_*^2$ vs. η)

The pronounced effect of the damping function is seen from eddy viscosity distribution, as depicted in Fig. 4.7. The effect of the damping function reduces eddy viscosity near the free surface and shows the vertical parabolic shape of distribution. It is seen from the Fig. 4.7 that, the distribution of eddy viscosity exhibits the deviation near the boundary from that of the numerical results and the empirical curve. The possibility of such convex shape of the profile near the wall may cause due to the functional form considered. This in turn indicates that, the expected parabolic distribution of eddy viscosity can be guaranteed, satisfying Reynolds equation if and only if logarithmic law and functional form of $1/\eta$ for turbulent energy dissipation are considered. However, owing to the asymptotic nature of the solution (Takemitsu 1990), the higher order terms could not play well in the derivation. This is the reason present functional form employed in the derivation, which lead to the convex shape of eddy viscosity near the wall. By changing the wall function value, or incorporation of the higher order terms may reduce this propensity near the boundary region.

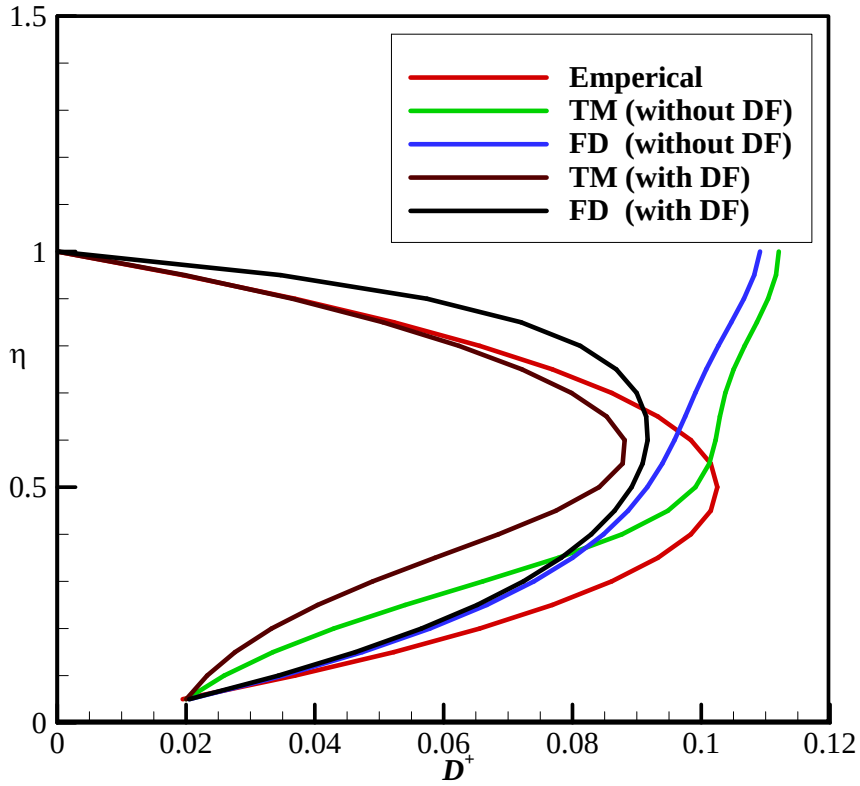

Figure 4.7. Vertical distribution of eddy viscosity

($D^+ = D/hu_*$ vs. η)

4.6.2 Non-uniform Flow

For non-uniform flow, the analytical results are compared with the experimental data of Song and Graf (1994). Two different flows conditions; accelerated and decelerated flows are selected for the comparisons. Wherever possible, numerical results of finite difference scheme are also included. The theoretical distributions of non-dimensional velocity for accelerated and decelerated flows are plotted on semi-logarithmic scale, as shown in Fig. 4.8. The logarithmic velocity distributions for accelerated and decelerated flow cases are also depicted in Fig. 4.8. In the inner region of the flow, the distribution of the velocity for decelerated flow is nearly in good agreement with the log-law. However, the distribution of velocity in accelerated flow is deviated from the log law distribution. It is because the maximum velocity for the accelerated flow is obtained much earlier than the experimental case. For decelerated flow, velocity profile is fuller compared to the accelerated flow, indicating the attainment of maximum velocity near the free surface. This is also seen from

Fig. 4.9, where vertical distributions of streamwise velocity for accelerated and decelerated flows are plotted along with the experimental data. The numerical results of finite difference scheme are also included into the Fig. 4.9. It is evident from the figure that, the comparisons of theoretical results of decelerated flow are in close agreement with the experiment.

The inclusion of damping function causes velocity near the free surface for decelerated flow to be little higher than the velocity determined without incorporating the damping function. However, for accelerated flow no such behaviour is observed for both the finite difference and theoretical results.

Besides deviation of the streamwise velocity from the experimental data, the distribution of vertical velocity is in good agreement with the experimental results. As shown in Fig. 4.10, the vertical velocity for the decelerated flow is positive and that for accelerated flow is negative. Very small effect of damping function is observed on the vertical velocity for decelerated and accelerated flow case.

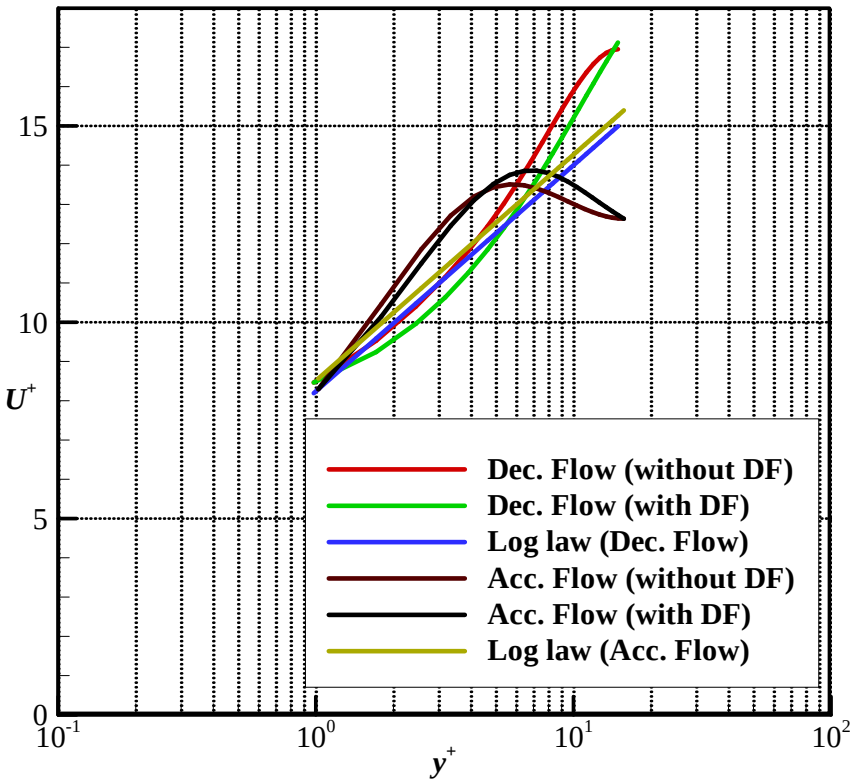

Figure 4.8. Vertical distribution of streamwise velocity for non-uniform flow

$$(U^+ \text{ vs. } y^+ = u_* y / \nu)$$

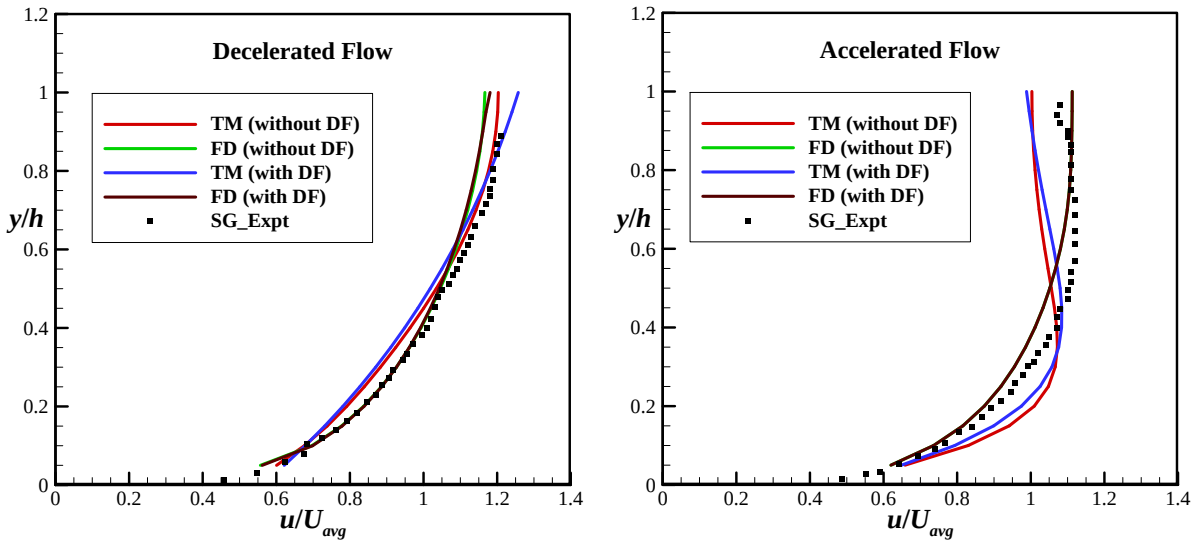

Figure 4.9. Vertical distribution of streamwise velocity in accelerated and decelerated flow

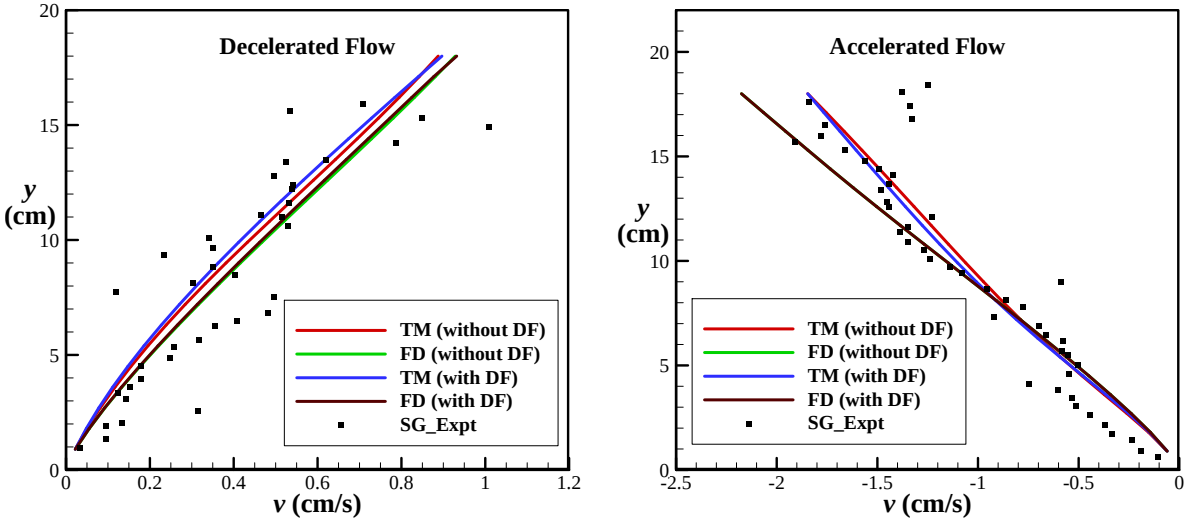

Figure 4.10. Distribution of vertical velocity in accelerated and decelerated flow

Dimensionless forms of the horizontal and vertical components of the turbulence intensity are illustrated in Fig. 4.11 and 4.12. The distribution of turbulence intensity for uniform flow is also included to analyse the effect of decelerated and accelerated flow. In comparison with the uniform flow distribution, the turbulence intensities of decelerated flow shows convex shape; while the turbulence intensities of accelerated flow shows concave shape of the profile. It is evident from the experimental data that, the wall function values for

decelerated flow is larger and for accelerated flow; it is smaller than the uniform flow case. Incorporation of new wall function for non-uniform flow as mentioned earlier, could not evaluate the expected value at the boundary. Only little decrement in accelerated flow case and increment for decelerated flow case is observed with employment of such wall function. Thus, clear necessity for derivation of new wall function values is required to reproduce the reasonable distributions of the turbulence intensities near the boundary.

Incorporation of the damping function produced the convex form of the distribution for decelerated flow, however for accelerated flow the distribution is little larger than the uniform flow distribution. The effect of damping function did not reduce the turbulence intensity near the surface. This is in consistent with the discrepancy observed in the case of uniform flow.

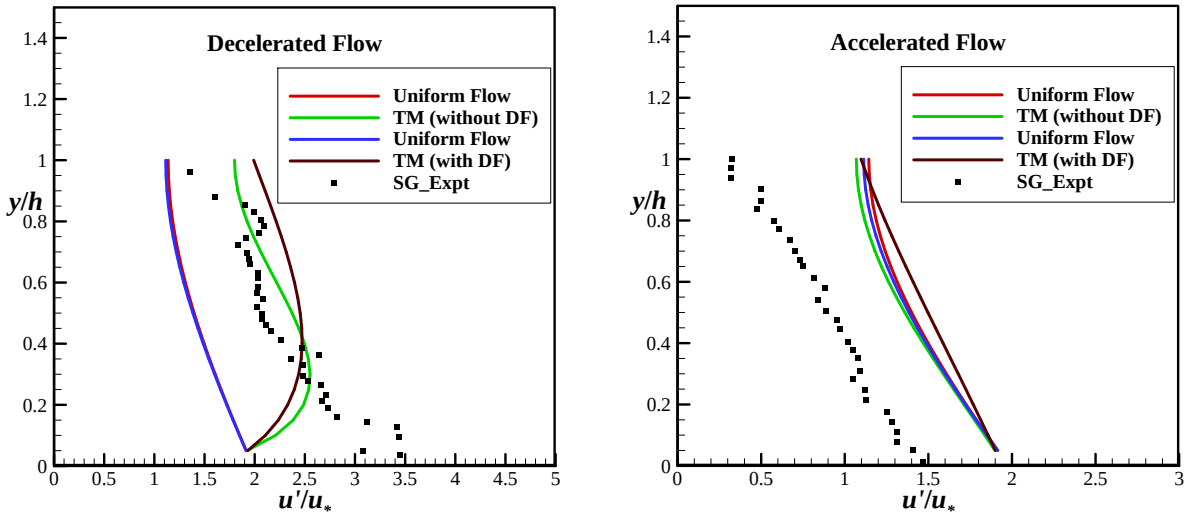

Figure 4.11. Distribution of streamwise turbulence intensity for non-uniform flow

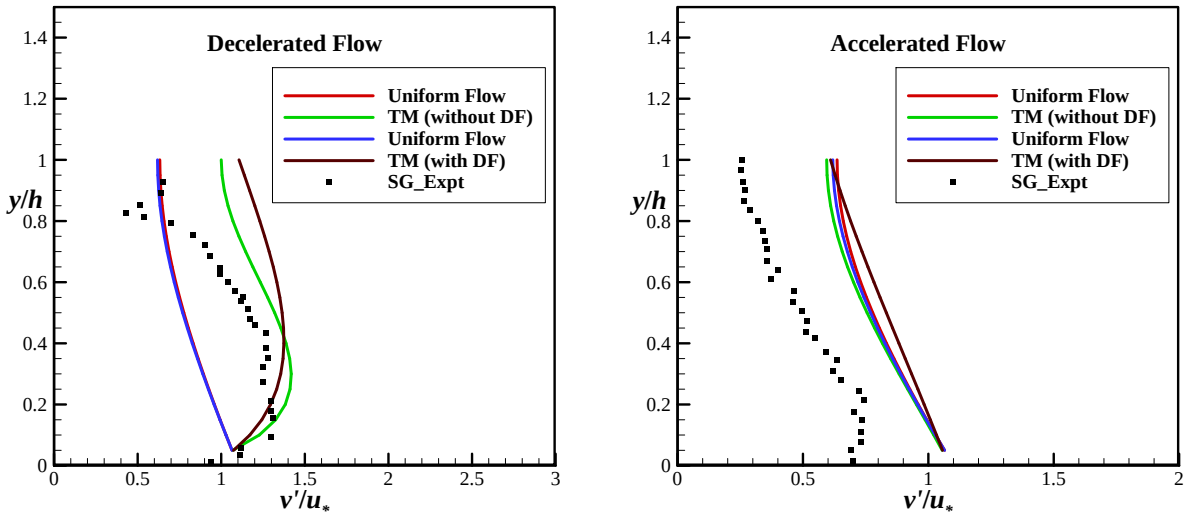

Figure 4.12. Distribution of vertical turbulence intensity for non-uniform flow

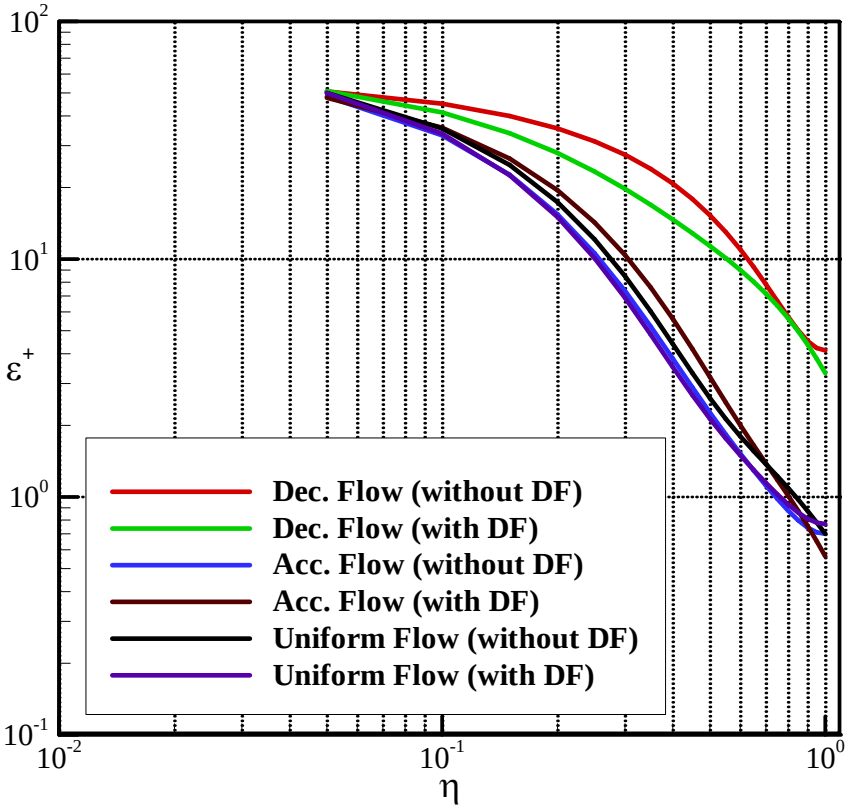

Figure 4.13. Vertical distribution of turbulent energy dissipation rate for non-uniform flow. ($\varepsilon^+ = \varepsilon\, h/u_*^3$ vs. η)

The vertical distribution of the turbulent energy dissipation rate by including and excluding the damping function for non-uniform flow is exhibited in Fig. 4.13. Depending on the nature of the flow, intensity of energy dissipation decreases towards the free surface. This in turn indicates that, the turbulent energy is dissipated much for accelerated flow as compared to the decelerated flow. The effect of damping function for both the flow cases depicted increment in the turbulent energy dissipation near the free surface compared with the distribution obtained without damping function.

Because of the nature of energy dissipation for non-uniform flow, eddy viscosity distribution shows deviation from the uniform flow distribution. Song and Graf (1994) reported that, turbulent mixing is damped in accelerated flow and amplified in the decelerated flow. Hence, the distribution of eddy viscosity is smaller for accelerated flow and larger for decelerated flow in comparison with the uniform flow. Similar tendency is observed for theoretical model, even if the damping function is included into the derivation. (Fig. 4.14). It is already mentioned that, the nature of the functional form causes propensity of eddy viscosity near the wall. This propensity of eddy viscosity near the boundary is clearly observed for the accelerated flow case. However, due to interdependency of the distributions, deformation in the turbulent energy distribution adjusted the shape of the profile of eddy viscosity in decelerated flow case. Nevertheless, the overall tendency of eddy viscosity depicted the reduction near the free surface as an effect of the damping function.

4.7 Summary

In this chapter, an effective analytical solution for the standard k-ε model is proposed for uniform and non-uniform flow. To begin with theoretical model for uniform flow, the effect of damping function is included into the derivation. The validity of the analytical results are checked in comparison with the empirical results and the numerical results of the finite difference scheme. The comparisons showed that the functional forms considered for reproduction of the distributions are suitable. These functional forms can reproduce reasonable distributions of the velocity, turbulent kinetic energy k, turbulent energy dissipation rate ε and eddy viscosity in uniform flow. The introduction of the damping function was unable to produce the damping effect on vertical fluctuations. However, damping effect reduced the length scale near the free surface and a negligible effect of

damping function on velocity distribution is also observed near the free surface. The pronounced effect of damping function is seen from the eddy viscosity distribution.

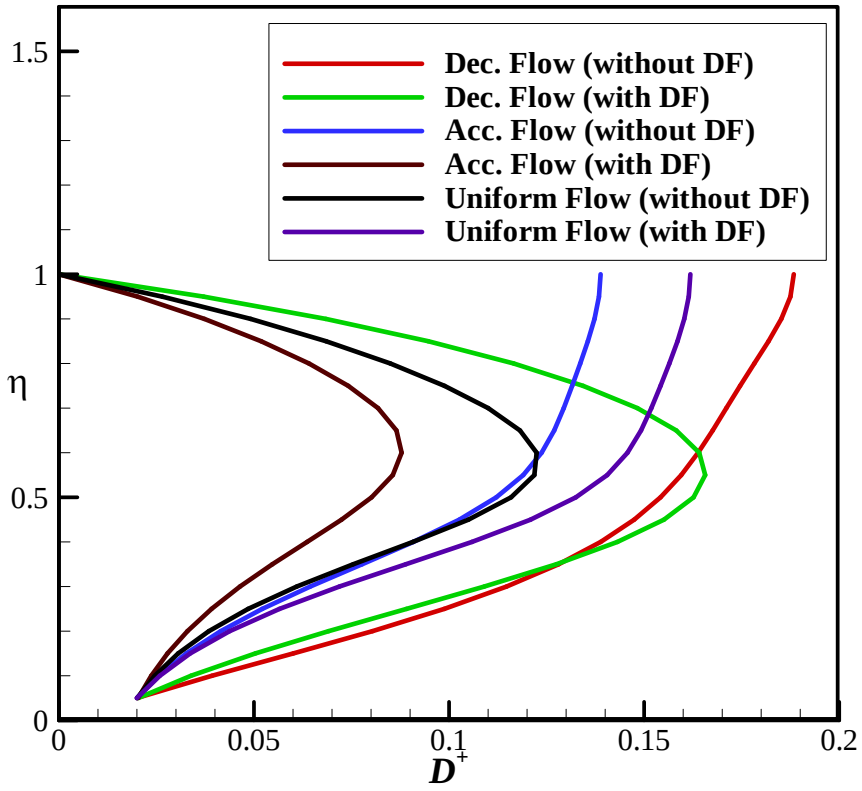

Figure 4.14. Vertical distribution of eddy viscosity for non-uniform flow

($D^+ = D/hu_*$ vs. η)

In addition to the uniform flow analysis to conduct the non-uniform flow analysis, non-uniformity is included into the derivation. The results of analytical method are compared with the experimental data for accelerated and decelerated flows. The analytical results indicated that, the behaviour of the flow velocities; both in longitudinal and vertical direction are similar to that of experimental results, with some deviation observed in accelerated flow due to earlier attainment of maximum velocity. Owing to the wall function values for non-uniform flow, turbulence intensities diverted near the boundary compared to the experimental results. On the other hand, the nature of the turbulent energy dissipation rate and eddy viscosity satisfied the conditions of the flow. The presence of the damping function acted well, even with different flow conditions of non-uniform flow. However, inconsistency

of the damping function similar to the uniform flow in regards with instability in the model is also reported in this case. Therefore, further modifications in the model are necessary to overcome this instability. Nevertheless, this analytical solution can be used in depth-averaged model to reproduce the flow properties.

4.8 References

Elkaim, D., Reggio, M., and Camarero R. (1992). "Simulating two-dimensional turbulent flow by using the k- ε model and the vorticity-stream function formulation." *Int. J. Numer. Meth. Fluids*, 14, 961-980.

Hosoda, T. (1990). "Turbulent diffusion mechanism in open channel flows." *PhD. Thesis*, *Kyoto Uni*., (in Japanese).

Jobson, H. E., and Sayre, W. (1970). "Vertical transfer in open channel flow." *J. Hydraul. Div*., ASCE, 96(3). 703-724.

Kimura, I., and Hosoda, T. (2003). "A non-linear k- ε model with realizability for prediction of flows around bluff bodies." *Int. J. Numer. Meth. Fluids*, 42, 813-837.

Kironoto, B. A., and Graf, W. H. (1994). "Turbulence characteristics in rough uniform-open channel flow." *Proc. of the ICE-Water Maritime and Energy*, 106(4), 333-344.

Launder, B. E., and Spalding, D. B. (1974). "The numerical computation of turbulent flows." *Computational methods in Applied Mechanics and Engineering*, (3), 269-289.

Nakagawa, H., Nezu, I., and Ueda, H. (1979). "Turbulence of open channel flow over smooth and rough beds." *Proc. Japanese Soc. Civil Eng*., 241. 155-168.

Nezu, I. (1977). "Turbulent structure in open-channel flows." *PhD. Thesis*, *Kyoto Uni*., Japan.

Nezu, I., and Nakagawa, H. (1987). "Numerical calculation of turbulent open-channel flows in consideration of free-surface effect." *Mem. Fac. Eng., Kyoto Univ*., 49(2). 111-145.

Nezu, I., and Nakagawa, H. (1993). "Turbulence in open-channel flows." *IAHR Monograph*.

Rodi, W. (1980). "Turbulence models and their application in hydraulics." *IAHR publication*, Delft.

Song, T., and Graf, W. H. (1994). "Non-uniform open-channel flow over a rough bed." *J. Hydrosci. Hydraul. Eng.*, 12(1). 1-25.

Speziale, C., Abid, R., and Anderson, E. (1990). "Critical evaluation of two equation models for near-wall turbulence." *ICASE Report* No. 90-46, NASA Langley Research Center, Hampton, Virginia, 1-26.

Takemitsu, N. (1990). "An analytical study of the standard k-ε model." *J. Fluids Eng., Transc. ASME*, 112. 192-198.

Tsujimoto, T., Saito, A., and Nitta, K. (1990). "Open-channel flow with spatial acceleration or deceleration." *KHL Progress Report*, Hydr. Lab., Kanazawa Uni., Japan

Wilcox, D. (1988). "Reassessment of the scale-determining equation for advanced turbulence models." *AIAA Journal*, 26(11). 1299-1310.

Yoshizawa, A. (1994). "Non-equilibrium effect of the turbulent-energy-production process on the inertial-range energy spectrum." *The American Physical Society*, 49(5). 4065-4071.

Chapter 5

ANALYSIS OF HYDRAULIC JUMP BY 1D DEPTH-AVERAGED AND 3D URANS MODEL

5.1 Preliminaries

Hydraulic jump is a classical problem cause due to transition of flow from supercritical state to subcritical state. The formation of hydraulic jump is characterized by intense mixing, air entrainment, energy dissipation, roller formation and change in water surface elevation. This characteristic of jump as an energy dissipater is always been a point of interest for many researchers. Several studies, both experimental and numerical have been conducted so far to clarify the various aspects of the hydraulic jump.

After the pioneer work of Bidone (1819), this local phenomenon had been the subject of repeated experimental investigation. Bakhmeteff and Matzke (1936), seems to be the initial contributor who made the phenomenon of the hydraulic jump clearer. Following their study in fluid flow, Rouse et al. (1958) measured the flow pattern of the hydraulic jump in an air duct so as to allow greater insight into the phenomenon. These studies were helpful to determine the water surface profile, length of the jump and to know the turbulent characteristics of the jump (Rouse et al. 1958). However, Chow (1959) determined the location of the hydraulic jump formation numerically, and reported that the specific forces of both sides of the jump are equal at the point of jump formation.

Based on Peregrine and Svendsen's (1978) model, Battjes and Sakai (1981) experimentally investigated the turbulence induced by a breaking water surface. Although they performed the measurements with the help of Laser Doppler Velocimeter (LDV), the

obtained data did not agree to the flow under the jump, because of large depth beneath the airfoil.

Numerical investigation of the jump has also gained an importance with the advent of the computers. Earlier, most of the researchers were considering the hydrostatic pressure distribution to solve the St. Venant equations numerically (For example, Abbott et al. 1969; Katopodes 1984). However, Basco (1983) showed that the pressure distribution is not hydrostatic. He assumed the vertical velocity variation stating zero velocity at the bed to maximum at the free surface and proposed Boussinesq equations to include the non-hydrostatic pressure variations. Numerical studies in one-dimensional flow are then performed with the solution of Boussinesq equations (Gharangik et al. 1991). With the increase of popularity of turbulence model, some researchers considered the turbulence modeling for simulation of the hydraulic jump numerically in 1D or 2D flow. (For instance, Chippada et al. 1994; Ma et al. 2001; Zhao et al. 2004).

Not only experimental and numerical studies but also theoretical studies of hydraulic jumps had been performed by few researchers. Narayanan (1975) in his study, treated plane turbulent wall jet as a hydraulic jump in turbulent flow, just like what Rajaratnam (1965) showed experimentally. The model based on integral momentum and continuity equations is used to calculate the kinematics of mean motion within the jump. By this means, he could reproduce the decay of the maximum velocity, variations of the surface velocity, growth of the boundary layer and the surface profile of the jump. However, the surface profile obtained with this theory showed discontinuity with the experimental data. On the other hand, Madsen and Sevendsen (1983) developed turbulent closure model to determine the velocity field and the surface profile of bores and hydraulic jumps. For their model, they reduced the turbulent closure model in terms of non-equilibrium kinetic energy by expressing the dependency of turbulent energy dissipation on a mixing length. Before considering the turbulent closure, they subdivided the flow region into turbulent wedge region and potential flow region (see Fig. 5.1). In figure 5.1, the region indicating the constant velocity, bounded by thickness $a(x)$ is the potential flow region and the flow bounded by thickness $b(x)$ is the turbulent wedge region. This helped them to solve the depth-integrated equation for the velocity in the whole region because of nonoccurrence of shear stresses explicitly in the momentum equations. They showed that the surface profile obtained with the model is in good agreement with the

experiment and it is insensitive to the velocity profile. By considering the different values of the constant in third order polynomial function of the depth-integrated form of the velocity, they could reproduce the good comparison with the measured data. Although, they considered the turbulence closure model and depth-integrated form of the velocity, their model is bit complicated. That even reproduces reasonable results only when the different values for the constant are considered.

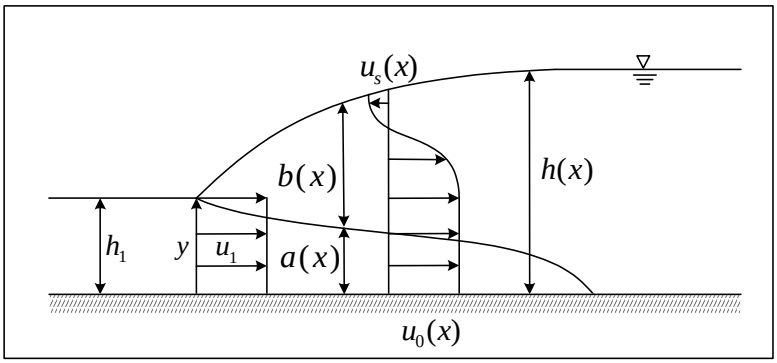

Figure 5.1. Pictorial representation of Madsen et al. (1983)'s model

Thus, to develop rather simple model for the determination of the continuous water surface profile of the jump, theoretical analyses is performed. Starting from the simple analytical solution of the momentum equation with eddy diffusivity term, the effect of bed shear stress is introduced for the determination of the profile of the jump. In order to obtain the water surface profile and velocity distribution together in hydraulic jump the deformation principle is considered in the later part of the analysis. To check the performance of the model, experimental data of Bakhmeteff and Matzke (1936), Gharangik et al. (1991) and theoretical and experimental data of Madsen et al. (1983) are considered for the comparisons.

5.2 Model analysis using momentum equation with eddy diffusivity term

The momentum equation assuming the hydrostatic pressure and including the eddy diffusivity term is:

$$\frac{d}{dx}\left(h\,U^2 + \frac{g}{2}h^2\cos\theta \right) = \frac{d}{dx}\left(D_m h \frac{dU}{dx} \right) + gh\sin\theta - \frac{\tau_{bx}}{\rho} \qquad (5.1)$$

where, x = streamwise distance; h = flow depth; U = depth-averaged velocity; θ = angle made by the streamwise slope with the horizontal; D_m = eddy diffusivity coefficient; g = gravitational acceleration; τ_{bx} = bed shear stress; ρ = mass density of fluids.

Using continuity equation,

$$h\,U = q \tag{5.2}$$

and by the definition of bed shear stress,

$$\frac{\tau_{bx}}{\rho} = C_f U^2 \tag{5.3}$$

Eq. 5.1, can be expressed as,

$$\left(-q + g\,h^3\right)\frac{dh}{dx} - D_m q\left(\frac{dh}{dx}\right)^2 + D_m q h\frac{d^2h}{dx^2} + C_f\,q^2 = 0 \tag{5.4}$$

where, horizontal bed is considered. The eddy diffusivity coefficient can be correlated to the discharge by similarity function as

$$D_m = \alpha\,q \tag{5.5}$$

where, α is a proportionality factor.

To derive the simple analytical solution for the continuous water surface profile of the hydraulic jump, initially, the bed shear stress term is neglected. Thus, Eq. 5.4 is reduced to the form given as

$$\frac{dh}{dx} = -\frac{1}{D_m q}\left(q^2 + g\frac{h^3}{2} - M_0 h\right) \tag{5.6}$$

The momentum flux M_0 is defined as

$$M_0 = \frac{q^2}{h_1} + g\frac{h_1^2}{2} \tag{5.7}$$

Transforming Eq. (5.6) into the following form by using h_1, h_2 and h_3 as

$$\frac{dh}{dx} = -A\left(h - h_1\right)\left(h - h_2\right)\left(h - h_3\right); \quad \text{where } A = \frac{1}{D_m q}\frac{g}{2} \tag{5.8}$$

The purpose of incorporating h_3 is to satisfy the equation mathematically, even though this depth has completely no effect on the jump.

Integrating Eq. (5.8) from critical depth h_c to h, the exact solution for the continuous profile of the jump is obtained as

$$a_1' \ln\left(\frac{h-h_1}{h_c-h_1}\right) + a_2' \ln\left(\frac{h-h_2}{h_c-h_2}\right) + a_3' \ln\left(\frac{h-h_3}{h_c-h_3}\right) = -A'\left(x-x_c\right) \tag{5.9}$$

where, x_c is the location of the critical depth and constants a_1', a_2', a_3' and A' are defined by following equations

$$a_1' = \frac{a_1}{b}; \qquad a_2' = \frac{a_2}{b}; \qquad a_3' = \frac{a_3}{b}; \qquad A' = \frac{A}{b} \text{ and } \quad b = \left(a_1\ a_2\ a_3\right)^{1/3} \tag{5.10}$$

Here,

$$a_1 = \frac{-1}{\left(h_1-h_2\right)\left(h_3-h_1\right)};\ \ a_2 = \frac{-1}{\left(h_1-h_2\right)\left(h_2-h_3\right)} \text{ and } a_3 = \frac{-1}{\left(h_2-h_3\right)\left(h_3-h_1\right)}$$

To check the performance of the analytical method, the water surface profile obtained by Eq. (5.9), is compared with the experimental result of Madsen et al. (1983). The hydraulic parameters of the experimental data are tabulated in Table 5.1. As shown in Fig. 5.2, different values for the coefficient of the proportionality factor α are used to reproduce the water surface profile of the jump. However a comparison shows that, the proposed analytical method is not able to reproduce the characteristics of surface profile of the jump appropriately. That is, though different values of α are considered, sharp increment of water depth from upstream depth h_1 and gradual lessening of gradient of water surface profile is not reproduced by the analytical method. From the definition of turbulent diffusivity coefficient, which is $h\,u_*$ (u_* is the friction velocity), it is considered that the values of α occurred in the range of 0.005 to 0.1. Contrary to these values, the length of the hydraulic jump is fit well with the experimental data for α = 1.0. This implies the further necessity to review the meaning of eddy diffusivity term.

Additionally, the numerical simulation of Eq. 5.4 by using 4th order Runge-Kutta method is performed to examine the effect of bed shear stress on water surface profile of the jump. The simulations are conducted under the experimental conditions of Gharangik et al. (1991) for different Froude number (see Table 5.1 for hydraulic conditions). The calculation proceeds by providing the values of water depth and the derivative of water depth as an initial condition. The presence of second order ordinary differential equation is responsible for two boundary conditions at the upstream end. The experimental depths are not the conjugate depths, hence, adjusting the derivative of water depth at the upstream location

comply with the experimental depth of water at the downstream end. The results of the numerical (Num) simulation for Froude number 4.23, 5.74, 6.65 and 7 are plotted with respective experimental data, as shown in Fig. 5.3. In this case also, different values of α are considered to obtain the water surface profile of the jump. Here, the coefficient of friction velocity is considered as 0.01. All these results justify the existence of continues water surface profile of the hydraulic jump passing through the critical depth even if the bed shear stress and eddy diffusivity term are included. The comparisons of the water surface profile with the experimental data shows that, with the increase of the value of α, the water surface profiles of the hydraulic jump come closer to the experimental results. It is also seen from the figures that, the Froude number of the hydraulic jump is in directly proportional to α value. In other words, if the Froude number of the hydraulic jump increases, the values of the proportionality factor α increases and vice versa. Following the observations of the relationship between the Froude number and the proportionality factor, further study is required to characterize the weak jump and the strong hydraulic jump.

Table 5.1. Hydraulic parameters of numerical simulation

Experimental case	**Upstream depth, h_1 (m)**	**Velocity u_1 (m/s)**	**Froude Number**	**Downstream depth, h_2 (m)**
Madsen et al.	0.0728	1.808	1.97	0.175
Bakhmeteff and Matzke	0.0765	1.720	1.98	0.175
Gharangik et al.	0.043	2.737	4.23	0.222
	0.040	3.578	5.74	0.286
	0.024	3.255	6.65	0.195
	0.031	3.831	7.0	0.265

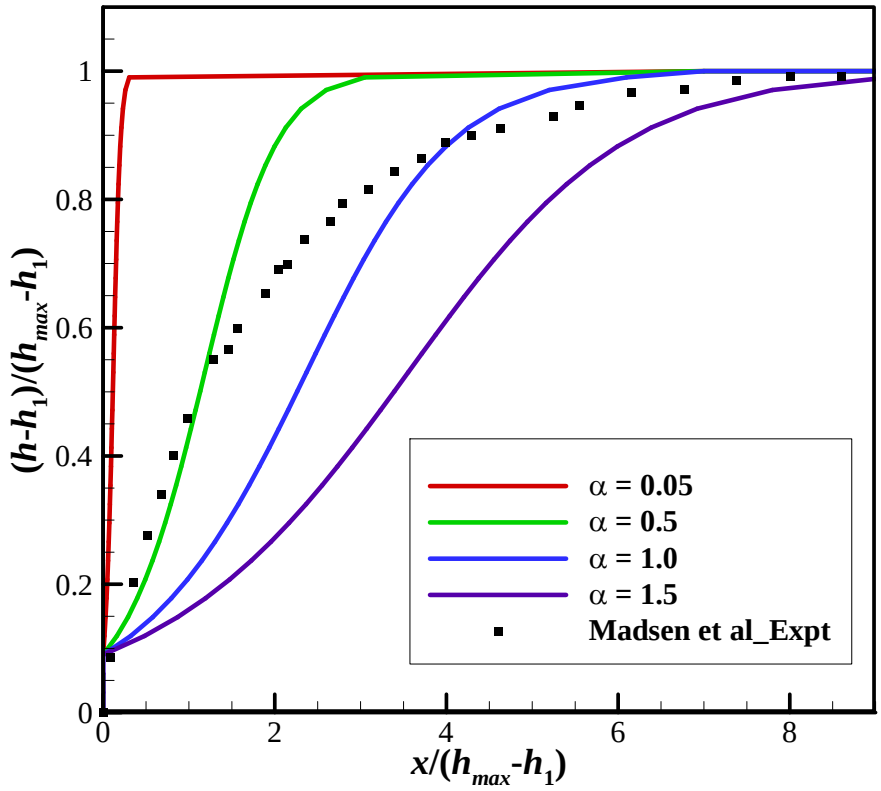

Figure 5.2. Analytical solution for water surface profile of hydraulic jump

So far, analytical solution of Eq. (5.6) and numerical solution of Eq. (5.4) are performed to prove the existence of the solution for continuous water surface profile passing through the critical depth. However, to validate the condition of Eq. (5.4) analytically, it is expressed as

$$h = h_0(x) + C_f \, \delta h_1(x) \tag{5.11}$$

where, $h_0(x)$ is satisfied by analytical solution of Eq. (5.9). It is re-described as

$$F(h_0) = -\frac{1}{A'} \ln\left\{ \left(\frac{h_0 - h_1}{h_c - h_1}\right)^{a'_1} \left(\frac{h_0 - h_2}{h_c - h_2}\right)^{a'_2} \left(\frac{h_0 - h_3}{h_c - h_3}\right)^{a'_3} \right\} = (x - x_c) \tag{5.12}$$

By using Taylor's series, the expansion of $F(h_0)$ around a critical depth is given as

$$F(h_0) = x - x_c = b_1(h_0 - h_c) + b_2(h_0 - h_c)^2 + b_3(h_0 - h_c)^3 + \cdots\cdots \tag{5.13}$$

Substituting Eq. (5.11) into Eq. (5.4) and after simplification, following equation is obtained.

$$3gh_0^2\frac{dh_0}{dx}\delta h_1+\left(gh_0^3-q^2\right)\frac{d\delta h_1}{dx}-2D_m q\frac{dh_0}{dx}\frac{d\delta h_1}{dx}$$

$$+D_m qh_0\frac{d^2\delta h_1}{dx^2}+D_m q\frac{d^2h_0}{dx^2}\delta h_1+q^2=0 \tag{5.14}$$

Expressing δh_1 using Taylor series as

$$\delta h_1=\beta_1\left(h_0-h_c\right)+\beta_2\left(h_0-h_c\right)^2+\beta_3\left(h_0-h_c\right)^3+\cdots\cdots \tag{5.15}$$

Substituting δh_1 and $dh_0/dx=1/\left(dF(h_0)/dh_0\right)$ into Eq. (5.14), the relations between the coefficients of power series for δh_1 are derived. That is

$$\beta_2=\frac{2\,D_m q\alpha_1\beta_1+2\,D_m qh_c\alpha_2\beta_1-q^2\alpha_1^3}{2\,D_m qh_c\alpha_1} \tag{5.16}$$

$$\beta_3=\frac{\left[-6gh_c^2\alpha_1^2\beta_1+2\,D_m q\left(\alpha_1\beta_2+4\alpha_2\beta_1+3h_c\alpha_3\beta_1\right)-6\,q^2\alpha_1^2\alpha_2\right]}{6\,D_m qh_c\alpha_1} \tag{5.17}$$

These relations shows that, by providing the gradient at the critical depth, i.e. β_1 and the critical depth h_c; the other coefficients can be calculated. The other two coefficients indicate the water depth at the upstream and downstream end. Hence, the surface profile passing through the critical depth between two boundaries of jump can be evaluated by using the Eq. (5.11).

The whole analysis until now is describing the fact that, continuous water surface profile can be obtained between the conjugate depths of the hydraulic jump. Of course, the nature of the surface profile obtained is based on the eddy diffusivity value selected during the calculation. Thus, in order to reproduce the water surface profile of the hydraulic jump more accurately, simple depth-averaged model is developed. The formulation of the model is based on the concept of velocity deformation, which is similar to the method of the model of the unsteady open channel flow described in the 2nd Chapter. The details of the depth-averaged model evaluation are described henceforth.

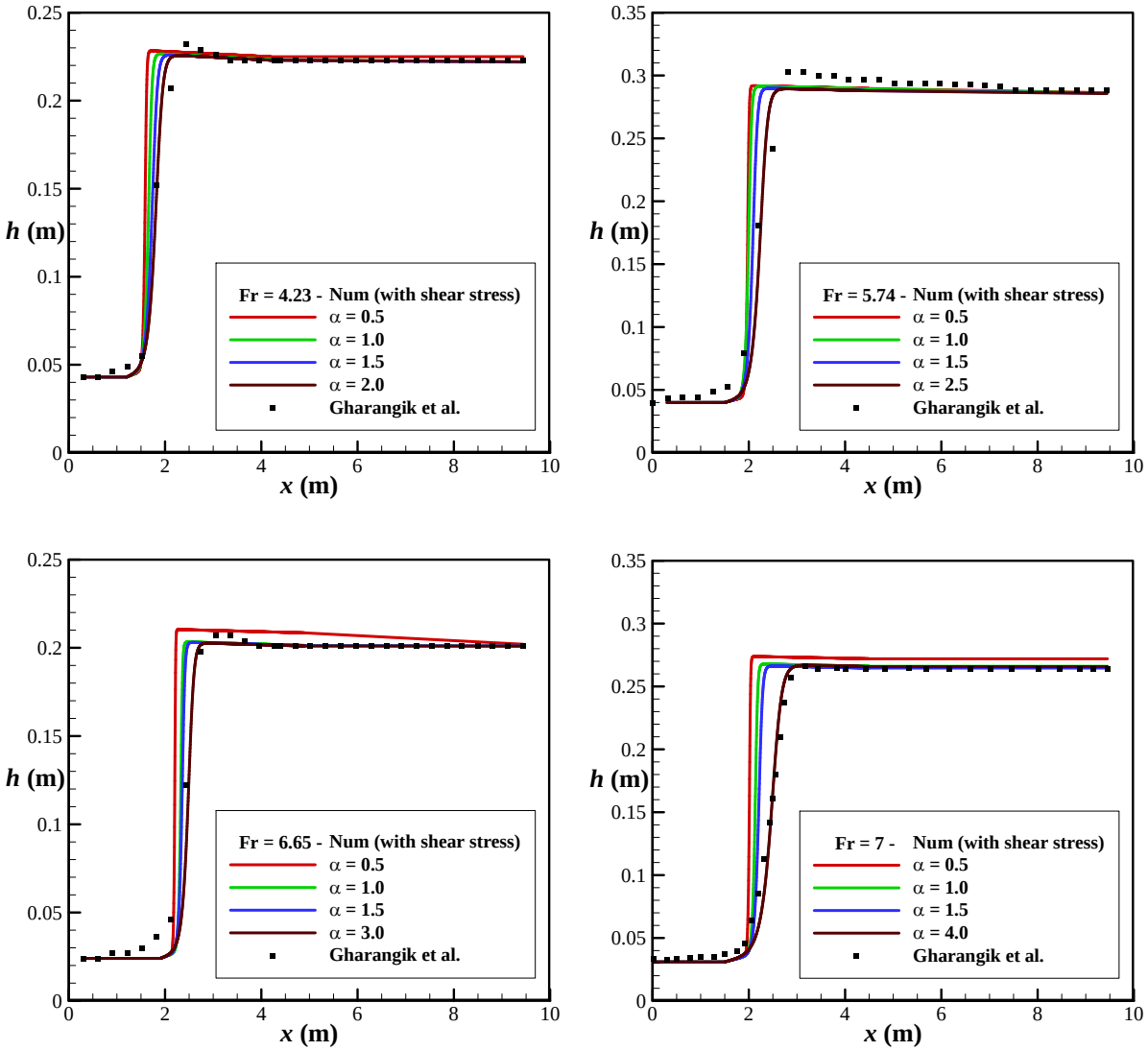

Figure 5.3. Numerical solution for water surface profile of hydraulic jump

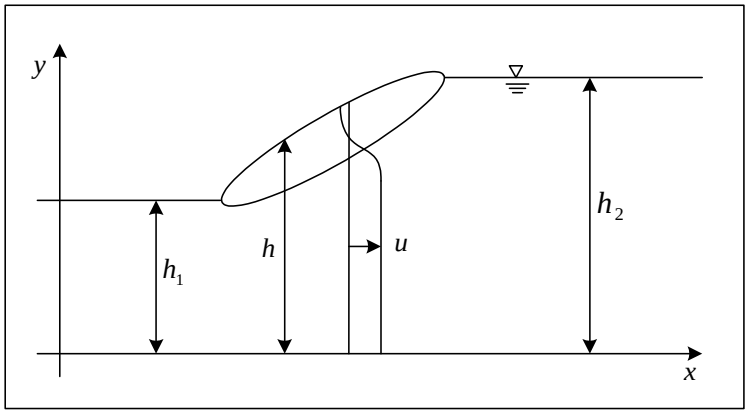

Figure 5.4. Schematic diagram of hydraulic jump

5.3 Depth-averaged model formulation

Referring to Fig. 5.4, the fundamental form of the streamwise velocity is expressed by the power series of relative depth as

$$u = u_0 + u_1\eta + u_2\eta^2 + u_3\eta^3 + u_4\eta^4 + \cdots \text{ where } \eta = y/h \tag{5.18}$$

From the continuity equation, the vertical velocity distribution is represented as

$$\int_0^y \frac{\partial v}{\partial y} dy = v = -h\sum_{i=0}^{4}\left(\frac{\partial u_i}{\partial x} - i\frac{u_i}{h}\frac{\partial h}{\partial x}\right)\frac{\eta^{i+1}}{i+1} \tag{5.19}$$

Madsen et al. (1983) reported that, the pressure variation has very small effect on the horizontal balance. Therefore, for present study the hydrostatic pressure distribution is considered.

$$p = \rho g\left(h\cos\theta - y\right) \tag{5.20}$$

The steady form of the equation of motion in *x*-direction is

$$u\frac{\partial u}{\partial x} + v\frac{\partial u}{\partial y} = g\sin\theta - \frac{1}{\rho}\frac{\partial p}{\partial x} + \frac{\partial}{\partial y}\left(\frac{\tau_{xy}}{\rho}\right) + D_{my}\frac{\partial^2 u}{\partial y^2} \tag{5.21}$$

The shear stress has small influence on the jump height depending on the Froude number (see Madsen et al. 1983). Thus for simplicity, and to make the model as similar as to the Madsen et al. (1983)'s model, shear stress is neglected from the derivation. Substituting Eq. (5.18), (5.19) and (5.20) into the equation of motion, the coefficients of velocity are expressed into the form as,

$$u_2 = \frac{h^2}{2\,D_{my}}\left(u_0\frac{\partial u_0}{\partial x} + g\frac{\partial h}{\partial x}\right) \tag{5.22}$$

$$u_3 = \frac{h^2}{6\,D_{my}}u_0\left(\frac{\partial u_1}{\partial x} - \frac{u_1}{h}\frac{\partial h}{\partial x}\right) \tag{5.23}$$

$$u_4 = \frac{h^2}{12\,D_{my}}\left(u_0\frac{\partial u_2}{\partial x} - 2\frac{u_0u_2}{h}\frac{\partial h}{\partial x} - u_2\frac{\partial u_0}{\partial x} + \frac{u_1}{2}\frac{\partial u_1}{\partial x} - \frac{u_1^2}{2h}\frac{\partial h}{\partial x}\right) \tag{5.24}$$

here, D_{my} indicate the eddy diffusivity.

It is already mentioned that Madsen et al. (1983), neglected the shear stress so as to get the uniform flow velocity in non-turbulent region of the flow. This implies that the distributions of velocity are bound by the expression they used in the turbulent wedge.

However, further downstream of the jump and near the bed, where non-turbulent region exist, the velocity distribution is uniform. Considering these facts, in present analysis the gradient of velocity distribution at bed is set to zero by assuming only even terms of power series. In other words, due to omission of shear stress term, u_1 and hence, u_3 are found to be zero.

The depth-averaged continuity and momentum equations are expressed by using only coefficients u_0 and u_2 as

$$\frac{q}{h} = u_0 + \frac{1}{3}u_2 \tag{5.25}$$

$$h\,u_0^2 + \frac{2}{3}h\,u_0 u_2 + \frac{1}{5}h\,u_2^2 + g\,\frac{h^2}{2} = M_0 \tag{5.26}$$

Defining coefficient *X* by relation

$$X \equiv u_0 - \frac{q}{h} \tag{5.27}$$

Substituting Eq. (5.27) into the momentum equation (Eq. 5.26)

$$h\left[\left(u_0 - \frac{q}{h}\right) + \frac{q}{h}\right]^2 - 2\,h\left[\left(u_0 - \frac{q}{h}\right) + \frac{q}{h}\right]\left(u_0 - \frac{q}{h}\right) + \frac{9}{5}h\left(u_0 - \frac{q}{h}\right)^2 + g\,\frac{h^2}{2} = M_0 \tag{5.28}$$

The expression for coefficient X is given by

$$X = \sqrt{\frac{5}{4}\left(\frac{M_0}{h} - \frac{q^2}{h^2} - g\,\frac{h}{2}\right)} = \frac{1}{2\,h}\sqrt{\frac{5g}{2}}\sqrt{-(h-h_1)(h-h_2)(h-h_3)} \tag{5.29}$$

This expression ensures that X is always positive between h_1 to h_2.

To derive the depth-averaged model consistent with water surface profile equation, initially, u_2 is represented by substituting $U = q/h$ as a first approximation for u_0 in Eq. (5.22). The second approximation for u_0 is then determined from the continuity equation as

$$u_0 = \frac{q}{h} + \frac{g\,h^2}{6\,D_{my}}\left(-1 + \frac{q^2}{g\,h^3}\right)\frac{\partial h}{\partial x} \tag{5.30}$$

The second approximation for u_2 is obtained by re-substituting u_0 of Eq. (5.30) into Eq. (5.22). That is

$$u_2 = \frac{1}{2\,D_{my}h}\left[q + \frac{1}{6\,D_{my}}\left(q^2 - g\,h^3\right)\frac{\partial h}{\partial x}\right]\left[-q\frac{\partial h}{\partial x} - \frac{1}{6\,D_{my}}\left(q^2 + 2\,g\,h^3\right)\left(\frac{\partial h}{\partial x}\right)^2\right.$$

$$+\frac{h}{6\,D_{my}}\left(q^2-g\,h^3\right)\frac{\partial^2 h}{\partial x^2}\Bigg]+\frac{1}{2\,D_{my}}g\,h^2\,\frac{\partial h}{\partial x} \tag{5.31}$$

Because of the singularity observed for gradient of water depth in the first approximated solution the second approximations for the coefficients are considered. This approximation (Eq. 5.31) is then solved in conjunction with Eq. (5.29) (as shown in Eq. 5.32) to determine the water surface profile equation for the hydraulic jump.

$$u_2 = 3\left(\frac{q}{h}-u_0\right)=-3X \tag{5.32}$$

Therefore, water surface profile equation obtained by above consideration is represented as

$$q^2+g\frac{h^3}{2}-M_0 h+\frac{1}{45\,D_{my}^2}\left(q^2-gh^3\right)^2\left(\frac{\partial h}{\partial x}\right)^2+\frac{q}{135\,D_{my}^3}\left(q^2-gh^3\right)\left(2q^2+gh^3\right)\left(\frac{\partial h}{\partial x}\right)^3$$

$$+\frac{1}{810\,D_{my}^4}\left[\frac{q^2}{2}\left(2q^2+gh^3\right)^2+\left(q^2-gh^3\right)^2\left(q^2+2gh^3\right)\right]\left(\frac{\partial h}{\partial x}\right)^4=0 \tag{5.33}$$

5.3.1 Water surface profile of the hydraulic jump

The estimation of water depth is carried out from the upstream point where initial depth is h_1. Assuming the increment of Δh, water depth satisfying the Eq. (5.33) is figured out. The calculations performed for each Δx from upstream to downstream direction.

The water surface profile obtained with this case is plotted in Fig. 5.5. The experimental data of Madsen et al. (1983) and Bakhmeteff and Matzke (1936) are used for the comparisons. For the proportionality factor α = 0.09, the obtained results shows reasonable agreement with the experimental data. Although, α = 0.09 is considered as reasonable in this study, it is necessary to discuss the appropriateness of value of α. The water surface profile exhibits the smooth increment from initial depth h_1 to its consecutive depth h_2. However, the length of the jump for the theoretical model is bit smaller than the experimental results. Although little discrepancy is observed between the analytical and the experimental results in the recirculation zone, the overall tendency of the water surface prolife is in good agreement with the experimental data of Madsen et al. (1983).

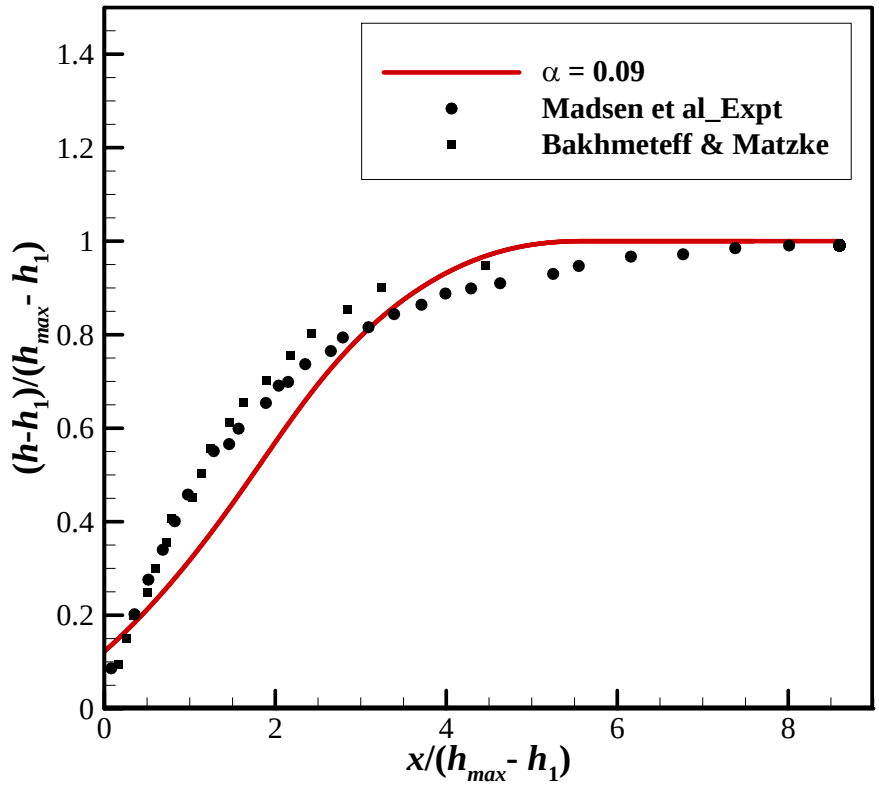

Figure 5.5. Water surface profile of hydraulic jump obtained by depth-averaged model

5.3.2 Velocity distribution in the hydraulic jump

The distributions of velocities in consistent with the water depth are compared with the experimental and theoretical results of Madsen et al. (1983). The distributions are plotted for different depths as shown in Fig. 5.6. In these figures, two different distributions of velocities for analytical results are shown. The first distribution is evaluated by considering only two coefficients. That is, only coefficient u_0 and u_2 are considered. Contrarily, in another distribution, higher order coefficient (4^{th} power of η) is added in order to make zero gradient condition for the velocity at the free surface. The comparisons of the velocity distributions with the experiments shows that, at upstream and downstream end of the jump the depth is constant. Thus, the velocity profile exhibits the constant distribution as an averaged velocity. However, in the recirculation zone of the hydraulic jump, the velocity deforms and indicates the better agreement with the previous theoretical results. Unlike the theory of Madsen et al. (1983), the present analysis described that, the surface profile is sensitive to the form of the velocity profiles. Therefore, the assumptions employed for

determination of velocity produce reasonable distribution satisfying the continuity equation for each velocity profile. From the viewpoint of the accuracy of the distributions, it is observed that the deformation of the velocity is achieved well to some extent. Thus, it is necessary to improve the model by employing the higher order terms in the formulation. It is worth mentioning here that, the model proposed herein does not contain eddy viscosity term as a turbulent transfer term as described in section 5.2. Instead, it is considered as a momentum transfer term caused due to the deformation of the velocity. However, the relation between these two is necessary to be clarified for further understanding.

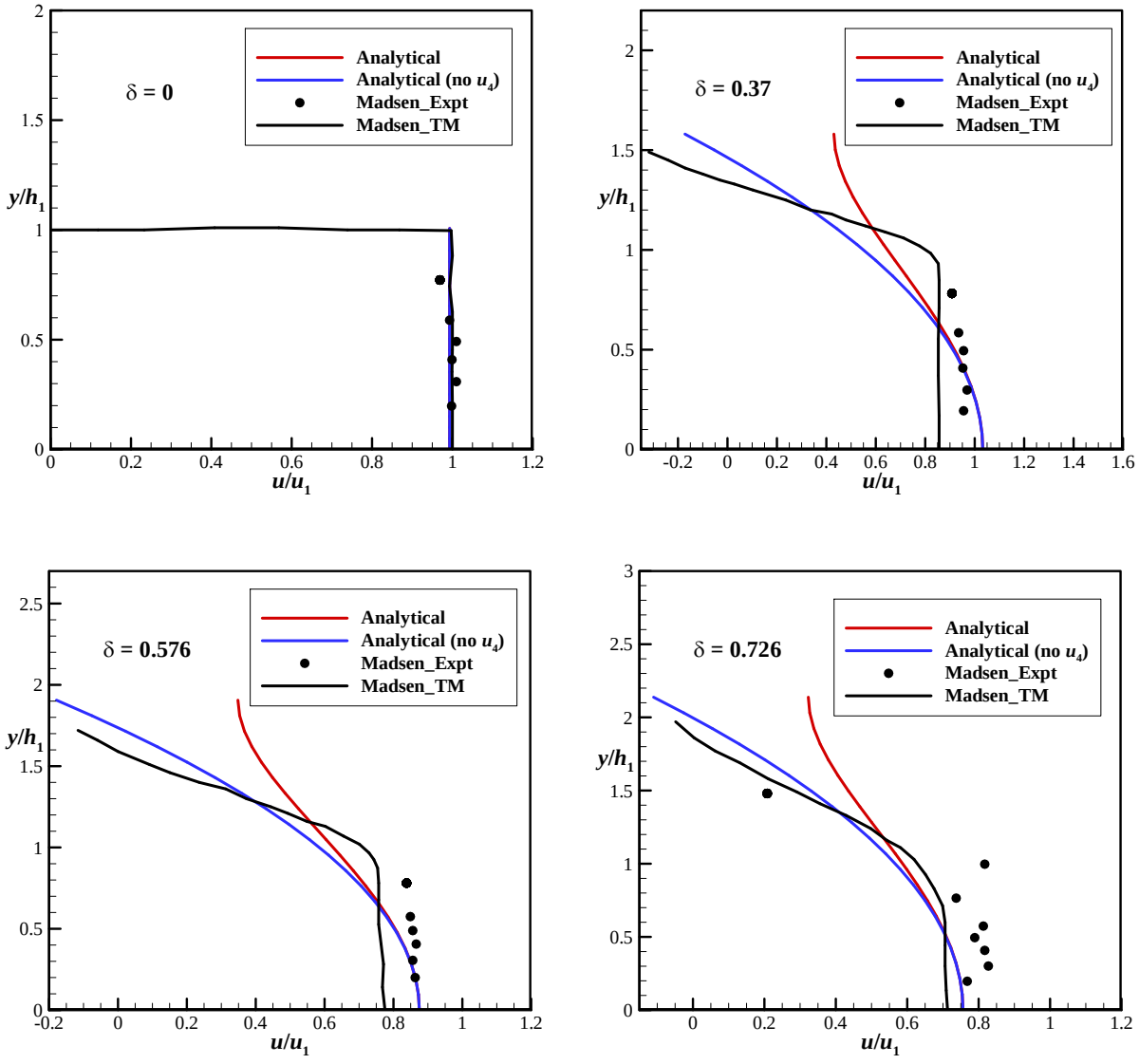

Figure. 5.6a. Velocity distribution for different depths

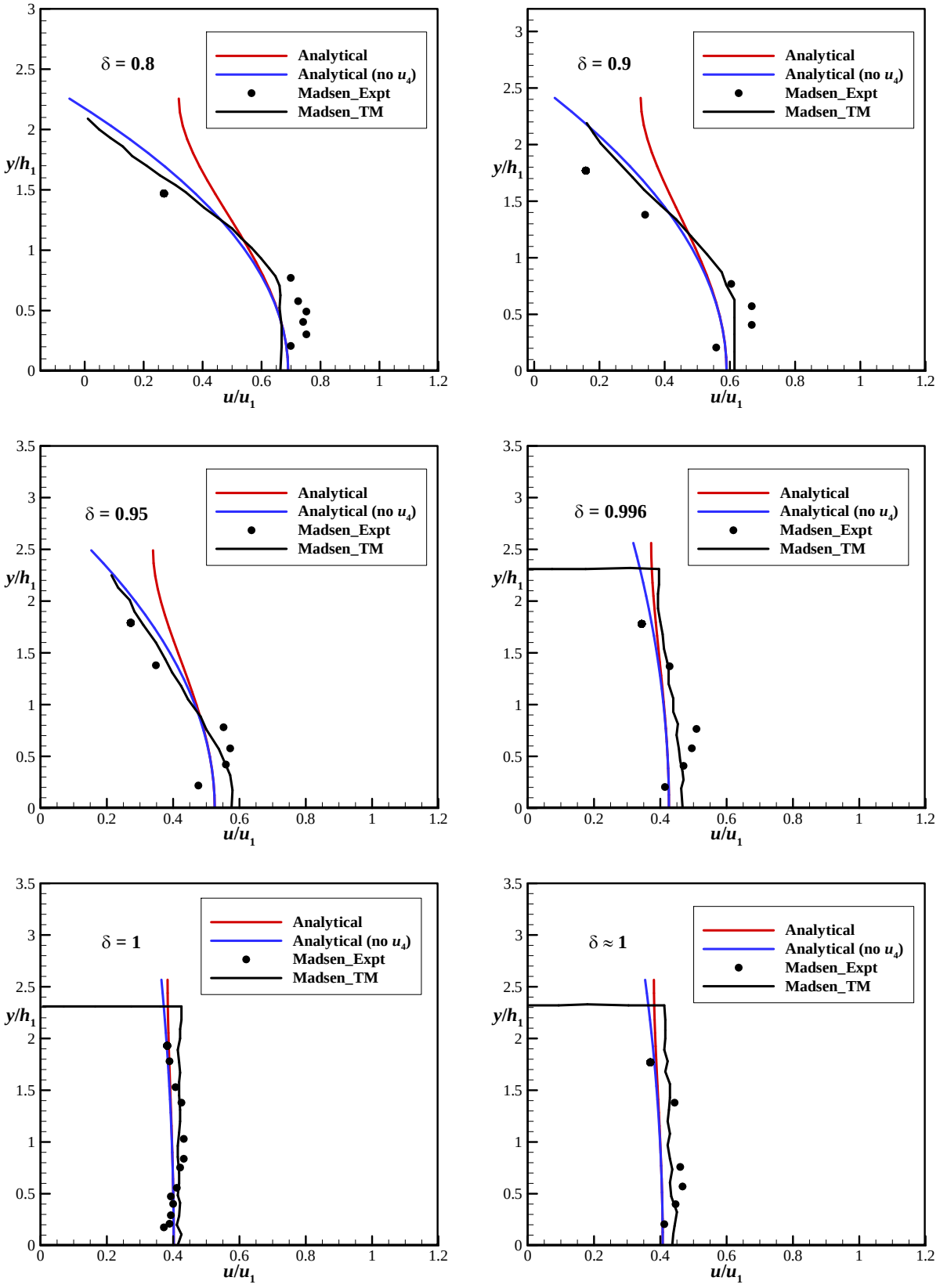

Figure. 5.6b. Velocity distribution for different depths.

5.4 Numerical simulation of hydraulic jump by using 3D URANS model

In this section numerical simulation of hydraulic jump by using 3D unsteady RANS model is described. The detail description of the model is already presented in Chapter 3. Hence, only computational condition and the numerical results of the hydraulic jump are depicted here.

5.4.1 Computational conditions

For numerical simulations of the hydraulic jump by using both the standard and non-linear *k-ε* model, the experimental condition of Madsen et al. (1983) is used. The numerical grids for the whole domain are set as $\Delta x = 0.05$; $\Delta y = 0.03$ and $\Delta z = 0.00728$. For both the simulations, Δt is set to be 0.000005. For inlet boundary condition constant discharge is provided at the upstream end. This in turn provided the supercritical velocity as an initial condition for all time steps. For downstream boundary condition subcritical depth is held constant. Numerical simulations are conducted until the steady state of the hydraulic jump is obtained.

5.4.2 Results and discussions

The results of the numerical simulations of hydraulic jump are compared with Bakhmeteff and Matzke (1936) and Madsen et al. (1983)'s experimental data.

5.4.2.1 Water surface profile

The water surface profiles of the hydraulic jump obtained by 3D URANS model considering both the standard and non-linear *k-ε* model are plotted in Fig. 5.7a. The experimental data of Bakhmeteff and Matzke (1936) and Madsen and Sevendsen (1983) are also depicted in Fig. 5.7a. The corresponding vector diagrams of both the models are depicted in Fig. 5.7b and Fig. 5.7c. The surface profile obtained for the standard *k-ε* model is in reasonable agreement with the experimental data. Contrary, the surface profile of the non-linear *k-ε* model is less steep than the experiments; indicating that the flow is not as steady as the one obtained by using the standard *k-ε* model. Madsen and Sevendsen's (1983) already stated that, the surface elevation is in proportional to the local energy dissipation. This, in

turn express that, for non-linear *k*-*ε* model the energy dissipation is much smaller than the experiments. Hence, the profile is not in good agreement with the experimental data.

5.4.2.2 Vertical distribution of streamwise velocity

The vertical distributions of non-dimensional streamwise velocity are plotted at different depths by referring to the experimental data (Fig. 5.8). In this case, theoretical results of Madsen et al. (1983) are also included for the sake of comparisons. The distributions of streamwise velocity are in close agreement with the theoretical results in the former part of the recirculation zone of the hydraulic jump. Though the measured data is little scattered, theoretical and hence numerical results are within the experimental reach; satisfying the continuity equation for each velocity profile. In the latter part of the recirculation zone, the measured data is in good agreement with the numerical results of both the models. This indicates the overall tendencies of the velocity profiles obtained from the standard and non-linear *k*-*ε* models are reproduced well within the accuracy of experiments.

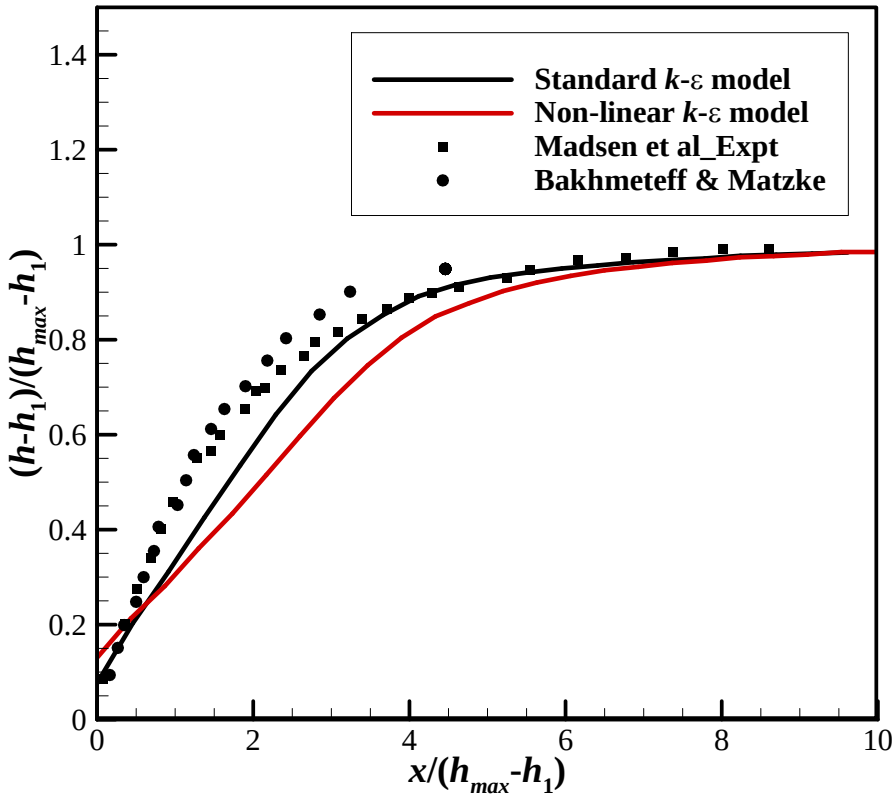

Figure 5.7a. Water surface profile obtained by 3D URANS model

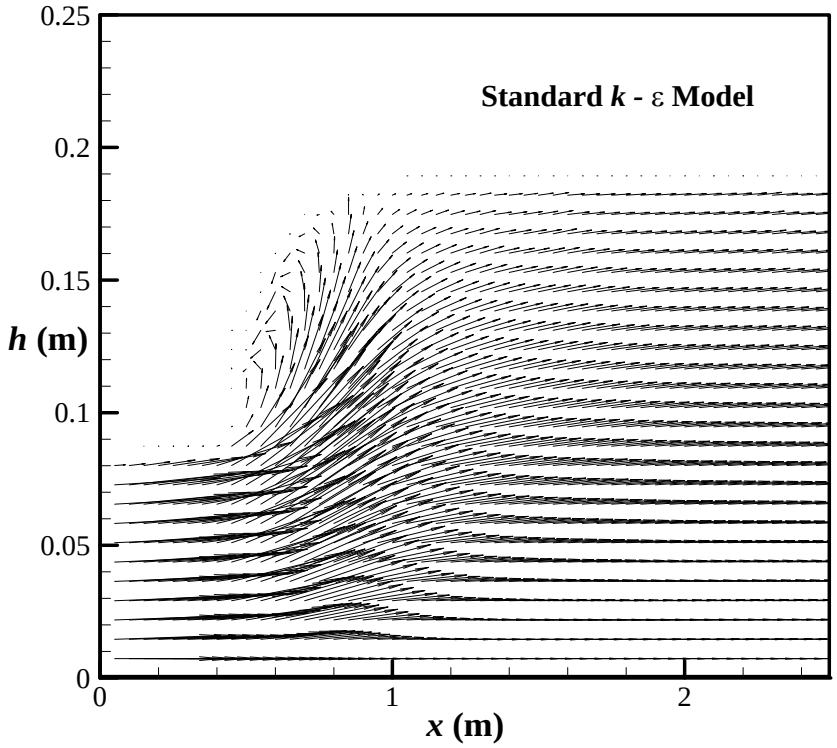

Figure 5.7b. Vector diagram of hydraulic jump obtained by the standard *k*-*ε* model

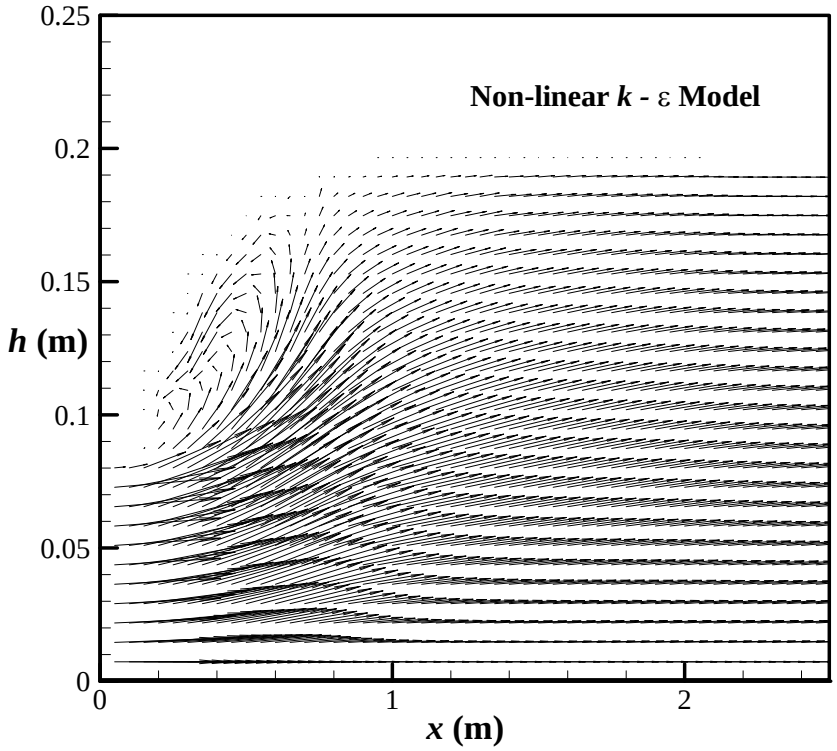

Figure 5.7c. Vector diagram of hydraulic jump obtained by non-linear *k*-*ε* model

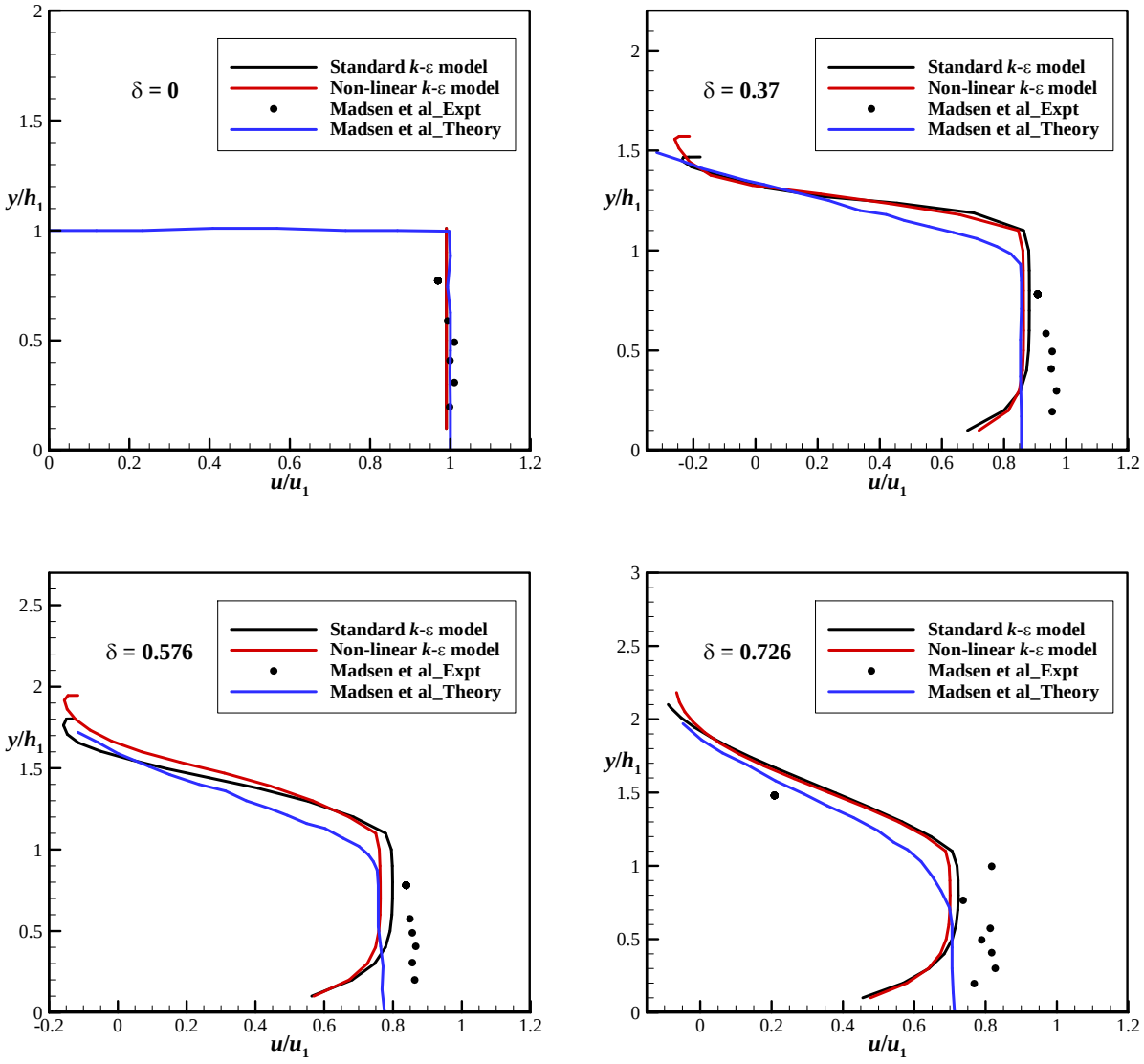

Figure 5.8a. Vertical distributions of streamwise velocity for different depths

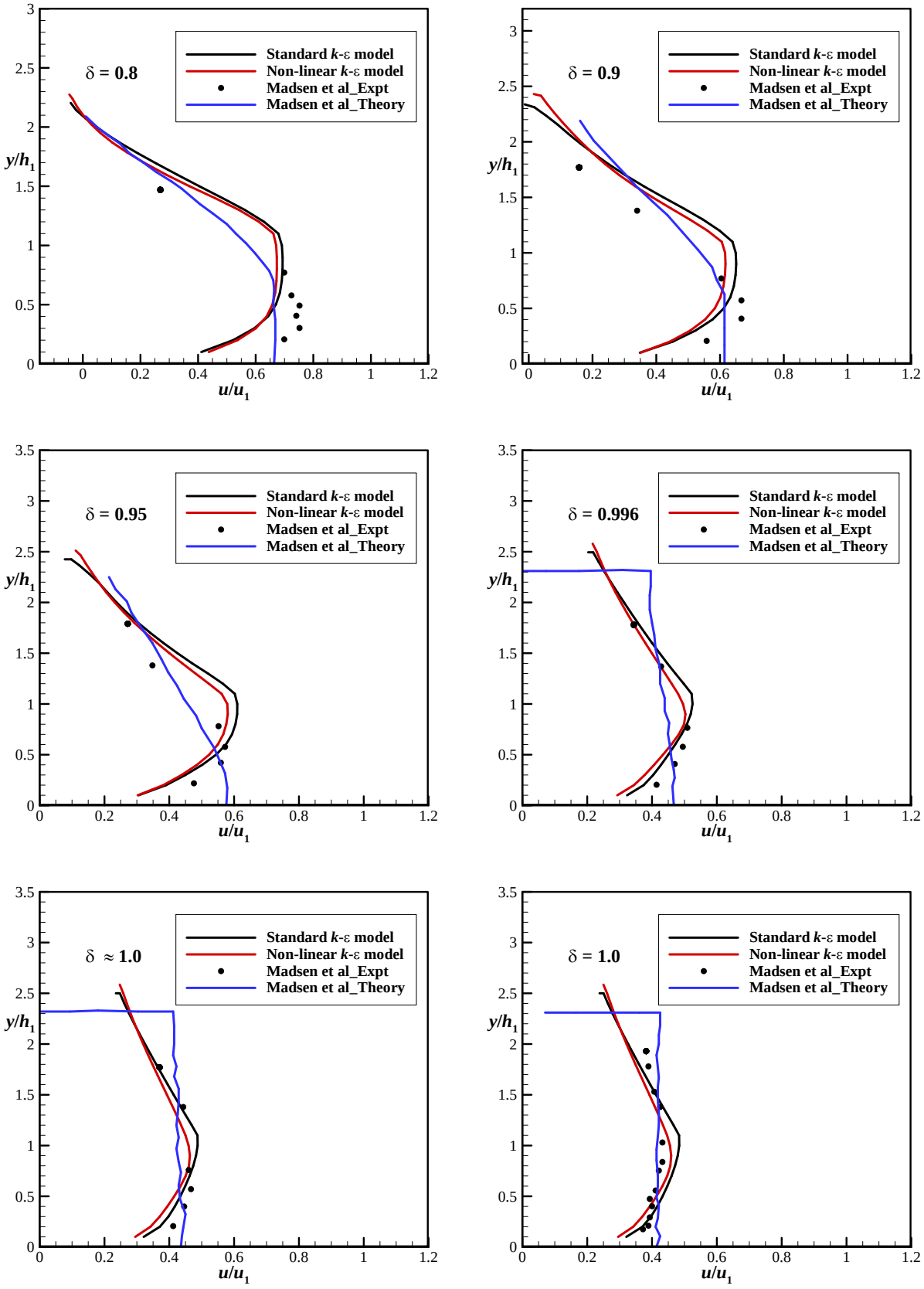

Figure 5.8b. Vertical distributions of streamwise velocity for different depths

5.4.2.3 Streamwise turbulence intensity

In Fig. 5.9, the vertical distributions of non-dimensional streamwise turbulence intensity component are illustrated along with the theoretical results of Madsen et al. (1983). For this particular case, three different curves of theoretical results are used for the comparisons. These three curves are obtained because of different values for coefficient 'A' are considered. Here, 'A' is the coefficients of third order polynomial considered in the theory of Madsen et al. (1983). Three different values of that coefficient indicate the effect of shear stress in the formulation. For instant, value A=2, corresponds to zero shear stress at the water surface. For values, less than 2 indicates the non-zero values of shear stress at the free surface. This is because Madsen et al. (1979) already reported that, in highly turbulent region of the surface roller, shear stresses are non-zero at the local mean water level. Accordingly, values 1.4 and 1.0 are selected for the comparisons.

For numerical results, two curves for each model (standard and non-linear k-ε model) are plotted. These curves indicates two different locations (x = 1.2 m and x =1.6 m) within the reach of recirculation zone. In Madsen et al. (1983)'s theoretical analysis, it is not mentioned clearly that, at which location the distribution is drawn. Additionally, it is already mentioned that they divided the flow region into the turbulent flow region and the potential flow region part. Therefore, the analytical results are plotted only for the turbulent region part and not for the potential flow region part. Although, it is possible to calculate the thickness of the potential flow region through their theory, it is not sure that this thickness also represents the potential flow region for the numerical simulation. Nevertheless, for the sake of comparisons in numerical results, the turbulent flow regions are decided with the help of their analysis. As shown in Fig. 5.9, convex shape near the bottom is still observed for the standard k-ε model. However, for non-linear k-ε model, in the later part of the recirculation zone (where x =1.6 m), the distribution shows similar tendency as like the theoretical results. Apart from the water surface profile and velocity distribution, the difference between the standard and the non-linear k-ε model is more visible in this case. In other words, the characteristic of streamwise turbulence intensity is reproduced well by the non-linear k-ε model as compared to the standard k-ε model.

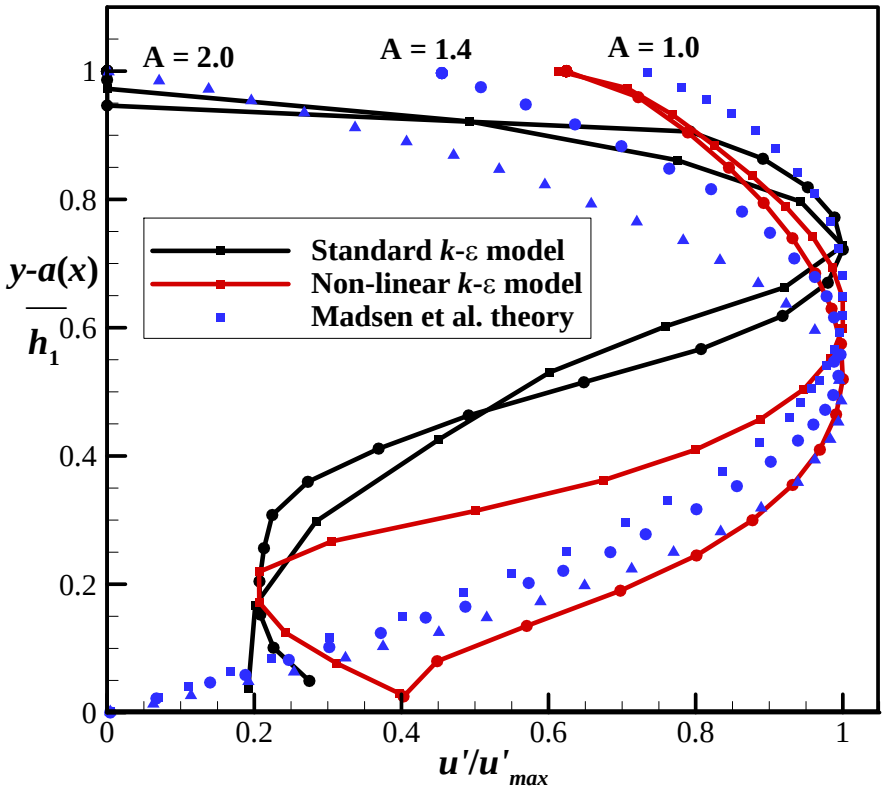

Figure 5.9. Vertical distribution of streamwise turbulence intensity

5.5 Summary

In this chapter, a simple theoretical model for determination of water surface profile and velocity distribution is developed in successive steps providing the existence of the solution. Additionally, the numerical simulations of the hydraulic jump by using the 3D URNAS model are also discussed.

Initially, the performance of the proposed analytical solution is analyzed by comparing the results with the previous experimental and theoretical results. Begin with the analytical solution of the momentum equation with eddy diffusivity term; the exact solution for water surface profile of the hydraulic jump is derived. In addition to the eddy diffusivity term, bed shear stress is also included into the momentum equation and it is solved numerically to get the water surface profile of the jump. Finding out the deficiency of those previous methods, a simple depth-averaged model is then proposed. The analytical solution obtained by the depth-averaged model satisfied the findings of the previous studies indicating

the reasonable agreement of the water surface profile with the experimental data. The assumptions employed for the velocity distribution also provided reasonably good agreement with the previous studies. However, further improvement is required to obtain the better comparison.

In the later part of this chapter, 3D URANS model is used to reproduce the characteristics of the hydraulic jump by using the standard k-ε and the non-linear k-ε model. The comparisons of water surface profile reproduce close agreement with the experimental data for the standard k-ε model as compared to the non-linear k-ε model. Besides the water surface profile for non-linear k-ε model, the comparisons of velocity distribution and streamwise turbulence intensity are in close agreement with the experimental and theoretical data. The performance of the non-linear k-ε model over the standard k-ε model could easily distinguish from the velocity and the streamwise turbulence intensity distributions.

5.6 References

Abbott, M. B. (1979). "Computational hydraulics: elements of the free surface flow." Pitman Publishing Ltd., London, England.

Bakhmeteff, B. A., and Matzke, A. E. (1936). "The hydraulic jump in terms of dynamic similarity." *Trans*., ASCE 101, 630-647.

Basco, D. R. (1983). "Introduction to rapidly-varied unsteady, free surface flow computation." *USGS, Water Resour. Invest. Report* No. 83-4284. U.S. Geological Service, Reston, Va.

Battjes, J. A., and Sakai, T. (1981). "Velocity fields in a steady breaker." *J. Fluid Mech*., 111, 421-437.

Bidone, G. (1819). "Observations sur le hauteur du ressaut hydraulique en 1818." Report, Royal Academy of Sciences, Turin, Italy. (in French).

Chippada, S., Ramaswamy, B., and Wheeler, M. F. (1994). "Numerical simulation of hydraulic jump*." International J. Num. Meth. in Eng*., 37, 1381-1397.

Chow, V. T. (1959). "Open channel hydraulics." McGraw-Hill Book Co., Incl., New York.

Gharangik, A. M., and Chaudhry, M. H. (1991). "Numerical solution of hydraulic jump." *J. Hydraul. Eng.*, 117(9), 1195-1211.

Katopodes, N. D. (1984). "A dissipative Galerkin scheme for open channel flow." *J. Hydraul. Eng.*, 110(4), 450-466.

Ma, F., Hou, Y., and Prinos, P. (2001). "Numerical calculation of submerged hydraulic jump." *J. Hydraul. Res.*, 39(5), 493-503.

Madsen, P. A., and Svendsen, I. A. (1983). "Turbulent bores and hydraulic jumps." *J. Fluid Mech.*, 129, 1-25.

Narayanan, R. (1975). "Wall jet analogy to hydraulic jump." *J. Hydraul. Div.*, 101(3), 347-359.

Peregrine, D. H., and Svendsen, I. A. (1978). "Spilling breakers, bores, and hydraulic jumps." *Proc. 16th Coastal Eng.*, Chapter 30, 540-550.

Rajaratnam, N. (1965). "The hydraulic jump as a wall jet." *J. Hydraul. Div.*, 91(5), 107-131.

Rouse, H., Siao, T. T., and Nagaratnam, S. (1958). "Turbulence characteristics of the hydraulic jump." *J. Hydraul. Div.*, 84(1), 1528-1-30.

Zhao, Q., and Misra, S. K. (2004). "Numerical study of turbulent hydraulic jump." *17th ASCE Eng. Mech. Conf.*, Univ. of Delaware, Newark, DE. 1-7.

Chapter 6

TRANSITION FROM UNDULAR JUMP TO STRONG HYDRAULIC JUMP

6.1 Preliminaries

In previous chapter water surface profile analysis is conducted by using 1D depth-averaged model. However, the numerical analysis is performed by excluding the Boussinesq term from the basic equation. The undular jump is one of the fundamental flows which considered the effect of vertical acceleration (Hosoda et al. 1994). In this type of the jump, the flow is characterized by free-surface undulations of decreasing amplitude which extend for a considerable distance downstream of the transition (Fig. 6.1), and replace the roller structure of the conventional jump (Montes et al. 1998). Undular jumps have been experimentally studied and described by many researchers but more extensive tests were performed by Chanson (1995).

Bakhmeteff and Matzke (1936) conducted the series of experiments for different Froude number. Through their investigations, they characterized the transitions of jump from undular to direct jump. Iwasa (1955) reported the limiting condition for the existence of the undular jump experimentally by remarking the breaking characteristics of the undular jump. Hosoda et al. (1994) on the other hand, simulated the breaking process of undular jump by multiplying the damping function to the vertical acceleration term.

Concerning the previous study, in this chapter free surface profile analysis for steady open channel flow is performed by using the one-dimensional basic equation with the vertical acceleration terms. Initially, the wave characteristic of the undular jump is reproduced numerically using a suitable eddy diffusivity term. Following the study of the hydraulic jump

new empirical relationship between the Froude number and the turbulent diffusivity coefficient is proposed in succession. Finally, with the help of proposed empirical relationship transitions of flow from undular jump to strong hydraulic jump is explained.

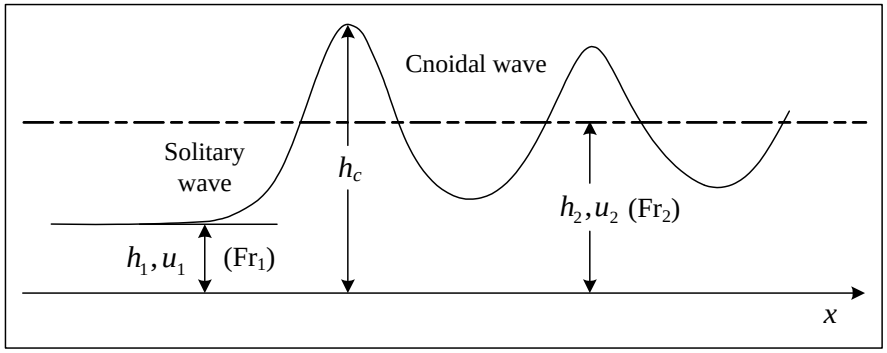

Figure 6.1. Schematic illustration of undular jump

6.2 Empirical relationship between Froude number and proportionality factor

The definition of turbulent diffusivity coefficient indicated that the value of α occurred in the range of 0.005 to 0.1. Contrary to this range, for water surface computation of hydraulic jump, different values of α are considered and the suitable value, which reproduce the reasonable agreement with the experimental data is employed (as shown in Fig. 5.3). This comparisons further lead to conclude that Froude number has a direct relationship with the turbulent diffusivity coefficient. Therefore, in order to compute the water surface profile for different types of jump, it is necessary to find a suitable relationship between the Froude number and the proportionality factor α. Consequently, the empirical relationship between the Froude number and the proportionality factor α is proposed with the help of comparisons of the numerical and the experimental data. This empirical relationship is expressed as

$$\alpha_1 = \alpha_0 + \alpha_0' \left(Fr_1 - 1\right)^{1.25} \tag{6.1}$$

where, $\alpha_0 = 0.01$, $\alpha_0' = 0.396$ and α_1 is a new proportionality factor.

6.3 Transition from undular jump to strong jump

To validate the applicability of the proposed empirical relationship, the computation of water surface profile of the jump for different Froude number needs to calculate. To do so,

experimental data of Bakhmeteff and Matzke (1936), Dunbabin (1996) and Montes et al. (1998) that consisting the range of Froude numbers 1.25 to 8.87 are considered for the simulations.

6.3.1 Numerical model

The momentum equation by including eddy diffusivity and the vertical acceleration term is given as

$$\frac{d}{dx}\left(h\,U^2 + \frac{g}{2}h^2\cos\theta + \frac{1}{3}h^2\,U^2\frac{d^2h}{dx^2} - \frac{1}{3}hU^2\left(\frac{dh}{dx}\right)^2 \right) = \frac{d}{dx}\left(D_m h\frac{dU}{dx} \right) + gh\sin\theta - \frac{\tau_{bx}}{\rho} \tag{6.2}$$

where, x = streamwise distance; h = flow depth; U = depth-averaged velocity; θ = angle made by the streamwise slope with the horizontal; D_m = eddy diffusivity coefficient; g = gravitational acceleration; τ_{bx} = bed shear stress; ρ = mass density of fluids.

Assuming the equilibrium between the gravity and the frictional terms and integrating Eq. 6.2, following equation is obtained.

$$\frac{q^2}{h} + \frac{gh^2}{2}\cos\theta + \frac{1}{3}q^2\frac{d^2h}{dx^2} - \frac{1}{3}\frac{q^2}{h}\left(\frac{dh}{dx}\right)^2 - D_m h\frac{d}{dx}\left(\frac{q}{h}\right) = M_0 \tag{6.3}$$

where, momentum flux M_0 is defined as

$$M_0 = \frac{q^2}{h_1} + g\frac{h_1^2}{2} \tag{6.4}$$

Representing Eq. (6.3), into the following form,

$$\frac{dh}{dx} = p\,; \qquad \frac{q^2}{3}\frac{dp}{dx} = \frac{1}{3}\frac{q^2}{h}p^2 - \frac{D_m q}{h}p + \left(M_0 - \frac{q^2}{h} - \frac{gh^2}{2}\cos\theta \right) \tag{6.5}$$

The singular point in the basic equation is the point satisfying the relation, $p = 0$ and $M_0 = q^2/h + gh^2/2$. That is these singular points are the two-depth satisfied by the conjugate relation. It is assumed that the depth obtained from the reduction of undulations at the downstream of the jump satisfied the conditions of the singular point. Singular points are classified in the following relation by linearizing the basic equation around this depth and for Fr <1.

$$\left(\frac{3D_m}{q}\right)^2 + 12\left(1-\frac{1}{Fr_1^2}\right) \quad \begin{matrix} > 0 & : & stable\ nodal\ point \\ < 0 & : & stable\ focal\ point \end{matrix} \tag{6.6}$$

As Whitham (1974) suggested that, the undular jump is corresponding to the region of stable focal point. On the other hand, it is considered that the region of stable nodal point have no meaning from the viewpoint of hydraulics, because D_m / q has very large value.

Therefore, to evaluate the transitions from focal to nodal point, the empirical relationship is needs to incorporate into the basic equation. To do so, eddy diffusivity coefficient is calculated as

$$D_m = \alpha_1\, q \tag{6.7}$$

6.3.2 Computational results

To evaluate the water surface profile for different types of jump, Eq. 6.3 is solved numerically by using the 4th order Runge-Kutta method. The calculation proceeds with the initial values of water depth and the derivative of depth as an initial condition. Depending on the Froude number, Δx is selected for the computation. Begin with the upstream depth and the derivative at the upstream end the numerical simulation is conducted by using new α_1 value based on Froude number. For the sake of comparisons the numerical results for $\alpha_1 = 0.01$ are also calculated. The selective comparisons of numerical results are shown in Fig. 6.2-6.5 and corresponding hydraulic variables of numerical simulations are tabulated in Table 6.1 and Table 6.2. The first crest of the solitary wave h_c for $\alpha_1 = 0.01$ and first crest of the solitary wave or conjugate depth h_2 (depending on Froude number) for new α_1 value are also tabulated in Table 6.1 and 6.2. It is evident from figures that, because of vertical acceleration term in basic equation, the wave characteristics of undular jump are reproduced well by the numerical simulation for small Froude number. As the Froude number, hence α_1 value increases, the free surface undulations downstream of the jump disappear and the jump reverts to a weak conventional jump. Further increase of Froude number leads to the roller formation and intense mixing of the strong hydraulic jump. To depict this transitional characteristics of jump from undular jump to strong hydraulic jump it is necessary to discuss the relation between the downstream depth and the Froude number.

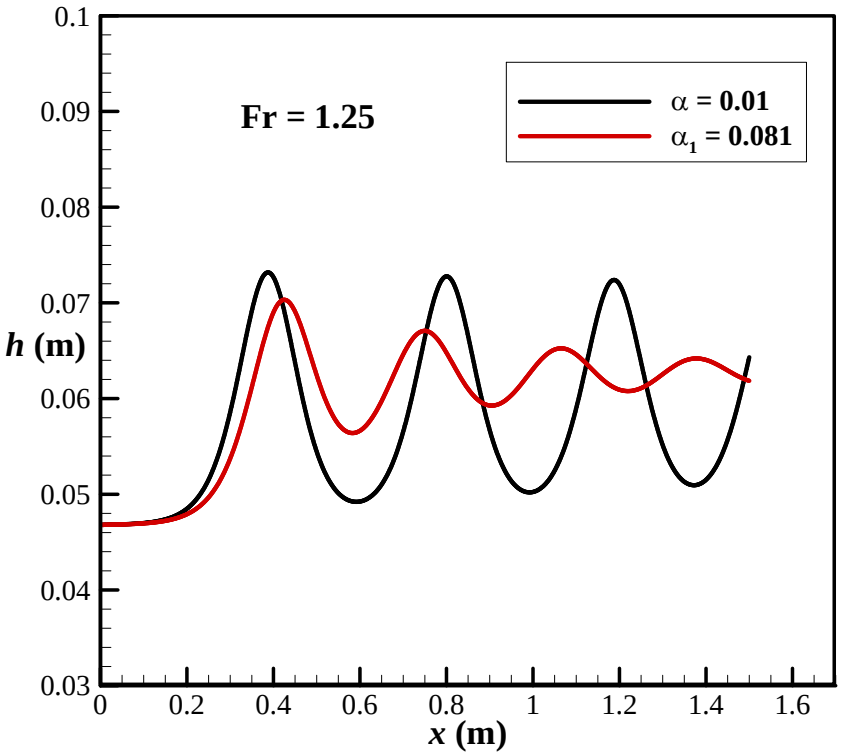

Figure 6.2. Computational result of water surface profile of jump for case C1

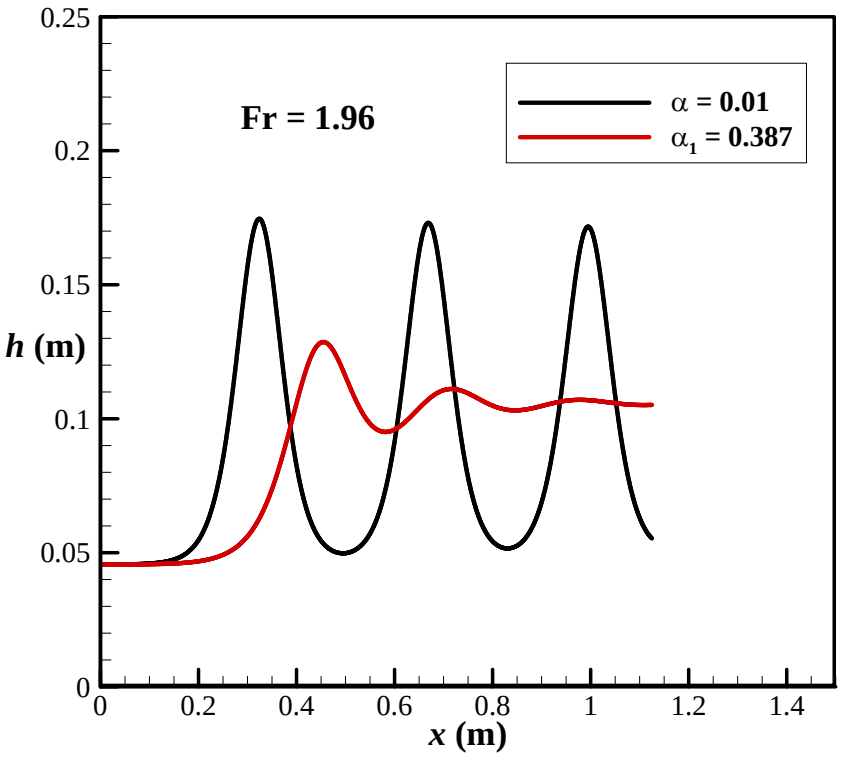

Figure 6.3. Computational result of water surface profile of jump for case C6

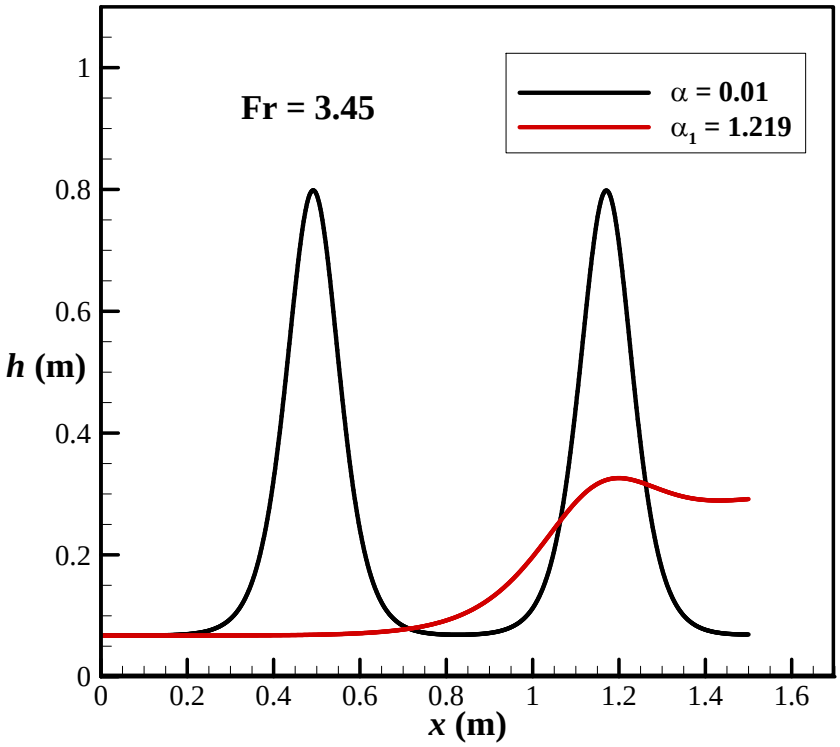

Figure 6.4. Computational result of water surface profile of jump for case S29

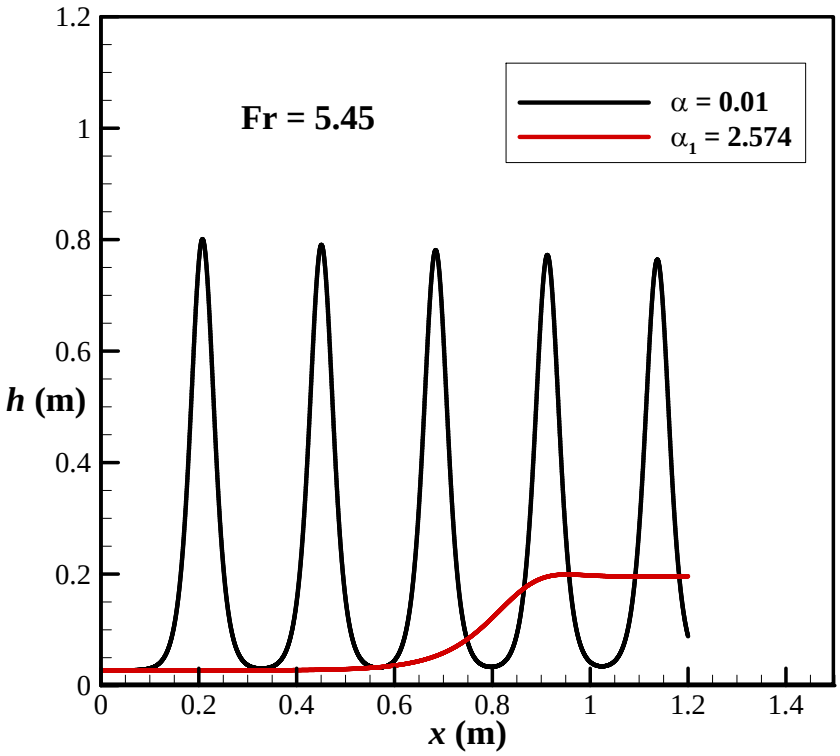

Figure 6.5. Computational result of water surface profile of jump for case S17

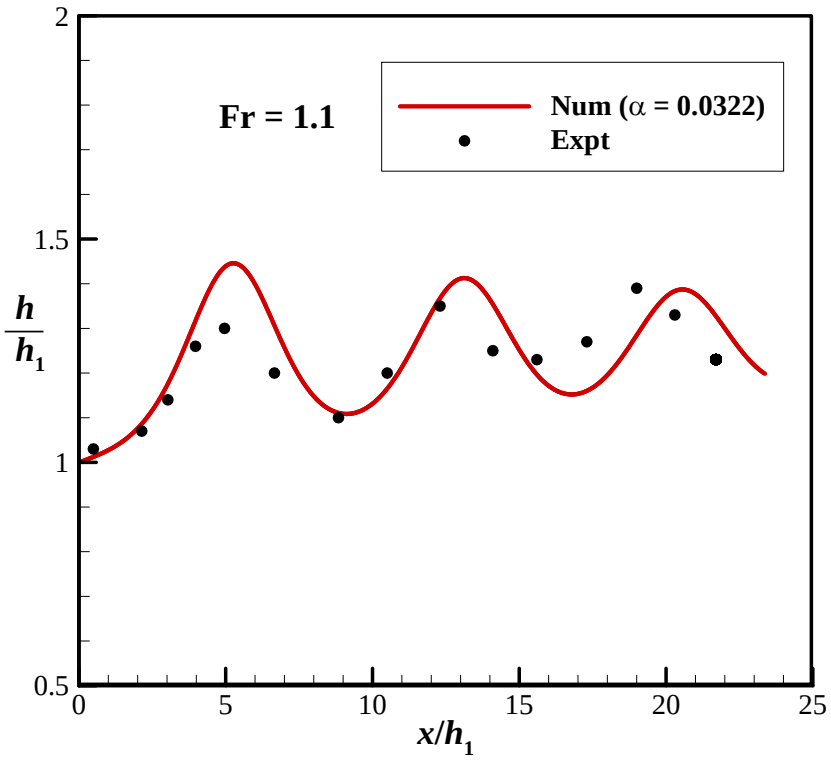

Figure 6.6. Comparison of the numerical result with the experimental data

Table 6.1. Hydraulic variables of Dunbabin (1996) and Montes et al. (1998)'s experimental data considered for numerical simulation

No.	h_1 (m)	Fr	Slope	q (m^2/s)	h_c (m)	h_2 (m)	α_1
C1	0.0468	1.25	0.0044	0.0397	0.0732	0.0703	0.081
C2	0.0292	1.27	0.0044	0.0198	0.0468	0.0448	0.086
C3	0.0420	1.48	0.0038	0.0399	0.0919	0.0822	0.169
C4	0.0240	1.70	0.0083	0.0198	0.0694	0.0569	0.264
C5	0.0384	1.70	0.0083	0.0400	0.1100	0.0907	0.263
C6	0.0456	1.96	0.0049	0.0598	0.1750	0.1290	0.387
C7	0.0210	2.10	0.0132	0.0200	0.0920	0.0639	0.456
C8	0.0191	2.40	0.0173	0.0198	0.1090	0.0666	0.611
D1	0.061	1.41	0.003	0.0631	0.109	0.102	0.112
D2	0.067	1.52	0.003	0.0792	0.142	0.128	0.159
D3	0.057	1.63	0.003	0.0695	0.151	0.128	0.233

Table 6.2. Hydraulic variables of Bakhmeteff and Matzke (1936)'s experimental data considered for numerical simulation

No.	h_1 (m)	Fr	q (m^2/s)	Expt. h_2 (m)	h_c (m)	h_2 (m)	α_1
S27	0.0771	1.94	0.1301	0.171	0.289	0.215	0.376
S30	0.0765	1.98	0.1316	0.175	0.301	0.219	0.399
S40	0.0686	2.12	0.1171	0.165	0.296	0.207	0.447
S43	0.0695	2.13	0.1219	0.168	0.313	0.214	0.469
S25	0.0774	2.31	0.1561	0.211	0.414	0.261	0.568
S45	0.0759	2.34	0.1531	0.208	0.414	0.258	0.580
S41	0.0695	2.57	0.1478	0.208	0.460	0.259	0.709
S24	0.0756	2.59	0.1687	0.233	0.507	0.284	0.718
S28	0.0759	2.92	0.1914	0.269	0.647	0.318	0.907
S26	0.0774	3.15	0.2122	0.301	0.765	0.346	1.040
S29	0.0674	3.45	0.1886	0.292	0.799	0.326	1.219
S36	0.0512	4.10	0.1486	0.265	0.855	0.288	1.637
S18	0.0381	4.56	0.1067	0.226	0.799	0.238	1.962
S6	0.0326	5.01	0.0918	0.215	0.802	0.219	2.238
S17	0.0271	5.45	0.0762	0.192	0.801	0.199	2.574
S39	0.0274	5.53	0.0786	0.202	0.834	0.204	2.631
S35	0.0189	6.69	0.0544	0.163	0.842	0.170	3.488
S37	0.0162	7.34	0.0472	0.153	0.865	0.159	3.972
S32	0.0143	7.89	0.0424	0.145	0.890	0.153	4.455
S34	0.0122	8.29	0.0349	0.133	0.829	0.137	4.740
S33	0.0119	8.63	0.0346	0.131	0.858	0.137	4.937
S38	0.0098	8.87	0.0268	0.116	0.768	0.118	5.248

As a basis for the comparisons and to check the validity of the empirical relationship the obtained numerical results are compared with the experimental data for Fr =1.1, as shown in Fig. 6.6. It is seen from the figures that, the downstream depth for the experiment is less than the conjugate depth. Therefore, the numerical results show higher amplitudes of the waves as compared to the experiment.

To ensure the transition of flow from undular to strong hydraulic jump by proposed empirical relationship; the relation between the maximum depth and the upstream Froude number is plotted in Fig. 6.7. As a basis for the comparison the crest depth of solitary wave (Eq. 6.8) given by Hosoda et al. (1994) and the curve for conjugate depth of the conventional hydraulic jump (Eq. 6.9) are included in Fig. 6.7. The experimental data of Iwasa (1955) is also included into the Fig. 6.7.

$$\frac{h_c}{h_1} = Fr_1^2 \tag{6.8}$$

$$\frac{h_2}{h_1} = \frac{1}{2}\left(\sqrt{1+8Fr_1^2}-1\right) \tag{6.9}$$

It is seen from figure that, for small Froude number, the first crest height of the undular jump follows the theoretical curve of solitary wave. From experimental investigation Iwasa (1955) reported that, the limiting condition of occurrence of the undular jump lies within the range of $Fr_1 = 1.5$ to $Fr_1 = 1.9$. Further he indicated that for $Fr_1 = 1.6$, the experimental points deviated from the theoretical curve of solitary wave. Bakhmeteff and Matzke (1936) defined this limit as a transitional zone; equivalent to $Fr_1 = 1.5$. The computed result with the proposed empirical relation also able to reproduce this characteristics indicating the deviation from the theoretical curve at $Fr_1 = 1.5$. As Froude number increases, the breaking of wave causes discontinuous profile of the water surface. Iwasa (1955) experimentally reported that range from $Fr_1 = 1.5$ to $Fr_1 = 1.9$, which corresponds to likely breaking or transition of the jump. The breaking or roller formation occurs from $Fr_1 > 2$. In Fig. 6.7, different colours represent the breaking process of the undular jump as indicated by Iwasa (1955). From the observations, the computational results contained within the depth ratios of 2.5-3.0 corresponding to the likely breaking phenomenon of the jump. Further increase of Froude number brings the computational results close to the conjugate depth, indicating the formation of strong hydraulic jump.

6.4 Summary

In this chapter, new empirical relationship between the Froude number and the proportionality factor is proposed using the help of numerical results of hydraulic jump. To

verify the applicability of the proposed relationship, one dimensional basic equation is solved numerically considering the vertical acceleration term. Different types of jump are computed based on the proposed relationship. The obtained results are then compared with the Froude number to assure the transition of flow from continuous water surface profile of undular jump to the discontinuous water surface profile of strong hydraulic jump.

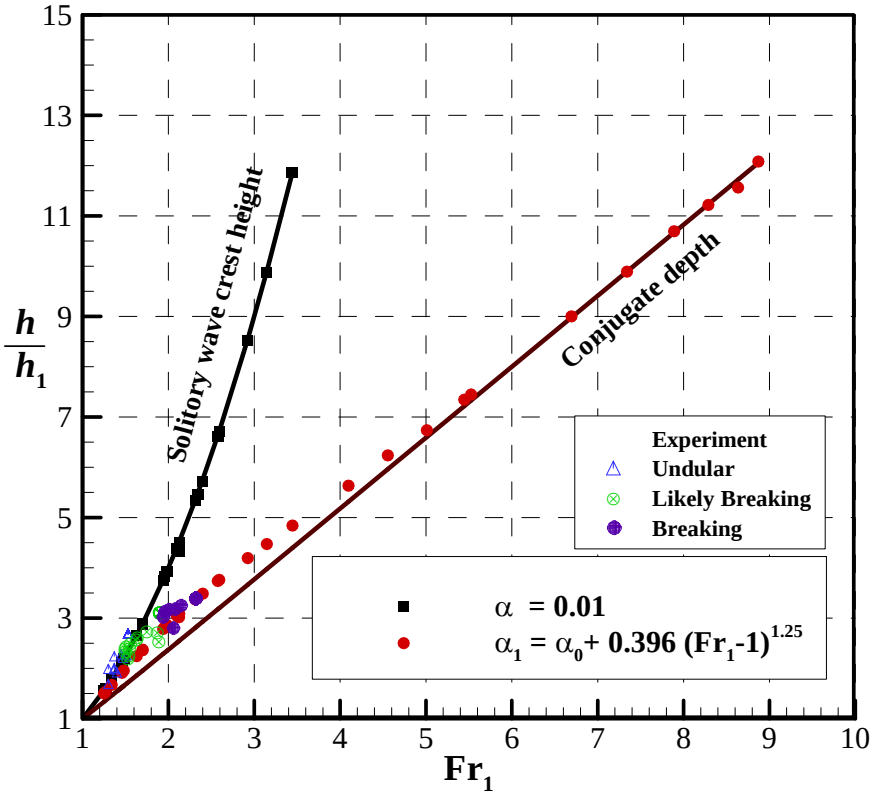

Figure 6.7. Transition from undular jump to strong hydraulic jump

6.5 References

Bakhmeteff, B. A., and Matzke, A. E. (1936). "The hydraulic jump in terms of dynamic similarity." *Trans*., ASCE 101, 630-647.

Chanson, H. (1995). "Flow characteristics of undular hydraulic jumps: comparison with near-critical flows." *Report CH45/95, Dept. of Civil Eng.*, Univ. of Queensland, Australia.

Dunbabin, R. (1996). "Velocity distributions within an undular hydraulic jump." *Honors Thesis, Dept. of Civil and Mech. Eng.*, Univ. of Tasmania, Australia.

Iwasa, Y. (1955). "Undular jump and its limiting condition for existence." *Proc. 5th Japan National Cong. App. Mech.*, 315-319.

Hosoda, T., and Tada, A. (1994). "Free surface profile analysis of open channel flows by means of 1-D basic equations with effect of vertical acceleration." *J. Japanese Soc. of Civil Eng*, 38, 457-462. (in Japanese).

Montes, J. S., and Chanson, H. (1998). "Characteristics of undular hydraulic jumps: experiments and analysis." *J. Hydraul. Eng.*, 124(2), 192-204.

Whitham, G. B. (1974). "Linear and nonlinear waves." Chapter 13, John Wiley and sons.

Chapter 7
CONCLUSIONS

7.1 Summary of the findings

To understand the fundamental characteristics of unsteady varied flows numerical and analytical studies are conducted for open channel flows. Beginning from simple one-dimensional depth-averaged model, the hydrodynamic behaviour of the unsteady non-uniform flows over smooth and rough beds is examined by 3D unsteady RANS model. The deficiency of one-dimensional depth-averaged model in production of velocity distributions led to further analysis for evaluations of flow properties. This is done by the analytical study of the standard k-ε model. In coordination with improvement of velocity distributions, other flow properties such as, turbulent kinetic energy k, turbulent energy dissipation rate ε and eddy viscosity are evaluated using the analytical solution. Additionally, the effect of damping function on the distributions of aforementioned properties near free surface zone is also verified analytically. After analyzing the characteristics of gradually varied unsteady flows, an analytical study based on deformation principle and the numerical study by using 3D unsteady RANS model are performed for rapidly varied unsteady flows. Finally, the transitions of flows from continuous water surface profile to discontinuous water surface profile for rapidly varied unsteady flows are discussed. The summary of these numerical and analytical studies of the research are concluded below under respective topics.

7.1.1 1D depth-averaged velocity deformation model

To overcome the inaccuracy of Engelund model and to propose friction velocity formula, simple depth-averaged velocity deformation model is derived in this chapter. The comparison of numerical results with the experimental data showed that, the characteristics of

bed shear stress is similar to the experimental one. It means that, the bed shear stress attains peak value before the peak depth appears and the maximum value of it increases with an increase in unsteadiness of the flows. Similarly, thickness of the loop characteristics of the streamwise velocity increases with an increase in unsteadiness of the flows.

Because of inclusion of additional shear stresses into the model, the deformation of the velocity distributions from that of uniform velocity distribution of the Engelund model is observed. This deformation between these two models is increases with an increase in unsteadiness of the flow and vice versa.

These characteristics are valid for both kinds of bed cases: smooth beds and rough beds. This suggests that the velocity deformation model is adequate for the unsteady varied flows over smooth bed and rough bed as well.

7.1.2 3D unsteady RANS model

The turbulent characteristics of unsteady non-uniform flows are studied well by the 3D unsteady RANS model. Similar to 1D model, two experimental conditions; smooth bed and rough bed condition, are computed. The behaviour of the model is compared in accordance with the numerical results of the standard and non-linear k-ε model. The distributions of bed shear stress and loop property of averaged velocity, turbulence intensities and Reynolds stresses in smooth bed cases followed the same trend. Though the distributions of Reynolds stresses during the passage of flood flows are diverted from those experimental results, turbulence intensities are in close agreements with the experimental data for high unsteadiness case. Contrary, for less unsteadiness case the distributions of Reynolds stresses and turbulence intensities (especially vertical component) are in good agreement with the steady state condition.

Apart from the comparisons in smooth bed case, the distributions of numerical results are in good agreement with the experimental data in rough bed case. In this particular case, the difference between the linear and non-linear k-ε model is more pronounced, indicating that the turbulence characteristics of the non-linear k-ε model are in good agreement to the steady state condition than the standard k-ε model.

7.1.3 Analytical solution of the standard *k*-*ε* model

For improvements of velocity distributions and examination of damping function on flow properties, an analytical solution of the standard *k*-*ε* model is developed. Initially, an effective analytical solution for uniform flow by excluding the damping function is derived. This solution is then compared with another analytical solution, which is deduced by including the damping function. The comparisons between two analytical solutions exhibited negligible effects of the damping function on the velocity distributions. Contrarily, the damping function illustrated small effect on energy dissipation rate near the free surface zone. Because of influence of the coefficient of the damping function, the distribution of turbulent kinetic energy was unable to produce the damping effect near the free surface. Although, some divergence observed for analytical results while in comparisons with the numerical results, the overall tendency is maintained well by the analytical results.

In non-uniform flow conditions, two kinds of flow: accelerated and decelerated flows are analyzed by including and excluding the damping function. The analytical results are then compared with the experimental data. The distributions of streamwise velocity for decelerated flows reproduced good comparison with the experiment than the accelerated flows. On the other hand, distribution of vertical velocity is in good agreement for both the cases. The characteristics of the turbulence intensities in respective flows are acquired well by the solution, except near the wall region. It is because of the wall function values employed for the non-uniform flow case. Similar to uniform flow analysis, in this case also, kinetic energy failed to reproduce the damping effect near free surface. Nevertheless, the effect of damping function on energy dissipation rate and on eddy viscosity is observed well. The nature of energy dissipation rate and eddy viscosity further satisfied the conditions of the flows. In other words, more energy dissipation is observed for accelerated flows than decelerated flows while comparing to the uniform flow distributions. Similar trend is observed for eddy viscosity distribution; where, the distribution of eddy viscosity is damped in accelerated flow and amplified in decelerated flow while in comparisons with the uniform flow.

7.1.4 Analysis of hydraulic jump

Following the deformation principle in gradually varied unsteady flows, an analytical solution for hydraulic jump is developed in successive steps. The analysis starts with the solution of momentum equation by including the eddy diffusivity term. The obtained results with this solution could reproduce the continuous profile of the jump between two conjugate depths. The solutions also brought the similar trend of continuous profile between two conjugate depths when bed shear stress term is included into the basic equation. However, obtained results from both the methods reproduced appropriate characteristics (in comparisons with the experiments) only for large proportionality factor. This led to further analysis for the evaluation of formation of the jump. The simple depth-averaged model by including the velocity deformation is then proposed. The behavior of the model is verified in comparisons with the experimental data. Though further improvement is required, it is found that the proposed model can reproduced the experimental characteristics from the view point of accuracy of the approximate distributions.

After analyzing depth-averaged model, the numerical simulations of the hydraulic jump by 3D unsteady RANS model considering the standard and the non-linear k-ε model is conducted in another section. The computed results are compared with the previous experimental and theoretical results. The comparisons of water surface profile showed that, more local energy dissipation is observed for the non-linear k-ε model. However, the vertical distributions of streamwise velocities for both models reproduced the close agreement with the theoretical results. The pronounced effect of the non-linearity is observed in streamwise turbulence intensity distributions, where non-linear k-ε model produced reasonable agreement with the previous theoretical data as compared to the standard k-ε model.

7.1.5 Transitions from undular to strong hydraulic jump

The numerical simulation of hydraulic jump led to conclude that the Froude number has a direct relationship with the turbulent diffusivity coefficient. This finding extended the objective of the analysis to propose that relationship. Thus, with the help of numerical results of hydraulic jump, empirical relationship between the Froude number and proportionality factor is proposed. The applicability of the empirical formula is verified by computing the different types of jump. This is done by introducing the empirical relation into the Boussinesq

equation and solving the equation numerically by using 4^{th} order Runge-Kutta method. The computational results reproduced the reasonable water surface profile for different Froude number. The comparisons of numerical results with the theoretical curves also showed that, the breaking process of the undular jump and transition to strong hydraulic jump is well characterized by the obtained results. This ensured the applicability of the proposed empirical relationship.

7.2 Recommendations for future studies

Based on the numerical and analytical results of proposed problems and in comparisons with the previous findings, this research leads to following recommendations for future works:

For one-dimensional depth-averaged model simulations are performed over rough beds without incorporating the sediment transport model. Because of which sediment transport characteristics was not able to produce during flood flows. Therefore, to study the behavior of the model in more practical way it is better to include the sediment transport model for further studies.

In analytical solutions of the standard k-ε model for non-uniform flow, the wall functions did not reproduce the similar characteristics as like the experimental results. Although, new wall function is proposed for present research, the effectiveness of the wall function is not satisfactory. Therefore, it is further necessary to derive the new wall function values for non-uniform flow. Along with wall function values further improvements in the analytical solution is also required to depict the effect of damping function on turbulent energy production.

Only analytical solution for standard k-ε model is derived here for the sake of evaluation of flow properties. So as to next, simple depth-averaged model can be developed based on these findings.